GEO-CHEMO-MECHANICAL MODELING OF SEDIMENTARY ROCKS: APPLICATION TO UNCONVENTIONAL RESERVOIRS AND GEOLOGICAL CO_2 SEQUESTRATION

BY

POOYAN KABIR

DISSERTATION

Submitted in partial fulfillment of the requirements
for the degree of Doctor of Philosophy in Civil Engineering
in the Graduate College of the
University of Illinois at Urbana-Champaign, 2018

Urbana, Illinois

Doctoral Committee:

Assistant Professor Ange-Therese Akono, Chair
Professor John Popovics, Co-Chair
Professor Gholamreza Mesri
Associate Professor Gianluca Cusatis, Northwestern University

Abstract

Due to their abundance, sedimentary rocks are playing a critical role in re-defining the world's energy landscape, leading to shifts in global geopolitics. The recovery of oil and gas from organic-rich shales, geological sequestration of CO_2 in sandstone host rocks and storage of nuclear waste in impermeable rocks are among the most challenging problems worldwide. Technical challenges and environmental concerns slow the growth of organic-rich shale exploration and exploitation worldwide. Similarly, the technical challenges and lack of financial incentives continue to slow the growth of geological storage of CO_2 worldwide. The engineering and scientific challenges emerge due to the extremely heterogeneous and anisotropic nature of these naturally occurring geo-composites at multiple length scales. Specifically, the effect of rate and speed of loading on fracture of organic rich shale, the effect of fabric and mineralogy on the mechanical behavior of organic-rich shales becomes of critical importance for petroleum engineers. Similarly, the effect of geochemical alterations in geomechanical behavior becomes of critical importance for storage of CO_2 in deep saline formations.

Thus, this thesis develops a comprehensive nano-investigation approach to assess the microstructure as well as the stiffness, strength and fracture properties of these naturally occurring geo-materials. Specifically, the effects of anisotropy, organic content and mineralogy on mechanical behavior of organic-rich shale are investigated. Similarly, the effect of geochemical alterations on host rock mechanical response are investigated. This is achieved by a comprehensive experimental micromechanics approach. This study utilizes advanced experimental and analytical techniques, i.e. analytical nanoindentation, scratch testing, environmental scanning electron microscopy, to provide the basis for assessment of microstructure and material invariant properties. Nanoindentation experiments and analysis tools are designed to probe and infer the elastic and strength properties of the geo-composites. Furthermore, scratch testing experiments are designed to probe and infer the fracture toughness of the geo-composites.

The results of this investigation show that organic-rich shale exhibit exceptional toughness due to toughening mechanisms operating at the nanometer scale in the kerogen and at the clay-kerogen interface. Furthermore, fracture behavior is anisotropic as a combined result of a layered microstructure and the intrinsic fracture behavior of clay. Additionally, the effect of geochemical alterations on host rock, Mt. Simon, is investigated using nanoindentation testing. The result of this investigation indicates a dissolution of feldspar during incubation regimes in slightly acidic brine and in CO_2-saturated brine. At the macroscopic length-scale, a weakening of the rock is predicted based on the formulated multiscale nanomechanics framework. These findings are important and will inform advanced physics-based constitutive materials law for geomechanics simulation in energy-related application such as hydraulic fracturing in unconventional reservoirs or geological CO_2 sequestration in deep saline formations.

Dedication

To my lovely parents, Maman Parvin & Baba Mohammadreza, for their love and support and my beloved brother Poorya.

Acknowledgments

First and foremost, I would like to express my gratitude to my adviser, Prof. Ange-Therese Akono. Her continuous support, encouragements and patience have been instrumental to this work. I have cherished every one of our discussions and will look froward to many more years during my career. Also, I am grateful to my committee members: Prof. Mesri, Prof. Popovics and Prof. Cusatis for their fruitful advice along those years. I also thank my fellows and colleagues at UIUC, especially Kevin Anderson, Amrita Kataruka, Yue Cui, Kavya Mendu and Jiaxin Chen, who made this experience a lot more enjoyable. Also, special thanks to my friend Hossein Tabatabaie Yazdi for his wonderful comments and suggestions. Last but not least, I would like to extend my deepest gratitude, love and affection to my beloved family, for loving me, believing in me and wishing the best for me. I owe all my achievements to their pure hearts; such pure hearts that anything they dream for me comes true. I am truly grateful for my family, Mohammadreza, Parvin and Poorya.

Contents

Part I

General Presentation

Chapter 1

Introduction

Sedimentary rocks composed mainly of silicate particles derived by the weathering breakdown of older rocks and by pyroclastic volcanism are called siliciclastic sedimentary rocks. Sandstones, conglomerates, and shales compose the members of this group. Petroleum geologists are especially interested in sandstone because more than half of the world's reserves of oil and gas occur in these rocks. Shales are likewise of great interest because the organic matter contained in shales is the source material of oil and gas. In recent years, gas shale has gripped the attention of the scientific community. This is primarily due to the relevance of the material in energy harvesting applications such as hydrocarbon recovery from unconventional reservoirs, carbon dioxide geological sequestration in depleted reservoirs or nuclear waste storage. Over the last ten years, the natural shale gas share has grown exponentially, radically transforming the United States energy outlook. In 2011, the natural gas shale production represented 34% of the total production compared to 1% in 2000 [1, 2]. Shale gas is expected to rise to 67% of the overall production by 2035, generating lower natural gas prices and electricity prices [3]. The development of shale gas resources will also generate significant economic value as well as over 1.6 million jobs over the next 20 years [2]. This economic expansion will be supported by breakthroughs in the science and technology of shale gas extraction [1].

Organic-rich shale or black shale is a unique class of organic-inorganic nano-composite that plays a crucial role in several climate change mitigation strategies such as energy recovery from unconventional resources [4–9], carbon dioxide subsurface capture and storage [10–12] and nuclear waste geological disposal [13, 14]. Understanding the mechanical behavior of the source rock at the microscopic [15–17] and nanometer [18] length scale is key to achieve significant breakthroughs in the science and technology of horizontal well

drilling and hydraulic fracturing [19–21]. CO_2 geological sequestration involves pumping industrial carbon dioxide emissions into deep permeable geologic formations at a steady rate [10]. Potential suitable formations include aquifer, depleted oil and gas fields and coal seams. Maintaining the structural integrity of the well, preventing the occurrence of micro-seismic events, and understanding potential chemo-mechanics degradation processes in the source rock due to brine exposure are major concerns [22, 23]. Although a lot of attention has been given to coal seams, depleted organic-rich shale formations [24] represent an alternative yet unexplored. The safe disposal of radioactive wastes requires these wastes to be isolated from all ecosystems for thousands of years. Deep argillaceous formations with a low intrinsic permeability such as organic-rich shale have been investigated as potential repositories [13, 14]. Thus, it is important to understand the chemical as well as mechanistic properties and fracture properties of organic-rich shale [25].

Fossil fuels such as coal, oil, and natural gas currently provide and are expected to continue to provide the vast majority of energy needed to sustain societies. These fuels contain high percentages of one source of carbon element. Thus, while burning these fossil fuels, carbon reacts with oxygen to produce CO_2. Due to the reliance on fossil fuels for both energy production and industrial processes, the amount of CO_2 in the atmosphere has increased since the Industrial Revolution. This increase in the CO_2 production has led to an increase in global temperatures due to heat radiating back from the Earth's surface and getting trapped in the Earth's atmosphere. The use of natural gas and coal will continue to play a critical role in generating electricity for the next several decades. Thus, carbon dioxide mitigation is needed to control the atmospheric emissions. There are several methodology to reduce CO_2 emissions, e.g. end-use fuel switching, power generation efficiency, and fuel switching and carbon capture and storage (CCS) [1]. The United Nations Intergovernmental Panel on Climate Change concluded that CCS was a technology with potential for important contributions to the mitigation of green house gas emissions by 2030 [26]. CCS is an inevitable component of the broad portfolio of approaches and technologies that will be needed if climate change is to be successfully addressed.

Both organic-rich shale and sandstone are critically important for energy-related applications. Organic rich shale is critical for the oil industry in both exploration and exploitation applications. Meanwhile, sandstone is a desirable host rock for long-term storage of CO_2 in geological formations, due to its high porosity. The complex nature of shale and sandstone materials has challenged researchers to understand the mechanical

behavior of shale and sandstone as well as predict their elastic and strength properties. In addition, an improved understanding of the chemo-mechanical behavior of these materials can lead to a leap forward in the accuracy and usefulness of predictive models developed for them.

1.1 Industrial Context

Shales and sandstones are two of the most common sedimentary material of the Earth's crust and are commonly encountered by the petroleum industry and carbon storage industry. In particular, the low permeability of shale means that it is often a very tight formation and conventional methods would not work for extraction and recovery of oil and gas. Thus, organic-rich shale systems need to be fractured for an increase in porosity and permeability. The process of well stimulation by a pressurized liquid is referred to as hydraulic fracturing. The process involves the high-pressure injection of fracking fluid, water with sand or proppants suspended with the aid of thickening agents, into a wellbore to create cracks in the deep rock formations. Meanwhile, sandstone exhibits a high porosity compared to sedimentary basins which makes them the primary formation for storage of carbon dioxide. Figure 1.1 demonstrates the stages of hydraulic fracturing, the several stages of horizontal drilling are drilling, production casing, perforating gun, pressurize mixture of water and sand, and fissure generation.

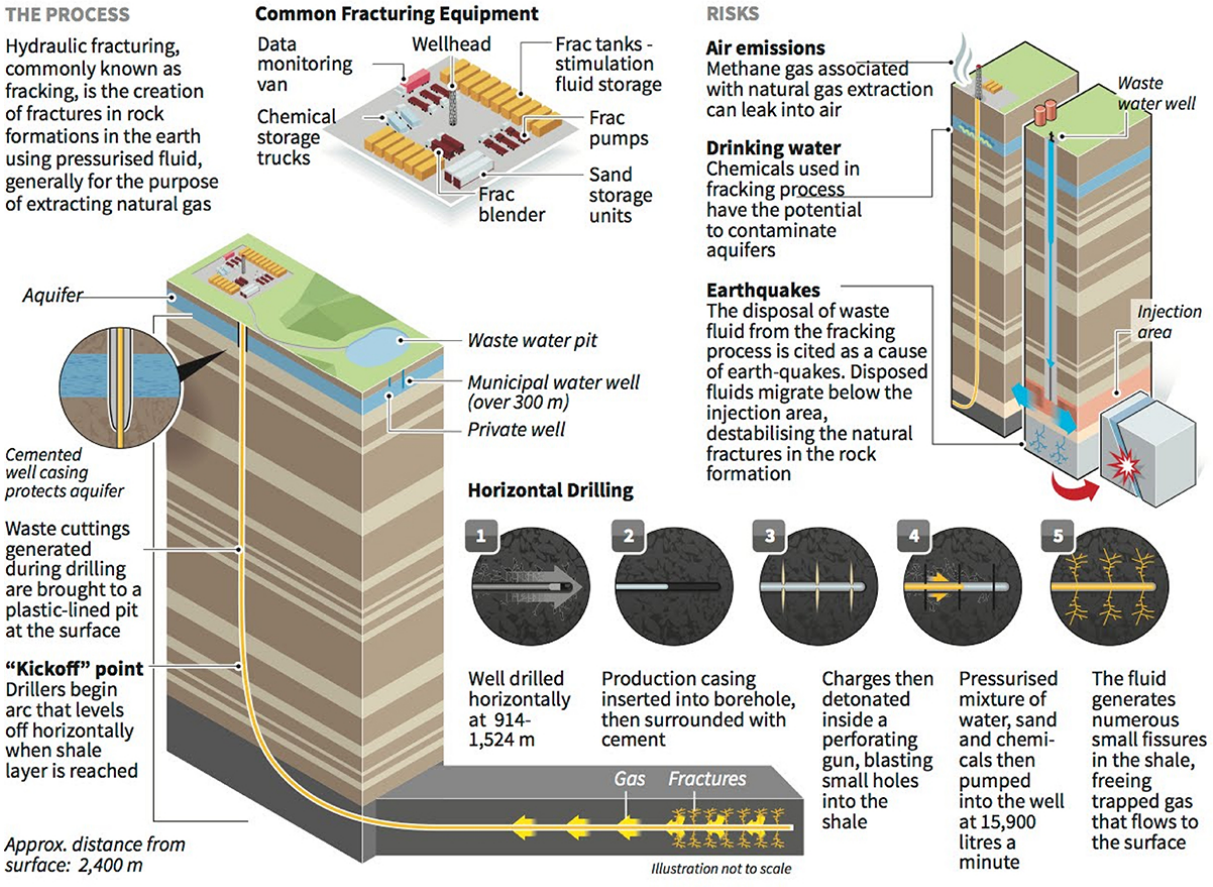

Figure 1.1: Schematic of hydraulic fracturing. Horizontal drilling stages are shown in detail. Adopted from [27].

Shale is commonly associated with the presence of organic material trapped and understanding the mechanical behavior of the material is important in both primary aspects of petroleum geo-engineering, exploration and exploitation. The elastic behavior of shale is of particular importance during seismic exploration. Meanwhile, strength behavior of shale is of critical importance during drilling operations, and fracture toughness is of critical importance during horizontal drilling and well stimulation. Borehole failures and wellbore stability problems are most frequently encountered when dealing with shale materials. Organic-rich shale is frequently modeled as an elastic homogeneous material with simplification on elastic and strength properties in reservoir modeling. However, organic-rich shale is an extremely complex material with a heterogeneous nature. This heterogeneity and anisotropic behavior pose some challenges for characterization, modeling and engineering design. Generally, engineers resort to field experiments and statistical analysis to correlate parameters of the stimulation design to well performance. Experimental parameters like number of stages, number of cluster per stage, number of perforations per cluster, perforation depth, perforation angle, type and amount of proppants are used to assess the efficiency of well-bore operations without properly accounting for the role of elastic anisotropy and heterogeneity of organic-rich shale. In addition, organic-rich shale may sustain a viscoelastic behavior where part of the well stimulation energy is consumed for viscous dissipation. Thus, a detailed characterization of these naturally occurring geo-composites is of fundamental importance. Figure 1.2 demonstrates a schematic diagram of possible carbon capture and storage systems. This figure illustrates the source for possible carbon capture storage and transport and storage options.

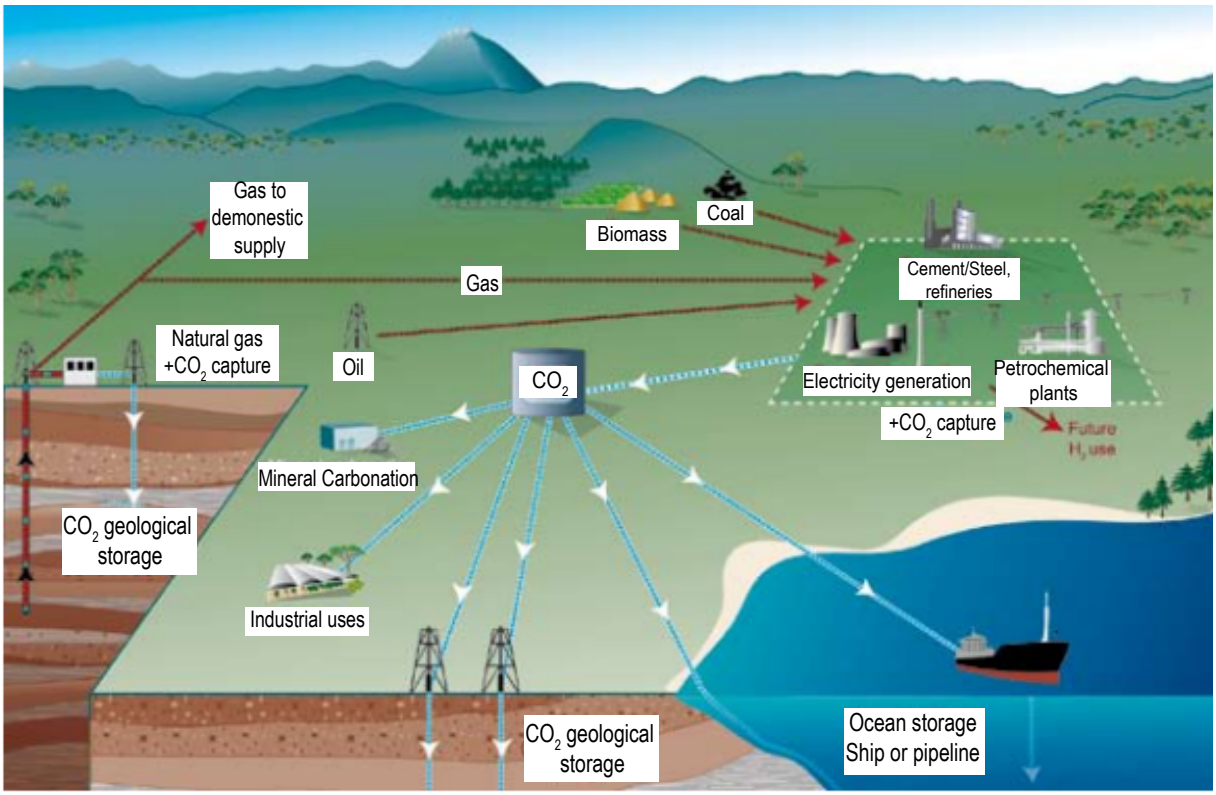

Figure 1.2: Schematic diagram of possible CCS systems. This schematic shows the sources for which carbon capture and storage might be relevant as well as CO_2 transport and storage options. Adopted from [28].

Sandstone rock is commonly associated with storage of carbon dioxide in saline formations. In particular, the high porosity and high permeability of these formations make them a feasible option for subsurface CO_2 storage. In theory, the trapping mechanisms for CO_2 in a saline aquifer are relatively well-known, although the rates and timing of the various processes still have to be better constrained through actual measurements. The CO_2 will end up either as a separate phase beneath a top seal, as residual gas saturating in the pore space, dissolved in the formation brine, or precipitated in a mineral phase. The question then arises as to which injection strategies can maximize the amount stored, or minimize the time to achieve such storage, and how the CO_2 will be distributed between these states over time. In oil production, heterogeneity and residual trapping are often problematic since they can reduce the expected recovery. For saline aquifer storage, however, where the purpose of injection is to trap the CO_2, both of these phenomena can be turned to advantages, if sufficient storage capacity is available. The storage of CO_2 on saline formations relies on field experiments and statistical analysis to correlate parameters of the reservoir to storage capacity. Parameters like number of wells, rate of flow, volume of injection, depth of injection and overlying geological formations are used to assess the efficiency of the design for the host reservoir. In addition to these challenges, a series of seismic events have been reported during and after injection of CO_2 in the host rock formation [10]. The seismic response of host rock formation cannot be captured without properly accounting for geochemical alterations due to injection of supercritical CO_2. The elastic behavior of the sandstone is important during seismic exploration. Meanwhile, the strength behavior of sandstone is of particular importance in the initiation of micro-seismic events due to alterations after injection of CO_2 in such formations.

A new approach to solving these problems is to identify fundamental units of sedimentary rocks and understand their mechanical behavior across multiple length-scales. Once these units have been identified (vary with formations) and characterized, it is possible to upscale the macroscopic behavior. In addition, a comparison of these units can be made to identify the effects of chemical reactions on volume of these units. Moreover, these units will be incorporated to upscale the macroscopic behavior of altered rocks. The work presented in this thesis provides an experimental, and theoretical basis on which the fundamental units of shale and sandstone are identified and characterized mechanically, where these units are incorporated to upscale mechanical properties of sedimentary rocks.

1.2 Research Questions

The first part of the study focuses on hydraulic fracturing and unconventional sources. The second part of the study focuses on sequestration of CO_2 in geological formations.

This research aims to answer the following questions:

Question 1: What is the effect of chemical make up of shale on the mechanical response, and how does elastic, strength and creep properties of organic-rich shale relate to the microstrucure of organic-rich shale?

Question 2: What is the effect of loading rate and speed on the fracture behavior of organic-rich shale?

Question 3: What is the effect of CO_2 injection on the geo-mechanical behavior of sandstone, and how does the supercritical CO_2-rock interaction alter the mechanical behavior of host rock?

The ultimate goal of this research, therefore, is to implement the materials science paradigm for two common sedimentary rocks, organic-rich shale and sandstone, that is to link composition and microstrucure to material performance.

1.3 Research Objectives

A comprehensive approach is presented to address the scientific challenge. The approach is composed of experimental investigations, theoretical and mathematical modeling. The effect of the microstructure and anisotropy of organic-rich shale on the elastic, strength and fracture properties of the material from the nanometer scale to the macroscopic scale is studied. In addition, the effect of geo-chemical alterations on mechanical properties of sandstone is studied. The approach is guided by the following research objectives:

Objective 1: Develop the analytical tools that allow the measurement of mechanical properties by indentation testing for organic-rich shale materials and sandstone materials. Organic-rich shale and sandstone materials are multiphase composites with frictional nature. We should adopt and extend classical indentation analysis for elasto-plastic materials and multiphase analysis of heterogeneous materials.

Objective 2: Develop the analytical tools that allow the measurement of fracture properties by scratch testing for organic-rich shale and sandstone materials. These materials are multiphase composites with an intrinsically multi-scale nature. We adopt and extend

the scratch analysis for viscoelastic materials and multiphase analysis of heterogeneous materials.

Objective 3: Investigate the effect of mineralogy and organic-content and microstructure fabric on the mechanical performance of organic-rich shale. In addition, the elasto-plastic mechanical response of shale at the nano and macroscopic scales is characterized and modeled.

Objective 4: Investigate fluid-rock reactions in Mt. Simon sandstone using scratch testing and nanoindetation testing.

1.4 Industrial and Scientific Benefits

Associated with the research objectives are some industrial and scientific benefits. They include:

- Fundamental understanding of the effect of mineralogy and microstructure on the mechanical performance of organic-rich shale materials.
- Assessment of the fracture properties of organic-rich shale materials in energy related applications.
- Assessment of geochemical reactions in Mt. Simon sandstone to enhance the understanding of microseismic events.

The improved understanding of the effect of mineralogy and microstructure on the mechanical performance provides a tool for petroleum engineers to develop a realistic reservoir model based on mineralogy log data. The fracture toughness values implemented in current modeling reservoirs are calculated based on the assumption of a homogeneous, isotropic material. Whereas, the assessment of fracture toughness in different directions provides a more realistic understanding of fracture properties. The geochemical alteration assessment will provide information for modeling the reservoir integrity. There is no clear understanding of geochemical processes in host rock after a short time and/or long time after injection. In turn, assessment of geochemical reactions in accelerated geochemical conditions, provides insight regarding the long term effect of these geochemical reactions on the mechanical response.

1.5 Outline of Dissertation

This dissertation is divided into five Parts. Part I deals with the general presentation of the topic. Parts II deals with experimental methods and developing the experimental tools necessary to investigate the chemical composition as well as mechanical properties of these geo-materials. In particular, Chapter 2 reviews the specimen preparation, atomic force microscopy, scanning electron microscopy, energy dispersive spectroscopy, X-ray diffraction and total organic carbon analyzer. Chapter 3 studies the principle of indentation methods, equipment, theory and advanced indentation methods. Chapter 4 reviews the principles of scratch testing, equipment and theoretical models. Part III of the study looks into the effect of microstructure, fabric and structural anisotropy on the mechanical response of organic-rich shale. Chapter 5 reviews the multi-scale structure of organic rich shale, reviewing the building blocks of organic-rich shale. Chapter 6 summarizes the results of micro-structural characterization of organic-rich shale in this study. In addition, Chapter 7 investigates the influence of mineralogy and fabric on elastic mechanical response of organic-rich shale. Furthermore, Chapter 8 & 9 probe the fracture toughness characterization of organic-rich shale. In particular, multi-scale nature of fracture processes in organic-rich shale and the effect of injection rate and anisotropy on hydraulic fracturing are studied.

Part IV deals with fluid-rock reactions and the impact on mechanical integrity with a specific focus on geological CO_2 storage. Chapter 10 reviews the general presentation of geological sequestration of CO_2 as well as the characterization of fabric and mineralogy of Mt. Simon. Chapter 11 investigates the effect of fluid-rock reactions on the elastic response of Mt. Simon sandstone and its effect at the microscopic length scale. Chapter 12 investigates the CO_2 induced alterations in the Mt. Simon sandstone fracture behavior. The fifth Part, i.e., Chapter 13 summarizes the results of this study and presents some perspectives on future research.

Part II

Experimental Methods

Chapter 2

Microstructural Observation Techniques

2.1 Introduction

Microstructural observation aims at linking fabric and composition of the material to a meaningful property. A review of several microstructural observation techniques is presented in this chapter. The experimental methods presented here, help to investigate the chemical composition, fabric, microstructure, surface roughness and organic content of the materials investigated in this study. The first step in the nano/micro mechanical characterization of materials is to prepare a specimen suitable for this type of investigation. The second step is the use of atomic force microscopy, which is a scanning probe microscope for investigation of local roughness of specimen surface. Furthermore, scanning electron microscopy is utilized to asses the microstructure and fabric of the material. In addition, energy dispersive spectroscopy is utilized to observe the chemical composition at different locations of interest. Although, energy dispersive spectroscopy provides useful information of local sites, X-ray diffraction is needed to characterize the bulk chemical composition of the specimens. At last, a review of total organic carbon analysis presented, which is used to assess the organic content of several shale specimens.

2.2 Specimen Preparation

Specimen preparation is one of the first and most critical step in investigating the behavior of materials, specifically in small-scale testing. The specimen preparation involves, cutting specimens into desired dimensions, commonly 25 mm by 25 mm. The cutting procedure is done using an air-cool cutting technique, precision diamond saw and slow-speed diamond saw. The utilization of each of these saws is dependent on the purpose of the investigation. The slow speed diamond saw is used to prevent the contamination of specimen with water. The water is substituted with a suitable chemical for that specific application. The next step in specimen preparation of specimen for small scale testing is grinding and polishing. Through a process spanning multiple months, various techniques are evaluated to determine the best methods for sample preparation and polishing. Ultimately, the biggest issue with polishing is complications due to the difference of particle hardness in the nature of the heterogeneous media. In addition, finding a suitable polishing medium for final polishing is challenging. There are significant issues with relief when testing for the proper polishing media. A number of lubricants and polishing cloths are tested. A solution is obtained by using a trial and error procedure each time.

A proper grinding and polishing procedure is the stepping stone to obtaining flat and perfectly polished surfaces for microscopic observation as well as subsequent mechanical testing. Prior to grinding and polishing, a diamond saw, IsoMet ^{TM}5000 Linear Precision Saw (Buehler, Lake Bluff, IL) is used to machine flat cylindrical specimens. Herein, a review of some protocols developed for a specimen is presented.

Protocol number 1 consists of mounting the specimen onto aluminum disk followed by manual grinding and semi-automated wet polishing using an automated grinder/polisher. The specimens are then mounted using cyanoacrylate adhesive on aluminum disks. Manual grinding is carried out using a level on top of the aluminum disk to maintain a flat top surface. Three grit sizes of Carbimet abrasive paper are employed: consecutively 240, 400 and 600 for several minutes each and using ethanol as a lubricant. Between each grit size, the specimen is rinsed in an ultrasonic bath for two minutes to prevent cross-contamination. For polishing, woven cloths are used along with diamond oil suspension, MetaDi® (Buehler, Lake Bluff, IL). The following solutions are used: 9 μm, 3μm, 1 μm and 0.25 μm consecutively for long duration of times. This procedure works well on shale specimens and yields a mirror-like surface. The lubrication and ultrasonic bath are done with ethanol to prevent hydration and intermixing of water with the micro-constituents

of organic-rich shale. Finally, after completing the protocol, the samples are air-dried and stored in a vacuum desiccator. Although this protocol yields a good surface polish, there is a tilt in the final specimen.

Moreover, protocol number 2 is designed to correct the observed tilt of the final specimen. In fact, a major issue detected was the presence of a steep slope on the final polished surface, which results from the current design of the AutoMet 250 power head. To circumvent this problem, we embedded the specimens in an epoxy resin. The specimens are wrapped in plastic before impregnation to prevent epoxy from reaching into the pore space. In other words, the epoxy works as a supporting media for the samples to redistribute the load during grinding and polishing and thus prevent tilting. Overall, casting the specimens in epoxy has improved the flatness of the final surface. This approach also removes the need for manual grinding, and as a result the whole process can be done in a semi-automated fashion. However, it leads to a poorer surface finish and significant cross-contamination of the specimens. Thus, another specimen preparation protocol is needed.

Protocol number 3 is developed which consists of manual grinding and manual polishing. It is found that the amount of relief could be significantly reduced by shortening the polishing time and using a different polishing cloth. Thus, manual grinding is carried out with ethanol as a lubricant while using three grit sizes for short duration of time for: 240, 400 and 600 consecutively. Afterward, polishing is carried out manually on a glass plate using a diamond oil suspension for short amount of time per diamond particle size: 9 μm, 3μm, 1μm, and 0.25μm. Another variation of the same protocol consists of a perforated cloth with embedded abrasives, during the manual polishing phase. In order to ensure a flat polished surface, the polishing cloth was placed on a rigorously flat glass surface. Although an improvement is achieved, this protocol does not yield the perfect polished specimen surface.

A breakthrough was made by introducing two additional grinding steps: using the grit size 800 and 1200, leading to protocol number 4. Considerable improvement in smoothness is finally made when a dry grinding and polishing procedure is tried, in which no ethanol or diamond suspension is used. In the first variation, the dry grinding is completed automatically with the base and head set at low revolution speeds of 200 rpm and 40 rpm, respectively. A minimal force of 1 lb was applied to the specimen to prevent cracks from propagating while still providing enough force to hold it securely against the sanding papers. In the most recent variations, a dry, semi-automated grinding and

polishing procedure with a dry, manual grinding and polishing procedure, both with time intervals varying from 1 to 15 minutes and minimal force, have been tried. Instead of moving to polishing with diamond abrasives after the 600 grit size paper, two additional grinding steps using 800 grit size and 1200 grit size paper are added. The resulting surface of this procedure is reflective under the light and no scratches are present when observed under the microscope.

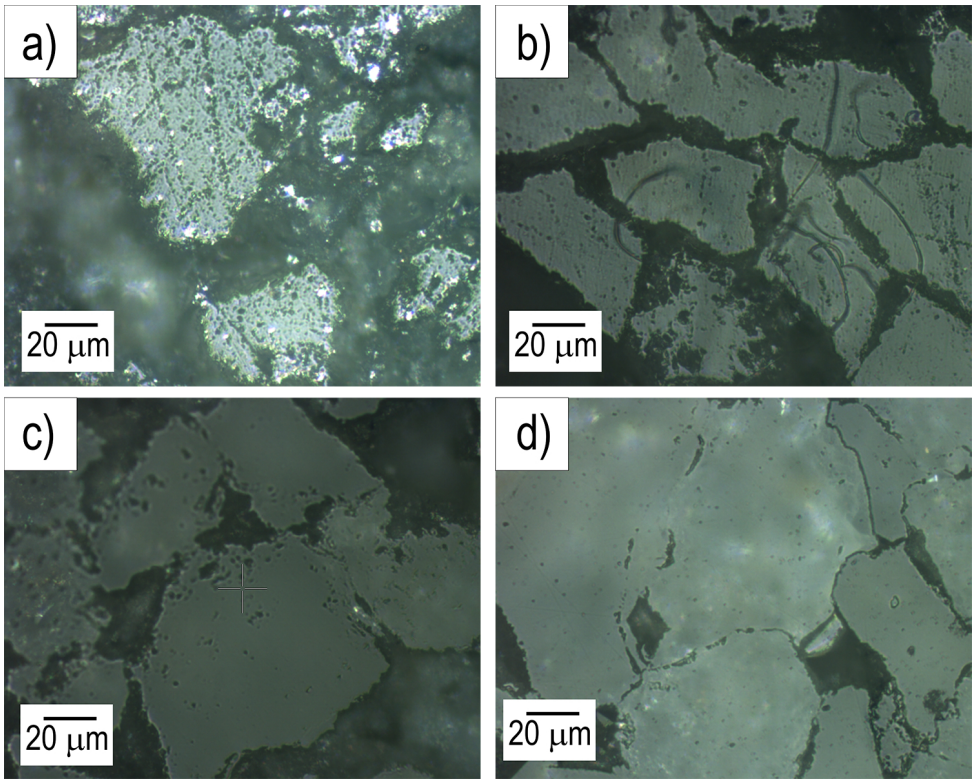

Figure 2.1: Optical microscopy images of Polished Toarcian B1 specimen: a) Protocol 1, b) Protocol 2, c) Protocol 3, d) Protocol 4.

Figure 2.1 demonstrates the final polish of several protocols. The difference in the optical microscopy images are due to different steps and different cloths used.

As demonstrated through the use of up to 4 grinding and polishing protocols, there is not a unique protocol that will be applicable to all gas shale specimens in order to yield a flat and mirror-like surface. Instead, the protocol must be tailored to the specimen and typically results from several trials and errors. Yet some principles remain. A longer polishing time will result in a better and smother finish. Moreover, cleaning the surface more often either with an ultrasonic bath and proper cleaning solution or using compressed

air will reduce cross contamination.

As discussed by Winter [29], it is virtually impossible to remove all defects in the polished sample: the objective is to obtain a satisfactory polished sample for the required testing, which means that, depending on the length scale of examination and testing and the additional use of image analysis and processing, some scratches or pull-outs might be acceptable.

2.3 Atomic Force Microscopy

The atomic force microscope (AFM) belongs to a series of scanning probe microscopes invented in the 1980s [30]. The series of these microscopes started with scanning tunneling microscope (STM), which was used for imaging of conductive and semi-conductive materials [31, 32]. On the other hand, the scanning near-field microscope was invented which gave access to microscopy with light below the optical resolution limit [33, 34]. The last one of the series is the AFM, invented by Binning et al. [35]. The AFM allowed the imaging of the topography of conducting and insulating surfaces, in some cases with atomic resolution.

In AFM, the sample is scanned by a sharp tip, radius of around 10 nm, which is mounted to cantilever spring. While scanning, the force between the tip and the sample is measured by monitoring the deflection of the cantilever. A topographic image of the sample is obtained by plotting the deflection of the cantilever versus its position on the sample. Alternatively, it is possible to plot the height position of the translation stage. This height is controlled by a feedback loop, which maintains a constant force between the tip and the sample.

Image contrast arises because the force between the tip and the sample is a function of both tip-sample separation and the material properties of the tip and the sample. In an AFM force measurement the tip attached to a cantilever spring is moved towards the sample in normal direction. Vertical position of the tip and deflection of the cantilever are recorded and converted to force-versus-distance curves. The AFM has been applied to problems in a wide range of disciplines such as: solid-state physics [36] , semiconductor science and technology [37], molecular engineering [38], polymer chemistry [39], surface chemistry [40], molecular biology [41], cell biology [42] and medicine [43].

The AFM consists of a cantilever with a sharp tip at its end that is used to scan the specimen surface. The cantilever is typically made from silicon or silicon nitride with a tip

of radius of curvature on the order of nanometers. When the tip is brought into proximity of a sample surface, forces between the tip and the sample lead to a deflection of the cantilever according to Hooke's law. Depending on the situation, forces that are measured in AFM include mechanical contact force, Van der Waals forces, capillary forces, chemical bonding, electrostatic forces, magnetic forces, casimir forces, solvation forces, etc. The AFM can be operated in a number of modes, depending on the application. In general, possible imaging modes are divided into static (contact) modes and a variety of dynamic (non-contact) modes where the cantilever is vibrated or oscillated at a given frequency.

In contact mode, the tip is moved across the surface of the sample and the contours of the surface are measured either using the deflection of the cantilever directly or, more commonly, using the feedback signal required to keep the cantilever at a constant position. Because the measurement of a static signal is prone to noise and drift, low stiffness cantilevers are used to achieve a large enough deflection signal while keeping the interaction force low. Close to the surface of the sample, attractive forces can be quiet strong, causing the tip to snap-in to the surface. In ambient conditions, most samples develop a liquid meniscus layer. Because of this layer, keeping the probe tip close enough to sample for short-range force to become detectable, while preventing the tip from sticking to the surface, presents a major problem for contact mode. Dynamic contact mode was developed to bypass this problem. In tapping mode, the cantilever is driven to oscillate up and down at or near its resonance frequency. This oscillation is commonly achieved with a small piezo element in the cantilever holder. The amplitude of this oscillation usually varies from several nm to 200 nm. In tapping mode, the frequency and amplitude of the driving signal are kept constant, leading to a constant amplitude of the cantilever oscillation as long as there is no drift or interaction with the surface. The interaction of forces acting on the cantilever when the tip comes close to surface cause the amplitude of the cantilever's oscillation to change as the tip gets closer to sample. This amplitude is used as the feedback that goes into the electronic servo that controls the height of cantilever above the sample. The servo adjusts the height to maintain a set cantilever oscillation amplitude as the cantilever is scanned over the sample. A tapping AFM image is therefore produced by imaging the force of the intermittent contacts of the tip with the sample surface.

Figure 2.2: Asylum Research MFP-3D ^{TM}Stand Alone AFM. Adopted from [44].

The AFM studies in this study was performed in Materials Research Laboratory at University of Illinois at Urbana-Champaign. The AFM is a Asylum Research MFP-3D AFM. This AFM feature closed-loop, low noise, high precision scanners, with Q-controlled AC modes, piezo response imaging, contact mode with lateral force, and detailed force0disance measurements. This system allow scanning in air or liquid environments, and have extensive nano-manipulation and nano-lithography capabilities. Maximum lateral scan size on this instrument is 90 μm $\times$ 90 μm, and the maximum vertical range is 15 μm.

Figure 2.2 demonstrates the AFM head of MFP-3D AFM without the isolation panel. The sample holder can accommodate samples up to 3.4 inch $\times$ 1.5 inch, including glass slides and cover-slips. The instrument runs on an open user interface based on IGOR Pro incorporates professional-quality analysis and graphing capabilities. AFM analysis include section, histogram, roughness, particle analysis and masking.

2.4 Scanning Electron Microscopy

Microscopy is based on the use of the light microscope and could provide specimen resolution on the order of 0.2 microns. To achieve higher resolutions, an electron source is required instead of light as the illumination source, which allows for resolutions of about 25 Angstroms. The use of electrons not only gives better resolution but, due to the nature of electron beam-specimen interactions there are a variety signals that can be used to provide information regarding characteristics at/near the surface of a specimen. Thus, scanning electron microscope yields detail information about fabric of specimens. A review of scanning electron microscope and its part is presented here.

The scanning electron microscope instrument is made up of two main components, the electronic console and the electron column. The electronic console provides knobs and switches that allow for instrument adjustments such as filament current, accelerating voltage, focus, magnification, brightness and contrast. The electron column is where the electron beam is generated under vacuum, focused to a small diameter, and scanned across the surface of a specimen by electromagnetic deflection coils. The lower portion of the column is called the specimen chamber. The secondary electron detector is located above the sample stage inside the specimen chamber. Specimens are mounted and secured onto the stage. The stage is either manual or automatic. The manual stage controls are usually found on the front side of the specimen chamber and allow for x-y-z movement,

360 rotation and 90 tilt.

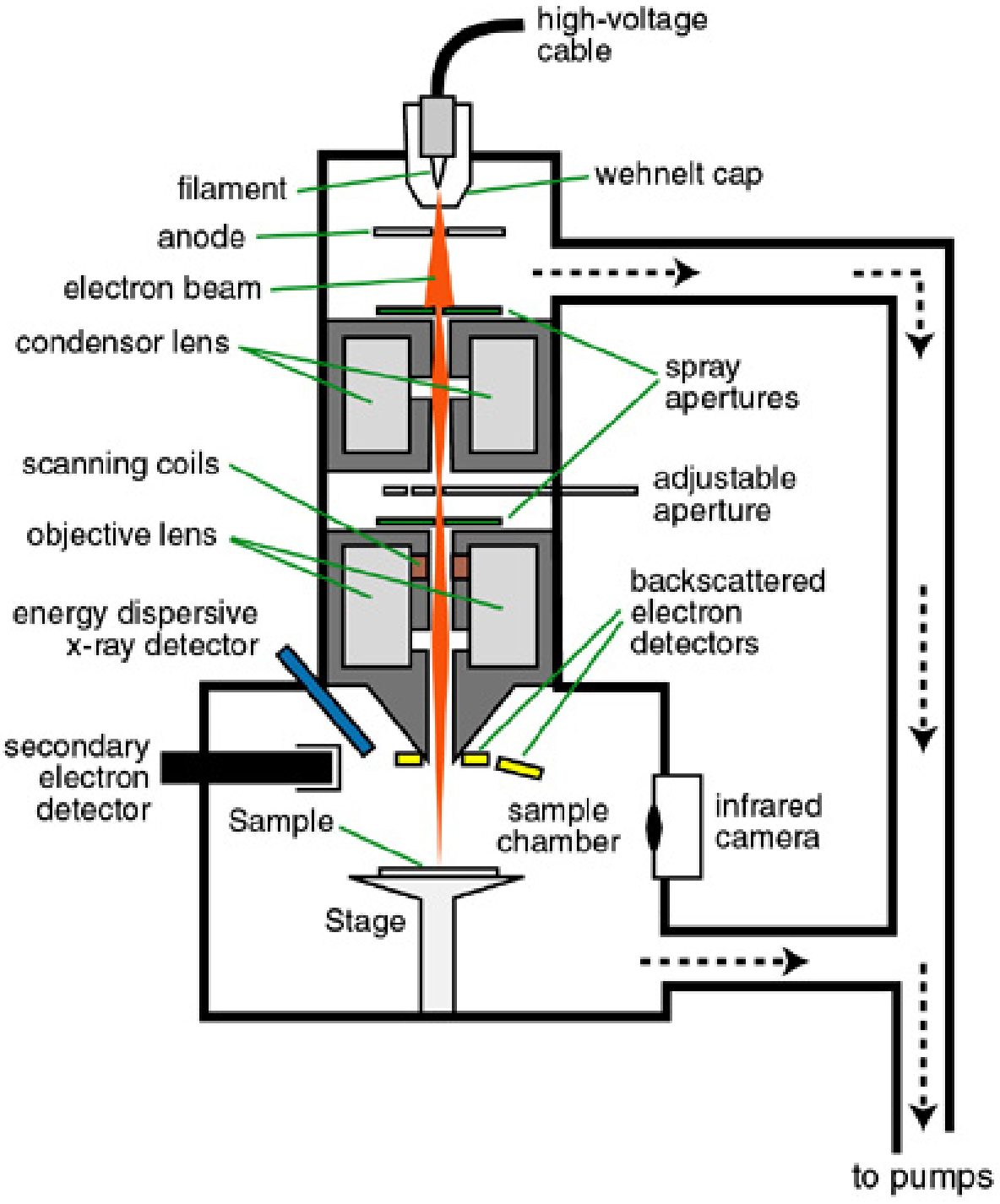

Figure 2.3: Schematic of scanning electron microscope column. Adopted from [45].

Figure 2.3 demonstrates a schematic of scanning electron microscope column. The scanning electron microscope consist of 5 major parts, electron gun, condenser lenses, apertures, scanning system, and specimen chamber. The electron gun is located at the top of the column where free electrons are generated by thermionic emission from a tungsten filament at $\approx$ 2700 °K. The filament is inside the Wehnelt which controls the number of electrons leaving the gun. Electrons are primarily accelerated toward an anode that is adjustable from 200 V to 30 kV. After the beams passes the anode it is influenced by two condenser lenses that cause the beam to converge and pass through a focal point. The electron beam is essentially focused down to 1000 times its original size. In conjunction with the selected accelerating voltage the condenser lenses are primarily responsible for determining the intensity of the electron beam when it strikes the specimen. Depending on the microscope one or more apertures may be found in the electron column. The function of these apertures is to reduce and exclude extraneous electrons in the lenses. The final lens aperture located below the scanning coils determines the diameter or spot size of the beam at the specimen. The spot size of the specimen will in part determine the resolution and depth of field. Decreasing the spot size will allow for an increase in resolution and depth of field with a loss of brightness. At the lower portion of the column the specimen, the specimen stage and controls are located. Images are formed by rastering the electron beam across the specimen using deflection coils inside the objective lens. The stigmator or astigmatism corrector is located in the objective lens and uses a magnetic field in order to reduce aberrations of the electron beam. The electron beam should have a circular cross section when it strikes the specimen however it is usually elliptical thus the stigmator acts to control this problem. At the lower portion of the column, the specimen stage and controls are located. The secondary electrons from the specimen are attracted to the detector by a positive charge.

The scanning electron microscopes work with electron beams emitted from the source. The ability for a SEM to provide a controlled electron beam requires that the electronic column be under vacuum at a pressure of at least $5*10^{-5}$ Torr. A high vacuum pressure is required for a variety of reasons. First, the current that passes through the filament causes the filament to reach temperatures around 2700 °K. A hot tungsten filament will oxidize and burn out in the presence of air at atmospheric pressure. Secondly, the ability of the column optics to operate properly requires a fairly clean, dust free environment. Third, air particles and dust inside the column can interfere and block the electrons before they ever reach the specimen in the sample chamber. In order to provide adequate vacuum

pressure inside the column, a vacuum system consisting of two or more pumps is typically present. Separate pumps are required because one pump isn't really capable of doing all the work but, in conjunction they can provide a good vacuum pressure relatively quickly and efficiently. A majority of the initial pumping is done by the action of a mechanical pump often called a roughing pump. The roughing pump operates first during the pump-down process and has excellent efficiency above 10^{-2} Torr. Although many mechanical pumps used in SEMs are capable of producing pressure better than $5 * 10^{-5}$ Torr, a very long pump down time would mostly be required. Pressure lower than 10^{-2} Torr are more easily acquired by the action of a turbo-molecular pump. Turbo-molecular pumps make use of a turbine that rotates at 20,000 to 50,000 rotations per minute to evacuate gas molecules and particulates found inside the column.

The FEI is designed to operate at three separate vacuum modes, high vacuum (10^{-6} to 10^{-7} Torr), low vacuum (0.1 to 20 Torr) and ESEM (0.1 to 20 Torr). In the low vacuum and ESEM mode of operation the pressure inside the specimen chamber operates at a lower pressure than that inside the actual column which is always at high vacuum. The high vacuum mode is typically where most SEMs operate. In this mode the highest resolutions and magnifications can be achieved, although it is not suitable for all specimens. Generally anything that is conductive and has a high density works well in high vacuum mode. Specimens that are non-conductive o have a low density are more suitable for the low vacuum mode or ESEM mode. The ESEM mode of operation is necessary for wet, non-conductive samples.

In scanning electron microscopy visual inspection of the surface of a material utilizes signals of two types, secondary and back-scattered electrons. Secondary and back scattered electrons are constantly being produced from the surface of the specimen under the electron beam however they are a result of two separate types of interaction. Secondary electrons are a result of the inelastic collision and scattering of incident electrons with specimen electrons. They are generally characterized by possessing energies of less than 50 eV. They are used to reveal the surface structure of a material with a resolution of $\approx$10 nm or better.

Back-scattered electrons are a result of an elastic collision and scattering event between incident electrons and specimen nuclei or electrons. Back-scattered electrons can be generated further from the surface of the material and help to resolve topographical contrast and atomic number contrast with a resolution of < 1 micron. While there are several types of signals that are generated from a specimen under an electron bean the x-ray

signal is typically the only other signal that is used for scanning electron microscopy. The x-ray signal is a result of recombination interactions between free electrons and positive electron holes that are generated with the material. The x-ray signal can originate from further down into the surface of the specimen and allow for determination of elemental composition through energy dispersive x-ray spectroscopy (EDS) analysis of characteristic x-ray signals.

Observation Techniques

The detailed nature of specimens fabric is of importance to ensure a successful grinding and polishing, locating the tested area, and composition of the specimen. A high quality scanning electron image provide substantial information about the fabric of specimens. Thus, as users begin to investigate a broader range of materials and encounter more complex analysis scenarios, satisfactory images become more difficult for inexperienced user. When the image is not clear enough or an image of a particular feature is seemingly impossible to obtain, it requires further problem solving to determine what the cause really is. This section will focus on the techniques for successful imaging.

Image disturbances: There are many types of image disturbances that occur while imaging specimens. In some cases these disturbances are attributed to defect with the instrument; however, more than likely the disturbances are due to operator's lack of experience, improper sample preparation, or external influences such as instrument vibration. Disturbances can be examined and corrected using a systematic approach based in their appearance. Figure 2.4 demonstrates the possible cause of image disturbances flowchart. The possible causes of image disturbances are categorized in four parts. The four parts are lack of sharpness, low image quality, noises and image distortion and deformation.

The accelerating voltage on the scanning electron microscope is adjustable from 200V–30kV. Choosing the right accelerating voltage is critical for obtaining a good clear image however the most suitable voltage level depends mostly on the type of material being examined. The more conductive the material the better it will behave under higher voltages. Higher voltages (15–30 kV) generally allow for high resolution at high magnifications although, this can damage the specimen very quickly if it is not highly conductive. Thus, when imaging polymers and ceramics it is more suitable to use voltages below 10 kV.

Figure 2.5 demonstrates the scanning electron microscopy at two different accelerating voltages. There is a noticeable difference between how surface structures appear clear at lower voltages. Furthermore, Figure 2.6 demonstrates the scanning electron microscopy at

Lack of Sharpness

- Improper accelerating voltage setting.
- Instability of gun emission caused by insufficient heating of the filament.
- Improper electron probe diameter.
- Improper setting and incorrect centering of objective aperture.
- Insufficient astigmatism correction
- Improper focal depth
- Too large magnification
- Specimen charge-up and magnetization
- Defocus of camera system

Low Image Quality

- Improper accelerating voltage setting
- Improper probe current setting
- Incorrect astigmatism correction
- Noise caused by excessive photomultiplier gain
- Improper contrast and brightness
- Improper specimen preparation process
- Improper photographic material
- Improper position relation between specimen and detector
- No Specimen tilting

Noise

- Instability of accelerating voltage and gun emission
- Discharge of detector
- Charge-up of specimen surface
- Burnt CRT or dusty CRT screen
- External stray magnetic field
- Mechanical Vibration

Image distortion and deformation

- Specimen Charge-up
- External stray magnetic field
- Electron beam damage
- Deformation of specimen during preparation
- Image drift caused by column interior charge-up
- Specimen drift on heating and cooling stages

Figure 2.4: Possible causes of image disturbances flowchart.

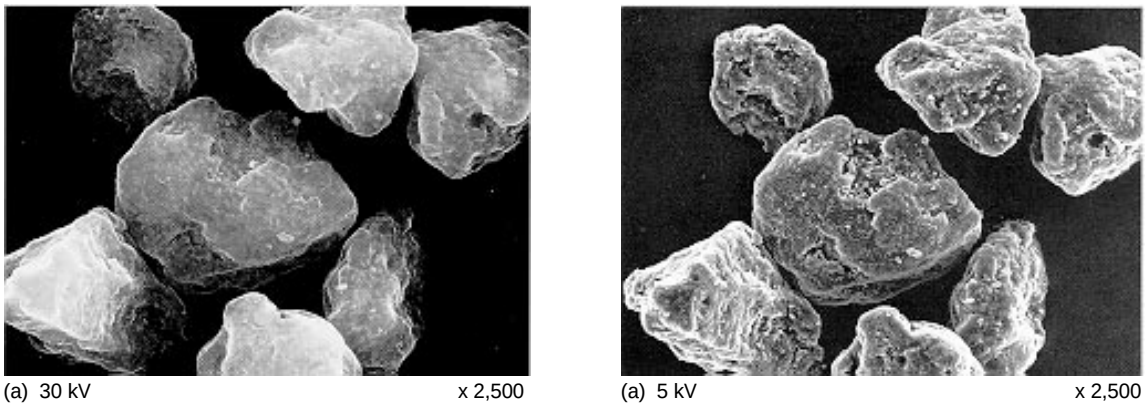

Figure 2.5: Scanning electron microscopy of mineral grains at different accelerating voltages: Notice how surface structures appear clear at lower voltages. Adopted from [46].

different accelerating voltages. This shows how the resolution is improved with increasing accelerating voltage.

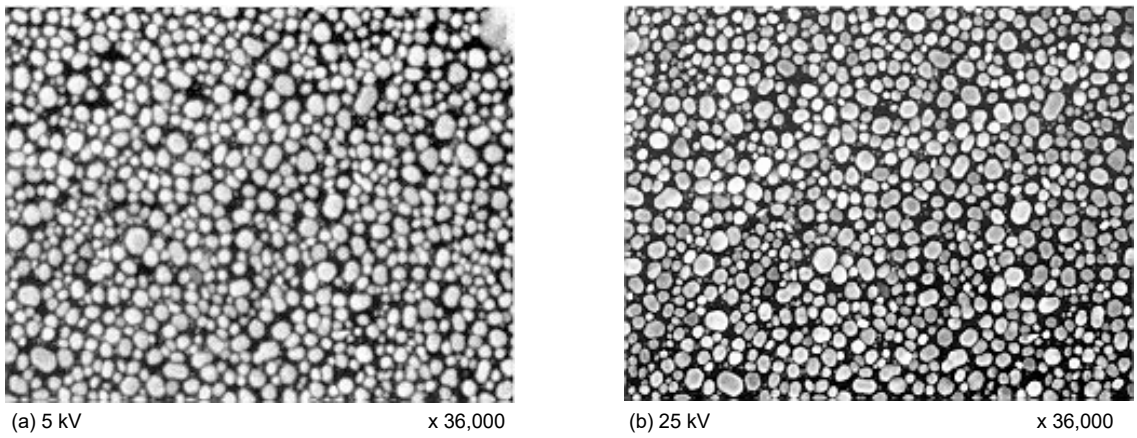

Figure 2.6: Scanning electron microscopy of evaporated Au particles at different accelerating voltages: Notice how the resolution is improved with increasing accelerating voltage. Adopted from [46].

Besides the accelerating voltage one's choice of working distance and spot size will greatly influence the image quality. As with accelerating voltage there exists a give and take situation when choosing the most suitable settings for working distance and spot size. A working distance of 10 mm should be used for imaging which allows for a good

depth of field while maintaining good resolution. In most cases, one may want to reduce the working distance to achieve better resolution especially when using lower accelerating voltages. Spot size restricts the bean current and will thereby cause for brightness and contrast compensations. Smaller spot sized will require higher brightness and contrast level thus there can be limits when using a small spot size. Smaller spot sizes allow for higher resolution and a greater depth of field.

Four different scanning electron microscopy instruments were used in this study. First, the JEOL 6060 LV, which is a scanning electron microscope with a thermionic tungsten source and roughly a 10 nm resolution. This instrument is excellent for larger features, geological samples and chip imaging. Figure 2.7 illustrates a JEOL 6060 setup with a computer. The large current for EDS chemical analysis and image mapping and low vacuum mode (2 Torr) for non-coatable samples.

Figure 2.7: JEOL 6060 V Scanning Electron Microscope at Fredrick Seitz Material Research Laboratory, University of Illinois at Urbana-Champaign. Adopted from [47].

Figure 2.8 illustrates the JEOL 7000 setup. JEOL 7000 has a Schottky thermal-field

emission source with a resolution of 2-3 nm. This scanning electron microscope has EDS capabilities with elemental composition and mapping. In addition this microscope has EBSD capabilities for crystallography. The wave dispersive spectroscopy is a high energy resolution of EDS which is available on this instrument. The specimens need to be coated on this platfrom using a gold sputter coating or palladium coating.

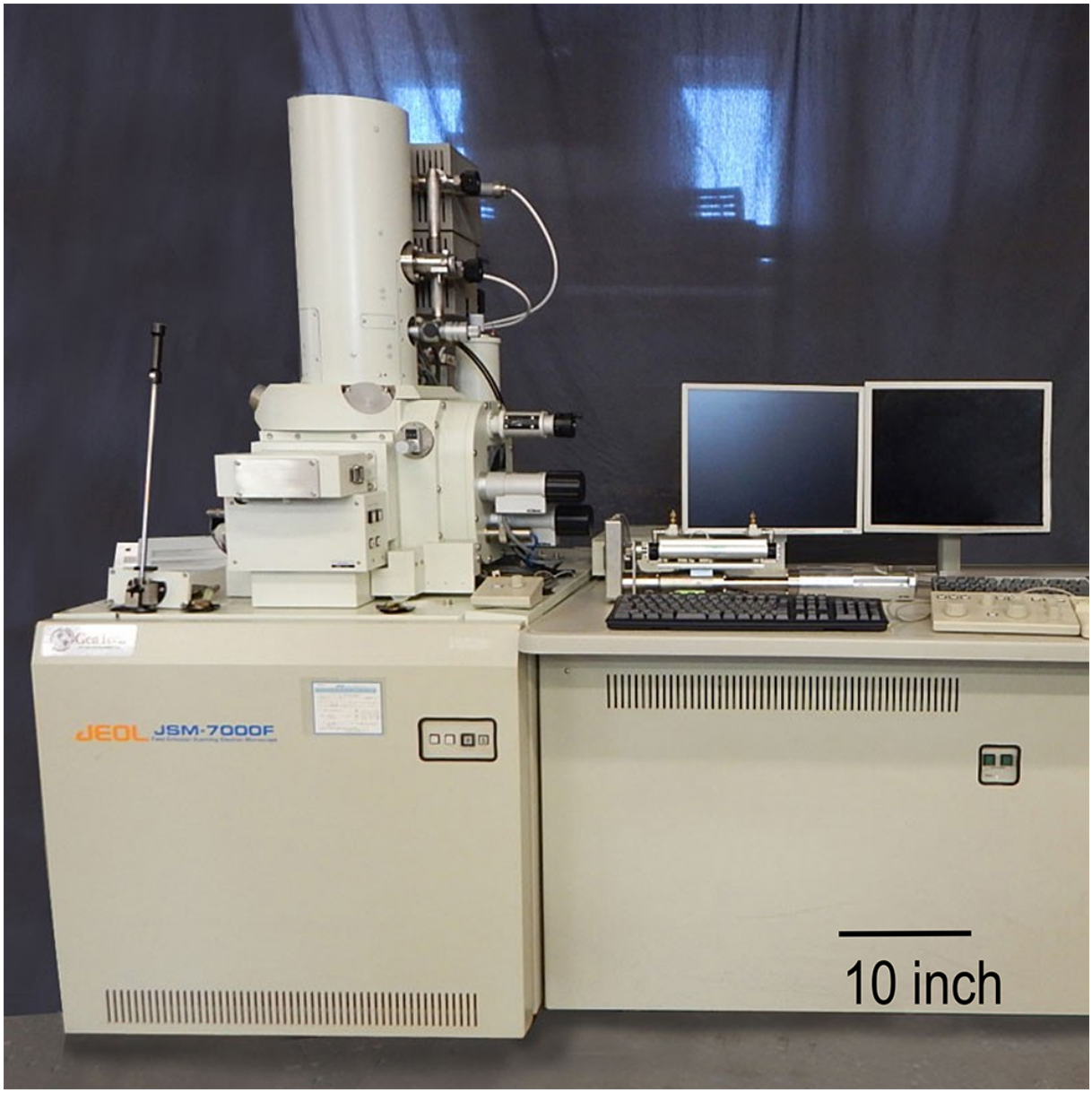

Figure 2.8: JEOL 7000 Scanning Electron Microscope at Fredrick Seitz Material Research Laboratory, University of Illinois at Urbana-Champaign. Adopted from [48].

The coating of the specimens are not desirable if further testing on the surface is needed. Thus, an environmental scanning electron microscopy is more suitable for high resolution imaging without the necessity of coating the specimens. Figure 2.9 demonstrates the setup of FEI Quanta 450. This setup is a field-emission environmental scanning electron microscope. This one has a Everhart-Thornley secondary electron detector. Robinson series 6 scintillator-type backscattered electron detector (BSD) plus solid-state low and standard voltage BSDs. This instrument is equipped with Peltier-effect heating/cooling stage (20 ∘C above/below ambient).

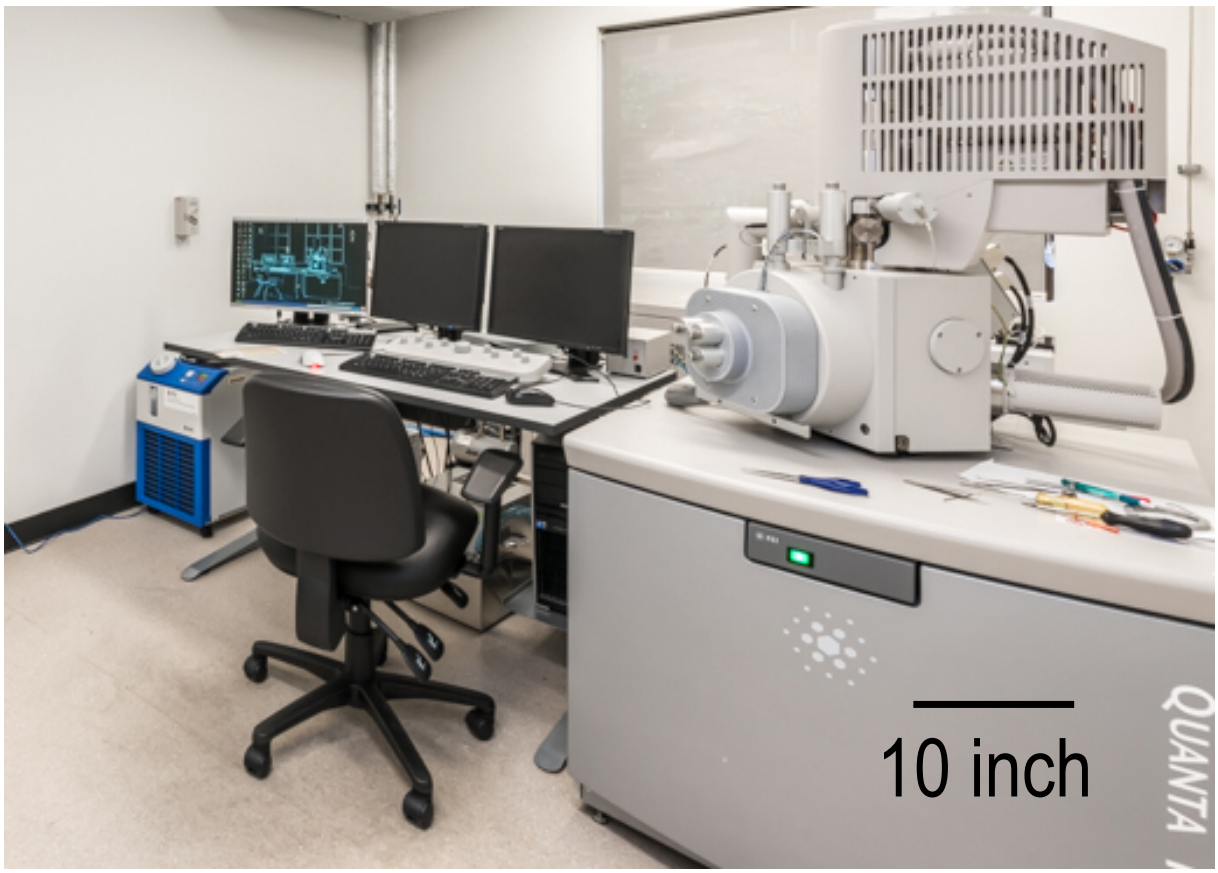

Figure 2.9: FEI Quanta 450 Scanning Electron Microscope at Imaging Technology Group, Beckman Institute at University of Illinois at Urbana-Champaign. Adopted from [48].

In addition to the FEI Quanta 450, a newer version of this instrument is used in this study. The FEI Quanta 650 is a scanning electron microscope at Electron Probe Instrumentation Center at Northwestern University. Figure 2.10 demonstrates the FEI 650 Qunata setup. FEI Quanta 650 has a Schottky field emission gun for high resolution

and excellent beam stability. This system allows for SE imaging of wet and insulating sample up to 4000 Pa chamber pressure. The resolution of this SEM is of < 2 nm at 30kV in high vacuum and < 2nm at 30 kV is environmental scanning electron microscope and < 3.5 nm at 3kV in low vacuum mode. The stage is automatic, programmable stage with 6 inch wafer capacity. This instrument has standard E-T SE detector, solid state BSE detector and gaseous BSE detector.

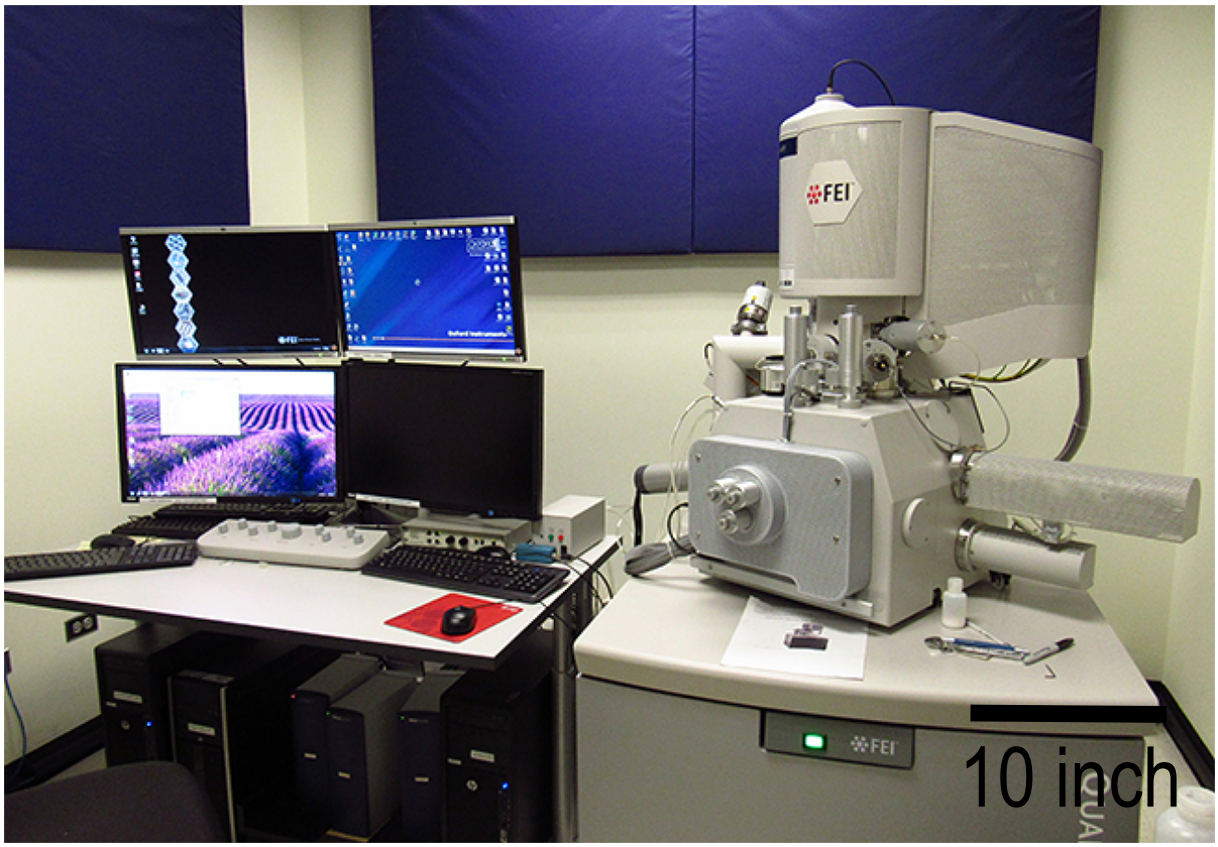

Figure 2.10: FEI Quanta 650 Scanning Electron Microscope at Electron Probe Instrumentation Center, Northwestern University. Adopted from [49].

2.5 Energy Dispersive Spectroscopy

Energy-dispersive X-ray spectroscopy is an analytical technique used for the elemental analysis or chemical characterization of a sample. This method relies on an interaction of source of X-ray excitation and the sample. The characterization capabilities of this

method are due to the fundamental principle that each element has a unique atomic structure allowing a unique set of peaks in its electromagnetic emission spectrum. A high-energy beam of charged particles is needed to simulate the emission of characteristic of X-rays from a specimen. The principle works on the ground of moving atoms. At rest, an atom within the sample contains ground state electrons in discrete energy levels or electron shells bound to the nucleus. The incident beam may excite an electron in an inner shell, ejecting while creating an electron hole where the electron was. The difference in energy between the higher energy shell and lower energy shell will be released in the form of a X-ray. The number and energy of the X-rays emitted from specimen can be measured by an energy-dispersive spectrometer. As the energies of the X-rays are characteristic of the difference in energy between the two shells and of the atomic structure of the emitting element. Thus, EDS allows characterization and measurement of elemental composition of the specimen.

The primary components of the EDS are: electron beam, the X-ray detector, the pulse processor and the analyzer. Electron beam excitation is used in electron microscopes, scanning electron microscopes and scanning transmission electron microscopes. A detector is used to convert X-ray energy into voltage signals; this information is sent to a pulse processor, which measure the signals and passes them onto an analyzer for data display and analysis. The most common detector on these systems used to be Si detector cooled to cryogenic temperatures with liquid nitrogen. Newer system are often equipped with silicon drift detectors (SDD) with Peltier cooling systems.

EDS can utilized to determine which chemical elements are present in a sample. Moreover, the relative abundance of each element can be calculated. The accuracy of this quantitative analysis of sample composition is affected by various factors. Many elements will have overlapping X-ray emission peaks. The accuracy of the measured composition is also affected by the nature of the sample. X-rays are generated by any atom in the sample that is sufficiently excited by incoming beam. These X-rays are emitted in all directions, and so they may not all escape the sample. The likelihood of a X-ray escaping in the specimen, and thus being available to detect and measure, depends on the energy of the X-ray and the composition, amount, and density of material it has to pass through to reach the detector. Due to X-ray absorption effect and similar effects, accurate estimation of the sample composition from the measured X-ray emission spectrum requires the application of quantitative correction procedures, which are sometimes referred to as matrix corrections.

The EDS mapping in this study was done in two different systems. One of the systems used is a JEOL 6060-LV scanning electron microscopy. Second system is the FEI Qunata 650 scanning electron microscopy. The Energy dispersive X-ray microanalyses of the JEOL 6060 LV system has the following specifications: iXRF EDS elemental analysis system, 10 mm ATW Oxford Instruments Si(Li) X-ray Detector, 130 eV resolution (Mn K0alpha), light element detection (Be-U), 0.1 % to 1 % sensitivities, qualitative analysis, quantitative analysis and digital X-ray mapping and imaging.

2.6 X-ray Diffraction

X-ray diffraction (XRD) is a non-destructive technique used to analyze material properties like composition, structure and crystallographic orientations. XRD is an important tool in mineralogy for identifying, quantifying and characterizing minerals in complex mineral assemblages. The method is versatile which can be employed to test different states of material, solid, powder or liquid forms. The XRD studies are performed on the unknown material and the test data is analyzed based on the reference database which is gathered over the past decades.

X-rays are electromagnetic waves (photons) with energy $\approx$ 125 eV–125 KeV (wavelength $\lambda \approx 0.01$–10 nm). When X-rays impinge on a material several interaction processes are possible. X-rays can be elastically or inelastically scattered by electrons in a material. Elastic scattering, responsible for the diffraction process (also known as Thompson scattering) corresponds to the case where the energy of the incoming and outgoing photons are equal. Inelastic (Compton) scattering refers to the case where the energy of the emitted photon is lower than the energy of the incoming photon. The energy difference is transferred to the scattering electron. XRD is sensitive to crystalline phases down to 0.1–1 wt%. Conventional XRD instruments use monochromatic x-ray radiation from Cu, Cr, Mo or Ag sources. Cu, in particular with the K-α line, which is the specific electronic transition in Cu used to generate a wavelength 0.15418 nm, energy 8.05 keV, is the most commonly radiation in laboratory sources. Typical probed volume in sample during XRD analysis depends on the X-ray penetration depth, which is a function of the X-ray energy, sample material and angle of incidence of the primary x-ray beam relative to the surface.

X-rays are generated in a sealed x-ray tube. Electrons are emitted by a hot filament, the cathode of the tube and they are accelerated due to the high voltage difference between the anode and the cathode. These accelerated electrons then interact with the target

material and a high speed and result in the removal of the electrons from the inner shells of the atoms of the material. These changes in the atomistic configuration of the material lead to the emission of characteristic X-ray radiation specific to that material and its composition. The nature of X-ray radiation will interact with the crystalline structure of the target material. This interference patterns form the basis of the diffraction study which is described by the Bragg's Law [50] $n\lambda = 2dsin\theta$. n is the order of interference, a positive integer, d is the inter-planar spacing between the atomic layers, 2θ is the angle between the incident and reflected beam and λ is the wavelength of the incident beam.

The principle of X-ray diffraction is used in the construction of X-ray diffractometer. The X-ray tube is arranged on one end of the instrument while the beam generated by the tube passes through openings which regulate the beam intensity, amplitude and the divergence that is directed onto the target sample. These diverged X-rays interact with the sample and undergo interference, then the reflected rays are captured using a detector. Similar to the initial beam divergence, these reflected rays pass through the slits to create convergence of the reflected X-rays generated from the target material. Figure 2.11 demonstrates the schematic of a X-ray diffraction system. This figure illustrates the main components of X-ray diffraction system: the tube, direct beam slits, the detector slits and the detector.

SIEMENS-BRUKER D-5000

The powder x-ray diffraction works with the principles described previously. X-ray diffraction study is one of the most common practices due to ease of installation and usage. While sample preparation remains a challenging task for rock material in presence of clay particles. Special treatment is needed to accurately identify and quantify the clay percentage. The Siemens/Bruker D-5000 X-ray diffraction instrument was used at Material Research Laboratory at University of Illinois at Urbana-Champaign. The instrument uses the Cu-K-alpha radiation with a corresponding wavelength of 0.15418 nm. The instrument consists of a Bragg-Brentano Configuration of the theta/theta vertical goniometer system. It also embodies the optical spinner rotation. The X-ray generated from the X-ray tube passes through the soller slit and divergence slit. After the beam interact with the material and undergoes interference. The reflected rays passes through a series of slits, a curve graphite monochromator and scintillation detector. This method and instrument is effective in the determination of amorphous phase contents in the mixtures.

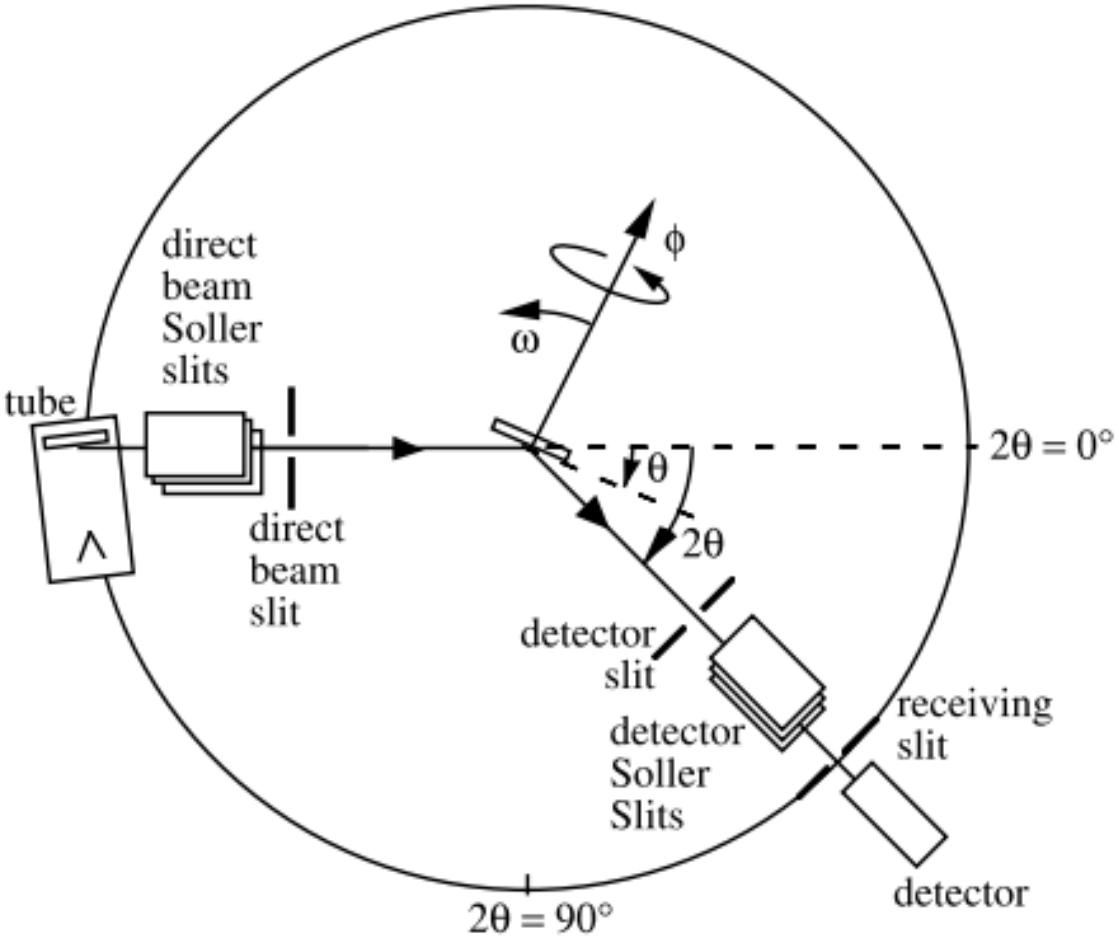

Figure 2.11: Schematic of X-ray diffraction instrument. Adopted from [51].

2.7 Total Organic Carbon Analyzer

Total organic carbon (TOC) is the amount of carbon found in an organic compound. TOC can be used to refer the amount of organic carbon in soil, or in a geological formation, particularly the source rock for a petroleum plays. TOC measures both the total carbon present and the inorganic carbon, which represent the content of dissolved carbon dioxide and carbonic acid salts. Subtracting the inorganic carbon from the total carbon yields TOC. There is another method to measure TOC which involves removing the inorganic carbon portion first and then measuring the leftover carbon. This method involves purging an acidified sample with carbon free-air or nitrogen prior to measurement, and so is more accurately called non-purgeable organic carbon (NPOC).

TOC measurement may be divided to three main stages independent of the method of analysis of TOC. These stages are acidification, oxidation and detection and quantification. Acidification is the stage where an addition of acid and inter gas sparging allows all bicarbonate and carbonate ions to be converted to carbon dioxide, and this inorganic content product vented along with any purgeable organic content that was present. Oxidation is the second stage, where the carbon remaining in the sample in the form of carbon dioxide and other gases. The oxidation will be done in several steps: High temperature combustion, high temperature catalytic oxidation, photo-oxidation alone, thermo-chemical oxidation, photo-chemical oxidation and electrolytic oxidation. The last step is the detection and quantification. Accurate detection and quantification are the most vital components of the TOC analysis process. Conductivity and non-dispersive infrared (NDIR) are the two common detection methods used in modern TOC analyzers. In this study we used a UIC Carbon coulometer ^{TM}to measure TOC of different shale samples. The measurement and analysis was performed based on ASTM D513.

2.8 Conclusion

In this chapter, a review of different observational and analytical tools is presented. The basics of specimen preparation, atomic force microscopy, scanning electron microscopy, energy dispersive spectroscopy, x-ray diffraction and total organic carbon analyzer. The specimen preparation section reviews the basics of grinding and polishing to prepare the specimen for mechanical testing. The atomic force microscopy section covers the basics of spectroscopy technique and is used to measure the roughness of specimen prepara-

tion. The scanning electron microscopy section reviews the instrument parts, operational procedure of the instrument and troubleshooting steps to obtain a high-quality image. The energy dispersive spectroscopy and x-ray diffraction methods are used to capture the mineralogy and elemental composition of specimens. In addition to the energy dispersive spectroscopy and X-ray diffraction, total organic carbon analyzer is used to find the total organic content of shale specimens.

Chapter 3

Indentation Methods

3.1 Introduction

In this chapter, a comprehensive review of indentation methods, theory, equipment and applications is presented. Indentation testing consists of probing the material of interest whose mechanical properties are unknown with another material whose properties are known. During the indentation tests, the load, P, applied and the depth, h, of the indenter with respect to the indented surface are continuously measured. This resulting P-h curve is utilized to condense experimental indentation data into two parameters: the indentation modulus, M, and indentation hardness, H. These two parameters are related to the elasticity content of the indented space while the indentation hardness stems from the strength properties. The focus of this chapter is to review recent developments in indentation analysis of elastic and viscoelastic materials, which enables connecting indentation measurements to the indented material properties. Furthermore, a review of theory behind the indentation testing is presented. This chapter reviews the classical tools of indentation analysis for homogeneous solids, that allow for the extraction of elastic and strength properties of the indented material. Indentation equipment capabilities and limitations are summarized here. Last but not least, the application of the indentation method to characterize the mechanical properties of materials are presented. This review defines a basis for original developments presented in future chapters, and the analytical developments presented here will be of critical importance for the experimental investigation of the fundamental properties of sedimentary rocks.

3.2 Principle

An indentation test consists of pushing an indenter vertically, with a known geometry, into the surface of a material of interest. The self-similarity of the indentation test is the underlying concept that allows linking the indentation properties to the material properties. In indentation testing, self-similarity implies that the displacement fields at any load P can be inferred from the displacement fields at a give load P_0. The conditions in which indentation problems are self similar are as follow [52, 53]. The shape of the indenter probe must be described by a smooth function whose degree is greater than or equal to unity. In addition, the constitutive relationships of the indented material must be described by a smooth function with respect to the strains or the stresses. During the contact process, the loading at any point must be progressive.

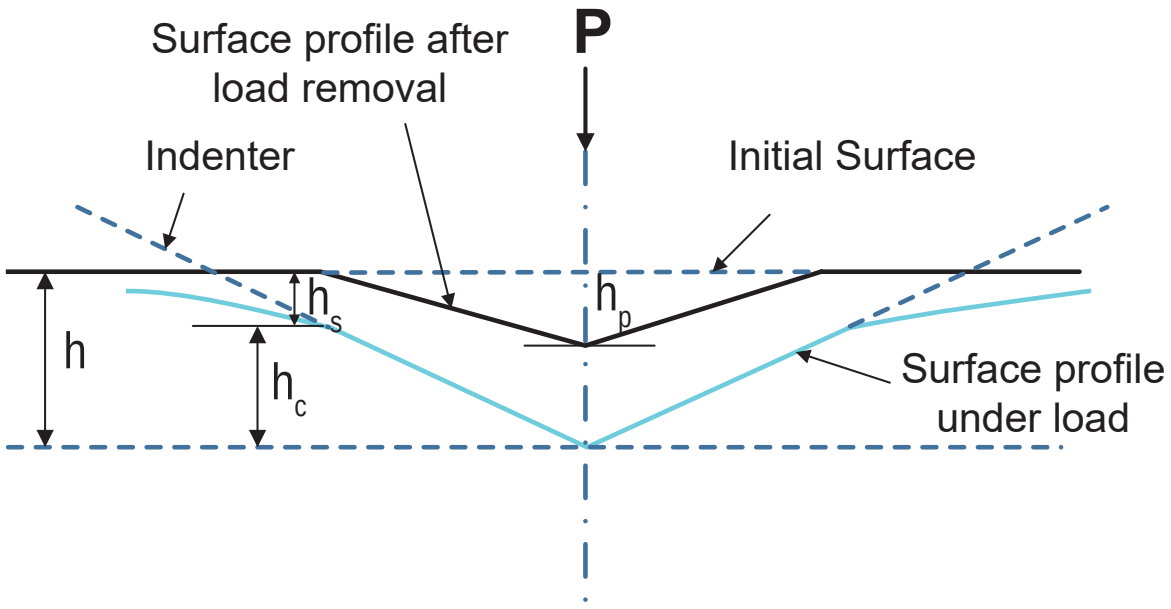

Figure 3.1: Schematic representation of indenter: Sample Contact schematic of Berkovich tip.

The elastic contact problem, which plays a key role in the analysis procedure, was originally considered in the late 19th century by Boussinnesq [54] and Hertz [55]. Boussinesq developed a method based on potential theory for computing the stresses and displace-

ments in an elastic body loaded by a rigid, antisymmetric indenter. His method has subsequently been used to derive solutions for a number of important geometries such as cylindrical and conical indenters [56, 57]. Hertz analyzed the problem of the elastic contact between two spherical surfaces with different radii and elastic constants. These classic solutions form the basis of much experimental and theoretical work in the field of contact mechanics [58] and provide a framework by which the effects of non-rigid indenters can be included in the analysis. Another major contribution was made by Sneddon, who derived general relationships among the load, displacement, and contact area for any punch that can be described as a solid revolution of a smooth function [59, 60]. His results show that the load-displacement relationships for many simple punch geometries can conveniently be written as $P = \alpha h^m$, where P is the force, h is the indentation depth and α, m are fitting coefficients.

Table 3.1 summarizes the indenter definition with area function relationships for Vickers, Berkovich, modified Berkovich and Cube Corner indenter. The total included angle for Vickers and Berkovich are 136 ° and 141.9 °, respectively. The developed contact area is the same for both Vickers and Berkovich tip. In addition to this indenters with defined shape, the spherical and conical indenters are the two other options.

Figure 3.2 demonstrates scanning electron microscopy of three different tips. The Berkovich, Vickers and Cube corner tips are shown in this image.

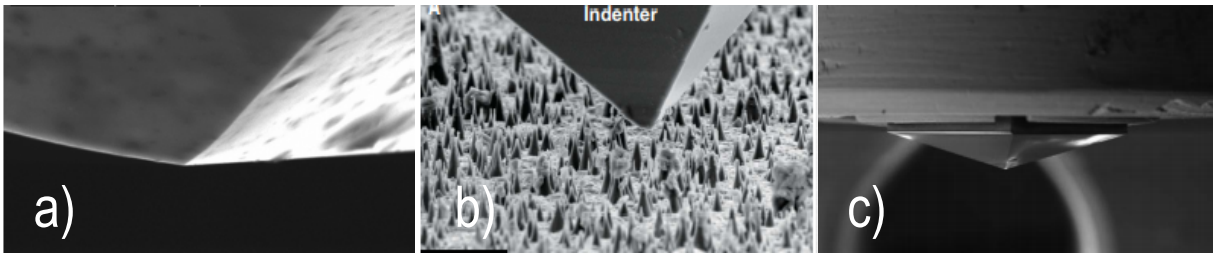

Figure 3.2: Scanning electron microscopy image of a) Berkovich tip. Adopted from [61], b) Cube Corner tip. Adopted from [62], c) Vickers tip. Adopted from [63].

Figure 3.1 demonstrates a schematic representation of indenter and the contact depth illustrations. The initial surface of the sample and surface profile after load removal are shown.

Great advances have been made over the past few decades in the development of techniques for probing the mechanical properties of materials on the sub-micron scale [64, 65].

Table 3.1: Indenter definition with area function relationships.

	Vickers	Berkovich	Modified Berkovich	Cube Corner
$a_t^{(1)}$	136 °	141.9 °	142.3 °	90 °
$a^{(2)}$	68 °	65.03 °	65.27 °	35.264 °
$\frac{A_d}{h^2}^{(3)}$	≈ 26.43	≈ 26.43	≈ 26.97	4.5
$\frac{A_p}{h^2}^{(4)}$	≈ 24.504	≈ 23.96	≈ 24.494	≈ 2.598
$\frac{A_d}{A_p}$	≈ 1.0785	≈ 1.1031	≈ 1.1010	≈ 1.7320

(1) a_t: total included angle
(2) a: angle between the axis of the diamond pyramid and the 3 faces
(3) A_d: developed contact area
(4) A_p: projected contact area

These advances have been made possible by the development of instruments that continuously measure force and displacement as an indentation is made [66–68]. The indentation load-displacement data that is derived can be used to determine mechanical properties even when the indentations are too small to be imaged conveniently. Since the indentation positioning capability of some of the instrument is also in the sub-micron regime, a means is available by which the mechanical properties of a surface can be mapped with such capabilities that can be described as a mechanical properties micro-probe [69–71]. The two mechanical properties measured most frequently using load and depth sensing indentation techniques are the elastic modulus, E, and the hardness, H. In a commonly used indentation test, data are obtained from one complete cycle of loading and unloading. The unloading data are then analyzed according to a model for the deformation of an elastic half space by an elastic punch which relates the contact area at peak load to the elastic modulus. Methods for independently estimating the contact area from the indenter shape function are then used to provide separate measurements of E and H.

3.3 Equipment

The equipment used in this study was an Anton Paar indentation unit. The indentation unit was contained in enclosed chamber to reduced the vibrations as well as surrounding noise. The nanoindentation equipments are usually described based on some quoted specifications. These specifications are: minimum contact force, force resolution, force noise

floor, displacement resolution, displacement noise floor, maximum number of data points, data acquisition rate, variable loading rate, unattended operation, specimen positioning, field of testing, resonant frequency, thermal drift, machine stabilization time, indentation time, tip exchange time, loading step, constant strain rate, topographical imaging, dynamic properties, high temperature testing and acoustic emission testing. The minimum contact force is typically limited by the noise floor of the instrument and the test environment. The value should be as low as possible so as to minimize the error associated with the initial penetration. The force resolution determines the minimum change in force that can be detected by the instrument. Force noise floor is the most important factor that determines the minimum contact force attainable by the system. Any increase in resolution beyond the noise floor will only mean that the noise is being measured more precisely. The noise floor is generally limited by electronic noise or the environment in which the instrument is located. The displacement resolution is typically found by dividing the maximum displacement voltage reading by the number of bits in the data acquisition system. Displacement noise floor will determine what the minimum useable indentation depth. The displacement noise floor is one of the most important measured of performance of an instrument.
Maximum number of data points is the maximum number of data points that can be collected for a single test. More data points allow for better resolution of *pop-in* events and other features in the force-displacement curves. However, the data acquisition rate will be important for large data sets, since data should be collected as quickly as possible to minimize errors due to thermal drift. Data acquisition rate demonstrate how fast the machine will collect force and displacement data. The data acquisition rate should be as high as possible so as to allow the time for a tests to be shorter, thus minimizing errors due to thermal drift. Variable loading rate is useful for measurement of mechanical properties of some specimen materials where the properties depend upon the rate of application of load. This ability of vary the loading rate allows such studies to be performed. Slow loading may be desirable for some materials followed by a fast unloading.

Figure 3.3 illustrates the head of the nanoindetation tester. The head consists of a reference ring, electromagnetic coil, capacitive sensor and the indenter.

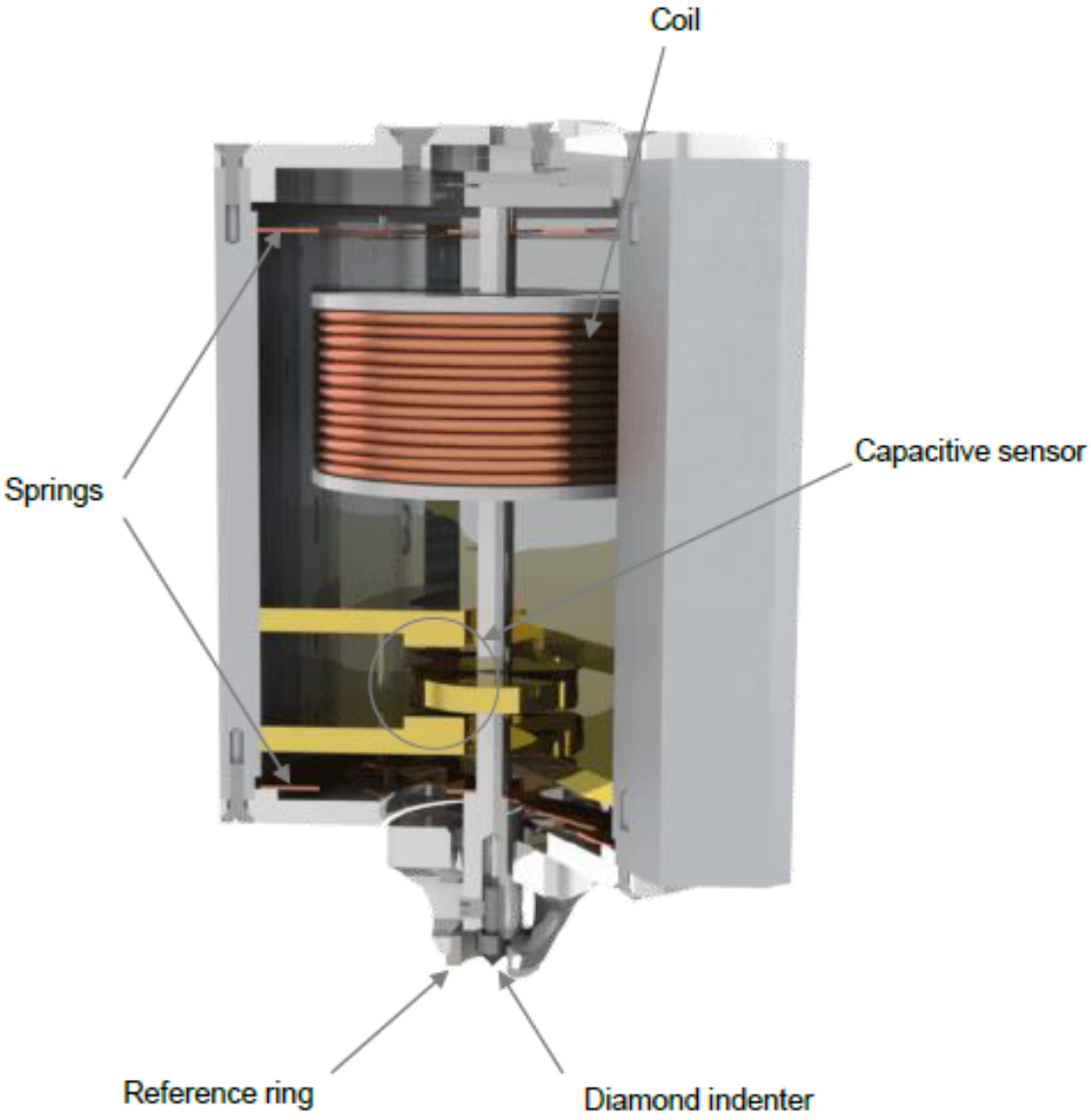

Figure 3.3: Schematic illustration of nanoindentation tester head (NHT^2), Anton Paar ^{TM}(Ashland, VA). Adopted from [72].

Unattended operation is the ability of the instrument to be programmed to collect the data on a single site, or an array of sites, while not requiring any operator intervention during the tests. Specimen positioning is a feature that shows how accurately the instrument can position the indenter. Most instruments allows 0.5 μm positioning resolution with optical rotary encoders. Field of testing is the dimension of the testing are accessible by the indenter based upon the maximum movement of the positioning stages. Resonant frequency is the natural resonant frequency of the instrument. It depends upon the mass of the instrument and the characteristics of the mounting springs and dampers. A high resonant frequency makes the instrument less susceptible to mechanical environmental interference. Also, a higher resonance allows higher-frequency dynamic measurements to be made. High frequency dynamic measurements can be made with a low resonant frequency system if the sample, rather than the indenter, is oscillated. Thermal drift is almost unavoidable surrounding the instrument if the temperature of the environment surrounding the instrument is not kept within very tightly controlled limits. Most instruments are supplied with an enclosure with very high thermal insulating properties.
Machine stabilization time is the time needed by the instrument to stabilize after initial power up. The time is usually dependent on the thermal characteristic of the measurements system. A short time allows for more efficient use of the test facility. Indentation time is the average time of a typical indentation cycle from load to full unload. A nanoindentation instrument should be able to perform a single indentation within one or two minutes. Tip exchange time is the time needed for the operator to change the indenter. Loading step can be applied in a variety of ways in typical nanoindentation instruments. A square root spacing of load increments gives an approximate even spacing of depth measurements. A linear spacing of load increments may provide a constant loading rate. The instrument should offer one or two options in this regard.
Constant strain rate testing involves the application of load so that the depth measurements follow a pre-defined relationship. Some nanoindentation instruments offer the ability of set the loading rate so as to give a constant rate of strain within the specimen material. This may be important for viscoelastic material or those that exhibit creep. Topographical imaging provides scans of a surface before it is indented for accurate tip placement and also provides immediate imaging after the indent is completed to measure the size of the residual impression. Such imaging can be done with an atomic force microscope accessory mounted as either another station on the instrument assembly or as an in situ device. Dynamic properties is the ability to measure the response of surfaces

under a sinusoidal or other oscillating load. This technique is important for measuring the viscoelastic properties of materials. The method usually involves the application of an oscillatory motion to the indenter or the sample. A lock-in amplifier measure phase and amplitude of force and displacement signals. High temperature testing is of considerable interest, to measure the mechanical properties of materials at their operating temperature. Some indentation instruments allow testing of smaller size samples at temperatures ranging from 5–500 °C. Acoustic emission testing allows the fitting of an acoustic microphone to the indenter or specimen for recording of non-linear events such as cracking or delamination of thin films.

The instrument used in this study was a Nano-Hardness Tester ™from Anton Paar (Ashland, VA). An indenter tip with a know geometry is driven into a specific site of the material to be tested by applying an increased normal load. Indenter displacement is measured using a capacitive transducer. Using the partial-unload technique, the contact stiffness and hardness of the specimen material can be calculated as a function of depth of penetration into the specimen. The indenter load is measured using a load cell attached to the indenter shaft.

Figure 3.4 shows the nanoindentation instrument. We can see the acoustic enclosure of that the instrument is placed in as well as the thermal isolation around the unit. The frame is stabilized by using a concrete slab to reduced the floor noise, while the indentation frame is floating on an anti-vibration table. Furthermore, Figure 3.4b shows the close up of the microscopic unit as well as the indentation head.

A particular feature of this instrument is the use of a sapphire ring reference ring that remains in contact with the specimen surface during the indentation. The reference ring provides a differential measurement of penetration depth and thus the load frame compliance and thermal drift are automatically compensated for. The sapphire ring also acts as a local environmental enclosure protecting the measurements spot from air currents, sound wavers, changes in humidity and changes in temperature, thus obviating the need for special environmental conditions in order to obtain perfect measurements. The ring also allows the working distance to be set very quickly as the ring contacts the surface before the indenter and so the final approach, to be made very slowly, tales place only over a few microns displacement. The specifications of the NHT2 ™are shown in Table 3.2.

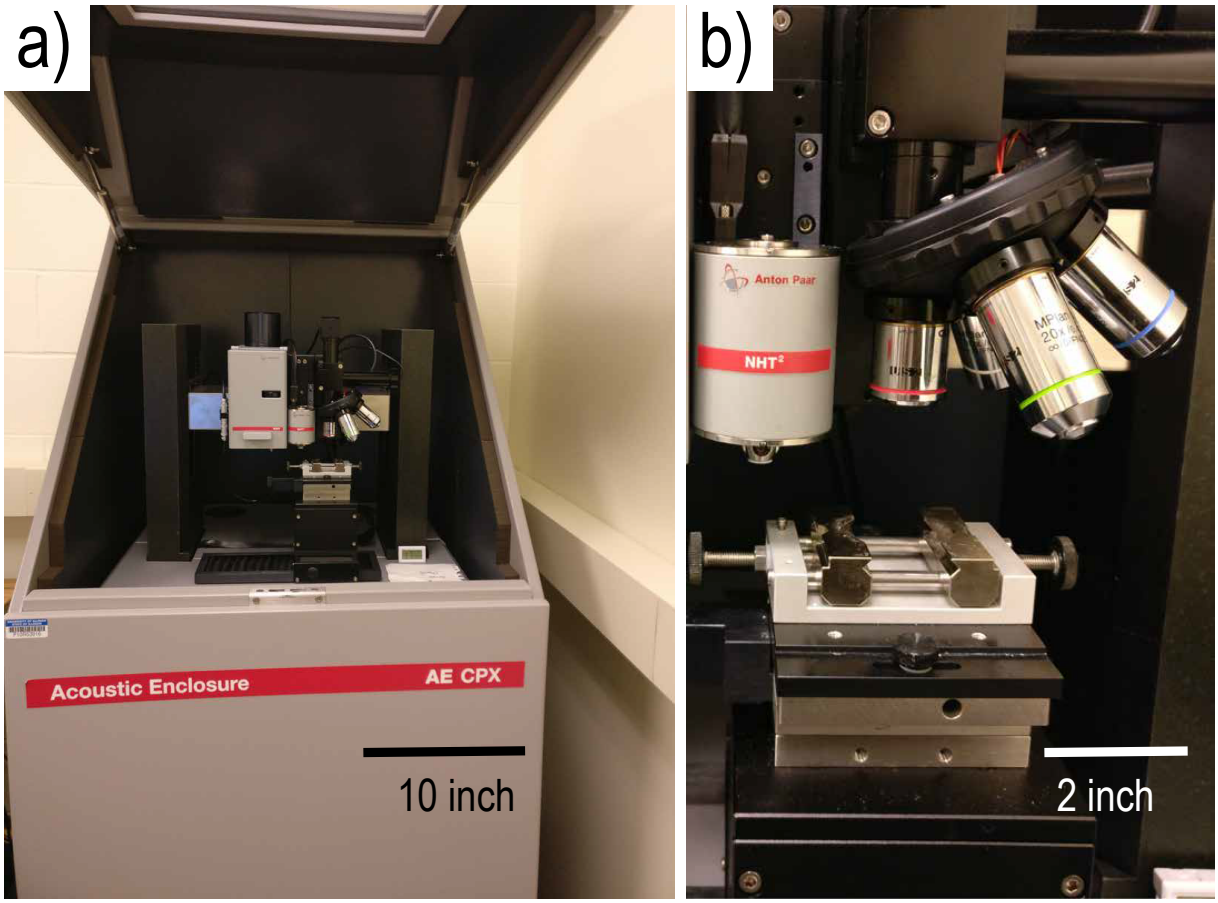

Figure 3.4: Photograph of Anton Paar CPX Nanoindentation Unit, University of Illinois at Urbana-Champaign.

Table 3.2: Specifications of the NHT2 ™.

Specifications	
Depth resolution	0.01 nm
Maximum indentation depth	>50 μm
Maximum load	500 mN
Load resolution	$\pm$ 0.02μN
Work table dimension	145 mm×70 mm
Usable areas with optical analysis	95 mm× 70 mm

3.4 Theory

A meaningful quantity in indentation hardness is the mean contact pressure of the contact and is found by dividing the indenter load by the projected area of the contact. The average contact pressure, when determined under conditions of a fully developed plastic zone, is taken to be the indentation hardness, H, of the specimen material. Analogously, the elastic modulus determined from the slop of the unloading of the load-penetration depth response in an indentation test. This value is called indentation modulus, M, of the specimen material.

There is a distinct difference between conventional definition of hardness and the hardness obtained by nanoindentation using depth sensing measurements. In conventional hardness tests, such as the Brinell test, the size of the residual impression in the surface is used to determine the area of contact and the hardness value. While, in depth sensing indentation tests, such as that used in nanoindentation, the size of contact area under full load is determined from the depth of penetration of the indenter and the elastic recovery during the removal of load. The latter method provides an estimate of the area of the contact under full load. Usually, the area given by the shape of the residual impression and that given by the depth-sensing techqnue are almost identical, but this is not always the case.

Figure 3.5 illustrates a typical indentation test curves. Figure 3.5a) shows the load vs time curve for a typical indentation test. The load consists of a linearly increasing load, a constant holding time and unloading portion. Figure 3.5 illustrates the load vs penetration depth for a single indent with loading, holding and unloading phase.

3.4.1 Boussinesq Problem

Boussinesq [54] solved the problem of stress distribution at any point X in a semi-infinite half space, homogeneous, isotropic and elastic material as a result of a point load, Q, applied on the surface.

$$\delta\sigma_z = \frac{3Q}{2\pi z^2}\left(\frac{I}{1+(r/z)^2}\right)^{5/2} \tag{3.1}$$

where $I = \frac{3}{2\pi}(\frac{1}{1+(r/z)^2})^{5/2}$

$$\delta\sigma_\theta = \frac{Q}{2\pi}(1-2\nu)\left(\frac{z}{(r^2+z^2)^{3/2}} - \frac{1}{r^2+z^2+z(r^2+z^2)^{1/2}}\right) \tag{3.2}$$

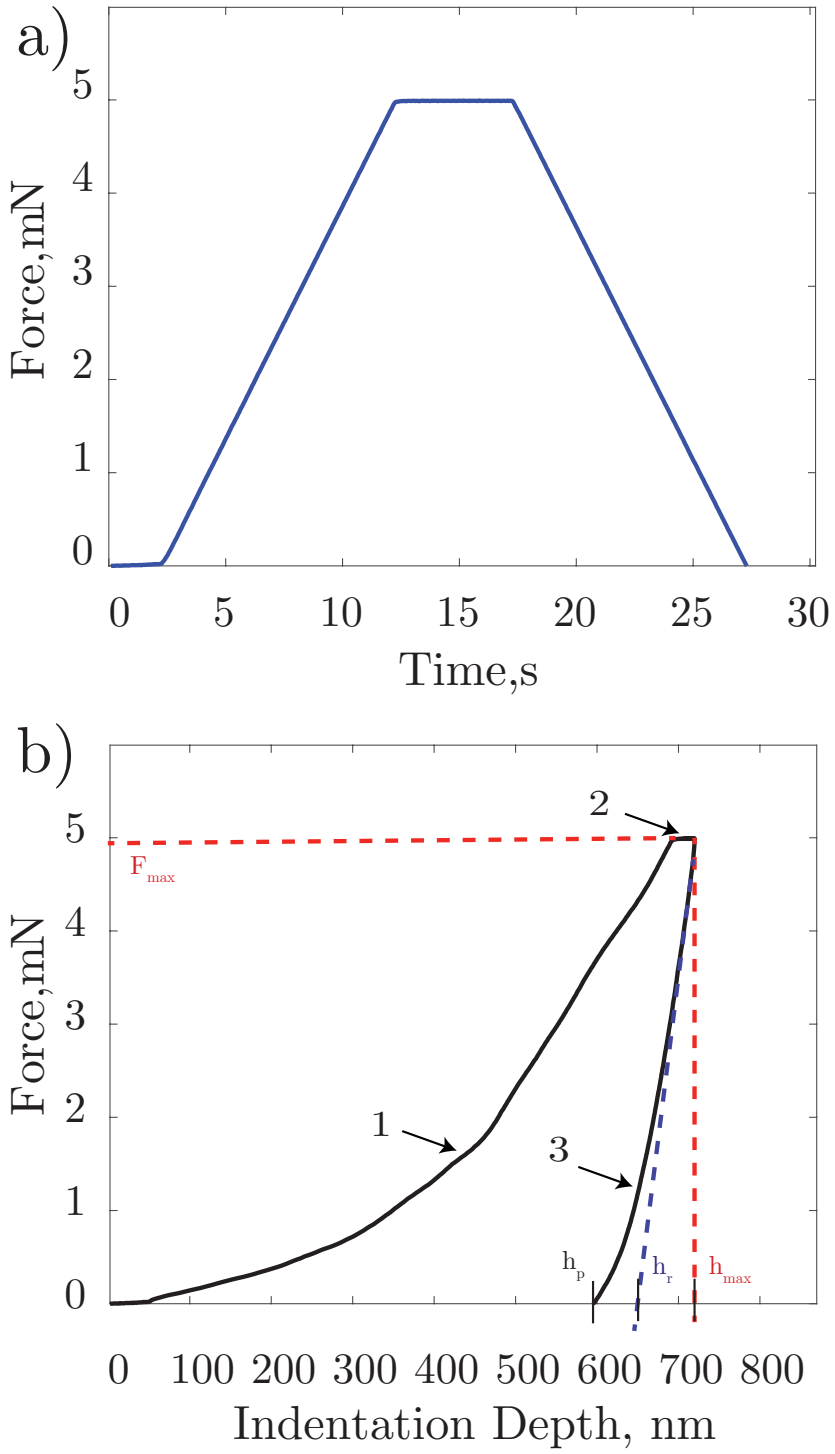

Figure 3.5: Graphical views of indentation test parameters a) Load vs time curve b) Load vs penetration depth of a single indent.

$$\delta\sigma_r = \frac{Q}{2\pi}\left(\frac{3r^2z}{(r^2+z^2)^{5/2}} - \frac{1-2\nu}{r^2+z^2+z(r^2+z^2)^{1/2}}\right) \tag{3.3}$$

where ν is the Poisson's ratio and z shows the vertical distance from the point load, and r is the horizontal distance from the desired point. The equations above shows changes in the stress state at different directions.

3.4.2 Hertz Contact Problem

Furthermore, an elastic contact problem can be defined for a contact of a rigid sphere and a flat surface. The stresses and deflections arising from the contact between two elastic solids are of particular interest. Hertz [55, 73] found that the radius of the circle of contact a is related to the indenter load P, the indenter radius R and the elastic properties of the contacting materials by Equation 3.4.

$$a^3 = \frac{3PR}{4E^*} \tag{3.4}$$

The quantity E^* combines the modulus of the indenter and the specimen using Equation 3.5.

$$\frac{1}{E^*} = \frac{(1-\nu^2)}{E} + \frac{(1-\nu'^2)}{E'} \tag{3.5}$$

where E' is the elastic modulus and ν' is the Poisson's ratio of the indenter. If both of contacting bodies have a curvature, then R in Equation 3.4 is their relative radii given by Equation 3.6.

$$\frac{1}{R} = \frac{1}{R_1} + \frac{1}{R_2} \tag{3.6}$$

In Equation 3.6, the radius of the indenter is always positive and the radius of the specimen to be positive if the center of curvature is on the opposite side of the lines of contact between the two bodies and h is the indentation displacement of the original surface in the vicinity of the indenter, and is given by Equation 3.7.

$$h = \frac{1}{E^*}\frac{3P}{8a}\left(2 - \frac{r^2}{a^2}\right); r < a \tag{3.7}$$

where a is the radius of the circle of contact. r is the distance between the center of contact and the point of contact. The distance from the specimen free surface to the depth of

the radius of the circle of contact at full load is $h_a = h/2$. Furthermore, the distance of mutual approach of distant points in the indenter and specimen, δ, is calculated by using Equation 3.8.

$$\delta^3 = \left(\frac{3}{4E^*}\right)^2 \frac{P^2}{R} \tag{3.8}$$

Substituting Equation 3.7 into 3.4 the distance of mutual approach is described as Equation 3.9.

$$\delta = \frac{a^2}{R} \tag{3.9}$$

Now substituting Equation 3.9 to Equation 3.8 the total depth of penetration,h_t, and penetration load are related by Equation 3.10.

$$P = \frac{4}{3} E^* R^{1/2} h_t^{3/2} \tag{3.10}$$

In the case of a conical indenter a similar equation holds where the radius of circle of contact is related to the indenter load by Equation 3.11.

$$P = \frac{\pi a}{2} E^* a cot\alpha \tag{3.11}$$

The depth penetration of the apex of the indenter, h_t beneath the original specimen free surface is given by Equation 3.12.

$$h_t = \sqrt{\frac{P\pi}{2Etan\alpha}} \tag{3.12}$$

where α is the cone semi-angle, E is the Young's modulus, and P is the force.

In indentation testing, pyramidal indenter are generally treated as conical indenters with an equivalent cone angle that provides the same area to depth relationship as shown in Table 3.1.

3.4.3 Berkovich Indenter

The Berkovich indenter is used for nanoindentation testing because of the sharper tip compares to the four-sided Vickers geometry, thus ensuring a more precise control over the indentaion process. The mean contact pressure is usually determined from a measure

of the plastic depth of penetration, h_p (cf. Figure 3.1), such that the area of contact is given by Equation 3.13.

$$A = 3\sqrt{3}h_p^2 tan^2\theta \tag{3.13}$$

where for θ =65.3$\circ$, Equation 3.13 reduces to Equation 3.14.

$$A = 24.5h_p^2 \tag{3.14}$$

and hence the mean contact pressure, H, is calculated by Equation 3.15.

$$H = \frac{P}{24.5h_p^2} \tag{3.15}$$

For both the Vickers and the Berkovich indenter, the representative strain within the specimen material is approximately 8%. In addition, for the case of a Berkovich indenter, a complete plastic responsive is assumed throughout. The distance h_p is calculated using Equation 3.16.

$$h_p = \left(\frac{P}{3\sqrt{3}Htan^2\theta}\right)^{1/2} \tag{3.16}$$

The distance h_r is easily determined from the intercept of the slope of the unloading curve using Equation 3.17. The unloading part of the indentation force penetration depth curve where the intercept of tangent line on unloading curve will result in h_r (cf. 3.5).

$$h_r = \left[\frac{2(\pi-2)}{\pi}\right]\frac{1}{2E^*}(PH\pi)^{1/2} \tag{3.17}$$

Thus, the total depth, h_t, is obtained by Equation 3.18.

$$h_t = \sqrt{P}\left[(3\sqrt{3}Htan^2\theta)^{-1/2} + \left[\frac{2(\pi-2)}{\pi}\right]\frac{\sqrt{H\pi}}{2\beta}\right] \tag{3.18}$$

The solution for a conical indenter of half-angle α, will reduce to Equation 3.19. This equation illustrates the $P \propto h_t^2$ relationship for elastic-plastic loading more clearly.

$$P = E^*\left[\frac{1}{\sqrt{3\sqrt{3}tan^2\theta}}\sqrt{\frac{E^*}{H}} + \left[\frac{2(\pi-2)}{\pi}\right]\sqrt{\frac{\pi}{4}}\sqrt{\frac{H}{E^*}}\right]^{-2} h_t^2 \tag{3.19}$$

3.4.4 Oliver and Pharr Method

The method was developed to measure the hardness and elastic modulus of a material from indentation load displacement data obtained during one cycle of loading and unloading. The application of the method was originally intended for application with sharp, geometrically self-similar indenters like the Berkovich triangular pyramid. Since, the method was understood to be more general than this and applies to a variety of axsisymmetric indenter geometries including the sphere.

A schematic representation of a typical data set obtained with a Berkovich indenter is presented in Figure 3.5, where the parameter P designates the load and h the displacement relative to the initial undeformed surface. Deformation during loading is assumed to be both elastic and plastic in nature as the permanent hardness impression forms. During unloading, it is assumed that only the elastic displacements are recovered. For this reason, the method does not apply to materials in which plasticity reverses during unloading. There are three important quantities that must be measured from the P-h curves: the maximum load, P_{max}, the maximum displacement, h_{max}, and the elastic unloading stiffness, $S = \mathrm{d}P/\mathrm{d}h$, defined as the slope of upper portion of the unloading curve during the initial stages of unloading. The analysis used in this method to determine Hardness, H, and elastic modulus, E. It is an extension of the method proposed by Doerner and Nix [65] that accounts for the fact that unloading curves are distinctly curved in a manner that cannot be accounted for by the flat punch approximation. The indentation experiments show that unloading curves are distinctly curved and usually well approximated by the power law relation shown in Equation 3.20.

$$P = \alpha(h - h_f)^m \tag{3.20}$$

where α and m are power law fitting constants. h_f is the final indentation depth. The power law exponent ranges from 1.2–1.6, which demonstrates that the punch approximation is not accurate, but also that the indenter appears to behave more like a paraboloid of revolution. The exact procedure used to measure H and E is based on the unloading processes shown schematically in 3.5, in which it is assumed that the behavior of the Berkovich indenter can be modeled by a conical indenter with a half angle of ϕ =70.3°. The basic assumption is that the contact periphery sinks in a manner that can be described by models for indentation of a flat elastic half-space by rigid punches of simple geometry. This assumption limits the applicability of the method because it does not

account for the pile-up of material at the contact periphery that occurs in some elastic-plastic materials. The elastic models, with assumption of negligible sink-in, is given by Equation 3.21. S is defined as the slop of the upper portion of the unloading curve during the initial stage of unloading.

$$h_s = \epsilon \frac{P_{max}}{S} \tag{3.21}$$

where ϵ is a constant that depends on the geometry of the indenter. The value of ϵ =0.75 is recommended due to empirical observation of unloading curve, which behaves like a paraboloid of revolution. Using this approximation to find the vertical displacement of the contact periphery, the displacement is derived by Equation 3.22.

$$h_c = h_{max} - \epsilon \frac{P_{max}}{S} \tag{3.22}$$

Defining *F(h)* as an area function that describes the projected area of the indenter at a distance h back from its tip, the contact area is $A = F(h_c)$. This area function, called the indenter shape function, must carefully be calibrated by independent measurements so that deviations from non-ideal indenter geometry are taken into account. These deviations can be considerable near the tip of the Berkovich indenter, where some rounding inevitably occurs during the production process and after testing. The indenter area function is calibrated using a reference material with known mechanical properties, mostly fused silica. The form of the area function is prescribed by Equation 3.23.

$$A = \sum_{n=0}^{8} C_n (h_c)^{2-n} = C_0 h^2 + C_1 h + ... + C8 h^{1/128} \tag{3.23}$$

where C_0, ... C_8 are constants determined by curve fitting procedures. A perfect pyramid or cone is represented by the first term alone. The second term describes a paraboloid of revolution, which approximates to a sphere at small penetration depths. In each case, the experimentally determined constants can be compared with the appropriate geometric description to verify the geometry. The higher order terms of equation 3.23 are generally useful in describing deviations from perfect geometry near the indenter tip and give the experimenter some flexibility in developing an area function that is accurate over several orders of magnitude in depth. Once the contact area is determined, the hardness can be

estimated by using Equation 3.24.

$$H = \frac{P_{max}}{A} \tag{3.24}$$

It is good to remember that this definition of hardness is based on the contact area under the load, it may deviate from the traditional hardness measured from the area of the residual hardness impression if there is significant elastic recovery during unloading. However, this is generally important only in materials with extremely small values of E/H.

Measurement of the elastic modulus follows from its relationship to contact area and the measured unloading stiffness through the relation shown in Equation 3.25. β is a dimensionless parameter that is used to account for deviations in stiffness caused by the lack of axial symmetry for pyramidal indenters.

$$S = \beta \frac{2}{\sqrt{\pi}} E_{eff} \sqrt{A} \tag{3.25}$$

where E_{eff} is the effective elastic modulus defined by Equation 3.26.

$$\frac{1}{E_{eff}} = \frac{1-\nu^2}{E} + \frac{1-\nu_i^2}{E_i} \tag{3.26}$$

The effective elastic modulus takes into account the fact that elastic displacement occur in both the specimen, with Young's modulus, E and Poisson's ration ν for the indenter and with elastic constants for the material being indented as E_i and ν_i.

Although Equation 3.26 was developed for elastic contact only and is often associate with flat punch indentation but it has been shown that it applies equally well ti elastic-plastic contact and that small perturbations from pure axisymmetry geometry do not effect it either. The correction factor β appearing in Equation 3.26 plays an important role for accurate mechanical property measurements. This constant affects not only the elastic modulus calculated from the contact stiffness by means of this relation. The hardness is affected because procedure for determining the indenter area function are based on this equation and area functions can be in error if the wrong value of β is used. Thus, without a good working knowledge of β, one is limited in the accuracy that can be achieved in the measurement of both H and E. For the case of small deformation of an elastic material by a rigid axsisymmetric punch of smooth profile, β is exactly one. However, usually real indentation experiments are conducted with non-axisymmetric indenters and

involve large strains, other values for β may be more appropriate. The complex nature of elastic-plastic deformation with pyramidal indentrs makes this a very difficult exercise with results that are not entirely satisfying. Herein, we review the factors that affect β factor for Berkovich indentation and attempt to draw some conclusions concerning what value is best. The value of β= 1.034 has widely been adopted for instrumented indentation testing with a Berkovich indenter. Vlassak and Nix [74] conducted independent numerical calculations for the flat-ended triangular punch using a more precise method and found a higher value, β= 1.058. Hendrix [75], noting that the pressure distribution for elastic deformation by a flat punch is not representative of the real elastic-plastic problem, adopted another approach to estimate β. Assuming the pressure profile is perfectly flat, he used simple elastic analysis procedures to show that β= 1.0055 for a Vickers indenter and β= 1.0226 for the Berkovich.

In addition, finite element simulations have been used to evaluate β and explore the factors that influence it. The finite element simulations have the advantage of including the effects of plasticity, but are subject to inaccuracies caused by inadequate meshing and convergence. Larson et al. [76] conducted full 3D finite element calculations for true Berkovich indentation for a purely elastic material and for four different elastic-plastic materials that simulate the behavior of alloys. For the purely elastic material, they found out that β is slightly dependent on Poisson's ratio, ν, through the relation, $\beta = 1.2304(1 - 0.21\nu - 10.01\nu^2 - 0.41\nu^3)$. In a similar study, a through finite element study of elastic-plastic indentation with a 68 ° cone has been conducted by Cheng and Cheng [77, 78]. Their calculations included a wide range of materials characterized by different E/σ_yrations, Poisson's ratio, ν and work-hardening exponent, n. The β value for non-work-hardening materials are considered to be 1.05, independent of E/σ_y and nu. Second, for both hardening and non-hardening materials the reported β value is 1.085, independent of E/σ_y and n. The wide range of βs reported in these studies makes it difficult to settle in on a single preferred value. On the other hand, what can be concluded is that there are valid reasons to expect that β for the Berkovich indenter should be slightly greater than unity.

One of the most important considerations in performing valid indentation is a well calibrated testing system. The system calibrations are based on a relation, $C = C_f + \frac{\sqrt{\pi}}{2E_{eff}}\frac{1}{\sqrt{A}}$. This relation states that the total measured compliance, C, is the sum of compliance of the load frame, C_f, and the contact. This assumes that the load frame

compliance is a constant independent of load. The frame compliance can be calculated is the area function is known. At shallow depths, corresponding to small contact areas at the beginning of an indentation experiment, the contact compliance is high and dominates the total measured compliance. On the other hand, as the contact depth increase, the contact compliance decreases and at some point the load frame compliance become more dominant factor. Thus, for measurements of large depths, the total load frame compliance must be known with great accuracy.

3.5 Advanced Methods

In this section, a review of two different advanced methods of indentation technique is presented. The first part of this section reviews the different methods for creep testing. While, the second part of this section reviews the basic concepts of grid indentation.

3.5.1 Creep Testing

The use of nanoindentation proven useful for determining the mechanical properties of solids, most notably elastic modulus and hardness. The Oliver and Pharr method [79]relies on an analysis of the unloading of load-displacement response. The method relies on plasticity occurring instantaneously upon satisfaction of a constitutive criterion. On the other hand, many materials have a time-dependent behavior when placed under load. Thus, a nanoindentation test method may not provide an adequate estimation of viscoelastic properties of interest. There are two different approaches to managing time-dependent behavior in nanoindentation testing. First, application of an oscillatory displacement or force, in which the transfer function between the load and displacement provides a method of calculating the storage and loss modulus of material. Second, the application a step load or displacement and subsequent measurements of depth or force as a function of time. The method used here in this study is the second one. If we neglect the effects of arising from formation of cracks, permanent deformation in a material under indentation loading is a combination of instantaneous plasticity, which is not time dependent and creep, which is time-dependent. Thus, in a nanoindentation tests, the depth recorded at each load increment will be the addition of that due to elastic-plastic properties of the material and that occurring due to creep.

The majority of indenters are load-controlled, which make performing creep tests easier

to perform experimentally than indentation relaxation tests. In this part, we look into the indentation creep tests, where the load is held constant at its maximum value P_{max} while monitoring the indentation depth h(t). A creep tests can be performed by loading to the maximum force,P_{max}, and keep it constant for the holding time, t_h and then reduced the force to zero. There are several methods to analyze the indentation creep tests. Several researchers developed detailed theoretical solution for viscoelastic indentation creep [80–84]. A motivation for such modeling is the behavior of materials at elevated temperatures [85, 86]. Here a review of several models developed for creep tests is presented. In general, time dependent properties of materials are conventionally analyzed in terms of mechanical models such as those shown in Figure 3.6.

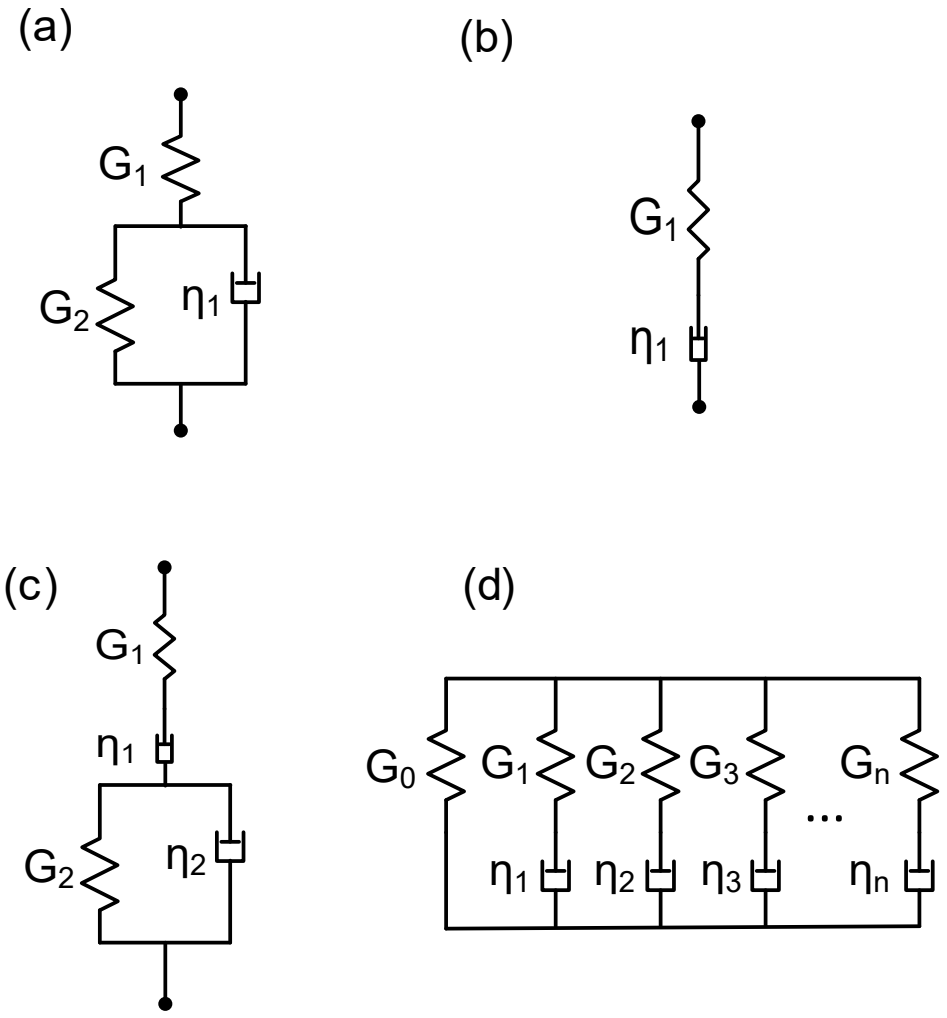

Figure 3.6: a) Three element Voigt and dashpot presentation, b) Maxwell representation of a visco-elastic material, c) four-element combined Maxwell-Voigt model ,d) Generalized Maxwell model.

A model demonstrated by Cripps [87] was developed based on the work of Radok [88] and Lee and Radock [89]. In their work, the viscoelastic contact problem is analyzed by using a correspondence principle in which elastic constants in the elastic equations of contact are replaced with time dependent operators. In the case of a conical indenter, the three element Voigt model result in Equation 3.27. G_1 and G_2 are the shear modulus for Voigt model. η is viscosity term that quantifies the time-dependent property of the material.

$$h^2(t) = \frac{\pi}{2} P_0 cot\theta \left[\frac{1}{G_1} + \frac{1}{G_2}(1 - e^{-tG_2/\eta}) \right] \tag{3.27}$$

For a Maxwell model and a conical indenter, Cripps derives the relation between indentation depth and the physical properties of material by Equation 3.28. G_1 is the shear modulus for Maxwell model. θ is the effective angle of the indenter. t is the indentation time for this model.

$$h^2(t) = \frac{\pi}{2} P_0 cot\theta \left[\frac{1}{G_1} + \frac{1}{\eta} t \right] \tag{3.28}$$

In addition, the model for a four-element Maxwell-Voigt model reveals Equation 3.29

$$h^2(t) = \frac{\pi}{2} P_0 cot\theta \left[\frac{1}{G_1} + \frac{1}{G_2}(1 - e^{-tG_2/\eta_2}) + \frac{1}{\eta_1} t \right] \tag{3.29}$$

The equations above are expressed in terms of shear modulus, G. This model is a simple model which does not consider the formal treatment of the full problem. Thus, this is a simplified treatment of nanoindentation creep testing.

Another solution for creep indentation was developed by Vandamme et al. [90, 91]. In their study, they have developed a solution based on principle of viscoelasticity. They showed that it is possible to derive closed form solutions following the classical procedure of functional formulations of viscoelasticity. They have demonstrated the details for the 3-parameter Maxwell model, 4-parameter Kelvin-Voigt model and the 5-parameter combined Kelvin-Voigt-Maxwell model.

Here we present a summary of their viscoelastic models. Equations 3.30 and 3.31 show the relation between Young's modulus and shear modulus and bulk modulus.

$$G_0 = \frac{E_0}{2(1 + \nu_0)} \tag{3.30}$$

$$K_0 = \frac{E_0}{3(1-2\nu_0)} \tag{3.31}$$

where, G_0 and K_0 denote the shear modulus and bulk modulus respectively.

The response of the loading part of the indentation test, $y_L(t)$, for a 3-parameter Maxwell model results in Equation 3.32.

$$y_L(t) = \frac{1}{\tau_L}\left(\frac{5-4\nu_0}{1-\nu_0^2} + \frac{M_0}{\eta_1}\frac{t^2}{2} - (\frac{1-2\nu_0}{1-\nu_0^2})^2\frac{3\eta_1}{M_0}(1-e^{-E_0 t/3\eta_1})\right) \tag{3.32}$$

where $M_0 = 4G_0\frac{3K_0+G_0}{3K_0+4G_0}$.

The response for the holding phase, $y_H(t)$, is presented by Equation 3.33.

$$y_H(t) = \frac{5-4\nu_0}{1-\nu_0^2} + \frac{M_0}{\nu_0}(t-\frac{\tau_L}{2}) - (\frac{1-2\nu_0}{1-\nu_0^2})^2\frac{3\eta_0}{M_0\tau_L}(e^{E_o\tau_L/e\eta_0}-1)e^{-E_0 t/3\eta_0} \tag{3.33}$$

The 4-parameter Kelvin-Voigt model has one more dashpot and the response of the loading phase reveals the Equation 3.34.

$$\begin{aligned} y_L(t) = \frac{1}{\tau_L}((4 + \frac{M_0}{G_1} + \frac{M_0(1-2\nu_0)^2}{E_0+3G_1})t - \frac{\eta_1 M_0}{G_1^2}(1-e^{-G_1 t/\eta_1}) \\ - \frac{3\eta_1 M_0(1-2\nu_0)^2}{(E_0+3G_1)^2}(1-e^{-(E_0+3G_1)t/3\eta_1})) \end{aligned} \tag{3.34}$$

The response for the holding phase, $y_H(t)$, is presented in Equation 3.35.

$$\begin{aligned} y_H(t) = (4 + \frac{M_0}{G_1} + \frac{M_0(1-2\nu_0)^2}{E_0+3G_1} + \frac{\eta_1 M_0}{G_1^2\tau_L}(1-e^{G_1\tau_L/\eta_1})e^{-G_1 t/\eta_1} \\ + \frac{3\eta_1 M_0(1-2\nu_0)^2}{(E_0+3G_1)^2\tau_L}(1-e^{(E_0+3G_1)\tau_L/3\eta_1})e^{-(E_0+3G_1)/3\eta_1}) \end{aligned} \tag{3.35}$$

The loading response, $y_L(t)$, for the 5-parameter combined Kelvin-Voigt-Maxwell model is derived as Equation 3.36.

$$y_L(t) = \frac{1}{\tau_L}(\frac{5-4\nu_0}{1-\nu_0^2}t + \frac{M_0}{G_1}(t - T_2(1-e^{-t/T_2})) + \frac{M_0 t^2}{2\eta_1} - \frac{(1-2\nu_0)^2}{(1-\nu_0^2)(1/T_1 - 1/T_3)}[(T_3/T_2 - 1)(1-e^{-t/T_3}) + (1-T_1/T_2)(1-e^{-t/T_1})]) \tag{3.36}$$

and the response of the holding phase is shown in Equation 3.37.

$$y_H(t) = (\frac{5-4\nu_0}{1-\nu_0^2} + \frac{M_0}{G_1} - \frac{M_0 T_2}{G_1 \tau_L}e^{-t/T_2}(e^{\tau_L/T_2} - 1) + \frac{M_0}{\eta_1}(t - \tau_L/2) - \frac{(1-2\nu_0)^2}{\tau_L(1-\nu_0^2)(1/T_1 - 1/T_3)} \times [(T_3/T_2 - 1)e^{t/T_3}(e^{\tau_L/T_3}) + (1-T_1/T_2)e^{-t/T_1}(e^{\tau_L/T_1} - 1)]) \tag{3.37}$$

where, $T_1 = \frac{6\eta_1\eta_2}{E_0(\eta_1+\eta_2)+3\eta_1 G_2+\sqrt{E_0^2(\eta_1+\eta_2)^2+6E_0\eta 2G_1(\eta_2-\eta_1)+9\eta_2^2 G_1^2}}$, $T_2 = \frac{\eta_1}{G_1}$ and $T_3 = \frac{6\eta_2\eta_1}{E_0(\eta_1+\eta_2)+3\eta_2 G_1-\sqrt{E_0^2(\eta_1+\eta_2)^2+6E_0\eta_2 G_1(\eta_2-\eta_1)+9\eta_2^2 G_1^2}}$.

3.5.2 Statistical Indentation

Each indentation data demonstrate the mechanical response of the local point on the material. Commonly, composite materials have several phases with different mechanical properties. One way to capture different phases in a composite material is to perform a large enough number of independent tests on the surface of the material. Statistical indentation consists of performing an array of single indentation test on a desired surface. The concept of the statistical indentation (grid indentation) was used by several researches like Ulm and coworkers [92–94] to address the heterogeneous nature of the microstructure by expanding the use of the classical indentation technique. The grid indentation technique consists of conducting a large grid of indentations over the surface of the heterogeneous medium of interest. Each indentation experiment could be regarded as statistically independent, which make it feasible to apply statistical techniques. In turn, statistical analysis makes it possible to interpret the indentation results in terms of the mechanical properties of the individual material phases. The concept of statistical indentation was developed based on the Gedanken experiment. Let's consider a material composed of two phases with different mechanical properties. The grid indentation

principle can be introduced by considering an indentation test on an infinite half-space composed of two different material phases with contrasting properties, as shown in Figure 3.7. Assume that the characteristic length of the phases are D and the indentation depth is much smaller than the characteristic size of the phases, $h << D$. In these conditions, a single indentation gives access to the material properties of either phase 1 or phase 2. In contrast, consider an indentation performed at a maximum indentation depth that is much larger than the characteristic size of the individual phases, $h >> D$. Such a test measures the response of the composite material, and the properties obtained from such an indentation experiment are representative of the average properties of the composite material. The grid indentation methods requires performing a large array of indentations as displayed in Figure 3.7. As a result of the scale separability condition, most indentations will capture the properties of either one of the primary phases. For example, in the two-phase material two peaks are present in the frequency diagram, and those mean values represent the mechanical properties of the phases.

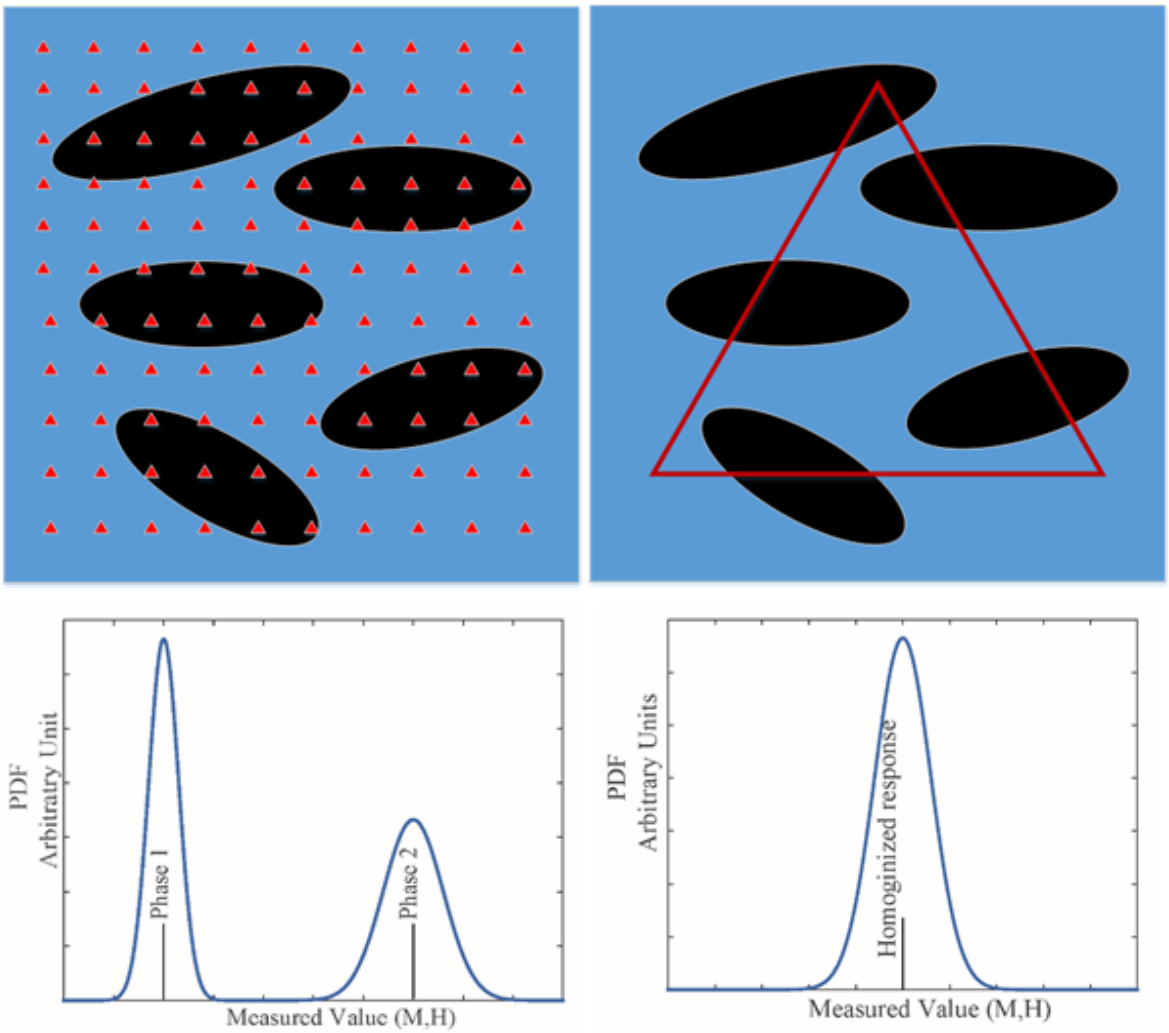

Figure 3.7: Schematic of statistical indentation analysis performed on a two-phase heterogeneous material, characterization of intrinsic phase properties from indentation of shallow depth, characterization of homogenized properties of two phase material. The left schematic demonstrates indents with small penetration depths. The right schematic demonstrates an indent with large penetration depth. M is the indentation modulus. H is the indentation hardness. Adopted from [95].

The experimental data obtained from the grid testing should be analyzed using statistical tools. Herein, I look into implementation of different techniques for this task.The implementation of the deconvolution technique for the indentation analysis begins with the generation of the experimental probability density function (PDF) or cumulative distribution function (CDF). An assumption should be made on the form and shape of the distributions associated with the properties of each material phase. It is assumed that in statistical modeling of the heterogeneous material, each phase has its own mechanical (indentation) value for that phase. A spread of experimental measurement is expected because of the noise and inhomogeneity nature of phases. The second assumption is that the distribution obeys a Gaussian distribution, which assumes the variability is distributed evenly around the mean value. The application of the grid indentation on the heterogeneous material will always result in some measurements probing the composite response of two or more material phase at some location. Each indentation test is considered as a single statistical event, with both extracted indentation modulus and hardness. The purpose of deconvolution is to determine the number of mechanical phases as well as their mean mechanical properties. Let N be the number of indentation tests performed, $(M_i, H_i)_{1\leq i\leq N}$ are the sorted values of the measured indentation modulus and harness. The N points of the experimental CDF for indentation modulus and hardness as shown in Equation 3.38.

$$F_M(M_i) = \frac{i}{N} - \frac{1}{2N}, F_H(H_i) = \frac{i}{N} - \frac{1}{2N} \tag{3.38}$$

After constructing the experimental CDFs, we need to construct the theoretical model CDF's. Consider the material to be composed of $j = 1-n$ material phases with sufficient difference in mechanical phase properties. Each phase occupies a surface fraction, f_i, of the indented surface. The distribution of the mechanical properties of each phase is assumed to be approximated by Gaussian distributions, described by the means of, average values, μ_j^M, μ_j^H and standard deviations of σ_j^M, σ_j^H . The CDF for each phase is given by Equation 3.39.

$$F(X_i; \mu_j^X, \sigma_J^X) = \frac{1}{\sigma_j^X} \int_{-\infty}^{X_j} exp(\frac{-(u-\mu_j^X)}{2(\sigma_j^X)^2})du \tag{3.39}$$

The $n \times 5$ unknowns $(f_i, \mu_j^M, \sigma_j^M, \mu_j^H, \sigma_j^H)_{1\leq j\leq n}$ are determined by minimizing the difference between the experimental and weighted sum of CDFs of different phases as shown in Equation 3.40. f_i is the volume fraction of phase i. μ_j^M demonstrate the mean value of

indentation modulus (M) for phase j. σ_j^M represents the standard deviation for indentation modulus (M) for phase j.

$$min\left[\sum_{i=1}^{N}(\sum_{j=1}^{n} f_j F(X_i;\mu_j^X,\sigma_j^X) - F_X(X_i))^2\right] \text{with} X = M, H \tag{3.40}$$

where the function F is defined as the probability density function of theoretical model. The constraint of the minimization problem requires that the surface fractions of the different phase sum to one. To ensure that individual phases exhibit sufficient contrast in properties, and avoid neighboring phases to overlap, the problem additionally constrained with $\mu_j^X + \sigma_j^X < \mu_{j+1}^X - \sigma_{j+1}^X$.

The approach of statistical deconvolution works based on minimizing the error between the experimental data, (M, H) and the theoretical model. The principle is to compute the total error and find a set of parameters to minimize this error while satisfying other constraints. For a given set of data, the error is due to the difference between the values of predicted modulus, M_{pred} and hardness, H_{pred}, and the experimental values of M_{exp},H_{exp}. The error minimization can be done in different definitions of error: absolute error, relative error and normalized absolute error [95].

3.5.3 Absolute Error

The absolute error, S, is defined by Equation 3.41 for each point [96].

$$S = (M_{exp} - M_{pred}(\mu,\sigma))^2 + (H_{exp} - H_{pred}(\mu,\sigma))^2 \tag{3.41}$$

where, M_{exp}, M_{pred} are experimental and predicted indentation modulus, respectively. H_{exp}, H_{pred} are experimental and predicted indentation hardness, respectively. The problem with this error is that it will give more dominance to points with high values compared to points with lower values. Since, in general the indentation modulus is much larger than the hardness (expressed in same units), the absolute error will lead to a good representation only for M and not of H.

3.5.4 Relative Error

The relative error, S_r, is defined by Equation 3.42 [96].

$$S_r = \left(\frac{M_{exp} - M_{pred}(\mu, \sigma)}{M_{exp}}\right)^2 + \left(\frac{H_{exp} - H_{pred}(\mu, \sigma)}{H_{exp}}\right)^2 \tag{3.42}$$

This error has the advantage of not favoring high values of M and H. However, it will give somewhat more importance to points with low values of M and H.

3.5.5 Normalized Absolute Error

The normalized absolute error, S_n, error uses the same normalization factor expect the denominator is M_0 and H_0 for the entire data set is defined by Equation 3.43 [96].

$$S_n = \left(\frac{M_{exp} - M_{pred}(\mu, \sigma)}{M_0}\right)^2 + \left(\frac{H_{exp} - H_{pred}(\mu, \sigma)}{H_0}\right)^2 \tag{3.43}$$

This definition of error helps to get the best minimization value, while fitting both experimental data best. One option to model the grid indentation is expectation-maximization algorithm [97–99]. This methodology is well-suited for the analysis of grid indentation data. In particular, normal mixture models are used to model multi-variate data based on efficient iterative solutions by maximum likelihood via the expectation–maximization algorithm. The mixture model for grid indentation data begins with considering each indentation event by a realization of the random two dimensional vector. The two dimensions correspond to the indentation modulus and hardness attributes. Mixture models are usually faced with the problem if multiple roots. The application of the maximum likelihood, expectation maximization for the analysis of grid indentation data on shale can be done with the use of EEMIX algorithm developed by Mclachlan et al. [100]. The EMMIX algorithm automatically fits a range of normal mixture distributions with unrestricted variance-covariance matrices. The optimal number of mixture components is determined using the Bayesian information criterion. Ortega [101] has used the EMMIX algorithm to analyze the indentation modulus and hardness obtained from grid indentation experiment on shale specimens. A second option for statistical analysis of grid indentation is cluster analysis. Cluster analysis is the automated identification of groups of related observations in a data set. The strength of this technique stems from its ability to determine the number of clusters in a data set and the uncertainty of experiments belonging to a cluster based on statistical criteria. The technique has been implemented in the R package

Mclust, a contributed package for normal mixture modeling and model-based clustering [102]. The package provides functions for model based approaches assuming different data models and implement maximum likelihood estimation and Bayesian criteria to identify the most likely model and the number of clusters. The initialization of the model is done by hierarchical clustering for various parametrization of the Gaussian model [102–104]. The best model can be identified by fitting model with different parametrization and number of components to the data by maximum likelihood determined by the EM algorithm, while implementing a statistical criterion for model selection. Deirieh [105] used the Mclust package in R software to process the data obtained from wave dispersive spectroscopy for chemical assessment of shale by means of statistical grid spectroscopy on shale specimen. The deconvolution can be programmed using a non-linear least square solver using the any programming software, i.e. MATLAB. In summary, the results of the deconvolution technique are estimates of the mean and standard deviation of indentation modulus and hardness for each mechanically distinct phase and en estimate of the volume fraction of each phase. The grid nanoindentation technique provides reliable estimates of the mechanical behavior of each phase in a complex heterogeneous composite based on direct mechanical measurements.

3.6 Conclusion

Indentation testing aims to provide mechanical properties of the indented surface, e.g. bulk mechanical properties. The review of current tools of indentation analysis in this chapter shows that the indentation quantities can be linked to material properties. The most important quantity of indentation measurements is the projected area of contact at the onset of unloading, which should be calibrated using a reference material. The time-dependent behavior of indentation modulus and hardness shows that the viscosity may have a non-negligible effect depending on the material. Several analytical tools where presented that allow the extraction of these viscous properties of a solid from an indentation test. In addition, the heterogeneous nature of most materials demand a higher number of tests to be carried out on the surface of the specimen. Statistical indentation aims to provide mechanical properties of the indented surface for a heterogeneous surface. The review of current tools of statistical indentation analysis in this chapter shows that the grid indentation technique can differentiate between various mechanical phases and provide reliable estimates of the volume fraction of each phase.

Chapter 4

Scratch Test Methods

4.1 Introduction

A scratch test consist of moving a sharp stylus on a surface of a material. During the tests, the vertical load is applied,F_V while the horizontal force, F_T, and penetration depth, h, of the indenter with respect to the scratched surface are contentiously measured. This resulting $F_T - h$ curve is utilized to condense experimental scratch tests into K_c parameter. The fracture driven processes occurring during the scratch is the underlying concept that allows capturing the fracture toughness of the specimen. The focus of this chapter is to review recent developments in scratch testing and analysis of tests. This enables connecting the scratch tests measurements to fracture properties. Furthermore, a review of the theory and its application to heterogeneous materials are presented. In this Chapter, a comprehensive review of principle, equipment, theory and application is explained.

4.2 Principles

The application of scratch test to determine the hardness of a material roots to ancient era. Carl Friedrich Christian Mohs, a German mineralogist formulated the Mohs scale of hardness in 1812. This method characterizes the relative hardness of minerals in a scale of 1 to 10. The materials of know hardness are used to scratch the material of unknown hardness. The principle lies on the fact that if specimen A can scratch specimen B, then specimen A is harder than specimen B. On the other hand, if specimen A does not scratch specimen B, then specimen B is harder than specimen A. If the two specimens

are equal in hardness then they will be relatively ineffective at scratching one another. This method provides a quick qualitative assessment of the hardness of the material and its resistance to scratch. It provides the foundation for the idea of using the scratch tests to characterize the mechanical properties of materials. Furthermore, several researchers utilized the idea and improved the technique over years.

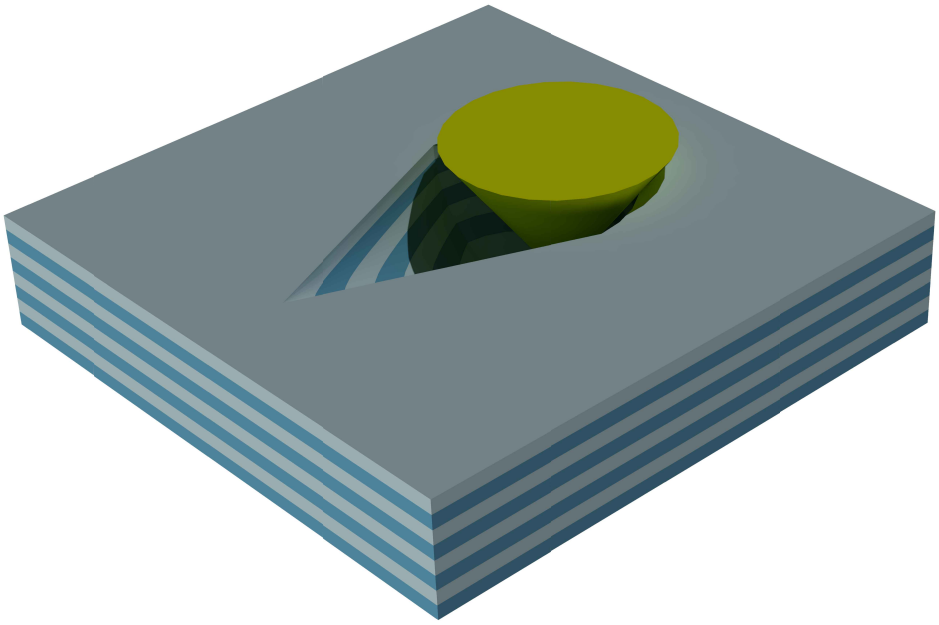

Figure 4.1: Schematic of scratch testing on a layered material. The stylus is shown as dark yellow probe used to scratch the surface of the layered material. The residual groove after the scratch test is shown.

The scratch test has been used in the industry for over 30 years for a wide range of applications ranging from adhesion of coatings and thin films to the strength of ceramics [106–109]. Recently, a new procedure is established to demonstrate the predominance of fracture processes and determine the shape of the cracks generated during the test [110]. In addition, in this study a dimensional analysis and finite element simulations is used to predict the scaling of the horizontal scratch force for both a strength dominated and a fractured-dominated process.

4.3 Equipment

The equipment used in this study is a version of continuous stiffness measurements (CSM) scratch testers, which is available for the ranges nano, micro and macro. These instruments provide precise surface characterization measurements. The scratch testing is employed for characterization of thin films and coatings. The mechanical properties such as adhesion, fracture and deformation can be measured using the CSM scratch testers. As mentioned in the previous section, the harder the material can scratch a softer material. Thus, the tip used for the scratch test is made of either diamond or a sharp metal. Diamond being harder than most of the materials tested in laboratory measurements is a reason for its wide application.

The scratch tester support a wide range of indenter base on the application. Some of these indenters are spherical indenter, Rockwell indenter and Vickers indenter. The spherical indenter is suitable for study of yielding, hardening and recreation of uniaxial tensile testing. In the case of spherical indenter, a transition from the elastic contact to plastic deformation is observed. One of the limitations of this indenter is the difficulty of obtaining a high quality spherical indenter using hard materials.

Another indenter is Vickers, which is a four-sided pyramid shape with a 68° angle between the center and the face of the pyramid. Its geometry define a very sharp pointed indenter which is suitable for indentation testing. The third indenter is Rockwell conical indenter. The Rockwell indenter consists of an apex angle, usually 120° and with a radius R at the tip. The radius can range base on the application, where commercially is available for 100 μm and 200 μm. The selection of the tip is based on the material parameters due to influence of the tip geometry on characterization. Akono et al. [111] showed that an axisymmetric probe is suitable for the fracture toughness characterization. Thus, in this study a spheroconical Rockwell C indenter tip with the $R = 200\mu$m.

The scratch test is carried out by moving a diamond indenter tip across the surface of the application of constant, progressive or incremental load modes. The CSM scratch tester (Anton Paar, Ashland, VA). This scratch tester offer a wide variety of features. On the key features is the constant surface referencing. This feature enables accurate coordination between the force and depth sensors. In addition, the electronically controlled active force feedback system is a unique feature to this instrument. The vertical force is an important factor in scratch tests, which is perfectly controlled due to the design of the force sensor and the active force feedback feature.

The sample for scratch testing is mounted on a friction table. A linear variable differential transformer (LVDT) is attached to the table which measure the horizontal force. This scratch tester offer a pre-scan mode which enables the displacement sensor to record the surface profile of sample before conducting the test. In addition, profiles can be measured after the testing as well. The surface profile is used to capture tilt and asperities on surface with a minimal force. The penetration depth, P_d is measured during the scratch depth. While, the residual depth, R_d, can be measured after the scratch test. Furthermore, optical microscope is synchronized with the scratch testing platform. This feature enables the capture of optical microscopy images of the test site. The optical microscopy is available at four levels of objectives $\times 5, \times 20, \times 50$ and $\times 100$. These correspond to magnifications from 200X to 4,000 X. The objectives are high quality Olympus objectives which is connected to the software through video camera software. This scratch testing modulus has a patented synchronized panorama mode. This feature enables the user to capture the entire scratch groove and correlate it to the data after the scratch test is performed. This further allows to correlate the data to the micro-mechanical features on the test specimen, a very indispensable tool in the case of material with heterogeneity. The panorama is a result of stitching of several microscopic images taken in sequence.

A more detailed description of methodology involved in the measurements is explained as follow. The specimen is placed on the friction table and then positioned under the optical microscope. The specimen of the specimen should be explored under the microscope under the optical microscope to position the right spot in case a series of tests are needed. Later, the scratch test/s can be launched, which moves the sample from under the microscope to that of the scratch tester. The table then raise on to the Rockwell tip, runs a pre-scan surface profile if selected where the load is kept at a minimum. Then, the scratch test will start promptly after returning to the beginning.

The load cell monitors the applied load using the force sensor and active feedback system. Penetration depth, P_d, is measured using LVDT sensor. Furthermore, acoustic sensor attached to the scratch head, which measures the acoustic emissions corresponding to the failure events occurring in the specimen. The testing should be in controlled environments with temperatures in the range of 23 ± 5 °C and a relative humidity less than 50 % as per ISO standards.

A review of technical specification of the instrument reveals the capabilities and limitations of the instrument. The instrument has a very fine resolutions for the parameters discussed so far in the above sections. Different parameters and their ranges are shown

below in Table 4.1 and Table 4.2.

Table 4.1: Scratch testing platform capabilities for fine range.

Maximum depth	100 μm
Depth resolution	0.3 nm
Maximum load	10 N
Load resolution	0.1 mN
Maximum friction load	10 N
Resolution friction load	0.1 mN
Central frequency	150 KHz
Dynamic range	65 dBae
Maximum amplification	200,000 X
Standard displacement rate	0.4 mm/min

Table 4.2 demonstrates the capability of the scratch instrument for large range.

Table 4.2: Scratch testing platform capabilities for large range.

Maximum depth	1000 μm μm
Depth resolution	3 nm
Maximum load	30 N
Load resolution	1 mN
Maximum friction load	30 N
Resolution friction load	1 mN
Central frequency	150 KHz
Dynamic range	65 dBae
Maximum amplification	200,000 X
Standard displacement rate	600 mm/min

Another feature of the instrument is the capability of prescribing the speed and rate of the vertical load applied to the specimen.

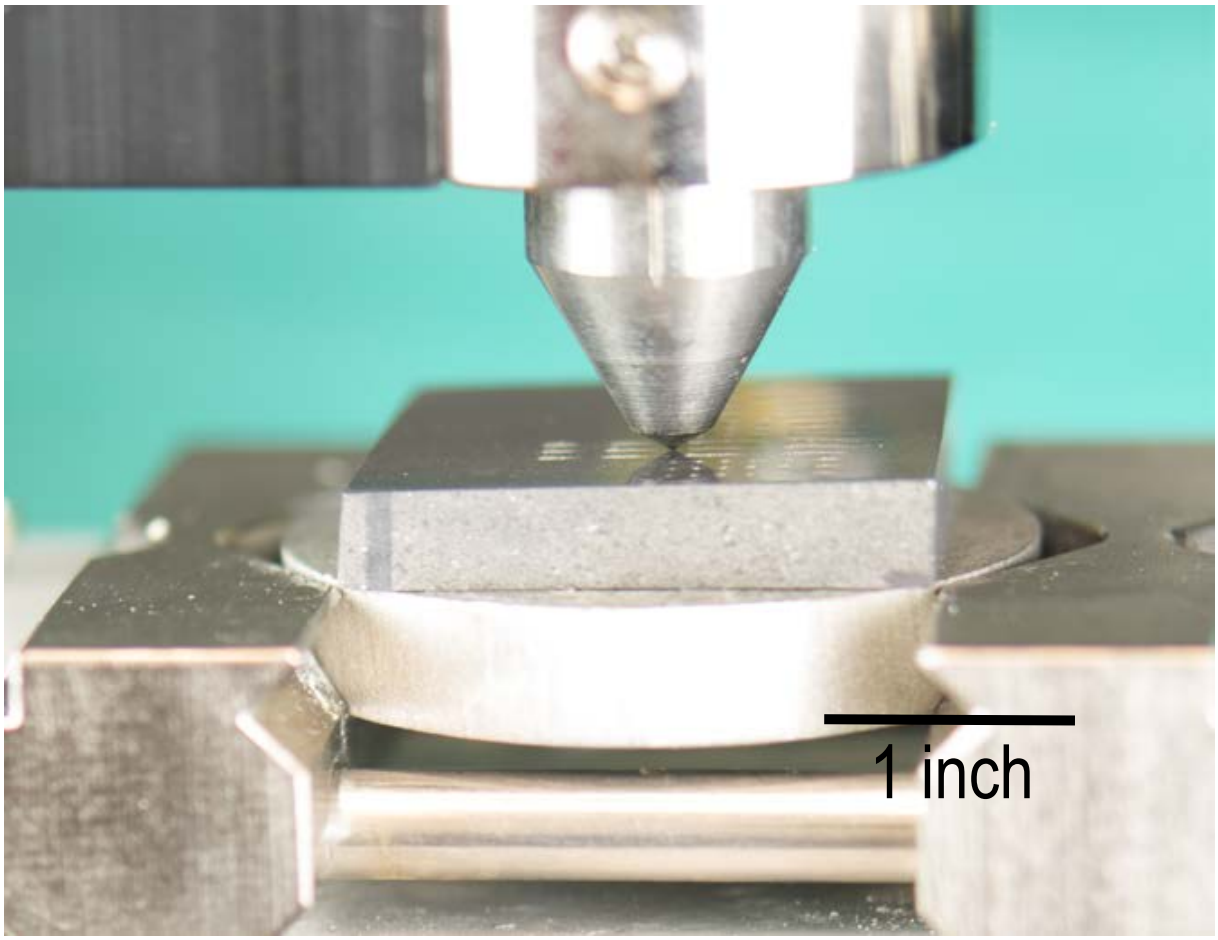

Figure 4.2: Photograph of a scratch sphero-conical tip sitting on a specimen. Credits: Akono, Kabir, University of Illinois at Urbana-Champaign, 2016.

4.4 Theoretical Model

As discussed in previous section, it was by shown that during scratch tests with a Rockwell C probe, fracture processes become predominant as the penetration depth increases [111]. Here, we review some of the theoretical development for analyzing the scratch test results.

The first model was developed using a linear fracture mechanics to relate the force to the material fracture toughness and to the geometry of the test. A comprehensive summary of the model developed by Akono et al. [110–112] is presented here.

Given a material domain Ω of boundary $\partial\Omega$, the energy balance of the system,$d\mathtt{U}$, is written by the first law of thermodynamics in Equation 4.1.

$$d\mathtt{U} = \delta\mathtt{W}_{ext} + \delta\mathtt{Q} \tag{4.1}$$

where $\mathtt{W}_{ext}$ is the sum of the energy supplied in form of work and $\mathtt{Q}$ is the sum of energy supplied in the form of heat. Furthermore, the second law of thermodynamics results in Equation 4.2.

$$\int_{\Omega} \varphi dt d\Omega = \theta_0 d\mathtt{S} \tag{4.2}$$

where φdt is the dissipation volume density and θ_0 is the reference temperature expressed in the absolute scale. To form the solution, consider a crack surface Γ in a linear elastic body. Let $\varepsilon_{pot}(\Gamma)$ be the potential energy associated with the fracture surface under prescribed loading conditions. The prescribed surface forces $\mathtt{T}^d$ and displacements, $\underline{\xi}^d$ are increased until the onset of crack propagation and then held constant. The intrinsic dissipation is expressed by Equation 4.3.

$$d\mathtt{D} = -d\varepsilon_{pot}(\Gamma + d\Gamma) = \mathtt{G}d\Gamma \tag{4.3}$$

where $\mathtt{G}$ is the amount of potential energy stored in the system which is released when the crack propagates by $\mathrm{d}\Gamma$. ε_{pot} is the potential energy of the system as the difference between the free energy and the external work due to prescribed body and surface forces.The onset of crack propagation is defined by a threshold law in Equation 4.4.

$$f := \mathtt{G} - \mathtt{G}_f < 0; \qquad (\mathtt{G} - \mathtt{G}_f)d\Gamma = 0 \tag{4.4}$$

Equation 4.3 is the standard format of evolution laws set up within the framework of the thermodynamics of irreversible processes. The crack propagates when the energy release rate $\mathtt{G}$ reaches a threshold $\mathtt{G}_f$, which is the fracture energy. Irwin relationship reads as Equation 4.5.

$$K_c = \sqrt{E'\mathtt{G}_f} \tag{4.5}$$

where K_c is a material property called fracture toughness.

Furthermore, the model is developed using a J-integral [113] to evaluate energy release rate, $\mathtt{G}$, using a contour integral surrounding the crack tip. Figure 4.3 illustrates a schematic of scratch tip in a solid material with the contour surrounding the crack tip.

Applying the boundary problem into the energy release equation, the energy release rate is derived by Equation 4.6.

$$\mathtt{G} = \int_C [\psi n_1 - \mathtt{T}.\frac{\partial \underline{\xi}}{\partial x_2}]ds \tag{4.6}$$

where $\mathtt{T}$ is the traction vector on the boundary. ψ is the free energy in the C domain.

A more detailed version of these derivations can be found in [110]. The development of the model into a axisymmetric probe (cf Figure 4.4c) is carried out by defining a monomial function of the form in Equation 4.7.

$$z = Br^{\epsilon} \tag{4.7}$$

where B is the height at unit radius and ϵ is the degree of the homogeneous function. r is the radius of the probe at agiven height z. The projected contact area A and perimeter p are given by Equations 4.8 and 4.9.

$$A(d) = \frac{2B\epsilon}{\epsilon + 1}\left(\frac{d}{B}\right)^{\frac{1}{\epsilon}+1} \tag{4.8}$$

$$p(d) = (\frac{d}{B})^{\frac{1}{\epsilon}}\beta(d) \tag{4.9}$$

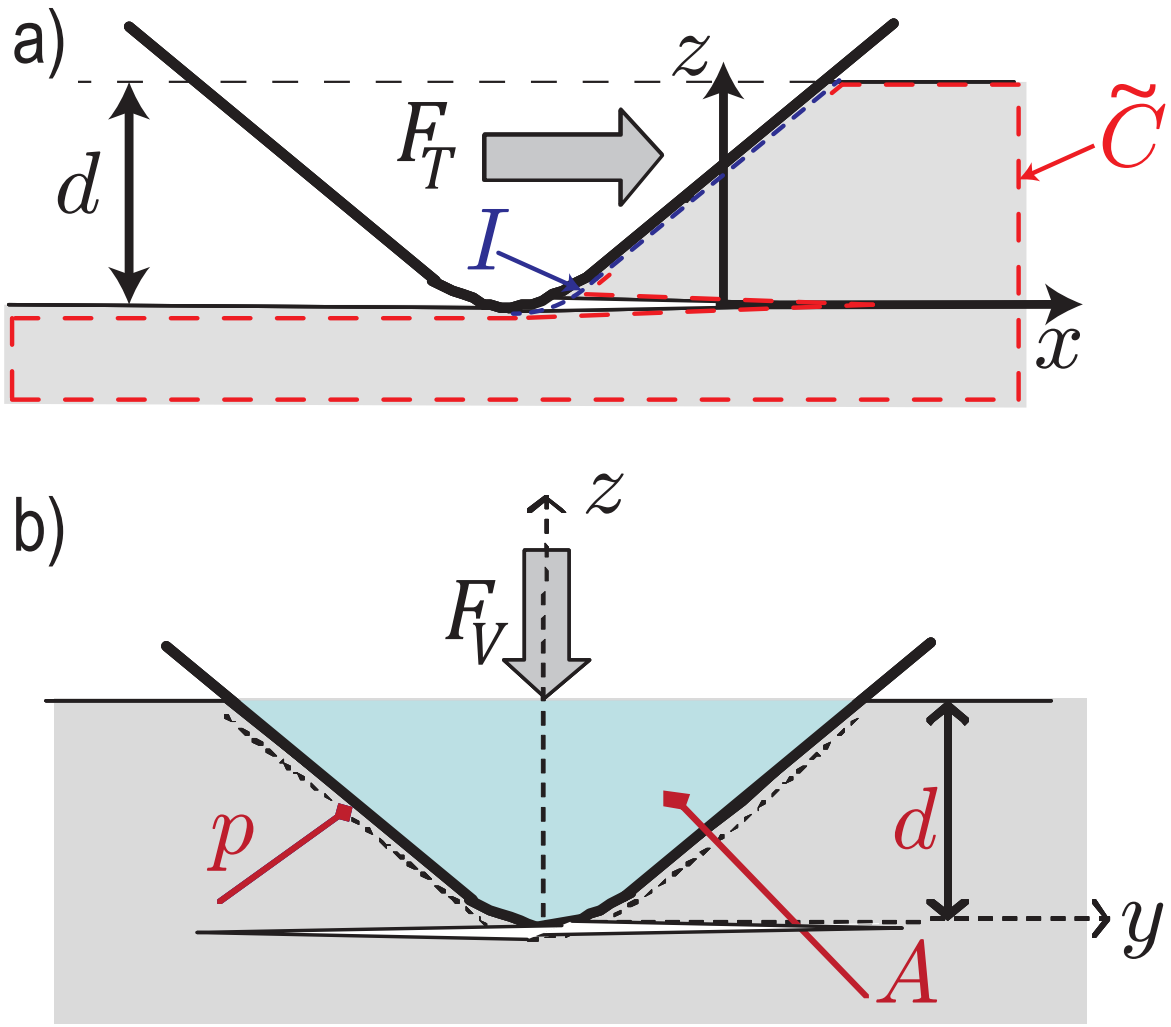

Figure 4.3: Schematic representation of a scratch testing on an elastic material. a) Side view. b) Front view. F_T is the horizontal scratch force, d is the penetration depth and ℓ is the scratch length. $\tilde{C}$ is a closed contour including the crack tip. Adapted from [114, 115].

where β is a dimensionless parameter defined by Equation 4.10.

$$\beta(d) = 2\int_0^1 [1 + (\epsilon d)^2 \left(\frac{d}{B}\right)^{\frac{-2}{\epsilon}} x^{2\epsilon-2}]^{\frac{1}{2}} dx \tag{4.10}$$

The scaling of the horizontal force F_T and the variation of function f and d then is derived by Equation 4.11 and 4.12. d is the penetration depth.

$$F_T \propto 2K_c(\frac{d}{B})^{\frac{1}{\epsilon}+\frac{1}{2}}(\frac{\epsilon}{\epsilon+1}\beta(d)B)^{\frac{1}{2}} \tag{4.11}$$

$$f(d) = \frac{4B\epsilon}{\epsilon+1}\left(\frac{d}{B}\right)^{\frac{2}{\epsilon}+1}\beta(d) \tag{4.12}$$

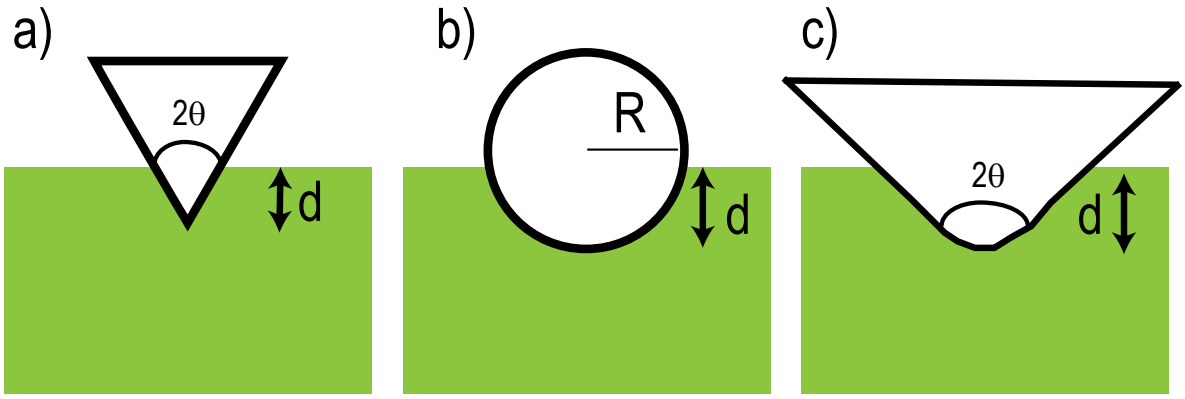

Figure 4.4: Common scratch probe geometries. a) Cone, b) Sphere, c) Spheroconical. Adopted from [110].

In particular Equations 4.11 and 4.12 will reduce to Equations 4.13 and 4.14 for a conical probe of half-apex angle θ (cf Figure 4.4a).

$$F_T \propto 2\frac{[sin\theta]^{\frac{1}{2}}}{cos\theta}K_c d^{\frac{3}{2}} \tag{4.13}$$

$$f(d) = 4\frac{sin\theta}{(cos\theta)^2}d^3 \tag{4.14}$$

While for a spherical probe of radius R (cf Figure 4.4b), Equations 4.11 and 4.12 will reduce to Equations 4.15 and 4.16.

$$F_T \propto 4[\frac{1}{3}\beta(\frac{d}{R})]^{\frac{1}{2}}K_c d R^{\frac{1}{2}} \tag{4.15}$$

$$f(d) = \frac{16}{3}\beta(\frac{d}{R})d^2R \tag{4.16}$$

These derivations will be used in different chapters for the models used for scratch testing. This summary builds a foundation for understanding and implementing fracture toughness characterization in this study. In the next section, a brief application of scratch testing to different material are presented.

4.5 Application to Heterogeneous Materials

The scratch testing has been used for several decades in the industry and academia. A wide range of applications ranging from adhesion of coatings and thin films to the strength of ceramics [106–109]. Although, new studies are focusing on the application of scratch testing on characterizing the fracture toughness of heterogeneous materials. In 2011, the scratching as a fracture process, from butter to steel was published. In this work, a fracture toughness model is developed for a rectangle blade with a back-rake angle. The materials tested in this studied are cement paste and Jurassic limestone [112]. Later in another study, with the help of linear fracture mechanics and use of airy stress functions the fracture toughness is revisited. In addition, a finite element simulation demonstrates the blade-material interface does not exhibit plastic deformation. Another set of scratch tests on cement pastes are carried out with different blades where the back-rake angle in all tests are 15°. The study showed that determination of fracture toughness from scratch tests from different scratch widths and depths are feasible [111].

Furthermore, in another study for experimental determination of the fracture tough-

ness via microscratch tests using linear elastic fracture mechanics is utilized to find the fracture toughness. In this study ceramics, polymers and metals are tested to cover a wide range of materials for this method. The results of this study demonstrates the applicability of the method to determine the fracture toughness using the $F_T/\sqrt{2pA} = K_C$ for a wide range of materials [114]. F_T is the lateral force measured during the scratch testing. p is the scratch perimeter. A is horizontally projected load-bearing area. The method is improved with inclusion of different intensity factor with simulations and several experiments. In addition, a rigorous calibration for the indenter shape is presented in this study [116]. Recently, the model is developed to consider the Bazant size effect law into the scratch testing of different material [117].

This section reviews most of the updates and development of the scratch test experiments and development of the theory. This review is essential to demonstrate the applicability of the method for heterogeneous material and wide variety of material that has been tested with this method. In recent years, the method has been applied to several heterogeneous materials. The microstructure-toughness relationships in calcium aluminate cement-polymer composites using instrumented scratch testing [118]. Fracture properties of the alkali silicate gel is tested using microscopic scratch testing [119]. The microscopic fracture characterization of gas shale is characterized via scratch testing [120].

4.6 Conclusion

Scratch testing aims to provide mechanical properties of the scratched surface, e.g. fracture toughness. The review of current tools of scratch testing and analysis in this chapter shows that scratch testing can be used to capture fracture toughness. The most important quantity of scratch testing is the projected area of the contact at the onset of testing. This value is calibrated using a homogeneous material with a known fracture toughness. In addition, heterogeneous materials require a large number of tests to be carried out. Thus, an array of scratch paths are performed to capture the heterogeneity of the material and specimens. In this Chapter, a comprehensive review of scratch testing is presented. This review of current tools of scratch testing and analysis demonstrates that the scratch measurements can be linked to fracture properties of material.

Part III

Effect of Microstructure, Fabric and Structural Anisotropy on Mechanical Response of Organic Rich Shale

Chapter 5

Multi-Scale Structure of Organic Rich Shale

5.1 Introduction

Sedimentary rocks are formed by the deposition and subsequent cementation of material at the Earth's surface and within bodies of water. Thus, sedimentary rocks are formed by the accumulation of sediments. Shale is a class of sedimentary rock composed of sedimented clay particles and quantities of larger particles. The shale can have any or all of the primary clay minerals: kaolinite, illite and smectite. This chapter discusses the review of shale as a sedimentary rock, its compositional characteristics and microstructural features. This information sets the stage for introducing multi-scale modeling investigation. Shale is a complex porous material with heterogeneities that manifest themselves at different scales. The adequate understanding of composition, microstructure and mechanical properties at different scales of observation is vital to understanding reservoir behavior. Furthermore, this chapter introduces several mutliscale models developed by several researchers. In addition, this chapter introduces common features and differences of these presented models.

5.2 Petrology of Organic-Rich Shale

Sedimentary rocks are formed from pre-existing rocks or pieces of live organisms. Commonly, they form from deposits that accumulate on the Earth's surface. These rocks

often have distinctive layering or bedding. Common sedimentary rocks are sandstone, limestone and shale. Clastic sedimentary rocks are the group of rocks made up of pieces of pre-existing rocks. Pieces of rock are loosened by weathering, then transported to some basin or depression where sediment is trapped. If the sediment is buried deeply, it becomes compacted and cemented, forming sedimentary rock. Sedimentary rocks may contain minerals and fossil fuels, enhancing their importance to economic reasons. The origins of sedimentary rock are related to natural deposition of sediments by water, wind and ice over long period of time. Their formation involves physical, chemical and biological geological processes. The first step is weathering of source rock by physical or chemical processes. This process lead to concentration of resistant particulates, in addition to creation of secondary products and the release of soluble elements. The second part is the removal process of these particulate and soluble constituents. The constituents are removed from land by erosion and subsequently transported by water, wind or ice to depositional basins. These transported sediments eventually reach a basin and are deposited. At last, the sediments are buried at the depositional basin by the younger ones and diagenesis occurs at increasing temperatures and pressures. At this stage, dissolution of some constituents and the generation of new minerals occur. Furthermore, the consolidation and lithification of these products result in the creation of a sedimentary rock. The particular sequence of sedimentary processes generate different type of constituents. Siliciclastic particles, chemical/biological elements and carbonaceous constituents. The relative proportions determine the fundamental types of sedimentary rocks. The dominant forms of sedimentary rocks encountered in terms of popularity are shale, sandstone and limestone.

Fine-grained siliciclastic rocks composed mainly by particles smaller than hundreds of micrometers are know as siltstones, mudrocks, mudstones and shales. The terms shale has been used for different terminology in the literature. First, a restrictive definition of laminated clayey rocks. Second, as a general group name for all fine-grained rock [121]. In recent literature, the term shale, mudstone and mudrock continue to be used for gine-grained siliciclastoc rocks [122]. In this work, the shale materials are investigated from a geomechanics perspective. Also, the shale investigated here have organic content that make them desirable for oil and gas applications. These material usually exhibit high amounts of clay content and smalls scale layering associated with the bedding direction. The rest of this part focus on some of the physical characteristics of shale materials including grains sizes, particle shape and orientations, mineralogy, porosity and permeability.

These physical characteristics are vital to the understanding of the relations between material composition, microstructure and the mechanical behavior of the rock.

5.2.1 Grain Size

Shale is mainly composed of small sized grains, which prevent the application of established methods to characterize the material. The grain size for rocks can vary depending on the source and diagenesis process. For some mudrocks and shales, an approximated average grain size distribution consist of 45% silt, 40% clay and 15% sand.

5.2.2 Particle Shape

The sediments usually undergo long processes until becoming rock masses, however the shape of fine silts and clay-size particles are only slightly modified by erosion and transport. In contrast to sand size particles, clays and fine silts tend to keep the original shape of the detrital sources or those of the mineral sources generated during diagenesis. Scanning electron microscopy studies reveal that most clay minerals exhibit flaky structures. Occasionally, the high abundance of clay minerals in shale cause micro-fabrics with preferred orientations and bedding planes.

The fabric of shale is intrinsically related to the orientations of clay particles, which are the result of complex processes during rock formation. Different different stages of suspension settling particles associate in different processes such as flocculation and aggregation. Several factors control the dynamics of clay particle settling in suspensions such as pH levels, presence of electrolytes, mineralogy content and particle size [123]. The fresh sedimentation stage is when the clays are not subjected to significant compaction, forming submicroscopic regions in which particles are structured in parallel array or domains [124]. These groups of clay crystals are oriented randomly in the overall clay matrix. The consolidation stage bring the clay domains close together thus the clay domains are tightly packed due to compaction. In some shale, clay sediments develop fissility, ability to split into thin slab along narrowly spaced planes parallel to the directions of natural bedding. Multiple factors affect the development of fissility in shale. The presence of dispersing agents in water such as organic substances dictates whether clay precipitates as dispersed particles or as flocculated structures. Two major microstructural changes

occurring during deposition is sedimentation and lithification of clay sediments.

5.2.3 Mineralogical Composition

Generally, shale is composed of clay minerals, fine-grained mica, quartz and feldspars. The particular mineralogy composition of each shale is dependent on several factors such as tectonic setting, depositional environments, formation age and diagenetic processes. Notably, diagenesis provokes important changes in the mineralogy make-up of shale. Smectite is transformed into illite or chlorite at burial temperature (70 °C–150 °C). In addition, Kaolinite is transformed into illite at similar temperatures. Thus, percentages of illite and chlorite tend to increase with deeper burial depths and longer time periods of burial. The clays are made up of basic units that involve silicon and oxygen. Common layers silicates are composed by the combination of two basic structural units: the silicon tetrahedron and the aluminum or magnesium octahedron. The clay minerals are made from these basic units based on arrangement of sheets of these units and the link between the successive layers. The basic structures of clay mineral groups are shown schematically in 5.1.

The common clay minerals in shale are: kaolinite, smectite and illite [126]. Kaolinite is a 1:1 clay mineral as it is composed of altering silica and octahedral sheets. The successive lauers are bonded by Van der Waals force and hydrogen bonds. This strong bond between layers inhibit any inter-layer swelling die to the presence of water. Kaolinite can occur as either well or poorly crystallized particles with lateral and thickness dimensions ranging between 0.1–4 μm and 0.05–2μm, respectively.

Smectite is a 2:1 clay mineral type. This clay consists of an octahedral sheet situated between two silica sheets. The bonding between layers provided by Van der Waals forces and cations balancing charge deficiencies are relatively week. Due to this relatively week bonding layers separation by cleavage or water adsorption is common. In smectite rich shale, a large amount of water is electrostatically bound to clay particle surfaces [126, 127]. Montmorillonite occurs as film-like, equi-dimensional structures with particle thickness in the nanometer range, but the characteristic long dimension can reach 1-2 μm.

Illite is a 2:1 mineral type, which atomic structure is similar to that of mica. Mica follows the three-layer silica-gibbsite-silica unit structure while some silicon positions are filled by aluminum creating a charge deficiency that is balance by potassium between lay-

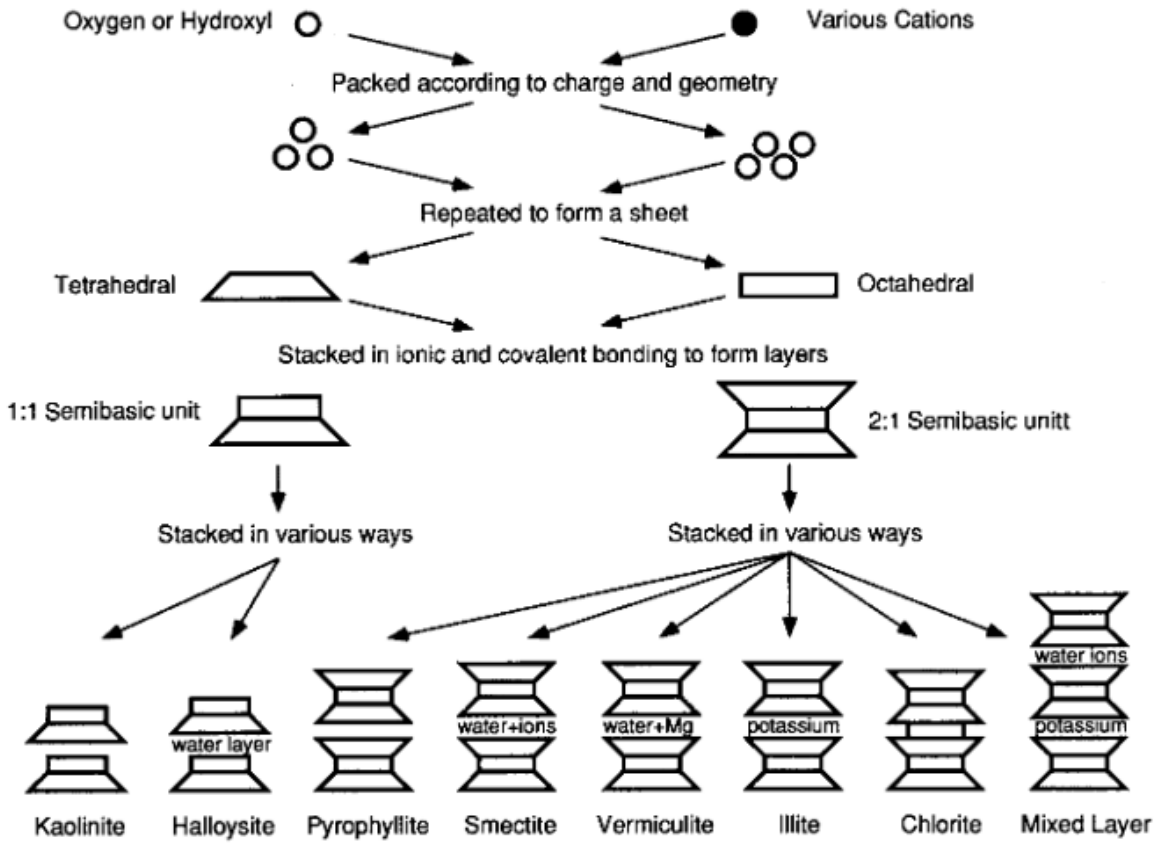

Figure 5.1: Pattern of clay minerals from Tetrahedral and Octahedral sheets. Adopted from [125].

ers. On the other hand, illite has contains less amount of potassium exhibiting randomness in the stacking of layers and its smaller particle size. Illite occurs as flaky particles with characteristic long dimension in the sub-micrometer and micrometer ranges, while the thickness is of nanometer dimensions [125, 128].

Among the non-clay minerals present in shale, quartz is the most abundant. Shale consist of quartz typically in silt-grade but the coarser grains do occur. During burial and diagenesis, chemical/biological processes lead to the dissolution of some part of the organic matter and to the transformation of the rest into an insoluble substance called kerogen. Kerogen is the solid, high molecular weight component of sedimentary organic matter. Kerogen is typically identified by optical or chemical methods. In petroleum chemistry, different types of kerogen are defined depending on the composition of the organic matter, most of which generate oil and gas upon burial and diagenesis [129].

Geochemists define kerogen as the fraction of sedimentary organic constituent that is insoluble in the usual organic solvents. Kerogens are composed of a variety of organic material including algae, pollen, wood, vitrinite and structureless material. The type of kerogens present in a rock largely control the type of hydrocarbons generated in the rock. The hydrogen content of kerogen is the controlling factor for oil vs gas yields form the primary hydrocarbon generating reactions. The type of kerogen present determines source rock quality. Generally, four basic types of kerogen are found in sedimentary rocks. Figure 5.2 shows the graph that defines these four basic kerogen types. This diagram cross-plots the hydrogen-carbon as a function of the oxygen-carbon atomic rations of carbon compounds. Table 5.1 summarizes different kerogen type definition and the amount of hydrogen and the typical depositional environment.

Table 5.1: Different Kerogen Type definition

Kerogen Type	Predominant hydrocarbon potential	Amount of hydrogen	Typical depositional environment
I	Oil prone	Abundant	Lacustrine
II	Oil and gas prone	Moderate	Marine
III	Gas prone	Small	Terrestrial
IV	Neither (primarily composed of vitrinite) or inter material	None	NA

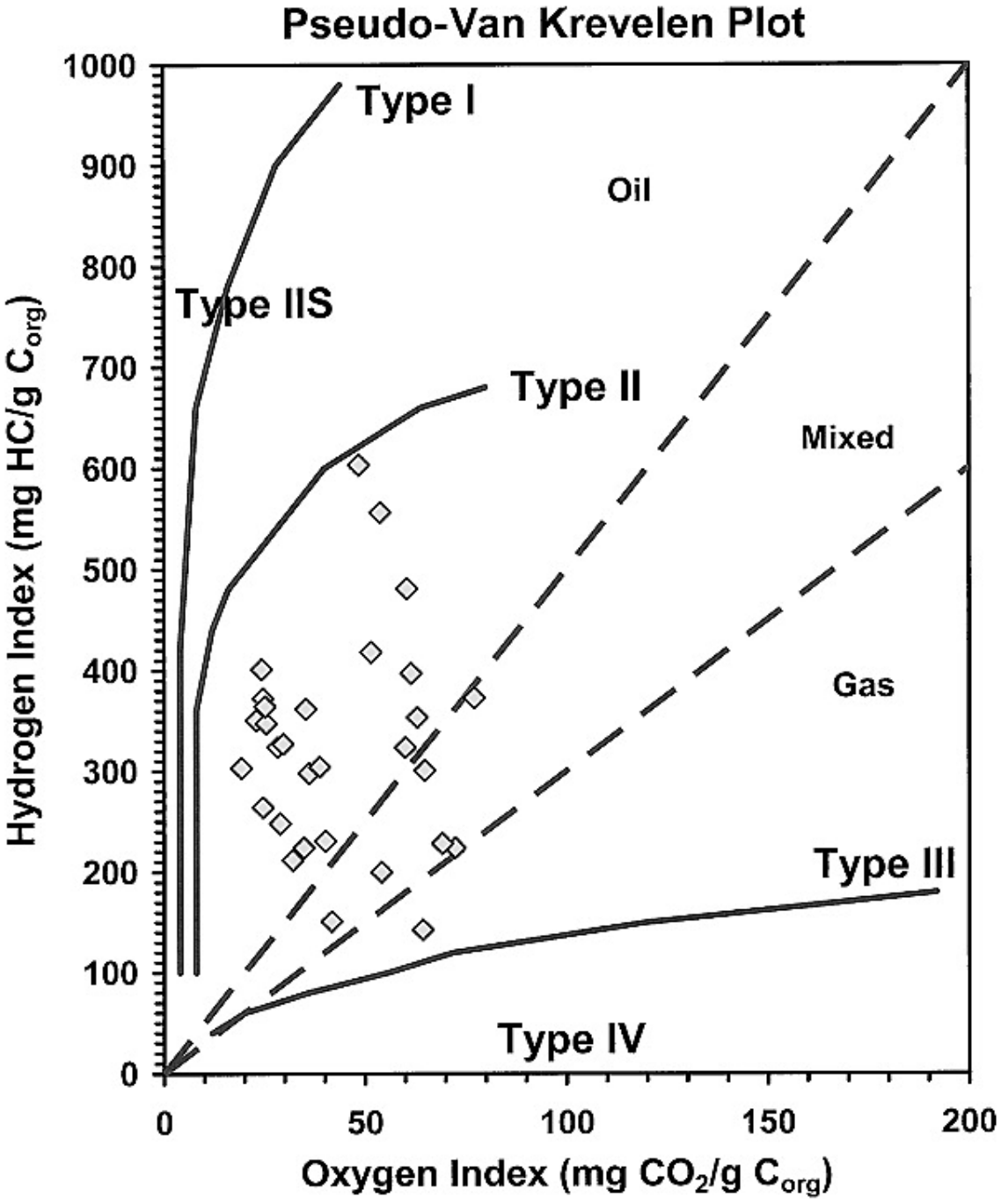

Figure 5.2: Typical reservoir source rock hydrogen and oxygen index data set plotted on a pseudo-Van Krevelen diagram. Points present the oxygen index and hydrogen index for shale materials extracted from several reservoirs. Adopted from [130].

5.2.4 Porosity

Generally, porosity describes the part of the material that is not occupied by mineral grains. This important material property is defined as the ration of the volume of pore space in the material over the total volume. Porosity is typically measured by fluid intrusion and density in difference methods. In addition to this total or physical porosity, hydrologists are concerned about the movement and transport of fluids. The transport porosity is defined as the volume of interconnected pore space divided by the total volume of rock. This effective porosity is commonly less than the total porosity, although their differences may be relatively small for coarse grained rocks.

The occurrence of porosity in shale particularly at small length scale sets the mechanical and transport behaviors of this sedimentary rock apart from those observed in rocks such as sandstone. The sequence of burial and diagenetic processes cause the formation of the majority of pore space at nanometer scales. The porosity present between conglomerates of clay is known to be very low, with maximum pore radii at 4.2 nm [131]. Combination of different technique like mercury intrusion porosimetry and small angle neutron scattering, the characteristic pore size in shale is of some nanometers [132–134]. This nano-sized pore in shale cause some amount of water or other pore fluids to be structured by their association with mineral surfaces. The potential transport or chemical reactions between solutes and water may be inhibited through some small pore throats, causing osmotic properties in some shales [135].

5.2.5 Permeability

Permeability is the ability of the medium to transmit a fluid from one point to another. Permeability is a complex function of particle size, shape, orientation and sorting. Shale permeability vary up to ten orders of magnitude and by three orders of magnitude at a single porosity, which can be explained by differences in grain sizes. The studies of pore size distributions shows that silt-rich mudstones are more permeable than finer mudstones. Increasing effective stress may cause collapse of larger pore spaces and thus losses porosity and permeability. The permeability in shale can be as low as 1nD (10^{-21} m^2) [136]. The permeability for some common geological material are For comparison an average porosity values are 10^{-4}–10^{0}, 10^{-6}–10^{-11}, 10^{-5}–10^{-8} darcy (1 darcy= $0.97\times10^{-12}m^2$) for sandstones, shale and granite, respectively. This low permeability of shale make it a

suitable geological seal due to its extremely low permeability. A clear understanding of different terminology in this chapter and next chapters is essential so Table 5.2 define the terminology.

Table 5.2: Different terminology of clay structure and mineralogy in this study.

Crystalline	A material with sufficient atomic ordering such that a X-ray diffraction pattern containing well defined maxima can be indexed using Miller indicies.
Plane	A plane is a plane of one or more types of atoms; e.g. a plane of Si and Al atoms.
Sheet	A tetrahedral sheet or octahedral sheet is composed of contentious two dimensional corner-sharing tetrahedra involving three corners and fourth corner pointing in any direction or edge-sharing octahedra, respectively.
Layer	A layer contains one or more tetrahedral and an octahedral sheet. There are two types of layers, depending on the ratios of the component sheets: a 1:1 layer has on tetrahedral sheet and one octahedral sheet, whereas a 2:1 layer has an octahedral sheet between two opposing tetrahedral sheets.
Inter-layer material	Inter-layer material separates the layers and generally consist of cations, hydrated cations, organic material, hydroxide octahedra and hydroxide octahedral sheets.
Unit structure	A unit structure is the total assembly and includes the layer and interlayer material.
Clay mineral	The term clay mineral is defined as any crystallite size to be consistent with mineral definition.

Quartz is one of the other common minerals in shales. It is a comparatively easy mineral to identify by petrographic examination in thin sections, although it can be confused by feldspar. Due to its superior hardness and chemical stability, quartz can survive multiple recycling. The quartz grains may display some degree of rounding acquired by abrasion during one or more episodes of transport, particularly by wind. Quartz can occur as single grains or as composite grains. Feldspar minerals is the third most abundant mineral in shales. Several varieties of feldspars are recognized on the basis of difference in chemical composition and optical properties. They are commonly divided into two broad groups: alkali feldspars and plagioclase feldspar.

Alkali feldspars consistue a group of minerals in which chemical composition can range through a complete solid solution series from $KAlSi_3O_8$ through (K, NA)$AlSi_3O_8$ to $NaAlSi_3O_8$. Due to common occurrence of potassium-rich feldspars this group usually

named as K-feldspar. Common members of this group include orthoclase, microcline and sanidine. Plagioclase feldspars form a complex solid solution series ranging in composition from $NaAlSi_3O_8$ (albite) through $CaAl_2Si_2O_8$ (anorthite). A general formula for the series is (Na, Ca) (Al, Si)Si_2O_8. Plagioclase feldspars can be distinguished from potassium feldspars on the basis of optical properties such as twinning by examination with a petrographic microscope. Potassium feldspars are generally considered to be somewhat more abundant overall in sedimentary rocks than plagioclase feldspars; however, plagioclase is more abundant in sandstones derived from volcanic rocks.

These definitions are most relevant to the modeling of clay rich rocks, in which the mechanical behavior of the clay-particle influence the macroscopic response. Precision in handling these terminologies will enrich the modeling descriptions of the clay fabric in clay rich rocks.

5.3 Multi-Scale Thought Models

In recent years, several researchers developed multi-scale thought models for gas shale. This section reviews some of the most prominent models in the literature.

Bennet et al. [137] provided a framework for characterization of Woodford shale in both the bedding plane normal and bedding plane parallel direction. In their study, they utilized focused ion beam milling, scanning electron microscopy and energy dispersive spectroscopy to characterize the shale at the scale of the clay and other silicate minerals. Nanoindentataion tests, spanning various length scales ranging from 200 nm to 5 μm deep were performed. They developed a thought model based on their observation. Figure 5.3 demonstrates the thought model used in Bennet et al. [137]. In their model, three general types of constituent materials, as well as pore space was adopted. Clay particles, other mineral particles and organic material. The mica flakes are not distinguished from clay particles and would be classified as clay particles. The majority of the matrix of the shale here appeared to be quartz and pyrite; notably, no carbonate minerals were observed. Thus, they categorized this to as QFP phase. The other constituents are clay and organic matter. Figure 5.3 demonstrates the multi-scale thought model of Bennet et al. study with four material phases.

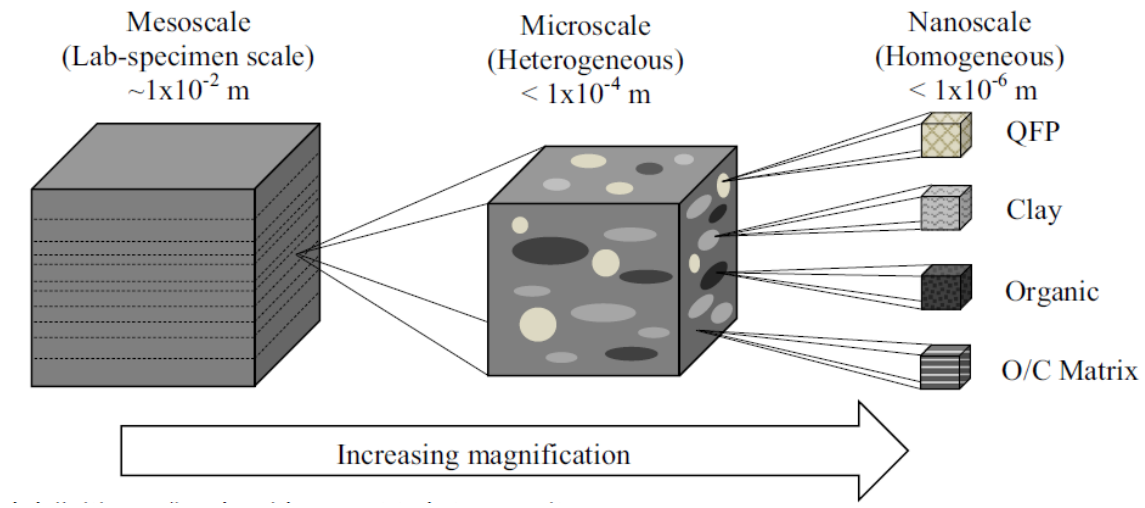

Figure 5.3: Schematic concepts and definitions of scale with respect to heterogeneity. Adopted from [137].

A fourth material phase, which is a composite of two materials, the organic/clay matrix. This description of the organic/clay matrix emerged from the observation that the mineral particles and pockets of organic material did not form a supporting skeleton with inter-granular contacts, but rather were embedded in a supporting matrix of composed of varying sizes of clay plate-like shaped particles mixed with organic material. To summarize, Bennet et al. [137] considers a four phase material model in nanoscale, and a heterogeneous microsclae material and a homogeneous mesoscale (lab scale specimen). Also, the found that the anisotropy of measured stiffness is most pronounced in the organic/clay matrix.

Another mutliscale model for structure of shale, originally presented by Ulm et al. [138]. Shale is a highly heterogeneous geo-composite, with heterogeneities which manifest themselves at various scales. Figure 5.4 illustrates the thought model presented by Ulm et al. [138]. At macroscopic scale, rock sample is considered at the scale of 10^{-3} m and above. This is the scale typically encountered for intact rock samples in the laboratory. At this scale, the rock is considered to be homogeneous, without containing large scale heterogeneities that might be associated with fracture, stratigraphic layering or other large-scale geological features. Three levels are considered; level 2 is the level of a porous clay and silt/sand inclusion composite, level 1 is the level of the porous clay composite,

and level 0 is the level containing a composite of clay minerals. In level 2 which is at scale of 10^{-5} to 10^{-4}, shale is seen as a composite of a porous clay phase and a silt or sand inclusion phase. Level 1 refers to scale on the order of 10^{-7} to 10^{-6} m, and focuses on the properties of the porous clay, which is seen as composite of clay particles and porosity. The last scale is the level of clay minerals , where a needle shape structure was seen for clays.

Later, this model was further developed to consider the porosity at the porous clay composite [139]. In their study, authors found that due to intrinsic anisotropy of the elementary building block and the scaling of this anisotropy with the clay packing density, the Biot pore pressure coefficients are almost isotropic. On the contrary, the Skempton coefficient, which quantify the pore pressure build-up under un-drained conditions in consequence of macroscopic stress application are highly anisotropic. Moreover, given the shale-invariant properties of the fundamental building block of shales, it is recognized that the poroelastic response of shale predominantly depends on the two properties: clay packing density and non-clay inclusion volume fraction.

In a similar study, Ortega et al. [140] compared the experimental and model prediction at multiple length scales to validate the use of the micro-mechanical model of shale as a tool for linking material composition to acoustic properties. In subsequent years, the multiscale model was developed to consider kerogen in the structure of the shale thought model. Monfared et al. [141], investigated the results of molecular simulation for two different organic maturity, mature and immature kerogen. In this latest model, anisotropy is introduced to the model as an intrinsic characteristic of clay with the stiffness properties. For the immature system, all measured porosity is assumed to be in the clay phase while microporous kerogen forms a continuous matrix leading to a matrix/inclusion texture. While in mature systems, the porosity is assumed to be self consistently distributed, in both organic and inorganic phases. This implies that all solid phases in each level of the model possess the same porosity. Figure 5.5 shows the schematic for the multi-scale maturity dependent model for organic rich shale.

Another multi-scale model was developed by Cusatis et al. [142]. Their model is in the order of clay-silt composite and bedding lamination and intact shale. At microscopic level, shale is a composite material made of porous clay, silt inclusion and organic matter; at lower length scale it exists as a porous clay/organic matter composite. The nanometer length level is the fundamental scale where elementary clay minerals are bounded to kerogen. At the macroscopic and mesoscopic levels, shale consists of a layered sedimen-

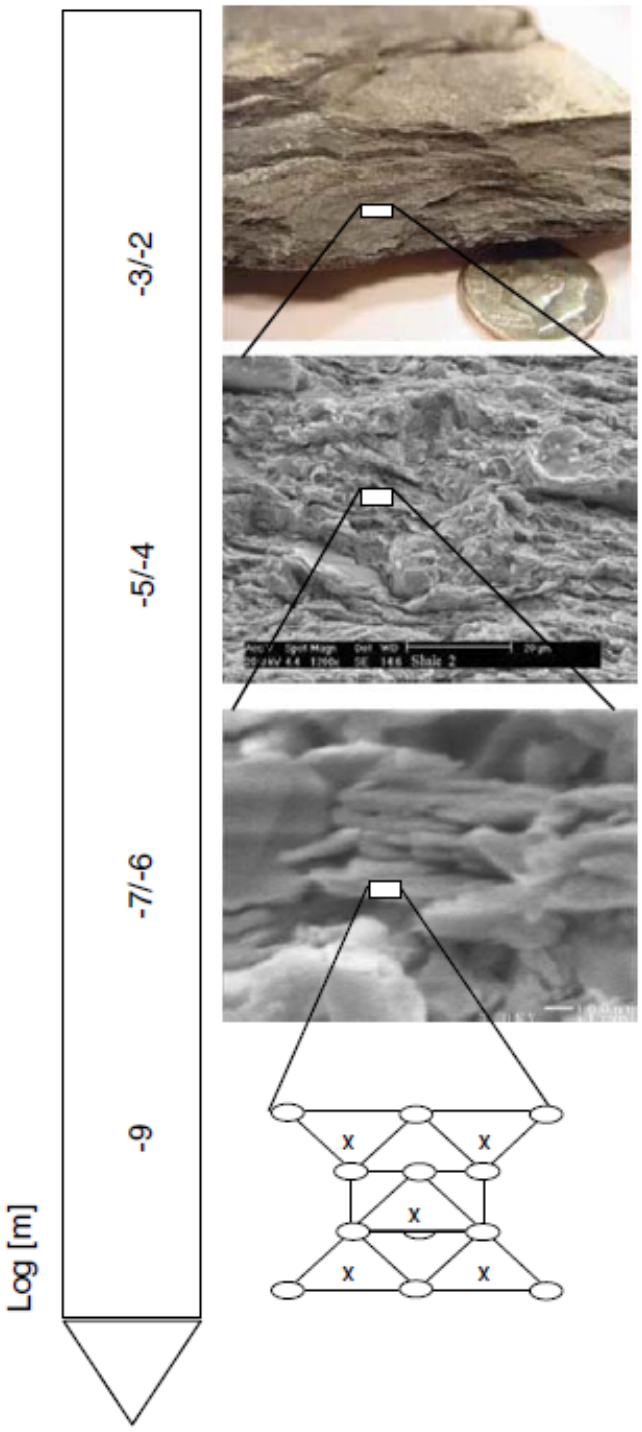

Figure 5.4: Multiscale structure of shales from top-down. Three level multiscale model of Shale. X in figures represents the building blocks of clay minerals, either a 1:1 layer or a 2:1 layer. Adopted from [138].

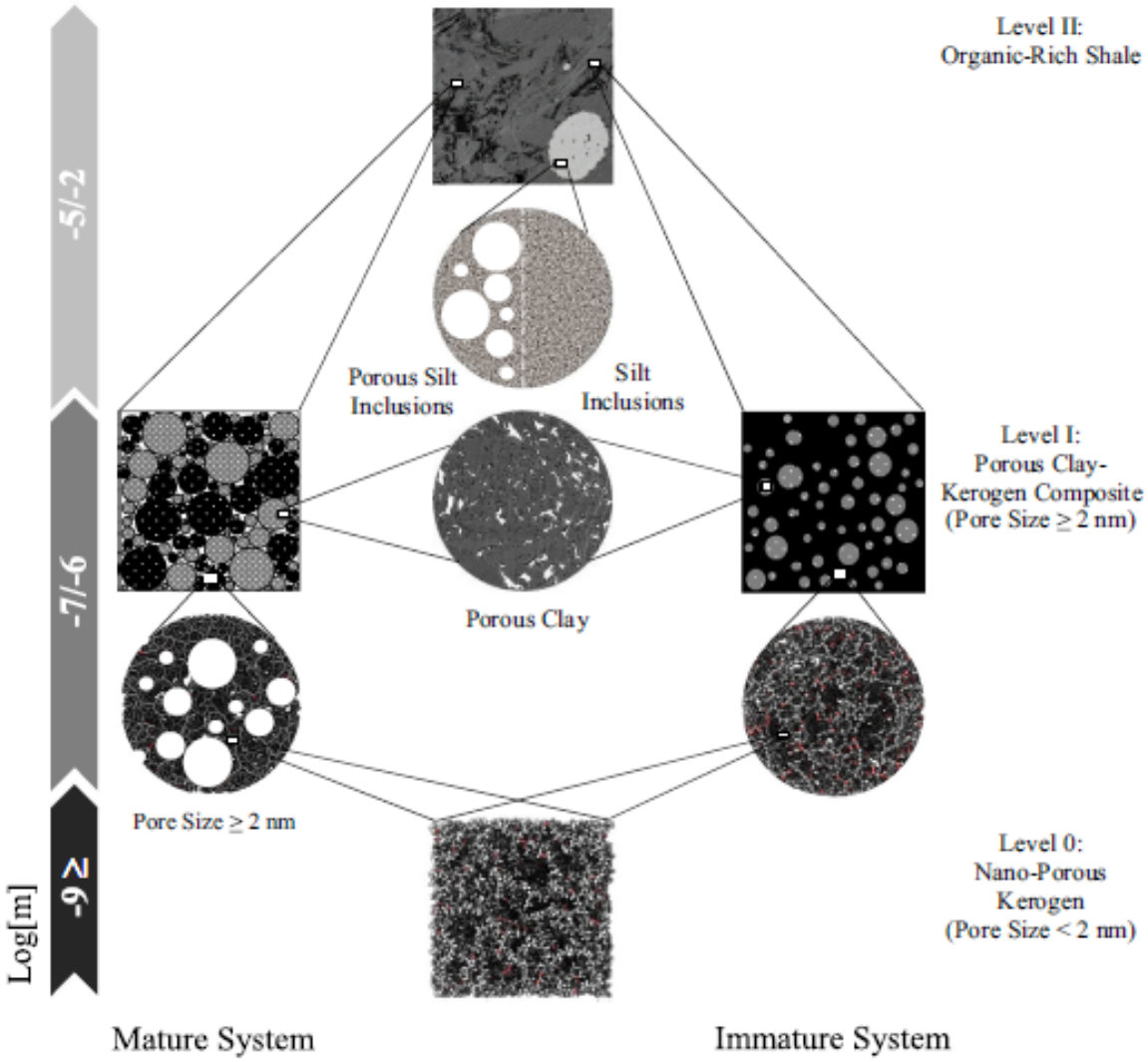

Figure 5.5: Schematics for the multi-scale maturity dependent model for organic-rich shales. At level 0, microporous kerogen forms the building block of the model. Level "I" of the model corresponds to the length scale relevant to nanoindentataion representing the composite response of porous clay and porous kerogen phases. Adopted from [141].

tary rock. It is often considered as as a transversely isotropic continuum, in which the anisotropy is induced by the presence of weak planes because of the sedimentation processes. Thus, in their model they assume shale samples to exhibit millimeter/micrometer grain size variability.

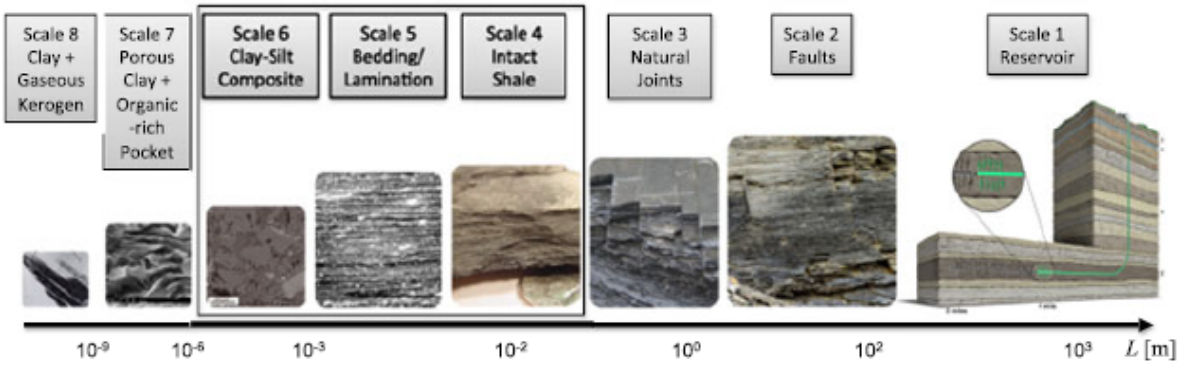

Figure 5.6: Multiscale structure of black shale. Adopted from [142].

Figure 5.6 demonstrates the multiscale structure of the shale presented in Cusatis et al. [142]. Their study is focused on scale 6–4 for this study. Furthermore, Figure 5.7 illustrates the detail for their model, where fine lamination is presented in a lattice discrete particle model system. The granular structure of the system was represented by spherical particles places at the center of the shale grain for grain generation.

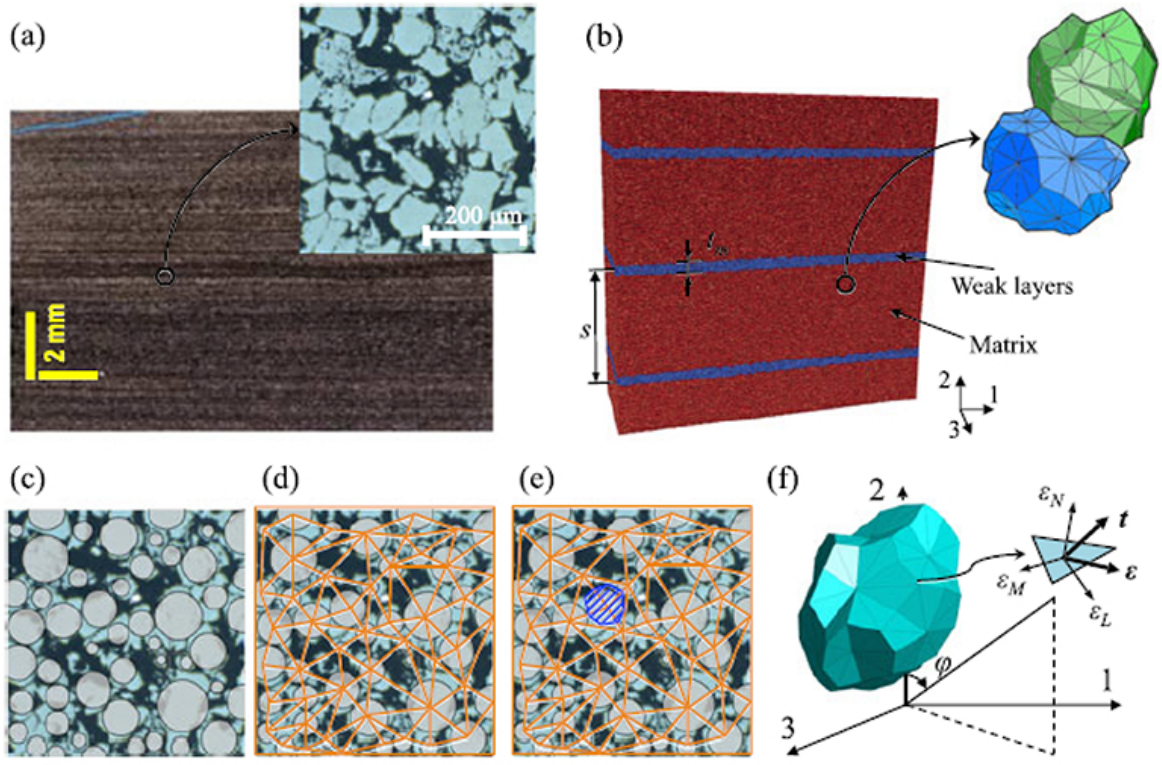

Figure 5.7: a) Finite lamination in Barnett shale and granular microstructure of Taorcian shale, b) a lattice discrete particle model system representing the laminated structure model and a zoomed view of grain interaction, c) spherical particles placed at the center of shale grains for grain generation, d) 2D representation of a polyhedral cell generated by a domain tesselalation, f) a 3D polyhedral cell representing a shale grain. Adopted from [142].

Last model presented here is developed by Bazant et al. [6, 143, 144]. The microplane modeling is used as a character of damage. The idea is to formulate the constitutive relation in terms of the stresses acting on a generic plane within the material. Initially the stress vector was assumed to be the projection of the stress tensor on this plane. It was shown that for quasi-brittle materials which exhibit softening damage this constraint must be replaced. For isotropic randomly heterogeneous materials, the microplane may be regarded as the tangent planes of a unit sphere surrounding every material point.

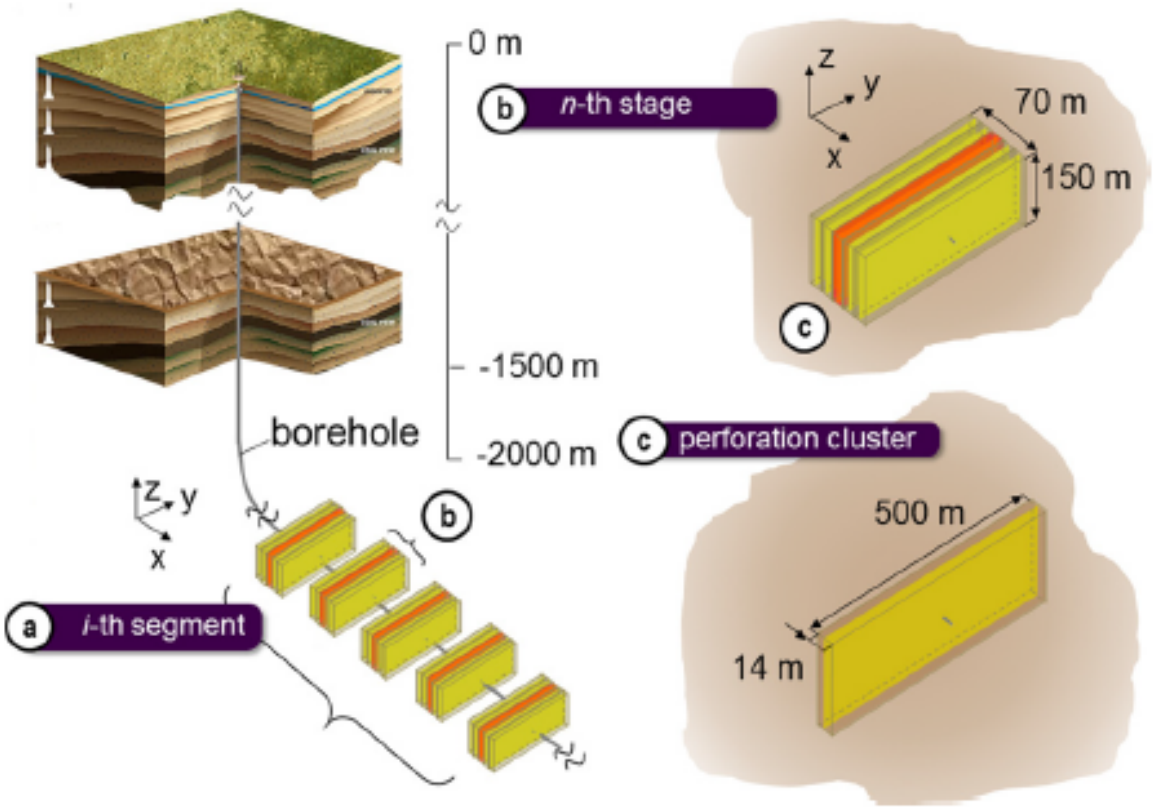

Figure 5.8: Overall scheme of hydraulic fracturing, reservoir scale to perforation cluster. Adopted from [143].

Figure 5.8 demonstrates the overall scheme of hydraulic fracturing with one of many segments, subdivided into several fracturing stages, each fracturing stage composed of several pipe perforation cluster and last one perforation cluster with several perforations along the pipes. The model developed by Bazant et al. [6, 143, 144] considers the reservoir

scale problem with a constitutive behavior for material. On the microplane constitutive model, they assume that the elastic moduli on the microplanes are constant up to the strength limit. The stress-strain relations for different components on the microplanes can be considered decoupled. To summarize, their model considers the constitutive model at material scale. This constitutive model is implemented at the perforation cluster and can be extended to the segment.

5.4 Conclusion

Multi-scale models aim to provide a fundamental understanding of the structure and processes involved. The review of current multi-scale models of shales in this chapter shows the importance of these model in the hydraulic fracturing while highlights the differences between them. One of the most important aspects of the multi-scale model is to understand the length scales of the problem. This behavior stems from the building blocks of the material. Several models where presented that allow the understanding of the multi-scale multi-phase behavior of organic rich shale. The review of current mutli-scale thought models help foster the modeling and provide reliable understanding of the structure of the organic rich shale.

Chapter 6

Micro-structural Characterization of Organic Rich Shale

6.1 Introduction

In this chapter, a detailed study the fabric and microstrucutre of different shale specimens in this study are presented. Here, a comprehensive investigation of mineralogy and fabric of each specimen in this study is presented. In this chapter, a through investigation of the fabric of the material and mineral composition of each material is presented. The characterization of the relative amounts of solid constituents in composite becomes important when modeling the material. For shale, the assessment of mineralogy composition is crucial for quantifying the volumetric contributions of clay and non-clay minerals to the overall mechanical response. The quantitative analysis of the mineralogy composition of shale specimens is typically obtained through X-ray diffraction measurements, although other methodologies are used such as infrared spectroscopy and energy dispersive spectroscopy. The mineralogy of each specimen was measured using X-ray technique. A wide range of mineralogy make-ups for the different samples testifies the diversity of materials investigated in this study. In addition to mineralogy of the specimen, the fabric of each specimen is investigated using scanning electron microscopy images.

X-ray powder diffraction was carried out to identify the minerals present in Marcellus, Niobrara, and Toarcian shale. The quantitative analysis of clays remains challenging [145, 146]. The main analytical difficulties in quantitative mineral analysis of rocks by XRD

are related to the chemical and structural characteristics of clay minerals, preparation methods, and factors disturbing three-dimensional periodicity. This can result in discrepancy between the intensity of XRD reflections of the same mineral in different specimens, which can lead to large analytical errors in quantitative analysis. [147] have shown that the preparation method plays a huge role in the quantitative assessment of clay minerals and associated minerals (quartz, feldspar, pyrite, calcite, etc). In summary there are four general approaches for XRD based quantification for minerals, clay minerals: known addition [148], absorption-diffraction [149], full-pattern-fitting [150, 151], mineral intensity factors [152, 153]. In this study we employ the mineral intensity factors with the so-called 100% approach which supposes that the sum of all phases quantities in a sample is 100%. X-ray diffraction methods has also been implemented to study the mineral composition of sandstones [151]. Therefore, to assess the mineralogy, powder X-ray diffraction was carried out at the Fredrick Seitz Materials Research Laboratory in collaboration with the Illinois State Geological Survey. A representative volume of the shale was used to make the powder form which passes through sieve number 60 (with a 250 μm opening). Afterward, the powder was milled using a McCrone Micronize Mill to prepare a homogenized particle size powder. Furthermore, the samples were top loaded into a 2.5 cm diameter circular cavity holders and run on Siemens D5000 where diffraction patterns were recorded by step scanning from 2-75 2θ. Quantitative X-ray diffraction analysis of clay-bearing rocks is a very challenging task, and proper procedure should be done when performing such analysis [154]. In addition to the powder diffraction, decantation of the clay particles were performed to measure the percentage of clays with ethylene glycol treatment. JADE$^{\text{TM}}$software and d-spacing was applied to identify and quantify the constituent minerals and their percentages respectively. Finally, the total organic content (TOC) of the organic-rich shale specimens was assessed using a UIC carbon coulometer following the standard ASTM D513.

6.2 Toarcian Shale

The Toarcian shale is the Schistes Carton that was deposited within an epicontinental sea during the early Toarcian, during a period of approximately 500,000 years. Total organic content of this reservoir ranges from 1 to 12 wt. % organic carbon [155]. The early Toarcian shales in the Paris basin are typically between 10 and 20 m thick, with maximum thickness in excess of 50 m [156]. The stratigraphic interval is dominated by

dark colored, moderately to highly laminated shales, which are dominated by illite and kaolinite. Calcite accounts for between 10 and 30 % of the rock with quartz accounting for between 5 and 20 % of the rock matrix. These shales are interrupted by Mg-rich calcite and dolomite concentration layers and carbonate beds [157]. The Paris basin is located at approximately 40°N latitude, and is one of a series of interconnected Liassic basins including the North Sea, NW German, SW German and Chalhac basins. These basins displayed intermittent communication with both the Arctic and Tethys [157]. An examination of the distribution of the organic content within the Schistes Carton reveals a general decrease in organic carbon content from the base of the unit to its top across the basin [158]. The specimens tested in this study are organic-rich shale specimens from Toarcian shale from Paris Basin. Specimens are mostly consist of micas group (illite, muscovite), ranging from 3.5 to 36.5 %. Another main component of the specimens are quartz phase, with a variation of 43.2 to 88.3 %. Chemical characterization of material reveals the percent of clay in the material as well as the mass or volume percent of micro-constituents. The clay content of the samples are ranged from 6.2 to 37 %. The density of the specimens are ranged from 2.64 to 2.73. The cored specimens as well as the prepared specimens are kept under the vacuum line (10 inch of mercury) to prevent any hydration and degradation of material in addition to degas and dry the specimen. Silica gels with diameter of 2 mm to 5 mm are used to absorb the humidity and keep the specimens dry under vacuum with its color-indicating properties. The specimens are extracted from the depth of 5106 m to 5130 m. Figure 6.2 demonstrate the location of the Paris Basin and the structural map of this basin.

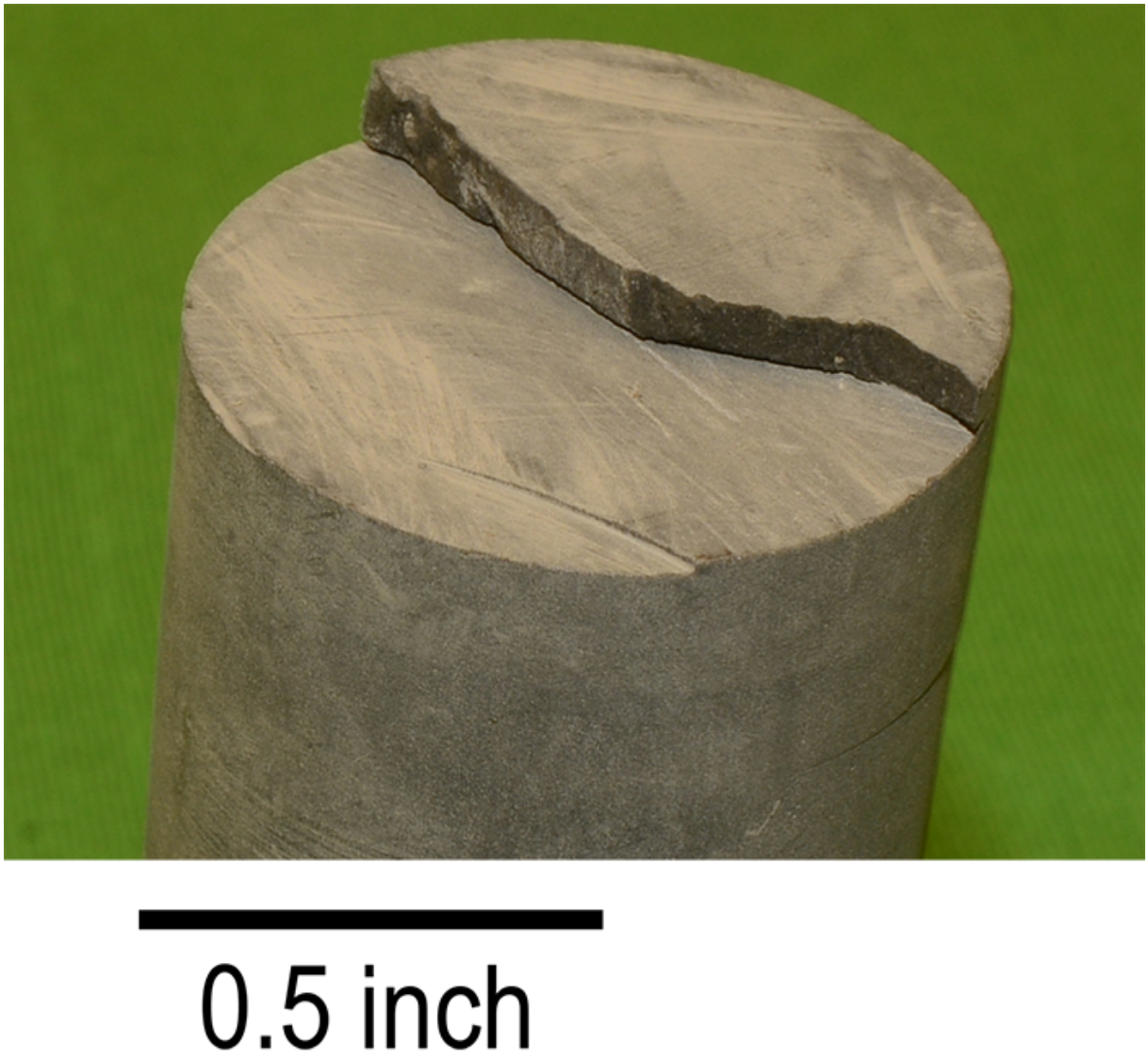

Figure 6.1: Photograph of Toarcian Core from Toarcian Paris Basin. Specimens are subsamples of this core. Credits: Akono, 2014.

Furthermore, Figure 6.1 demonstrates the core of Toarcian specimen. The specimens studied in this study are sub-samples of this core.

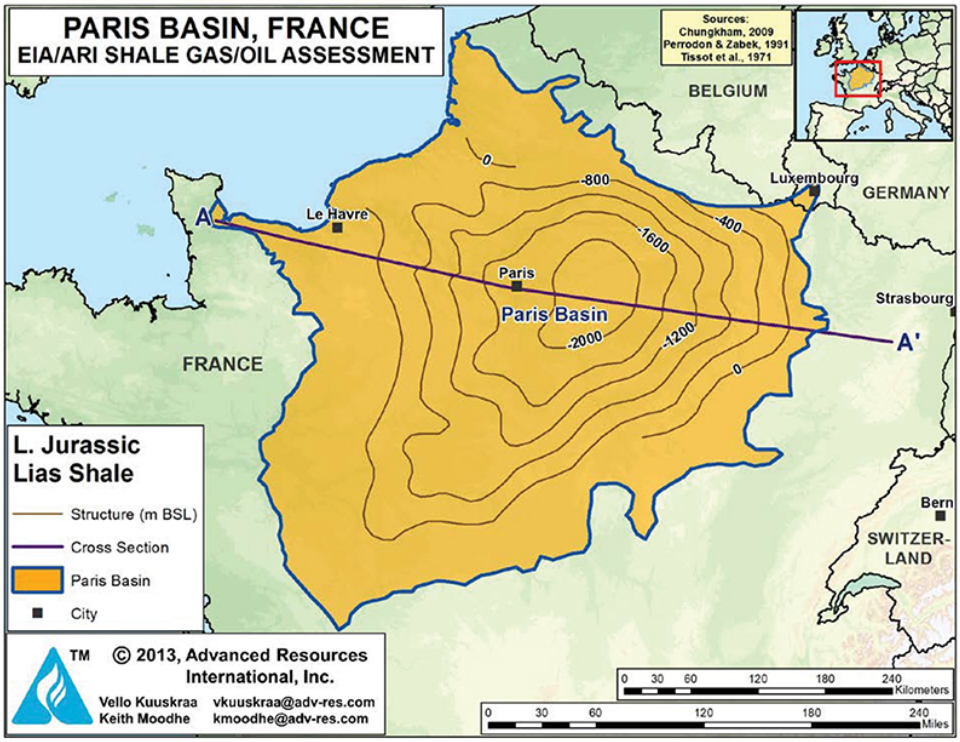

Figure 6.2: Index map and structural map of Toarcian Shale Paris Basin. Adopted from [159].

Let's observe the fabric of Toarcian specimens under scanning electron microscopy. Figure 6.3 demonstrates the microstructure of the Toarcian specimens, where the grains of quartz are dominant in the structure. The grains range from 5 μm to 400 μm. Furthermore, the organic matter is present as a pocket surrounding parts of the quartz grains. A closer look at these scanning electron microscopy images reveal the presence of presence of clay around the grains and in the between the quartz grains. Porosity on these specimens range from nm to μm size pores.

Furthermore, Figure 6.4 demonstrates the quartz crystal in Toarcian samples. The shape of this crystal is a hexagonal prism, topped by a hexagonal pyramid. This scanning electron microscopy image demonstrate the quartz grains with the presence of μm size porosity. The observation of the fabric of Toarcian shale, we observe a high amount of quartz in the structure of this shale. The fabric consists of quartz grains with isolated pockets of kerogen.

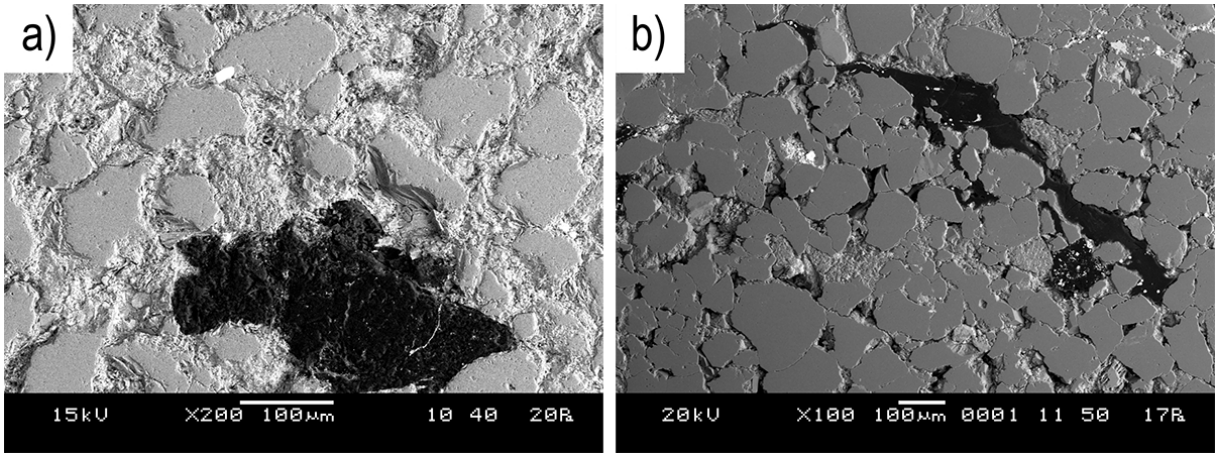

Figure 6.3: Scanning electron microscopy of a) Kerogen pocket around the quartz grain in Toarcian B1 specimen, b) Granular microstructure of Toarcian B1 specimen. The SEM images are taken at low vacuum without coating the specimen.

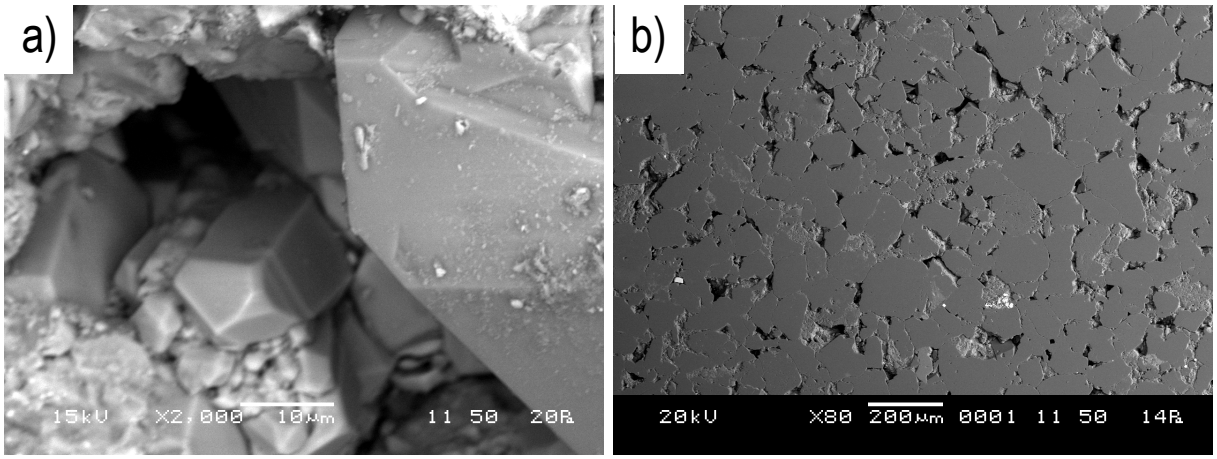

Figure 6.4: Scanning electron microscopy of a) Toarcian B2 specimen, b) Toarcian B1 specimen.

A better understanding of chemical composition is obtained by using X-ray diffraction study. Figure 6.5 shows an XRD diffractogram 2θ scan from an instrument under Bragg-Brentanp configuration using Cu radiation. The sample was a powder prepared from a Toarcian rock specimen obtained from a cored specimen. The basic general interpretation of this type of data is as follows:

The presence of diffraction peaks indicated that crystalline grains are present. In order to determinate if those peaks are from the same family of planes, which indicate a highly-oriented material, or from various grain orientations, which is more typical in a powder or polycrystalline sample, indexing of the pattern needs to be performed. Specific software can be used to determine the crystalline structure of the material based on the angular 2θ position of the observed peaks. Another method is to manually mark different peaks based on the mineral data present in the literature. For example Figure 6.5 demonstrates the indication of different minerals in XRD diffractogram of Toarcian B1 specimen. However, more commonly, the data are used in an automated search and match procedure in comparison against a database of power diffraction files in order to identify the materials present in the sample. Therefore the angular position and relative intensity of the peaks are the key parameters used in this finger printing approach.
Peak positions are used for unit cell determination and refinement. Relative comparison of peak areas can be used to provide quantitative determination between mixtures or the various phases present in the sample and to determine preferred orientation for a specific material. The angular width of the diffraction peaks can be used for peak shape analysis where information about crystalline size, micro-strain and defects in the material can be extracted. The shape of peak tails can be used to model and identify diffuse scattering used for point defect quantification.

An important point must be raised here is that a typical 2θ scan only probes the grain orientations with crystallographic planes parallel to the sample surface. Therefore care must be taken to ensure that sample preparation provides a powder with a random distribution of crystallographic orientations. Otherwise only a few grain orientations will be detected by this type of measurement, which can create difficulties in the identification of the present phases. The same problem can occur if preferred orientation is introduced when mounting the sample to the sample holder, for instance, pressing the powder too hard and therefore causing the gains to align in a particular direction.

In this type of measurement, during the rotation of both the detector and sample, the X-ray beam irradiates different surface areas and depth in the sample which can

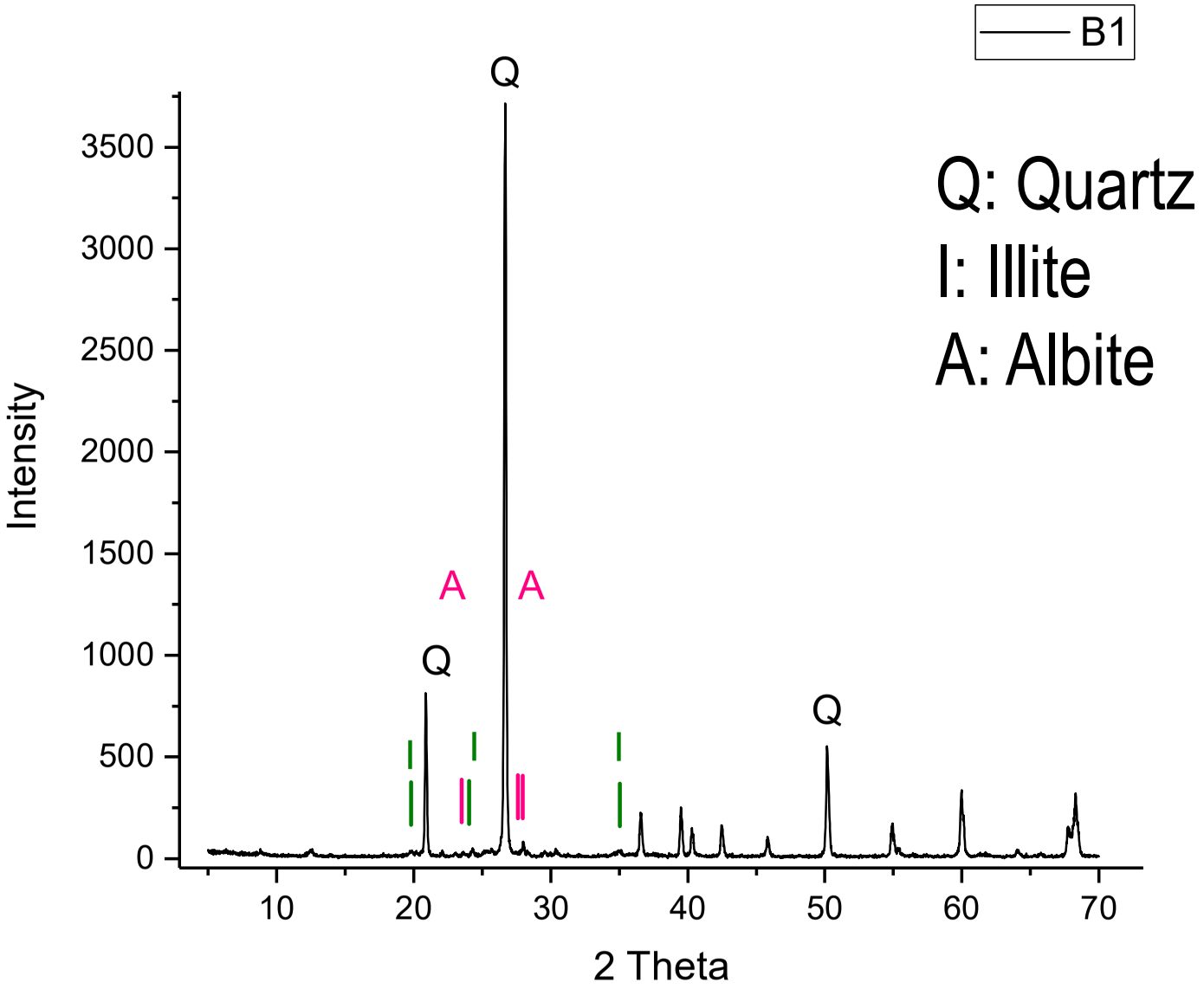

Figure 6.5: X-ray diffraction pattern, 2θ scan from a powder sample prepared from Toarcian B1 specimen. Manually identified quartz, albite and illite phases.

possibly vary the probed volume during the measurement. At lower 2θ angles, the X-ray beam penetration depth is small but it covers a large surface area. At high 2θ angles, a deeper volume is probed but covering a smaller sample surface. Proper care needs to be taken so that only the sample surface is irradiated, which can be accomplished by proper choice of divergence slit in the primary optics. If this issue is not taken properly, the use of peak areas at low angle may compromise quantitative analysis of mixtures and false determination of preferred orientation.

The preparation method is an important step in characterization of clay particles. So here we summarize steps taken to ensure the integrity of the samples. It may be necessary to dissolve the carbonates in some limestones and sediments before the clay minerals can be identified. However, treatment with strong acids to remove carbonate can attack the structure of clay minerals, and even dilute acid can attack the silicate layers vie interlayer regions and exposed edges. Thus, in this study we do not use acid treatment for specimens. We use decantation for separation of silt and clay for X-ray powder diffraction. Decantation is the gravity settling of particles in a suspension. Although more time consuming than centrifugation, decantation can also be used to separate the clay and silt sized fractions for X-ray powder diffraction. For this technique it is assumed that the coarse fraction (sand and gravel) has been removed and that the fine fraction has been retained as a suspension. After a muddy suspension is dispersed and allowed to settle, aliquots of clay suspension may be withdrawn from above 5 cm in depth at the times.

Bulk mineralogy of a sediment sample can be determined by X-ray diffraction with a randomly oriented powder mount. The random orientation insures that the incident X-rays have an equal chance of diffracting off any given crystal lattice face of the minerals in the sample. The use of a powder press to make randomly oriented powder mounts is undesirable because excessive force could cause preferred orientation of the crystallites. Although some orientation is inevitable but the proper technique can minimize preferred orientation.

Sample splits are commonly dried at 60 °C prior to the preparation of randomly oriented powder mounts. The mounts are typically X-rayed between the angles of 2 and 70 degrees 2θ using copper alpha radiation at a scanning rate of 2 degrees per minute. Grind the dried sample thoroughly so that it is easily brushed through the sieve. The particles should be finer than 0.062 mm to avoid fractionation of the minerals. The sieve is used only to achieve even distribution and to ensure that the grinding is complete. Brush the

sample through the sieve into the sample holder using a weighing paper and distribute evenly. Use a glass to pack the sample into the cavity firmly enough so that it will not fall out, deform or slide but not so firmly that preferred orientation will be produced on the opposite surface.

Another way to prepare bulk mineralogy samples is to prepare smear slide sample mounts. Thus, samples may be ground and smeared on the surface of a glass slide as a rapid means of preparing samples for X-ray powder diffraction. This mounting method seldom produces acceptable random orientation of the crystallites, resulting in diffraction maxima with relative intensities that are not accurately reproduced. Although not useful for semi-quantitative analysis, this method is useful for rapidly determining bulk mineralogy.

A method to find the swelling clays is to use an auxiliary treatment of these clays. Organic liquids, primarily ethylene glycol and glycerol are extensively used as an auxiliary treatment to expand swelling clays. Whether or not a mineral expands and the amount of expansion can provide essential supplementary information aiding clay-mineral identification. Swelling clays include smectites (i.e. montmorillonite, nontronite and beidellite), some mixed layer clays and vermiculite. In order to make sure that the sample is saturated with organic treatment we do the following: Pour ethylene glycol to about 1 cm depth in base of desiccator and place oriented aggregate mounts on the shelf of desiccator. Furthermore, place the desiccator in oven at 60 to 70 °C for about 4 hours or overnight. Longer times will not hurt samples. Do not remove mounts until they are ready to be run on the X-ray diffractometer.

Now that a detailed review of sample preparation for XRD measurements is presented, the measurements results from XRD studies are shown. Figure 6.6 shows the 2θ scan from a powder sample prepared from Toarcian specimen B1. Quartz peak is a dominant in this diffractogram at $2\theta = 26.739$.

Similarly, Figure 6.7 demonstrates the 2θ scan from a powder sample prepared from Toarcian specimen B2. Quartz peak is dominant at $2\theta = 26.739$. Dolomite peak is shown at 2θ =30.65 and the pyrite peak is shown at 2θ =33.162. It is worth mentioning that the graph is shown for the range of 2θ from 0–35 degree.

Finally, Figure 6.8 shows the XRD diffractogram of the Toarcian B3 specimen. The 2θ scan was obtained from a powder sample prepared based on the procedure described above. Figure 6.8 shows the quartz peak at $2\theta = 26.70$. Dolomite peak is at $2\theta =$

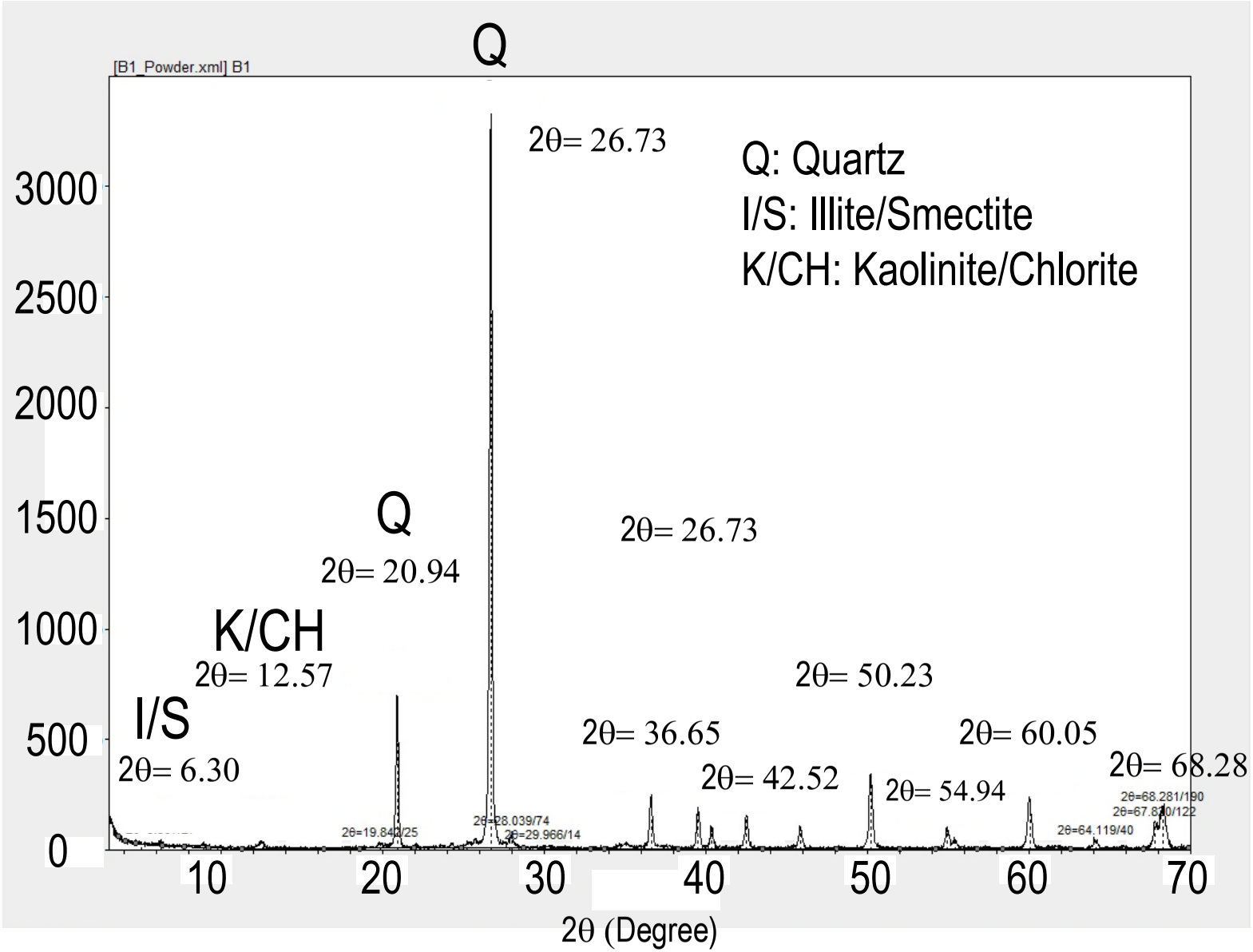

Figure 6.6: X-ray diffraction pattern, 2θ scan from a powder sample prepared from Toarcian specimen B1.

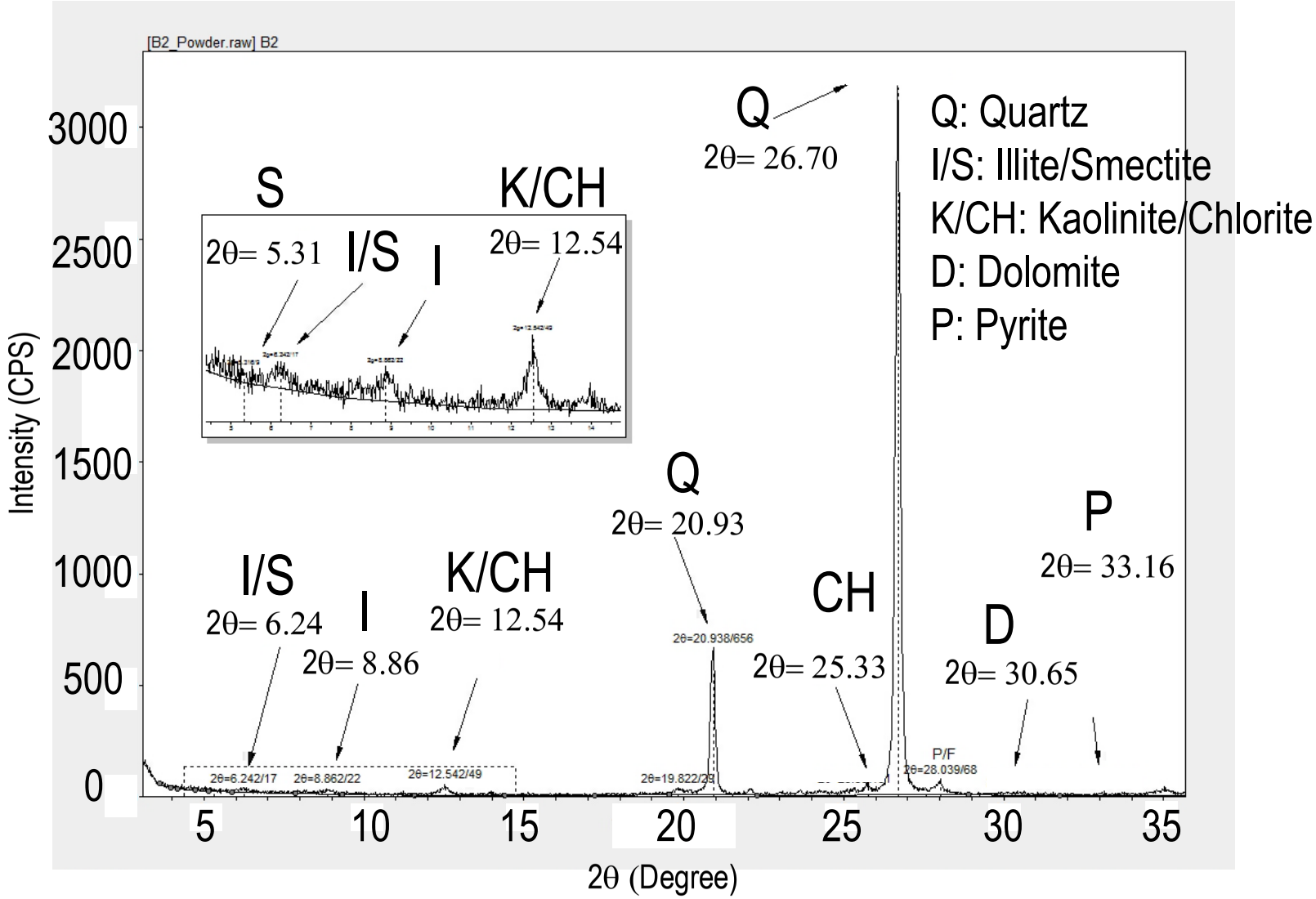

Figure 6.7: X-ray diffraction pattern, 2θ scan from a powder sample prepared from Toarcian specimen B2.

30.52 and pyrite at $2\theta = 33.07$. A more detailed part of this investigation is the lower diffraction angles where the presence of clay minerals are present. I/S demonstrate the mixed illite/smectite whereas I shows the illite and K/CH shows kaolinite and chlorite part of the clay fraction.

Table 6.1 summarizes the results of mineral composition of Toarcian specimens for three different specimens. It is observed that Toarcian specimens are high in quartz content as shown in scanning electron microscopy images of these specimens. The clay percentage of these specimens are around 2-3 %. The Toarcian specimens are not calcite rich or dolomite rich.

Table 6.1: Mineral composition in weight percent of the gas shale specimens for Toarcian Shale. Sid.= Siderite, Cal.= Calcite, Feld.= Feldspar

Material	Quartz	K-Feld.	P-Feld.	Calc.	Dolomite	Sid.	Pyrite	Clay
B1	87.0	3.0	5.5	0.5	0.0	1.0	1.0	2.0
B2	86.5	2.0	5.0	0.0	1.0	1.5	1.0	3.0
B3	87.0	3.0	4.0	0.0	1.0	1.0	1.0	3.0

6.3 Niobrara Shale

The Niobrara Total Petroleum System (TPS) produces oil and gas from fractured carbonate rock reservoirs in the Upper Cretaceous Niobrara Formation and equivalent rocks of the Southwestern Wyoming Province. The Niobrara TPS encompasses the area of eastern and southeastern Greater Green River Basin of southwestern Wyoming and northwestern Colorado. The Niobrara ranges in thickness from 900 to 1,800 feet and consists mainly of interbreed organic-rich shale, calcareous shale, and marl. The Southwestern Wyoming Province (SWWP) is a large sedimentary and structural basin that formed during Late Creataceous through Ecocene. The SWWP covers approximately 23,000 mi^2 and occupies most of southwestern Wyoming, parts of northwestern Colorado, and a small area of northeastern Utah 6.9.

The Niobrara formation at the southwestern Wyoming Province (SWWP) is a sedimentary basin that formed during the Larmide orogeny (Late Cretaceous through Eocene). The SWWP basin covers around 59,000 km^2 and occupies most of southwestern Wyoming, parts of northwestern Colorado, and a small area of northeastern Utah [160]. The Niobrara Formation was deposited during a period of high eustatic sea level and crustal subsidence in the Western Interior Seaway, resulting in a major transgression and conditions favor-

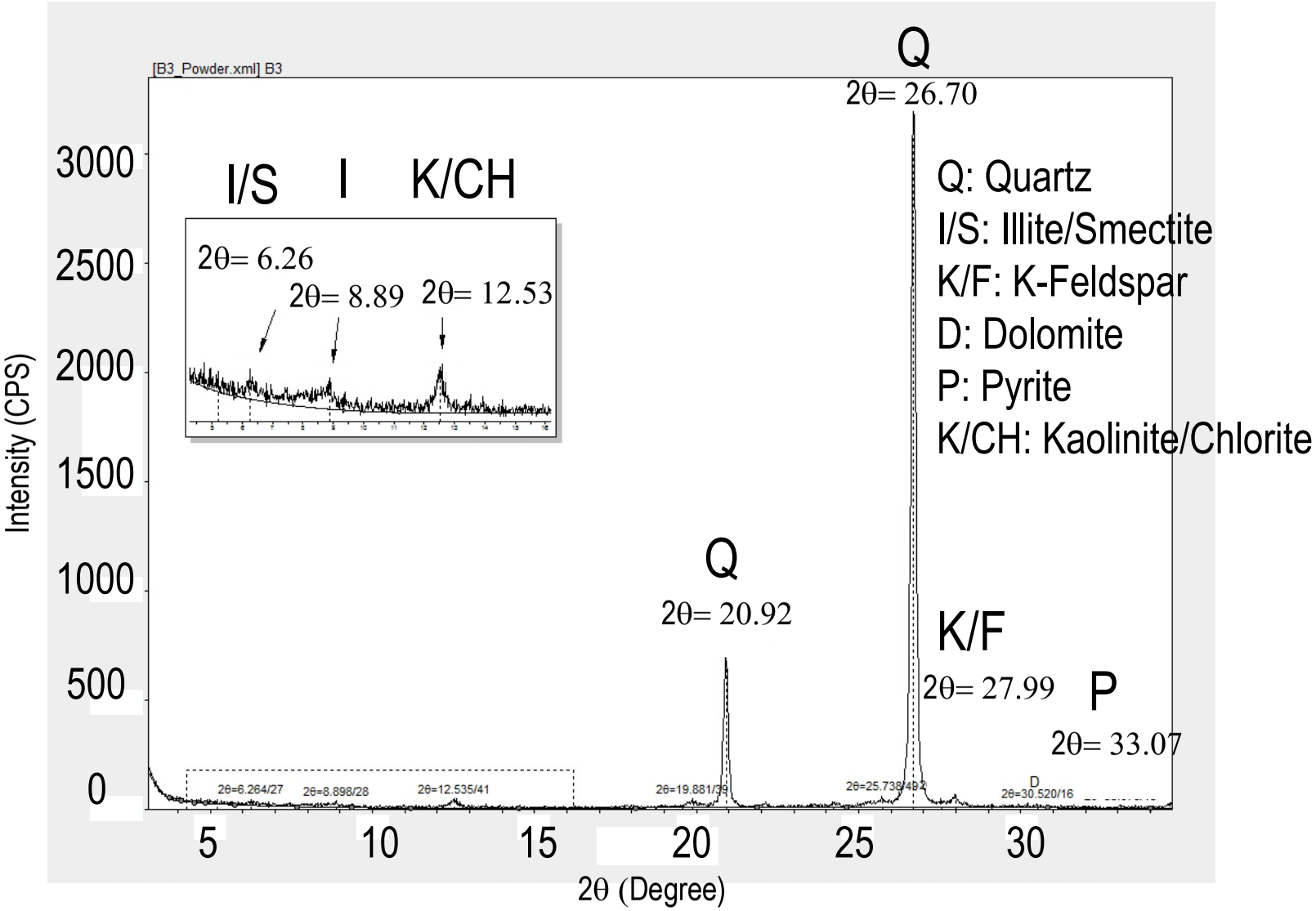

Figure 6.8: X-ray diffraction pattern, 2θ scan from a powder sample prepared from Toarcian specimen B3.

able for carbonate deposition. While in the eastern part of the seaway where clastic input was minimal, chalks and limestone, are the principal lithologies of the Niobrara in the Denver Basin at the eastern Colorado [161].

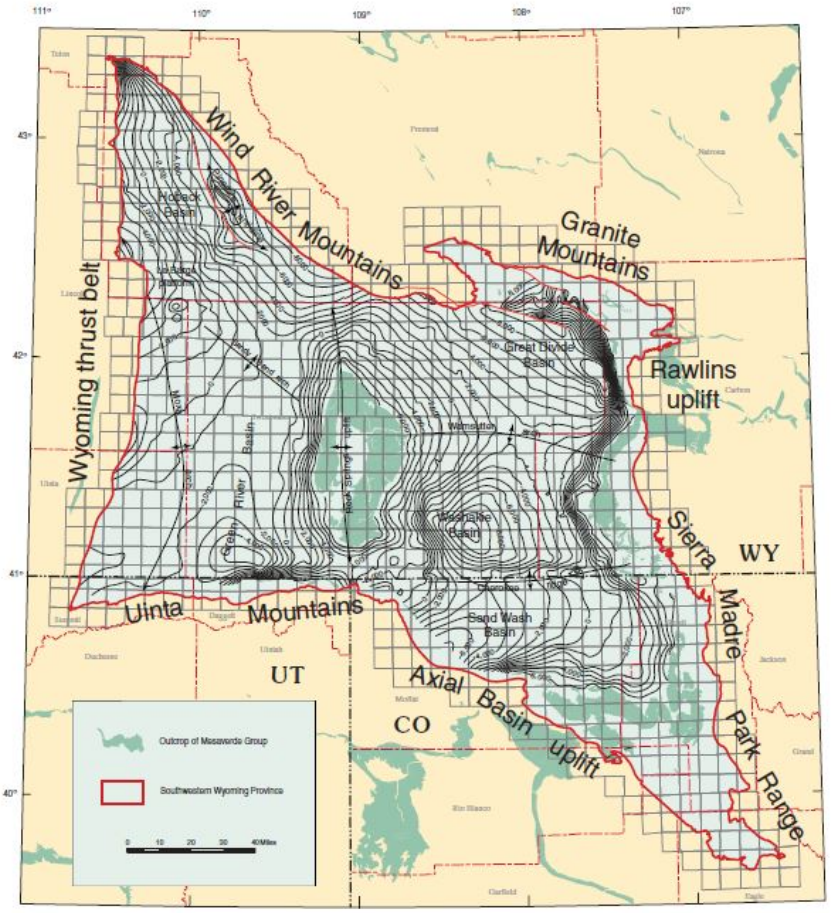

Figure 6.9: Index map of southwestern Wyoming, northeastern Utah, and northwestern Colorado showing the location of the Southwestern Wyoming Province, structural configuration, intrabasin uplifts, and sub-basins. Contour interval= 1,00 feet. Adopted from [160].

Figure 6.10 demonstrates the Niobrara core, as well as two sub-sampled and mounted specimens. The core is a 1 inch cube with the direction of the drilling marked on the specimen.

Figure 6.11 illustrates the fabric of Niobrara specimen. The fabric shows two color patterns. These patterns shows a preferred orientation which show the bedding layers of the material. The bright dots on Figure 6.11a-b) shows pyrite inclusions in the structure

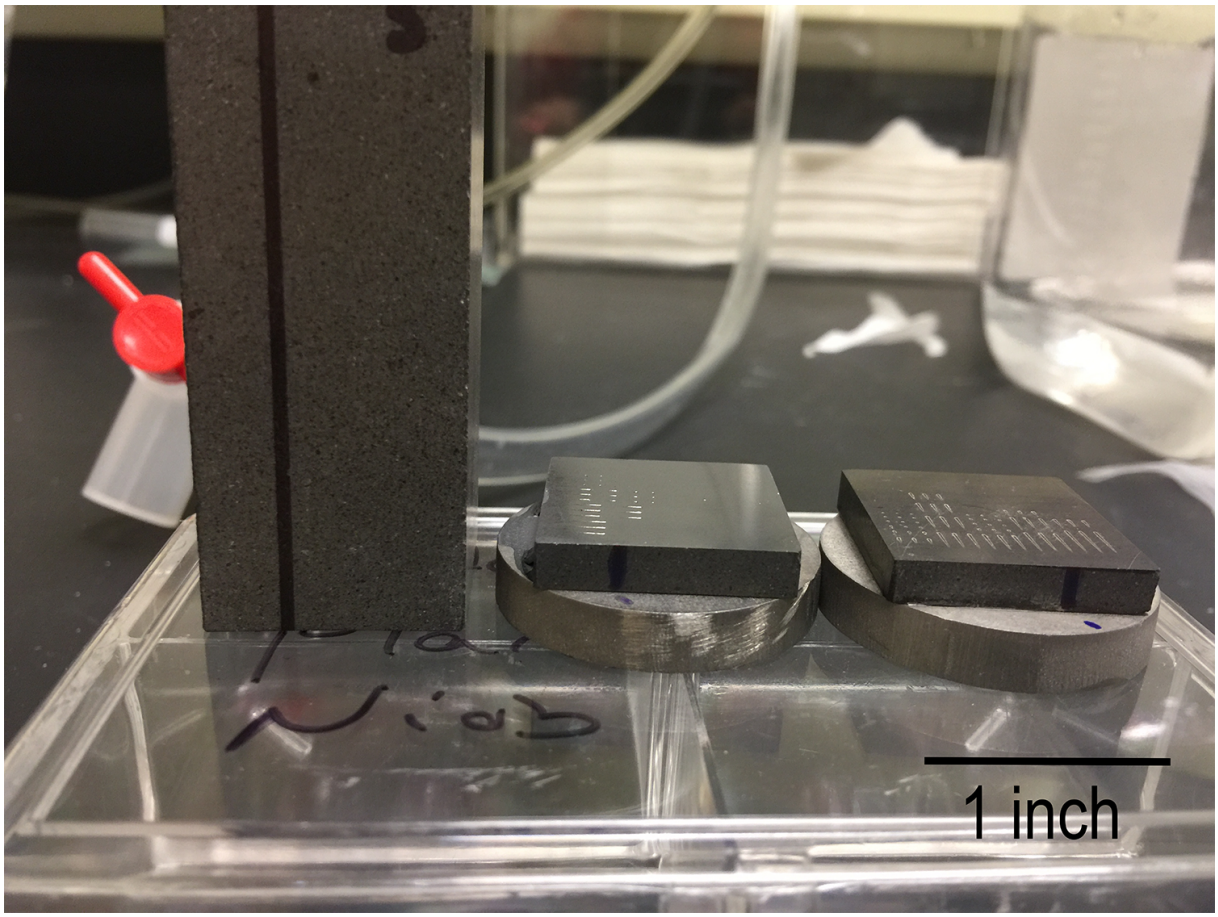

Figure 6.10: Photograph of Niobrara specimen core. Specimens are sub-sampled from the main core using a diamond saw.

of the specimen. Small pockets of organic matter is present in the fabric of the specimen. Some of these pockets are isolated while others are intermixed with the fabric of the shale. Thus, some further investigation of the fabric is needed. A higher magnification of

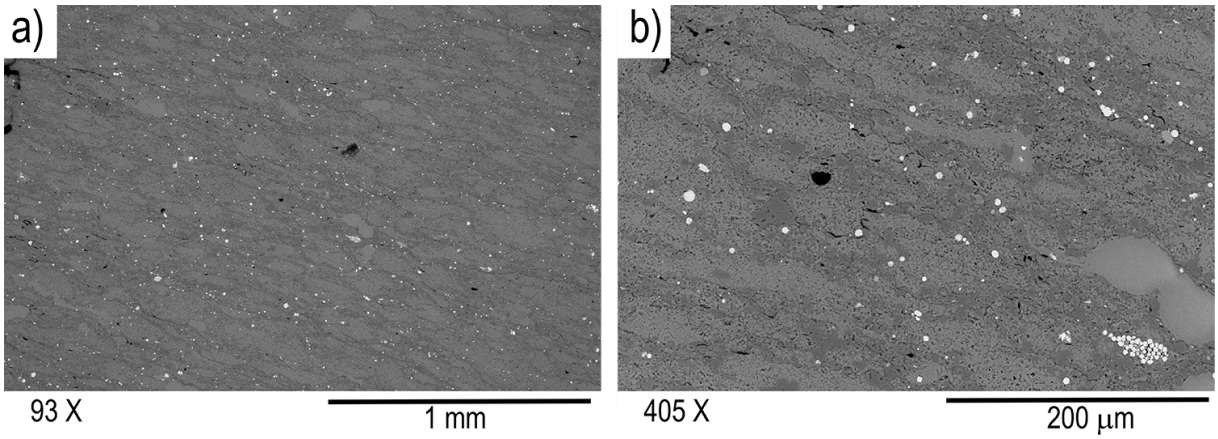

Figure 6.11: Scanning electron microscopy of a) Niobrara specimen in low vacuum and 93X magnification, b) Niobrara specimen in low vacuum and 405X magnification. The pyrite particles are present as bright points on the surface.

Similarly, Figure 6.12a) demonstrates a closer look at pyrite inclusions embedded in the calcite matrix of Niobrara specimen. A zoomed in image Figure 6.12b) demonstrate the organic matter as well as heterogeneous nature of material at this scale with microporosity. At the highest magnification, Figure 6.12c-d) illustrate the illite clay where the fabric of clay shows a preferred orientation. In addition, nanoporosity is present at this scale where the clay particles exhibit porosity.

Furthermore, we implement X-ray diffraction study to identify and quantify the mineral make up of Niobrara shale. Figure 6.13 demonstrates the XRD diffractogram for the range of 2θ from 0–70°. The XRD scan shows the presence of Calcite, quartz, dolomite, pyrite and illite in the first round of sample characterization.

Similarly, Figure 6.14 shows the powder specimen XRD intensity diagram where the 2θ ranges from 0–35. The graph demonstrate the highest peak to be representative of calcite, second highest peak as quartz. The sub-figure on the left side demonstrate the clay fractions and different types of clays present in this XRD scan.

Finally, Figure 6.15 demonstrates the glass slide 2θ scan of the Niobrara shale. This part is more focused on different clay particles present in Niobrara specimen. We observe smectite peak, illite/smectite peak, illite peak and kaolinite/chlorite peak in the subfigure

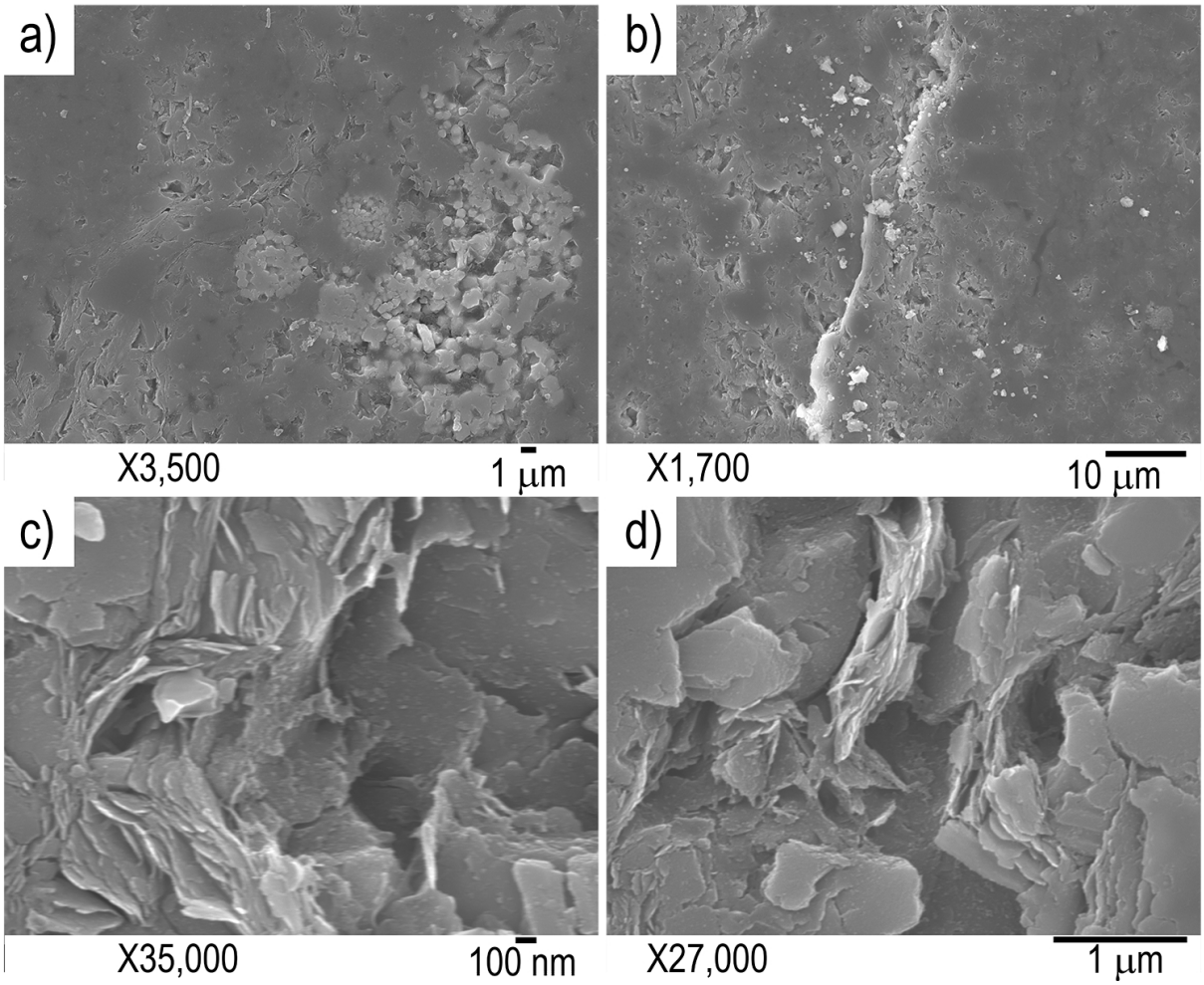

Figure 6.12: Scanning electron microscopy of Niobrara specimen: a) Pyrite framboids are present in the structure of the specimen at 3,500X magnification, b) fabric of the specimen is visible at 1,700X magnification, c) the clay fabric of illite is visible at 35,000X magnification, d) the fabric of clay and flaky structure of the clay is demonstrated in the structure of the specimen.

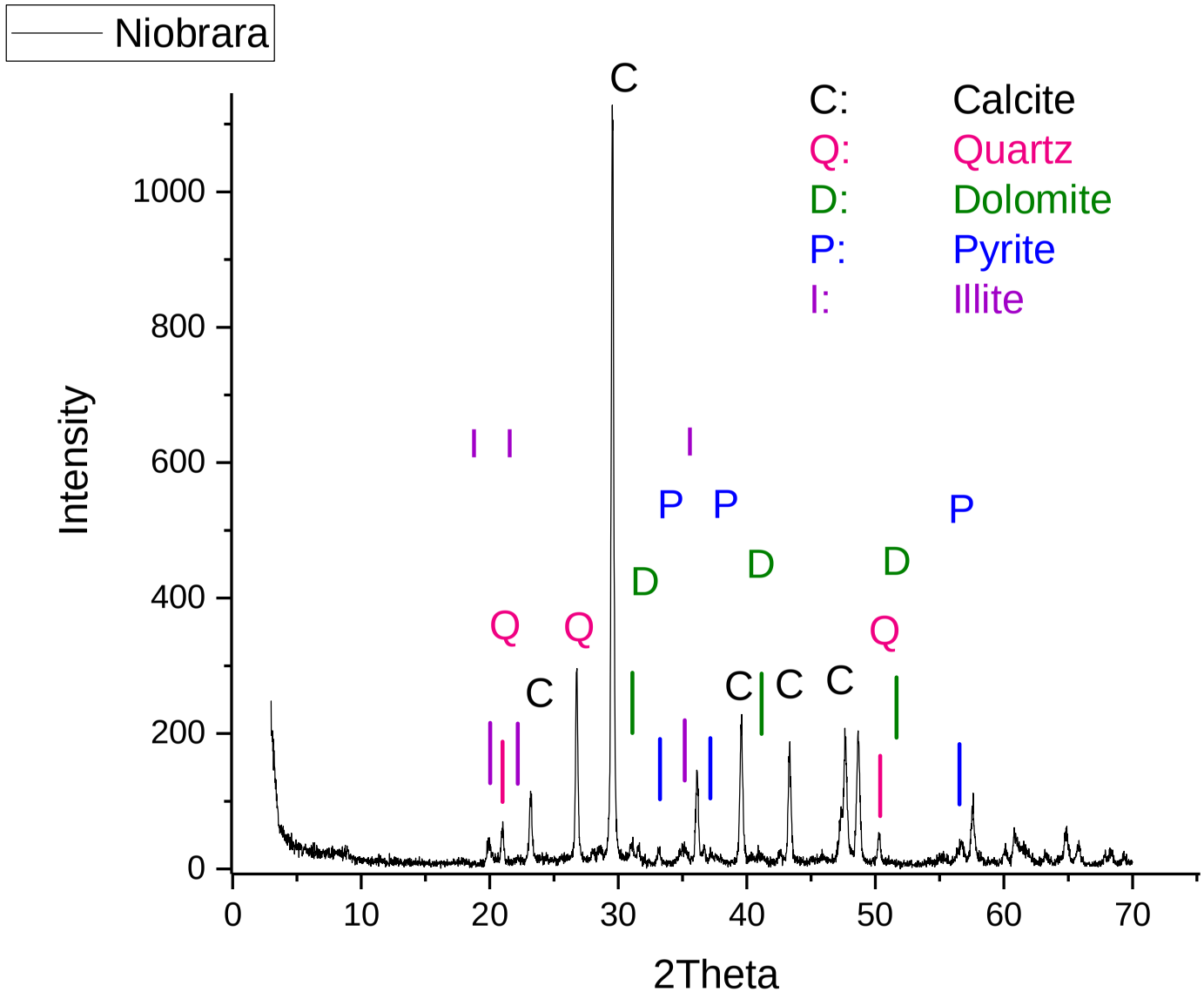

Figure 6.13: X-ray diffraction pattern, 2θ scan from a powder sample prepared from Niobrara specimen.

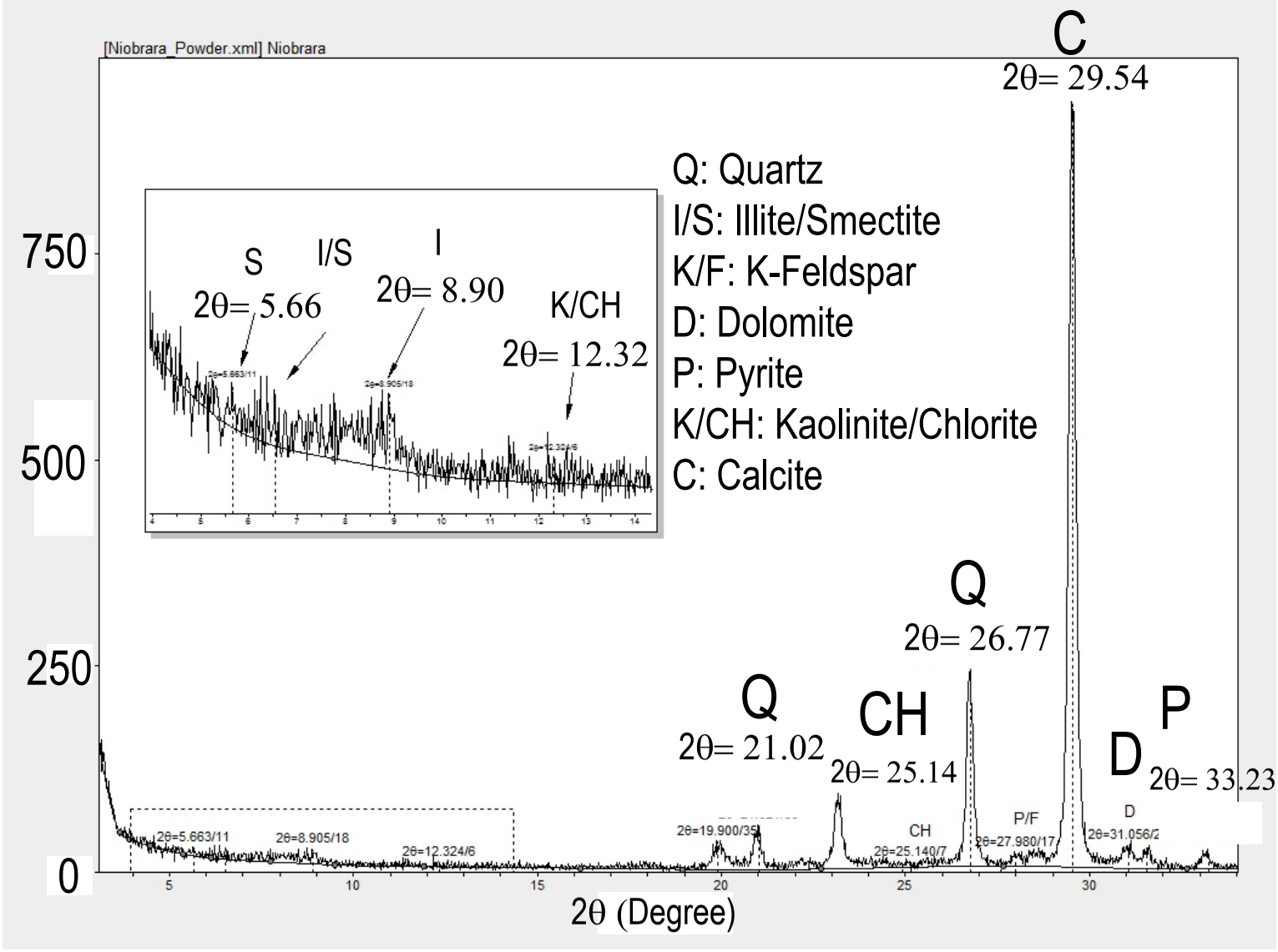

Figure 6.14: X-ray diffraction pattern, 2θ scan from a powder sample prepared from Niobrara specimen.

which ranges from 0–12 °. The subfigure on the right side of Figure 6.15 demonstrate the presence of quartz and calcite in the Niobara shale fabric.

Table 6.2 summarize different percentages of minerals in Niobrara shale specimens in this study. We observe that Niobrara shale is more calcite dominated in terms of mineralogy. The second highest percentage is quartz followed by siderite.

6.4 Marcellus Shale

The Middle Devonian-age Marcellus shale is the largest shale gas play in the U.S geographically. Depth of production for this reservoir is between 4,000 feet to 8,500 feet. This shale is the most expansive shale gas play, spanning six states in the northeastern United States. The Marcellus shale is bounded by shale above and limestone below. In 2003, Range Resources Corporation drilled the first economically producing wells into the Marcellus formation in Pennsylvania using horizontal drilling and hydraulic fracturing techniques similar to those used in the Barnett shale formation of Texas. The Marcellus shale covers an area of 95,000 mi^2 at an average thickness of 50 feet to 200 feet. While the Marcellus is lower in relative gas content at 60 scf/ton to 100 scf/ton, the much larger area of this play compared to the other shale gas plays result in a higher original gas-in-place estimate of up to 1,500 tcf. Figure 6.16 demonstrate the map of the Appalachian basin province showing the Macrellus shale and three different assessment units.

Figure 6.17 demonstrates the Marcellus sample after grinding and polishing. The reflection of overhead light is visible on the sample surface.

Figure 6.18 demonstrates the granular nature of Marcellus shale, we observer grains ranging from 10 μm to 400 μm in the scanning electron microscopy image. The presence of organic matter as pockets are present in this specimen. The bright points in the Figure 6.18b shows the pyrite particles.

Table 6.2: Mineral composition in weight percent of Niobrara Shale in this study

Quartz	K-Feldspar	P-Feldspar	Calcite	Dolomite	Siderite	Pyrite	Clay
14.5	1.5	3.0	65.0	2.0	8.0	3.0	3.0

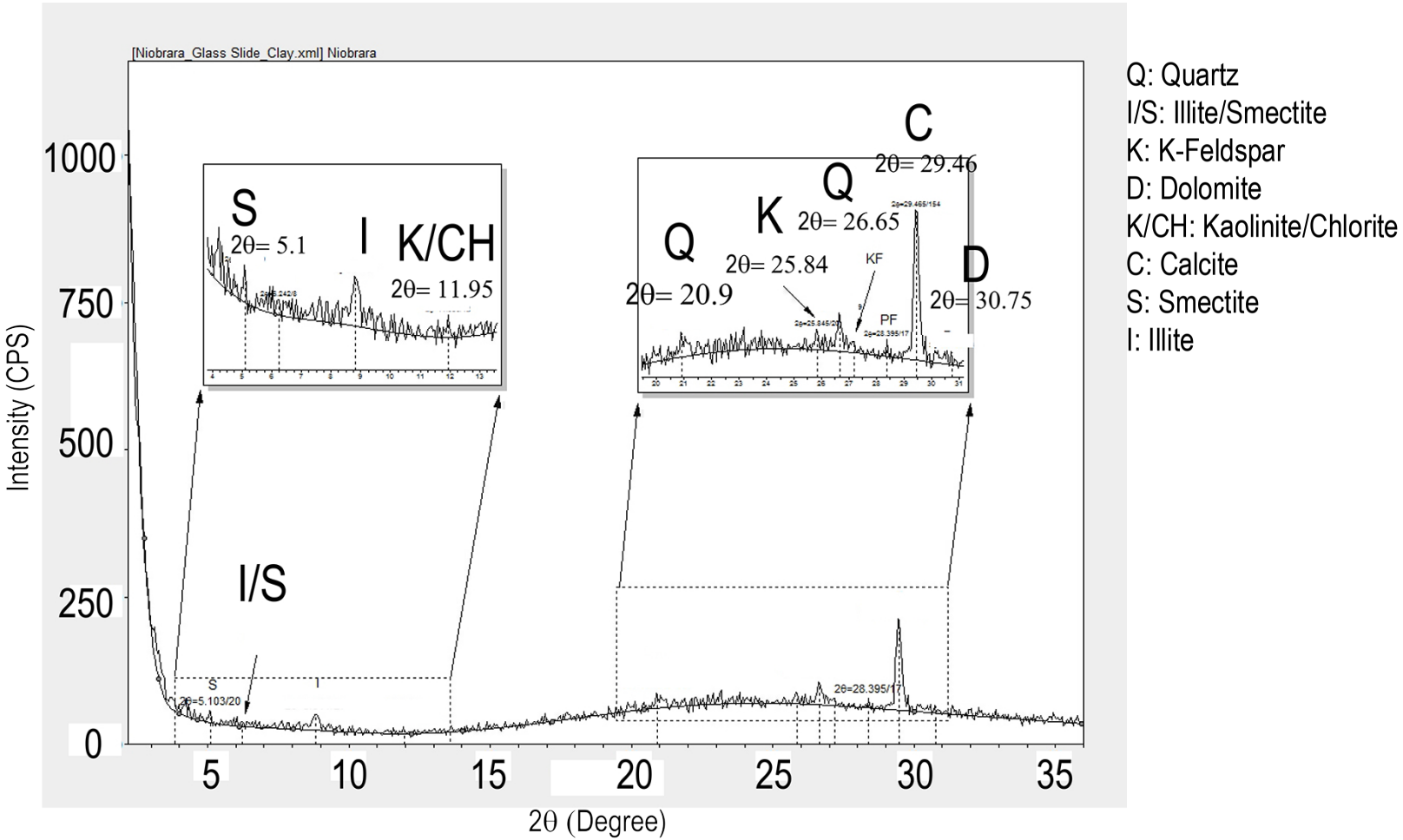

Figure 6.15: X-ray diffraction pattern, 2θ scan from a powder glass sample prepared from Niobrara specimen.

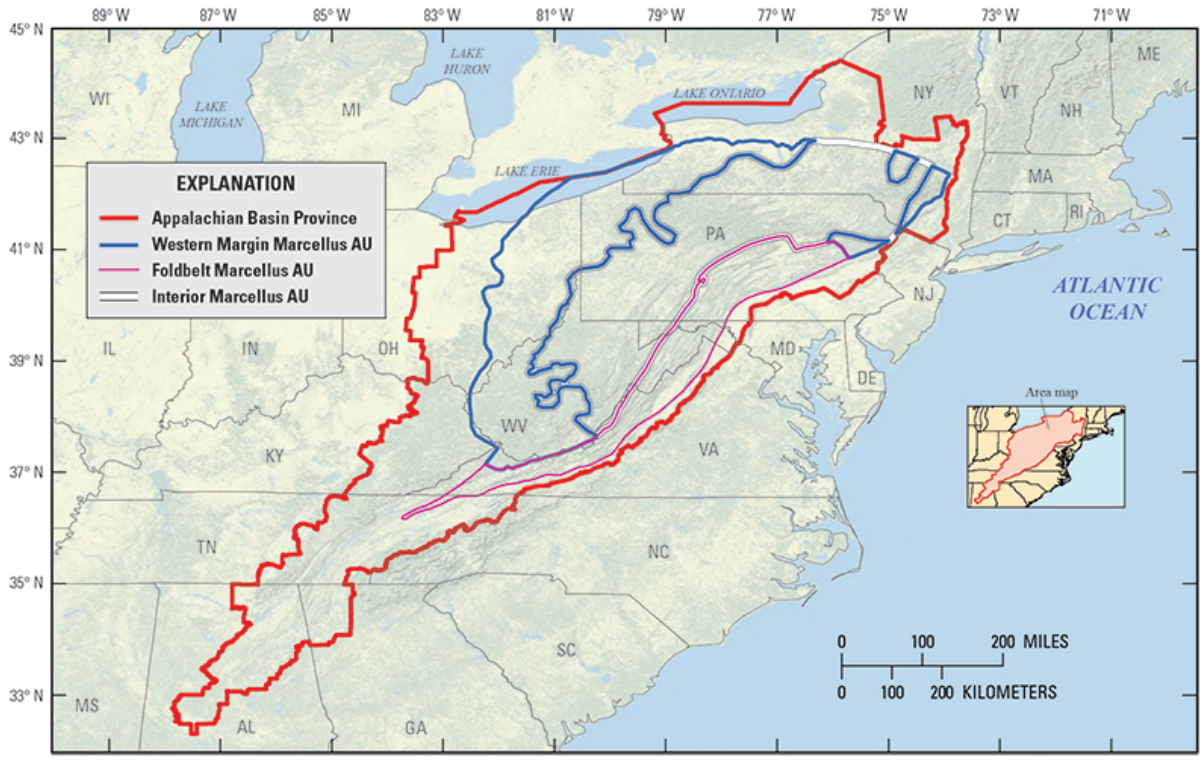

Figure 6.16: Map of the Appalachian Basin Province showing the three Marcellus Shale assessment units. Adopted from [162].

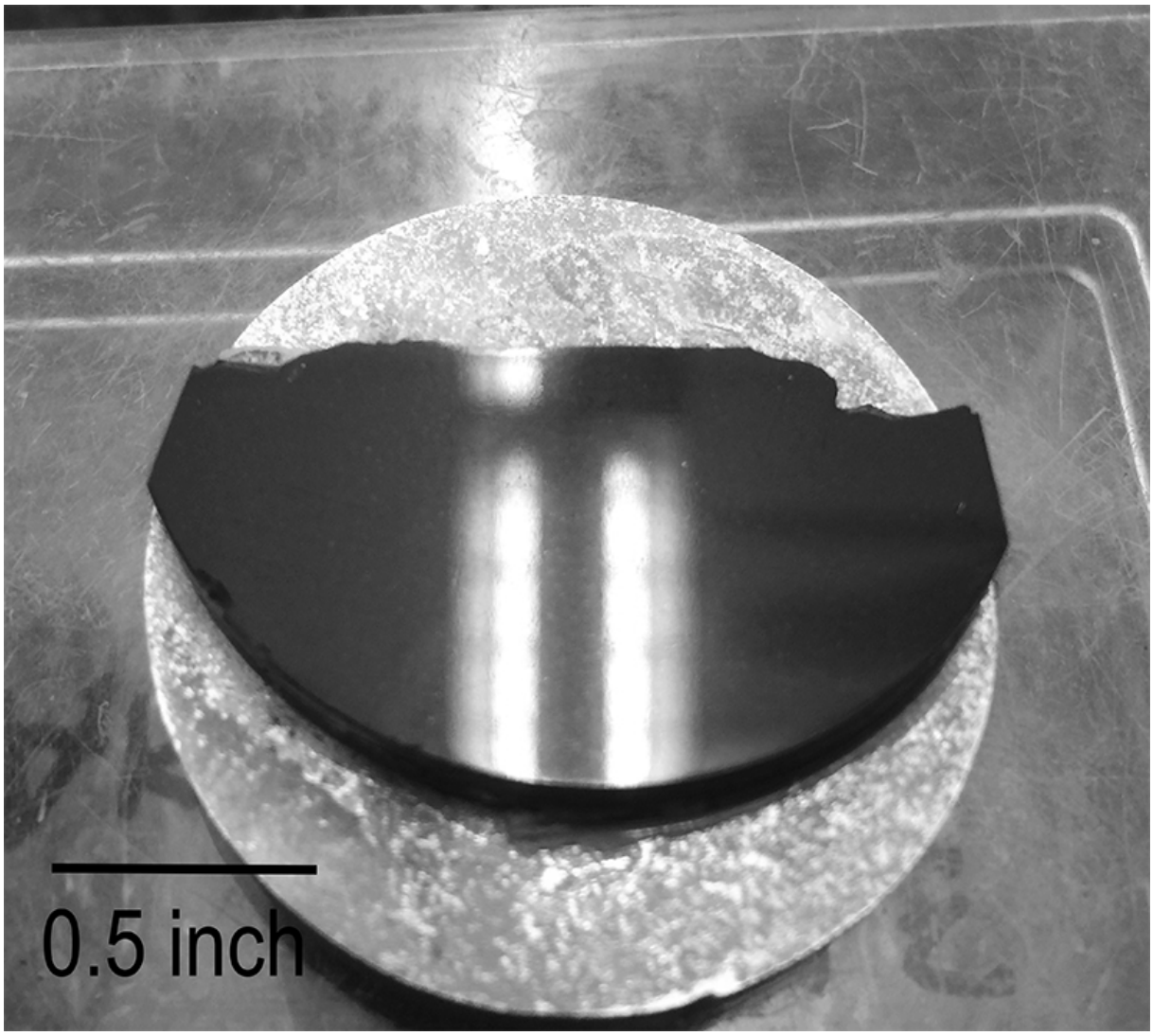

Figure 6.17: Photograph of Marcellus specimen mounted on an aluminum disk. The specimen is reflecting the overhead light after grinding and polishing.

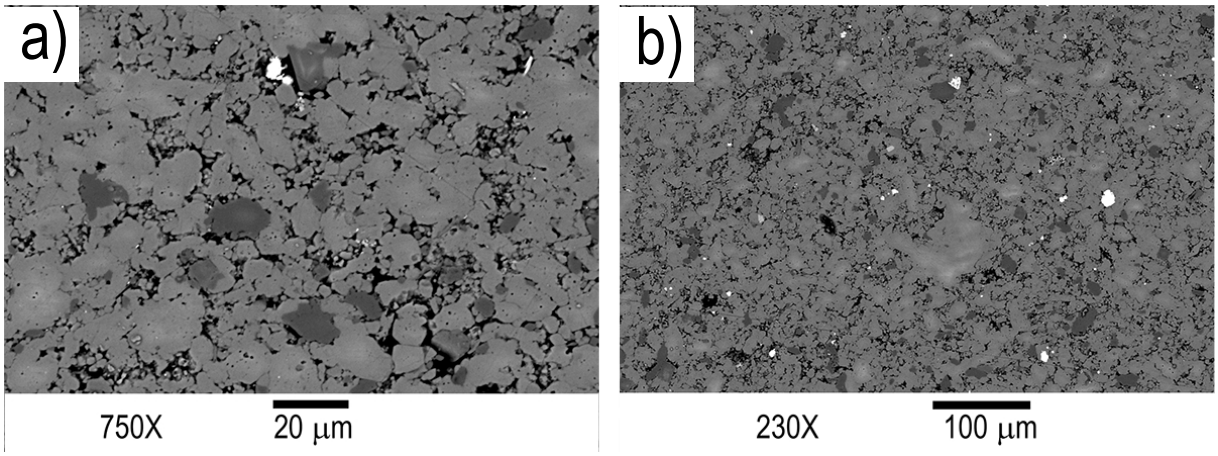

Figure 6.18: Scanning electron microscopy of Marcellus shale: a) Calcite and clay particles are present at 750X magnification , b) Pyrite framboids are present at bright points in the fabric at 230X magnification.

Figure 6.19 demonstrates the structure of the Marcellus shale. This series of scanning electron microscopy images shows the multiscale nature of Marcellus shale. As the magnification of images increase we observe that the fabric will change. Figure 6.19a) shows the grain structure of the specimen which appears to be homogeneous. Furthermore, Figure 6.19b) demonstrate the presence of heterogeneity with presence of tube like structure as well as irregularity on the surface. One more scale down, grains are visible from the structure as well as microporosity in the order of several μm. Finally, Figure 6.19d) demonstrate the presence of clay sheets which inhibit anisotropy because of their orientations. The fabric mostly represent illite clay particles at this scale. This series of scanning electron microscopy images demonstrated the presence of clay particles and different scales of the investigation in the shale studies.

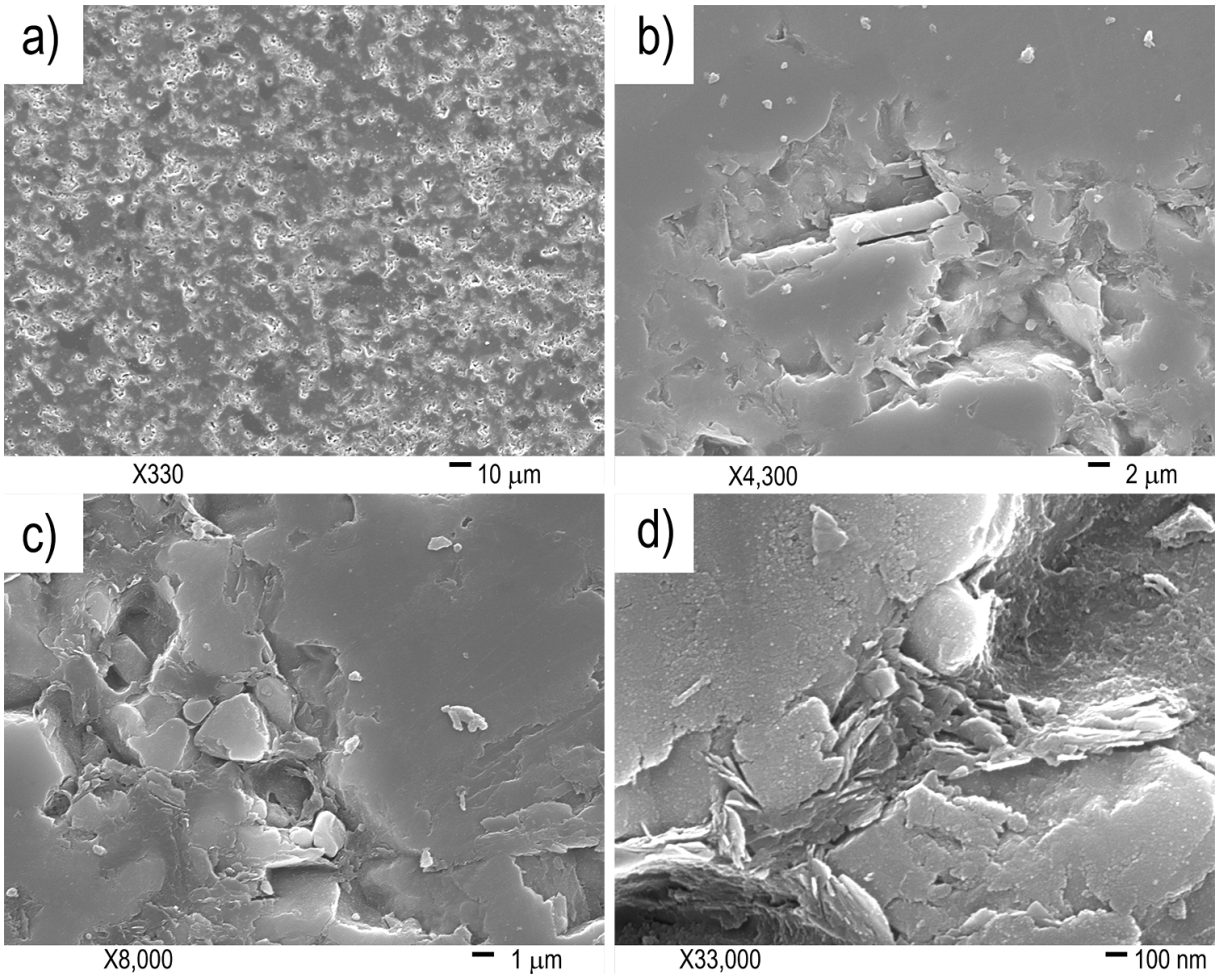

Figure 6.19: Scanning electron microscopy of Marcellus shale: a) porosity is present at 330X magnification, b) needle shape structure of a clay particle is observed at 4,300X magnification, c) calcite constitute a major part of the specimen, d) The illite structure is present at 33,000X magnification.

Finally, Figure 6.20 illustrates the presence of pyrite framboid in the structure of the Marcellus shale. The pyrite inclusion is embedded in the shale fabric. The granular nature of these particles in the fabric of the shale at this scale shows the multiscale structure of shale. Figure 6.20 demonstrate the presence of sheet like material at this scale. This fabric structure demonstrate the presence of layers at the μm scale.

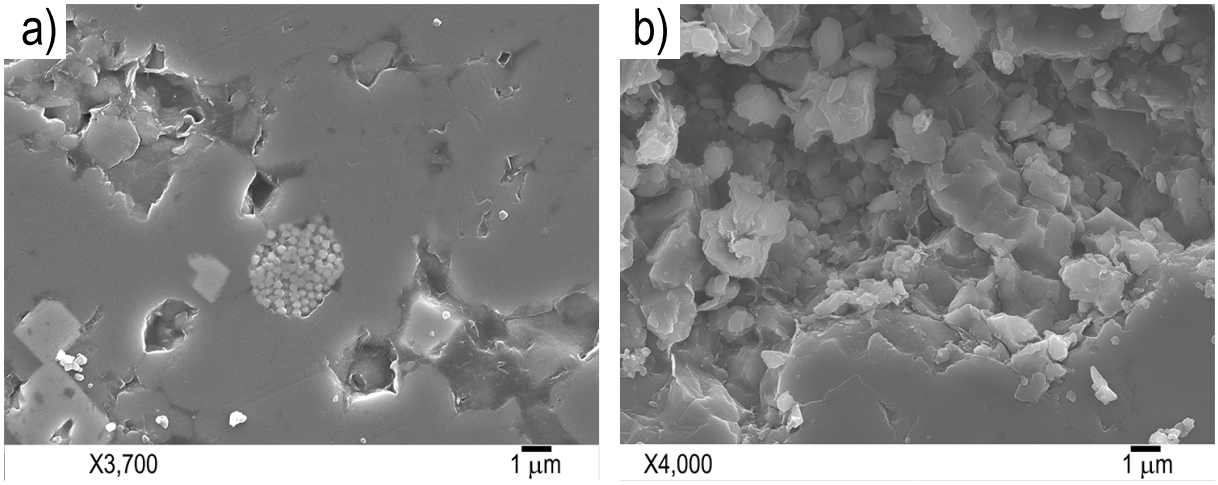

Figure 6.20: Scanning electron microscopy of Marcellus shale: a) Pyrite framboid is present at the fabric of specimen at 3,700X magnification, b) Clay particles present at 4,00X magnification.

Figure 6.21a) demonstrates the surface topography of a 40 μm $\times$ 40 μm for a Marcellus shale in 3D representation. The third dimension shows the depth/height of the asperities on the surface in μm. In addition, Figure 6.21b) illustrates a two dimensional representation of this 40 μm $\times$ 40 μm for the Marcellus shale.

Figure 6.22 demonstrates the XRD diffractogram for the range of 2θ from 0–35°. The XRD scan shows the presence of Calcite, quartz, dolomite, pyrite and illite in this chemical characterization. This information compliments the observations made using scanning electron microscopy.

Table 6.3 summarize different percentages of minerals in Marcellus shale specimens in this study. We observe that Marcellus shale is more calcite dominated in terms of mineralogy. The second highest percentage is quartz followed by siderite.

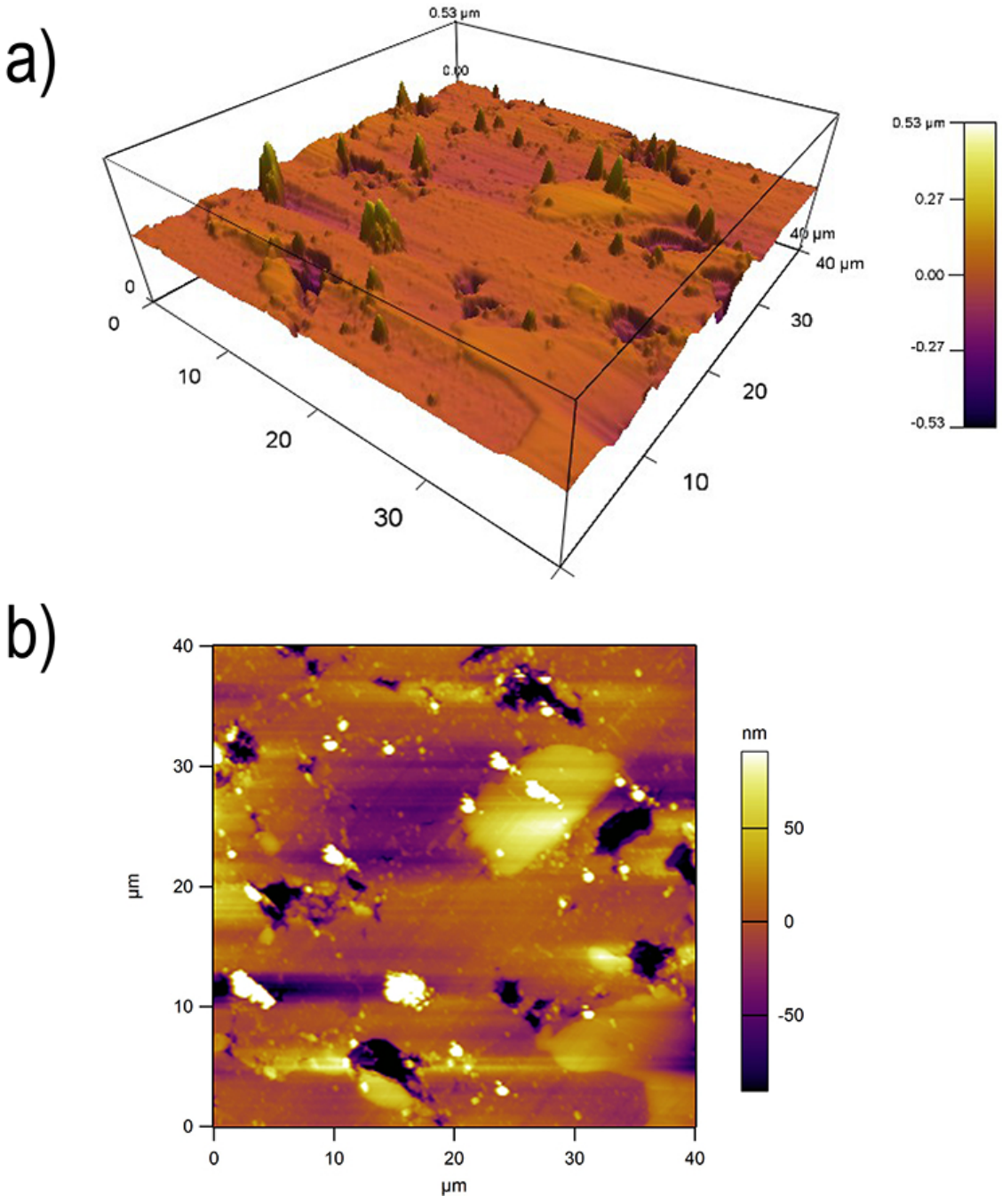

Figure 6.21: Atomic force microscopy of Marcellus specimen after grinding and polishing: a) 3-D image of polished surface, b) 2-D image of polished surface. The average surface roughness is 36 nm.

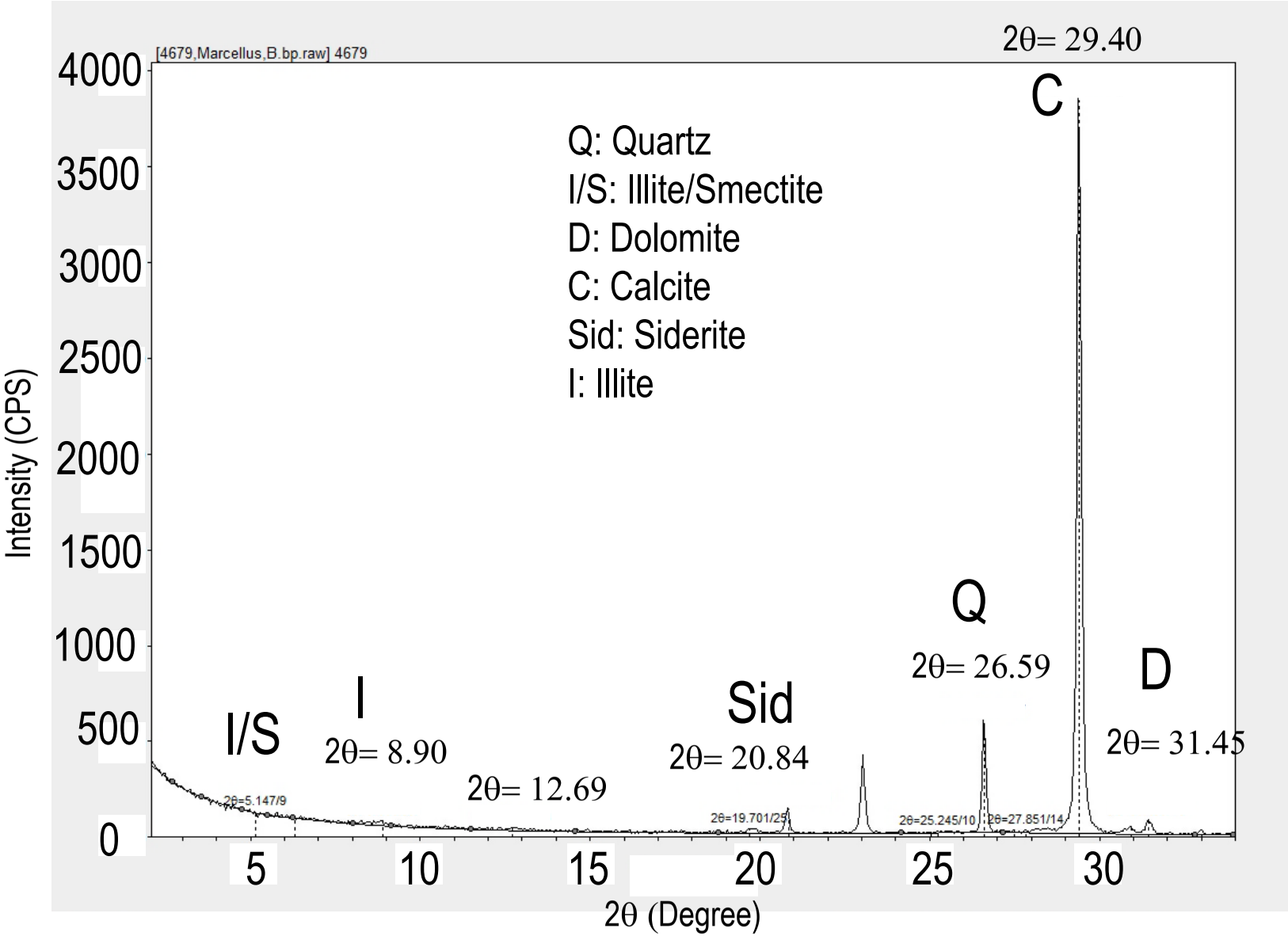

Figure 6.22: X-ray diffraction pattern, 2θ scan from a powder sample prepared from Marcellus specimen.

Table 6.3: Mineral composition in weight percent of Marcellus Shale in this study

Quartz	K-Feldspar	P-Feldspar	Calcite	Dolomite	Siderite	Pyrite	Clay
10.0	1.0	1.0	78.0	1.0	7.0	1.0	1.0

6.5 Conclusion

In this chapter, a comprehensive study of the fabric and mineral composition of the Toarcian, Niobrara and Marcellus shale specimens is presented. The detailed mineral composition of each specimen is presented using a consistent methodology. This comprehensive review of fabric and mineral content place the foundation for understanding the links between the mineralogy, fabric and the mechanical properties. The information presented herein is used in several consecutive chapters of this study.

Chapter 7

Does Mineralogy and Fabric Impact the Elastic Mechanical Response? A Chemo-Mechanical Perspective on Reservoir Heterogeneity

7.1 Introduction

A wide array of methods are commonly used to characterize the elastic properties of shale materials. These methods include uniaxial compressive tests, Brazilian tensile tests, and ultra-pulse velocity measurements. Yet, due to the intrinsically multi-scale nature of shale, the mechanical behavior needs to be explored even at smaller scales: microscopic and nanometer length-scales. Some conventional methods to measure the elasticity of rocks are the Brazilian tensile tests, uniaxial compressive tests, as well as the ultrasonic pulse velocity (UPV) [163]. UPV testing has been reported as a useful reliable nondestructive tool for assessing the mechanical characteristics of concrete material [164, 165] as well as rocks. Another way to measure the mechanical properties is using a P-wave amplitude to obtain the parameters that fully describe the elastic behavior of shale. This method was used to calculate the elastic properties of Marcellus shale [166]. Nano-indentation techniques were used to explore the mechanical properties of multi-scale organic-rich shale at the micrometer and nanometer scales [101]. In this Chapter, a comprehensive review of the material tested as well as the results of this investigation will be presented. The fol-

lowing sections contain nano-indentation testings from Niobrara, Toarcian and Marcellus shale.

7.2 Grid Indentation

As described in section 7.1, there are different ways to characterize the mechanical properties of the gas shale specimens. Herein, we take the approach of characterizing the mechanical properties at microscopic scale. Furthermore, these measurements were employed to estimate macroscopic elastic mechanical properties of the shale materials. Figure 7.1 a) demonstrates the indentation experiments set-up on a shale specimen where the head is sitting on a shale specimen. Figure 7.1 b) demonstrates the residual indentation grid on a gas shale specimen. The residual indent is dependent on the force applied on the specimen.

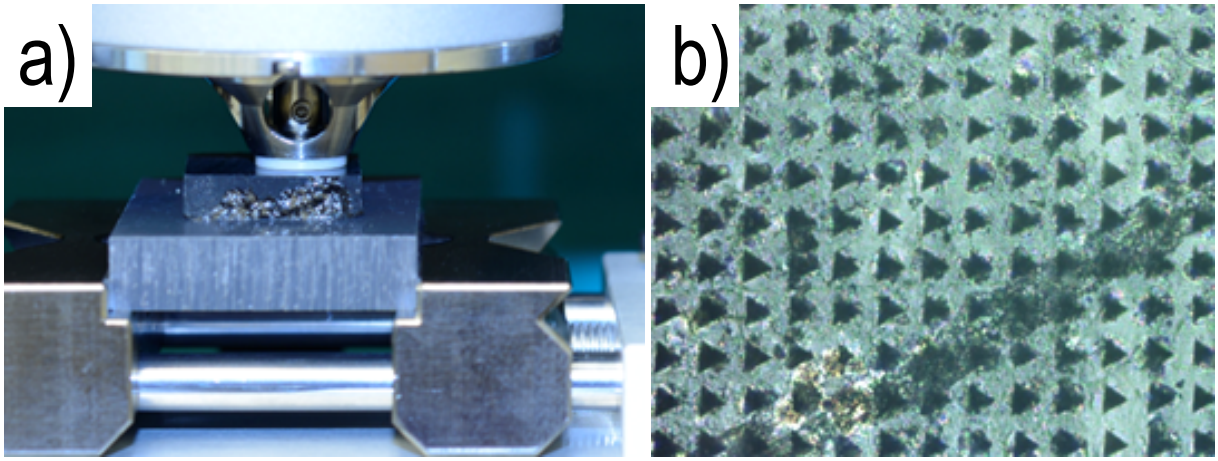

Figure 7.1: a) Indentation experiment on gas shale, digital photography of experimental set-up, b) Optical microscopy image of the residual indentation grid on specimen. Credit: Ange-Therese Akono, UIUC, 2015.

Table 7.1 summarize the grid indentation data carried out in Niobrara, Toarcian and Marcellus shale. The indentation tests are carried out on each of these specimens. The indentation loading scheme consists of loading, holding and unloading part. One of the most important characteristic of loading pattern in an indentation test is the maximum load, P_{max}. The summary of the maximum loads for each specimen is presented in Table 7.1. The load is increased linearly to a maximum P_{max} taking t_L, then hold constant for

t_H and at last decreased linearly to zero at t_U seconds.

Shale systems are consolidated over time and present a preferred direction. Thus, this consolidation will induce some bedding plane in the shale systems. The vertical well logs are extracted in a manner that vertical axis of the log is perpendicular to bedding plane. If the extracted log is cut into pieces and polished then we name them as $\perp$ to bedding. On the other hand if the extracted log is cut and rotated 90 ° and tested we name that $\parallel$ to bedding.

Table 7.1: Summary of Grid nanoindentation tests carried out on Niobrara, Toarcian B1, Toarcian B2, Toarcian B3 and Marcellus.

Material	Orientation	Maximum Load (mN)	Grid Size
Niobrara	$\perp$ to Bedding	100	10 × 10
	$\parallel$ to Bedding	100	10 × 10
Toarcian B1	NA	5, 20, 100	20× 20, 20× 20, 10 × 10
Toarcian B2	NA	5, 100	20× 20, 10× 10
Toarcian B3	NA	5, 100	20× 20, 10× 10
Marcellus	$\perp$ to Bedding	1, 5, 20, 100	20× 20, 20× 20, 20× 20, 10× 10
	$\parallel$ to Bedding	5, 20, 100, 400	20× 20, 20× 20, 20× 20, 10× 10

The deconvolution is performed using a MATLAB script developed in Prof. Akono's lab. The results of the deconvolution technique are estimates of the mean and standard deviation of indentation modulus and hardness for each mechanical phase. The result of deconvolution for a 20 × 20 grid indentation of a Toarcian B1 specimen is shown in Figure 7.2. The load level in the experiment was 5mN with loading time of 10 seconds, 5 seconds of holding and 10 seconds of unloading. The 400 data points yields three distinctive phases with different mean values for indentation modulus and hardness. The theoretical and experimental probability density function of both modulus and hardness are shown in Figure 7.2, with an excellent agreement. To visualize the grid of indentation performed on the specimen a map of indentation hardness or indentation modulus can be made. DeJong et al. [92] used this visualization technique to understand the location of different phases with respect to other phases in cement paste when altered in high temperatures.

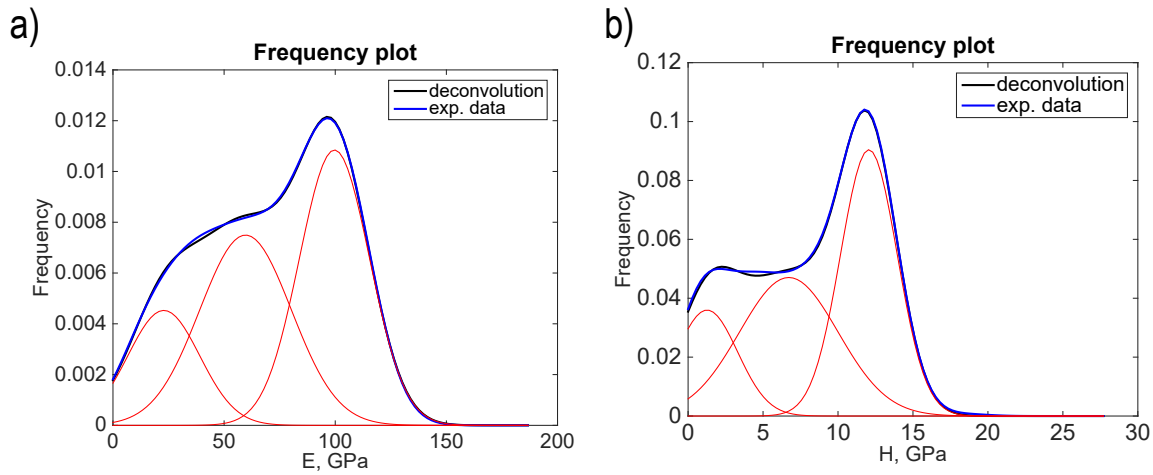

Figure 7.2: Probability density function graphs. a) E, Young's Modulus b) H, Indentation Hardness. Data of a 20 by 20 grid indentation experiment for Toarcian B1 specimen with spacing of 20 μm.

The result of the deconvolution algorithm is presented in Table 7.2. The 3 phases presented in this deconvolution can be assigned to different phases by comparing the values of the Young's modulus estimates for the micro-constituents of organic-rich shale (clay, quartz/feldspar and organic matter) that are shown in Table 7.2. For instance, the Young's modulus of Phase 3, 90.6 GPa, is in the range of values expected for quartz. Therefore, it is reasonable to assume that Phase 3 represents quartz. Estimates of the Young's modulus for kerogen/organic matter are in the range 7–16 GPa, slightly lower than the value for Phase 1, 20.43 GPa. One explanation is that Phase 1 is a composite phase made up of clay, air voids and organic matter. Finally, the remaining phase can be interpreted as the clay phase in the material, based on the estimated value of the modulus. Thus, statistical nano-indentation enables us to identify the micro-constituents of organic-rich shale. Furthermore, our findings agree with scanning electron microscopy observations and X-ray diffraction analysis.

Table 7.2: Mean values and standard deviation for elastic mechanical properties of different phases from grid indentation of Toarcian B1 specimen.μ is the mean value. σ is the standard deviation value. E is the Young's modulus. H is the indentation hardness

Phase	μ_E (GPa)	σ_E (GPa)	μ_H (GPa)	σ_H (GPa)	Volume Fraction (%)
1	20.43	5.02	2.04	0.21	7
2	60.68	12.92	4.3	0.44	45
3	90.60	10.61	9.4	0.29	48

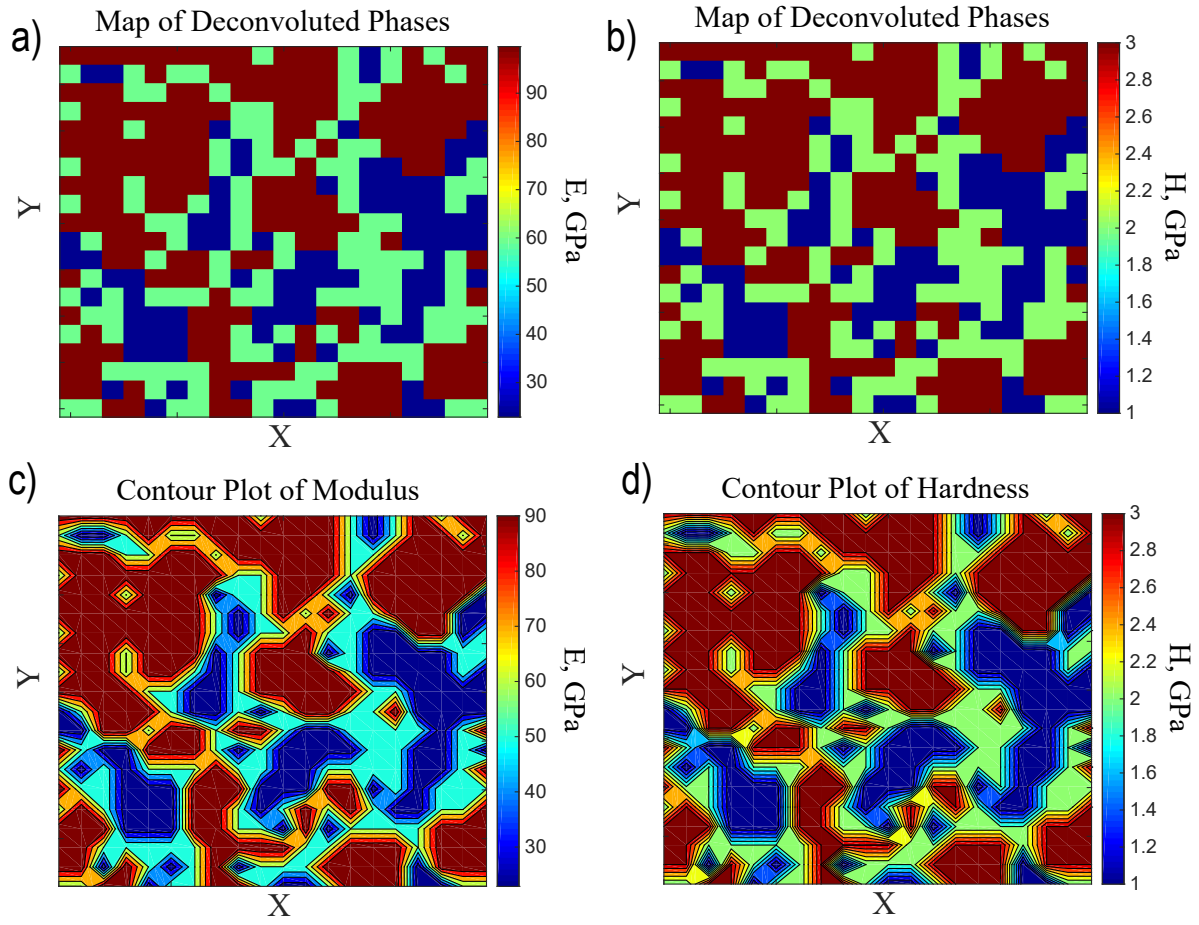

Figure 7.3: a) Discrete Map of different phases for indentation a) modulus and b) hardness. c) Contour plot of indentation c) modulus and d) hardness. Data of a 20 by 20 grid indentation experiment for Toarcian B1 specimen with spacing of 20 μm. The continuous map is made by linearly interpolating the discrete data over the whole surface. The script was developed in Prof. Akono's lab.

The maps created in Figure 7.3 are the results of deconvolution technique plotted based on their X and Y position in the grid. As discussed earlier the three-phase material can be observed in Figure 7.3, while each phase corresponding to a distinct mechanical phase. The mechanical map can be overlapped with the microstructural observation obtained from optical microscopy to obtain useful information regarding microstructure. Also a continuous map of mechanical properties can be made to have a continuous mechanical map as opposed to a discrete map. The continuous map is constructed by averaging neighboring points, either indentation modulus or indentation hardness while the spacing from the points was chosen in the experiment, based on the load level, indentation depth and characteristic size of different features in material.

7.3 Elastic Response via Nano-Indentation: A Micromechanics Scheme

Having connected the mechanical response to constituents at the nanometer length-scale, the last step is to bridge scales 4 to 7 and predict the macroscopic behavior. Herein, we apply micromechanics theory to estimate the mechanical properties of the shale material at the macroscopic scale with the use of the information gained from nano-indentation results. Budiansky [167] developed a model to determine the elastic moduli of a composite material made of with several constituents which are isotropic and elastic. The model is intended to apply to a heterogeneous materials composed of contiguous, spherical grains of each phase.

The model is developed by defining the effective shear modulus, G^*, of the composite material in terms of a uniform macroscopic shear applied to the boundary and the average shear strain of the material as described in Equation 7.1.

$$G^* = \frac{\tau_0}{\overline{\gamma}} \tag{7.1}$$

Then with the use of the Hill's Lemma [168] the elastic strain energy can be described as Equation 7.2.

$$U = \frac{1}{2}\int_V \tau_0 \gamma_{xy} dV = \frac{V(\tau_0)^2}{2G^*} \tag{7.2}$$

where V is the volume of the material being considered. γ_{xy} is the shear strain of the

material. However, the equation for the elastic strain energy, U, can be written in terms of individual constituent phases as Equation 7.3. G_N is the shear modulus of the Nth phase. n is the number of phases considered for the composite material.

$$U = \frac{1}{2}\int_V \frac{\tau_0 \tau_{xy}}{G_N} + \frac{1}{2}\int_V \tau_0(\gamma_{xy} - \frac{\tau_{xy}}{G_N})dV = \frac{V(\tau_0)^2}{2}\left[\frac{1}{G_N} + \sum_{i=1}^{n} c_i(1 - \frac{G_i}{G_N})(\frac{\overline{\gamma}_i}{\tau_0})\right] \quad (7.3)$$

where c_i is defined as the volume fraction of each phase. Solving for the composite shear modulus yields Equation 7.4.

$$\frac{1}{G^*} = \frac{1}{G_N} + \sum_{i=1}^{n} c_i(1 - \frac{G_i}{G_N})(\frac{\overline{\gamma}_i}{\tau_0}) \quad (7.4)$$

The next step is to assume a strain concentrations around spherical inclusion, which is obtained from Eshelby's inclusion derivations [169]. The final implicit expression of effective shear modulus can be obtained by use of Equation 7.5 and Equation 7.6.

$$\frac{1}{G^*} = \frac{1}{G_N} + \sum_{i=1}^{N-1}(1 - \frac{G_i}{G_N}\frac{c_i}{G^* + \beta^*(G_i - G^*)}) \quad (7.5)$$

$$\beta^* = \frac{2(4 - 5\nu^*)}{15(1 - \nu^*)} \quad (7.6)$$

where ν^* is the composite Poisson's ratio. Following the same derivation the bulk modulus is derived and presented in Equation 7.7 and Equation 7.8.

$$\frac{1}{K^*} = \frac{1}{K_N} + \sum_{i=1}^{N-1}(1 - \frac{K_i}{K_N})\frac{c_i}{K^* + \alpha^*(K_i - K^*)} \quad (7.7)$$

$$\alpha^* = \frac{1 + \nu^*}{3(1 - \nu^*)} \quad (7.8)$$

The composite Poisson's ratio, ν^*, can be found from equation 7.9 using elastic theory.

$$\nu^* = \frac{3K^* - 2G^*}{6K^* + 2G^*} \quad (7.9)$$

An insight to the shale material and its composition will help the modeling scheme presented herein. Organic-rich shale material consists of clay minerals, quartz inclusions, feldspar inclusions and an organic phase. The clay minerals are mostly kaolinite, il-

lite, smectite/illite, montmorillonite, muscovite and Chlorite. The inclusions are mostly quartz, pyrite, feldspar and calcite. Table 7.3 shows some literature values for the elastic modulus of these primary constituents. The deformation and fracture properties of shale depend on the mechanical properties of its basic constituents. This suggests that an understanding of the overall macroscopic mechanical properties of shale can be obtained by studying the deformation and properties of these constituents and how they upscale to the overall behavior of the composite material [170].

Table 7.3: Reported Young's modulus values of shale constituents.

Material	E (GPa)	Source
Kaolinite	30.3	[171]
Illite	73.9–84.3	[172]
Smectite/Illite	51.5	[172]
Montmorillonite	44.7–85.5	[172]
Muscovite	118.1	[173]
Chlorite	82.2-214	[172]
Pyrite	264–330	[174]
Quartz	80-100	[175]
Organic phase/Kerogen	7–16	[176]

The macroscopic elastic properties are calculated using statistical indentation data. The predicted macroscopic elastic properties are then compared to the literature value for comparison. The homogenization approach based on the Budiansky's model was implemented in an implicit algorithm written using Matlab. The theoretical model predicts a macroscopic elastic modulus of shale material of 24 GPa. This theoretical value is in the range of the values of elastic modulus reported for gas shale materials and measured using macroscopic scale testing techniques.

7.4 Mechanical Modeling: Reservoir Heterogeneity

The results of the previous section is used to calibrate a model based on the mineralogy of cores from wells. Mostly, the mineralogy of logs are obtained and recorded in reservoir characterization. The mineralogy data of wells are recorded in foot/inch spacings, where this can present with an accurate map of mineral composition of the fractured rock. Thus, development of an empirical or analytical solution between mineralogy and elastic response can yield helpful information regarding the reservoir mechanical response. Furthermore, this information can be implemented into a reservoir model with consideration of elastic

heterogeneity. The hydraulic fracture reservoir modeling are performed with assumption of elastic, isotropic material behavior. This is a step forward in considering a realistic 3D model for reservoir mechanical behavior. The limitations of this approach is that one has to calibrate the model for the specific gas play first due to the fact that fabric plays an important role as well as mineralogy in these investigations. Fabric of organic-rich shales are important characteristic of each reservoir.

7.5 Conclusion

In this chapter, a theoretical-experimental framework is provided for the microstructural and mechanical characterization of organic-rich shale at the nanometer and micrometer length scales. The starting point is to recognize the hierarchical nature of shale which calls for a thought model. Although organic-rich shale is composed of several basic elements, quartz/feldspar, gaseous kerogen, clay and air voids, the exact composition and the local arrangement depends on the scale of observation. In turn this has strong influence on the mechanical performance as expressed in terms of elasticity, strength and/or fracture properties. Accurate and precise small scale characterization relies on a rigorous material preparation technique. However, the exact sequence of steps must be tailored to each specific material. As mentioned earlier nano-indentation consists of pushing a hard pyramidal probe into a soft material and it is an accurate means to measure the elastic-plastic properties at the nanometer length-scale. Moreover, the grid indentation technique makes it possible to draw a compositional map based on the values of the indentation modulus and hardness. Applying statistical deconvolution methods to a large array of indentation tests enables one to decompose the response and identify the primary constituents of the materials. Micromechanics hold the key to a bottom-up approach where the behavior at the larger scale is predicted from the composition and microstructure at a smaller scale. The predicted macroscopic stiffness values agree with macroscopic measurements reported in the scientific literature. Thus, a demonstration of the power of nano-mechanics and micromechanics is utilized to shed light on the origin of the mechanical performance of gas shale by bridging the nanometer and macroscopic length scales. This an important development that will pave the way towards optimum hydraulic plant schemes for energy-harvesting from unconventional reservoirs.

Chapter 8

Multi-scale Nature of Fracture Processes in Organic Rich-Shale: Toughening Mechanisms

8.1 Introduction

In recent years, gas shale has gripped the attention of the scientific community. This is primarily due to the relevance of the material in energy harvesting applications such as hydrocarbon recovery from unconventional reservoirs, carbon dioxide geological sequestration in depleted reservoirs or nuclear waste storage. Over the last ten years, the natural shale gas share has grown exponentially, radically transforming the United States energy outlook. In 2011, the natural gas shale production represented 34% of the total production compared to 1% in 2000 [1, 2]. Shale gas is expected to rise to 67% of the overall production by 2035, generating lower natural gas prices and electricity prices [3]. The development of shale gas resources will also generate significant economic value as well as over 1.6 million jobs over the next 20 years [2]. This economic expansion will be supported by breakthroughs in the science and technology of shale gas extraction [1].

Organic-rich shale also called black shale, unconventional shale or gas shale is an impermeable source rock as opposed to conventional reservoir rock which is porous and permeable. This leads to a major challenge as a massive fracturing of the subsurface is needed to extract gas. Natural gas harvesting from low permeability shale is a complex operation that spans multiple length-scales. Directional drilling and hydraulic fracturing

are two major technologies essential to this process. Directional drilling consists in digging a vertical well in the rock source at a depth of 5,000–20,000 feet below the surface [177]. Next, laterals extending from 1,000–10,000 feet are drilled horizontally so as to access a wider portion of the subsurface [19, 178]. Meanwhile, hydraulic fracturing consists in injecting a mix of water, sand and chemical at a high pressure so as to propagate cracks in the source rock and thus release the trapped hydrocarbons. A major technological challenge is overcoming the rock fracture resistance and keeping the cracks open so as to obtain a dense and well-connected network of fractures. In order to address those technological challenges, it is important to get a fundamental understanding of fracture mechanisms and properties in gas shale. In turn, the insight gathered will extend to the broader realm of efficient energy-based operations such as carbon dioxide geological storage in depleted wells and nuclear waste storage. It will also fuel and accelerate the discovery of advanced composites structural materials with enhanced performance.

Although many investigations have focused on the assessment of the elastic-plastic properties of gas shale, the characterization of its fracture properties has not been fully explored. A major limitation is that most studies have been confined to the macroscopic sphere despite the fact that fracture is intrinsically a multi-scale phenomenon. Abousleiman and coworkers (Sierra *et al.*) [179] carried out Chevron notched semi-circular bend tests on 5-cm wide cylindrical cores of Woodford Shale. The recorded values of the fracture toughness ranged from 0.74 to 1.7 MPa$\sqrt{\text{m}}$ with the Upper Woodford shale exhibiting a fracture toughness much higher than that of the Lower Upper Shale. Chandler et al. [180] defined three orientations to capture the anisotropy of the fracture response. In the short-transverse configuration, the fracture surface lies in the bedding plane. In the arrester configuration, the crack propagates in a direction perpendicular to the bedding plane, whereas in the divider configuration, the crack propagates parallel to the bedding plane. Chandler and coworkers carried out short rod fracture toughness measurements on Mancos shale: the fracture toughness was found to be higher in the divider orientation than in the short-transverse and arrester ones.

At the microscopic scale, very few methods have been proposed to assess the fracture properties. Recently, Recently Liu [181] suggested the use of nano-indentation-based methods [182]. For instance, they carried out nano-indentation tests on Antrim shale using a sharp cube-corner tip so as to induce crack propagation [183]. Later, scanning electron microscopy and digital image analysis was employed to measured the crack length and correlate it to the fracture toughness. However, indentation-based methods tend to

yield qualitative results due to the need to measure the crack length using optical imaging methods. This can be very challenging especially for opaque materials such as shale and it can leads to a great level of inaccuracy and subjectivity.

We recall here the multi-scale thought model for shale developed by Ulm *et al.* to describe the different scales and constituents of organic-rich shale. The level 0 at the scale of nanometers is the level of elementary clay particles connected to a units of gaseous kerogen. At the level 1, 100 nm- 1 μm, there is a porous clay fabric made of clay minerals, pores and organic matter. At the level 2, 10 μm- 100 μm, exists a composite made of quartz and carbonate inclusions embedded in the porous clay fabric. Finally, level III is the macroscopic scale, mm-cm, where the solid exists as a layered composite. The bulk of unconventional shale fracture characterization has focused on the macroscopic sale. In this study, we explore level 1 and level 2 and investigate fracture at these length-scales.

Therefore, the objective of this work is to present a novel method to assess the fracture toughness and the fracture energy of organic-rich shale at the microscopic scale by integrating scratch testing and nano-indentation. In particular, we seek to capture the complexity of this material in terms of heterogeneity and anisotropy. We illustrate the method on three unconventional shale systems: Niobrara and Marcellus as well as Toarcian shale materials. This paper is organized as follows. First, we introduce the shale systems considered: we detail the specimen preparation procedure; then, we apply advanced imaging techniques including optical microscopy, scanning electron microscopy and x-ray diffraction analysis to observe the structural arrangement at small scales. Next, we present the micro-indentation tests; we also formulate a fracture mechanics framework that takes into account the transverse isotropic behavior of shale materials. Finally, we implement our method so as to measure the fracture properties and investigate the fracture mechanisms.

8.1.1 Grinding and Polishing Procedure

The nature of the surface plays an important role during microscopic examination and determine the accuracy of the small-scale mechanical characterization. Therefore, the objective of the preparation routine is to achieve a high quality polished surface characterized by a minimum amount of scratches, pitting and relief. This is a challenge for organic-rich shale because of the presence of both extremely hard and very soft (organic)

phases. A balance must be achieved between removing scratches and pits on hard grains while limiting the amount of intergranular relief [184]. In this endeavor, we adapted standard methods devised for cementitious and shale materials [185].

Prior to polishing, flat and thin slices of material were precisely cut using a low speed diamond saw. Afterward, the resulting 7-mm thick sections were mounted on a steel disk using a cyanoacrylate adhesive. In this study the Ecomet 250/ Ecomet 300 (Buehler, Lake Bluff, IL) provided optimum conditions in terms of time, convenience and degree of polish. This is a versatile semi-automated polished that can hold up to six specimens. As the base rotates samples on a flat platen, the power head applies an equal force, individually to each specimen. The different variables that can be controlled by the operator are: choice of polishing cloth, amount and type of abrasive, amount and type of lubricant, wheel speed and level of pressure.

The generic grinding and polishing procedure selected is described here. Grinding was carried out using a resin-bonded aluminum oxide pad. Three different grit sizes were employed for 2 minutes each: 240, 400 and 600, in consecutive order. Between each grit size, the specimen was cleansed by ultrasonic action in N-decane bath, to prevent contamination. Afterward, polishing was performed where both Texmet® and Trident® polishing pads were used in combination with micron-size polycrystalline diamond particles in suspension in oil-based solutions. For coarse polishing, 9 μm particles were used, whereas for fine polishing, we used consecutively 3 μm, 1 μm and 0.25 μm abrasives.

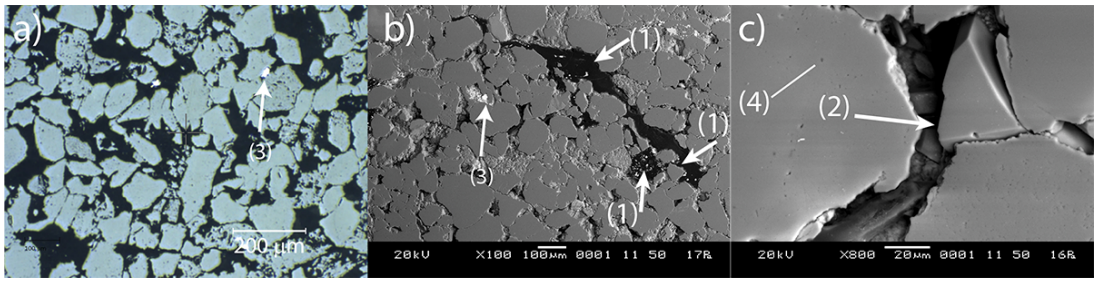

Figure 8.1: Optical and scanning electron microscopy for Toarcian shale. Several microstructural features can be observed: 1) pockets of gaseous kerogen, 2) interparticle pores, 3) quartz inclusions and 4) intraparticle pores.

The mineral composition of the specimens are reported in previous chapters. Where Toarcian is a quartz rich specimen. Niobrara is a calcite rich specimen. The fabric and the structure of the specimens are different.

Three gas shale materials were studied in this investigation. The Toarcian shale spec-

imens were provided by Total S. A. (Paris, France), a major oil & gas stakeholder in France. The Toarcian shale is a major organic-rich formation from the Paris Basin in France [3, 186]; in particular, the samples were extracted at a depth of 5000 meters below the earth surface.

Figure 8.1 displays digital photography, optical and scanning electron microscopy images of the Toarcian shale system. The optical microscopy observation was carried out with a Nikon microscope at magnification levels ranging from 20X to 100X. Meanwhile, both a JEOL 6060 LV and a JEOL 7000 LV scanning electron microscopes with a back-scattered electron detector were employed to visualize the microstructure after grinding and polishing. On both the optical microscopy and sem images, we can see a granular microstructure. The grain size ranges from 30 μm to 100 μm. In addition, there are (3) quartz inclusions in white. (2) Organic matter is visible on Figure 8.1 b) as a dark pocket. Moreover, Figure 8.4 reveals the presence of micropores in grains, 2.5-5 μm large, and micropores at the grain boundaries, 10-30 μm large.

Gas shale is a complex multi-scale composite material with a two-scale porosity [187]. We observed micron-sized pores within and between grains for our specimens. In addition, we expect the presence of nanometer-sized pores due to the small sizes of the clay minerals that are part of the chemical constitution. For instance, illite particles are typically 10-nm big whereas kaolinite particles are 1-micron in diameter and 0.1-micron thick [188]. Furthermore, Obrien and Slatt [189] carried out SEM and field emission scanning electron microscopy (FESEM) on Barnett and Woodford shale that revealed the presence of nanopores as well as clay floccules arranged in a house-of-card fashion. They reported several kinds of nanometer-sized pores: voids between clay flakes, between pyrite crystals, within the organic matter and finally voids that result from the dissolution of micro-organisms.

Table 9.2 lists the values of the Young's modulus and Poisson's ratio that were reported for the shale specimens considered. The elastic constants were characterized via mini-compression tests as well as ultrasonic pulse velocity tests. Because of the geological process of layer deposition that is at the origin of the rock formation, the mechanical behavior is generally assumed to be transversely isotropic with the axis of symmetry $\underline{e}_3$ being perpendicular to the bedding plane $(\underline{e}_1, \underline{e}_2)$. Figure 8.2 shows the orientation of the cylindrical specimens tested so as to measure the Young's modulus and Poisson's ratios in the bedding plane, E_1 and ν_{12}, and perpendicular to the bedding plane, E_3 and ν_{31}. For all three material, the elastic constant parallel to the bedding plane, E_1, is much higher

in the elastic constant perpendicular to the bedding plane, E_3.

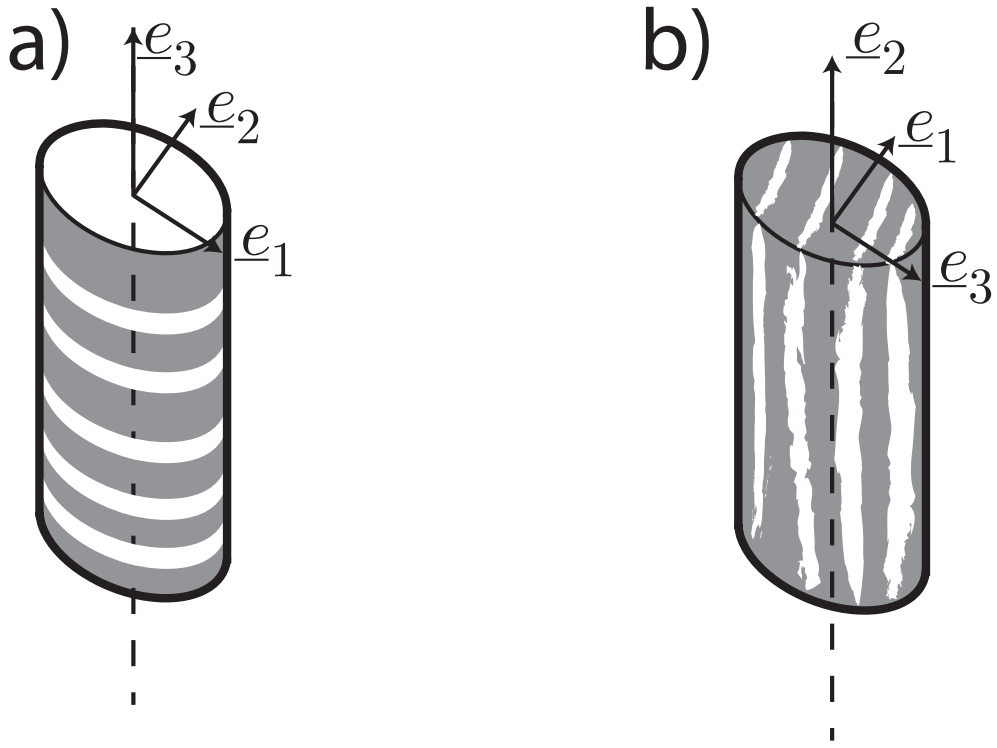

Figure 8.2: Elastic characterization of gas shale: specimen orientation for mini-compression and ultrasonic pulse velocity tests. a) specimen machined parallel to the axis of symmetry e_3. b) Transverse specimen cut perpendicular to the bedding plane (e_1, e_2). Courtesy of Prof. Akono.

Table 8.1: Elastic-plastic constant of organic-rich shale materials. E_3 is the Young's modulus measured along the solid's axis of symmetry; meanwhile E_1 is the modulus perpendicular to the solid's axis of symmetry. * Results from mini-compression tests; data courtesy of Total S. A., France. ** Results from [190]. *** Results from [142].

Material	E_1 (GPa)	E_3 (GPa)	ν_{12}	ν_{31}
Toarcian	23.5	17.3	0.2	0.22
Niobrara **	34.2	24.8	0.26	0.34
Marcellus ***	40	20	0.18	0.26

In this study, we employ microscopic scratch testing, which is a cutting-edge technique commonly used for quality control of thin films and coatings [109, 191, 192], in order to characterize the fracture properties. In our experiments, a sphero-conical stylus is drawn

across the surface of the sample under a linearly increasing vertical load as shown in Figure 8.4 a). The test is performed on an Anton Paar testing platform (Anton Paar, Ashland VA). The vertical force is prescribed via a piezo-actuated active force feedback loop so that any potential tilt of the specimen top surface has little influence on the vertical force history. A motorized XYZ stage as well as high-accuracy force and depth sensors record the specimen mechanical response. The resolution on the prescribed vertical force and on the measured horizontal force is 1 mN whereas the resolution on the measured penetration depth is 3 nm. In addition, an acoustic emission sensor keeps track of stress-induced damage events. Finally, an optical microscopy is integrated with the scratch routine so as to capture a panorama of the resulting groove immediately after scratch testing as shown on Figure 8.5 d).

Our starting point is the scratch fracture mechanics model that we developed in [112, 114–116] for linear elastic isotropic materials. Optical microscopy and scanning electron microscopy were employed to observed the residual groove after scratch testing. In particular, for tests on ceramics, metals and polymers [116], we observed a succession of curved cracks regularly spaced and perpendicular to the scratch direction. Based on these observations, in the theoretical model we focus on a single fracture event in which a horizontal crack emanates from the tip of the stylus below the surface and propagates horizontally thereafter. We employ an Airy stress function to evaluate the stress and strain fields ahead of the probe and then use a path-independent contour integral [113], the J-integral, to calculate the energy release rate $\mathcal{G}$ as a function of the scratch forces and scratch probe geometry. Under plane strain conditions, $\mathcal{G}$ can be expressed as:

$$\mathcal{G} = \frac{1-\nu^2}{E}\frac{F_T^2}{2pA} \tag{8.1}$$

where E and ν are respectively the Young's modulus and Poisson's ratio of the shale specimen. F_T is the measured horizontal force, p is the perimeter of the fracture surface whereas A is the value of load-bearing contact area as projected in the horizontal direction. To mark the onset of cracking, we utilize a threshold criterion applied to the energy release rate: crack propagation occurs once $\mathcal{G} = \mathcal{G}_f$, where the threshold value is the fracture energy $\mathcal{G}_f$, assumed to be a material constant. Equation 8.1 enables to connect the

fracture energy to the scratch toughness K_s, which is defined as:

$$K_s = \frac{F_T}{\sqrt{2pA\,(d)}} \tag{8.2}$$

The quantity $2pA$ is the shape probe function and its depends on the stylus geometry as well as the penetration depth d. The expression of $2pA$ was derived for different scratch probe geometries: flat punch, sphere, cone or sphero-conical. In particular, in our tests we will use the conical approximation; for a conical probe of half-apex angle θ, we have: $2pA = 4\tan\theta/\cos\theta\, d^3$. The shape probe function is calibrated prior to testing using a reference material of known fracture energy. The resulting function is then used as an input to measure the scratch toughness, $K_s = F_T/\sqrt{2pA}$.

Figure 8.3 illustrates the scratch probe and the crack in front of the probe as the scratch progress. The crack is a semi-circular crack in front of the tip of the scratch testing. This figure illustrates the crack opening and the location of this opening in 3D schematic.

Scratch testing induces a mixed mode fracture. Numerical simulations were carried out in Abaqus [116] considering a scratch test with a prism with varying back-rake angle θ. The mode mixity angle $\tan\gamma = K_{II}/K_I$ was found to increase with the back rake angle θ. Furthermore, Equation 8.1, based on the J-integral method, provided an accurate estimate of the energy release rate. Next, we define the vector $\underline{K} = \{K_I, K_{II}\}^T$. For elastic isotropic solids in plane strain conditions, the Griffith-Irwin relation [193, 194] yields $\mathcal{G}_f = (1-\nu^2)/E\,|\underline{K}|^2$, where $|\cdot|$ is the euclidean norm operator defined by: $|\underline{x}| = \sqrt{x_1^2 + x_2^2}$. Thus, our fracture criterion becomes $|\underline{K}| \leq K_c$, where K_c is the fracture toughness given by: $K_c = \sqrt{E\mathcal{G}_f/(1-\nu^2)}$. Therefore, for linear elastic isotropic materials and in the fractured-driven regime, the fracture toughness is equal to the scratch toughness shown in Equation 8.3.

$$K_s\,(F_T, d) = K_c \tag{8.3}$$

The question remains how to extend the model presented above to anisotropic materials. This is the focus of the next paragraph.

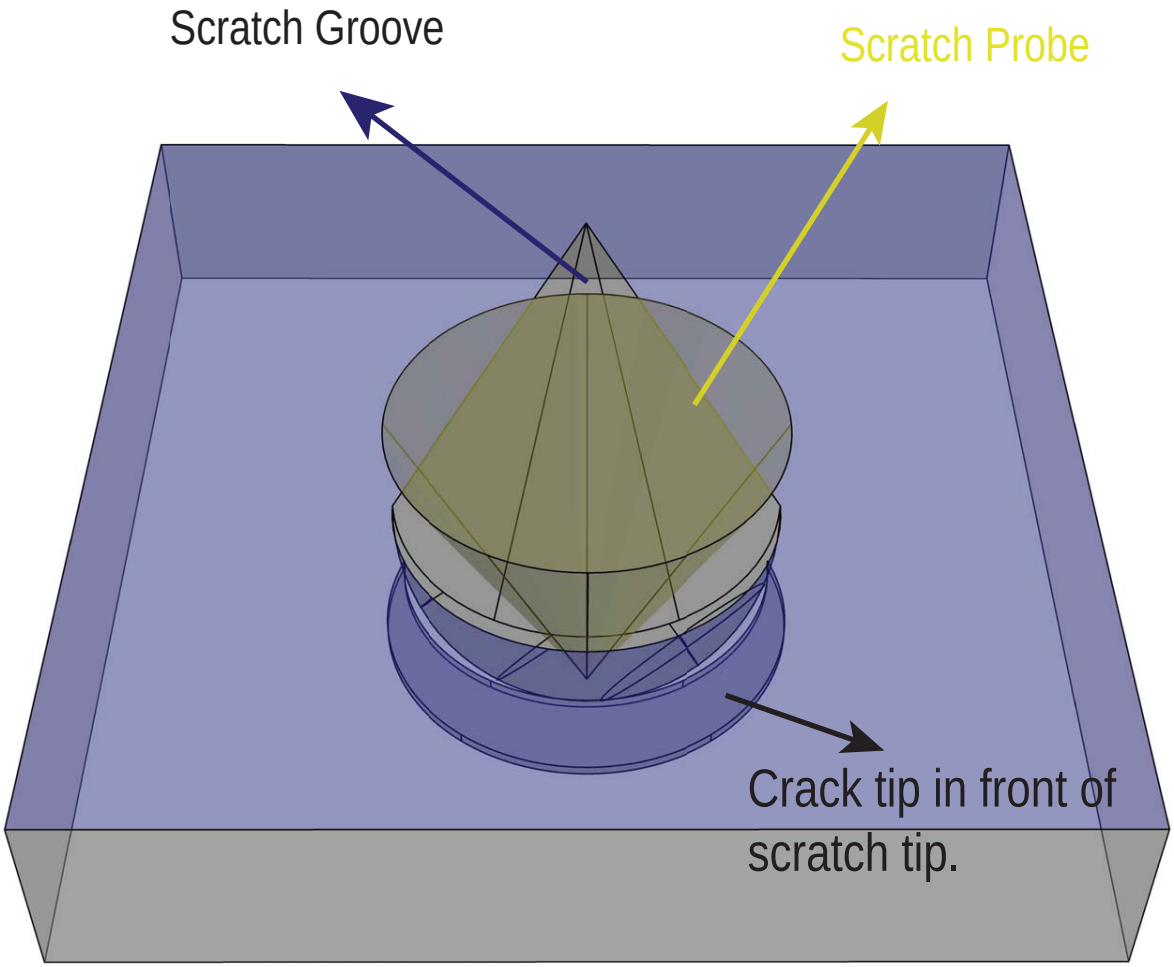

Figure 8.3: 3D schematic representation of scratch tip, scratch groove and crack in the fracture process.

8.2 Micro-Scale Fracture Energy of Gas Shale

In order to estimate the fracture energy, $\mathcal{G}_f$, we apply the J-integral for an anisotropic material. The theoretical solution was derived by Laubie and Ulm [195, 196] for fracture propagation in transversely isotropic materials. In particular, we must take into account the specimen orientation and the scratch direction with respect to the bedding plane. Herein, we study the case where both the scratch direction and the fracture plane are parallel to the bedding plane as illustrated in Figure 8.4 b). This orientation leads to cracks in the short -transverse configuration. Using Voigt notations, we denote $\mathbb{S}$ the transversely isotropic compliance tensor in the $(\underline{e}_1, \underline{e}_2, \underline{e}_3)$ Cartesian reference frame. $\underline{e}_3$ is the axis of symmetry and $(\underline{e}_1, \underline{e}_2)$ forms the plane of symmetry, which is also the bedding plane. For plane strain conditions, the energy release rate depends on the compliance tensor components and on the scratch toughness K_s according to:

$$\mathcal{G}_f = \left(S_{11} - \frac{S_{12}^2}{S_{11}} \right) K_s^2 \tag{8.4}$$

Where $\mathbb{S}$ is the compliance tensor. The components of the compliance tensor can be expressed as a function of the longitudinal Young's modulus E_1 and of the in-plane Poisson's ratio ν_{12}: $E_1 = 1/S_{11}$, $\nu_{12} = -S_{12}/S_{11}$. Therefore, we can rewrite Equation 8.4 as:

$$\mathcal{G}_f = \frac{1 - \nu_{12}^2}{E_1} K_s^2 \tag{8.5}$$

where the scratch toughness K_s is given by Equation 8.2. Thus, we observe a coupling between elasticity and fracture. A major consequence is that in the case of anisotropic materials, the scratch toughness K_s depends on the orientation. Nevertheless, we can combine the scratch tests with independents elastic characterization testing methods such as uniaxial compression or ultrasonic pulse velocity tests in order to estimate the fracture energy.

Figure 8.4a) displays a digital photograph of a scratch test on organic-rich shale. In the case of organic-rich shale, we must take into account the scratch orientation. We performed the scratch tests within the bedding plane as illustrated in Figure 8.4 b). In this configuration, the crack is short-transverse. In our tests, we employ a Rockwell C diamond probe characterized by a half-apex angle 60° and a tip radius of $R = 200$ μm. For each single test, the vertical force was increased linearly from 30 mN to 30 N meanwhile

the scratch speed was held constant and equal to 6 mm/min over a scratch path of 3 mm. The resulting depth of penetration spanned 3 orders of magnitude from tens of nanometers to close to 100 μm.

Another challenge when it comes to gas shale is to account for the heterogeneous microstructure and composition while maintaining a high level of accuracy. We include the heterogeneity via the polish of the top surface, the scratch length and the area of the tested region. As seen in Figure 8.1 using optical microscopy and scanning electron microscopy, this is a granular material with a grain size of 30-100 μm. The first step is to rigorously polish the surface to test so that the roughness is an order of magnitude less than the maximum penetration depth, herein $d_{max} \approx 80 - 100$ μm. This requirement, keeping a surface roughness that is negligible compared to the measured depth, is essential to accurately calculate the fracture properties. In our case, surface force profilometry carried out prior to testing revealed an average roughness of 1.8 μm, which is close to two orders of magnitude less than the maximum penetration depth. Second, the scratch length value, 3 mm, is selected so as to span a minimum of 30 grains. Finally, we carry out a minimum of 4 consecutive tests with a spacing of 2 mm between each test so as to cover an area, 3 mm $\times$ 6 mm, that includes more than 1800 grains. Ideally, one would like to carry a larger amount of tests. However, ensuring an average roughness an order of magnitude less than the maximum penetration depth over such a large area is a difficult task. That is why we developed advanced polishing and grinding methods like the one presented in the Materials and Methods section. Using this specimen preparation method and by carrying out 4 consecutive scratch tests of a length of 3 mm each, we achieved the balance between accuracy and getting enough statistical information.

Figure 8.4 c) superimposes the evolution curves of the horizontal force along with the acoustic emission for a single test on unconventional shale. In average, the horizontal force increases as the vertical force is increased along the scratch path. However, the horizontal force curve locally exhibits an irregular saw-tooth waveform shape as a result of the local heterogeneity as well as the succession of several microscopic fracture events. In fact, the acoustic emission log displays peaks that correspond to rapid releases of the elastic strain energy. In particular, each peak of the acoustic emission is followed by a sudden drop of the horizontal force. This indicates that the acoustic emission peak correspond to local micro-cracking events. Therefore, the acoustic emission log provides a physical evidence of fracture processes at work during the test. Furthermore, Figure 8.4 d) displays a panoramic view of the residual surface that was captured after observing

the tested specimen under an optical microscope and stitching digitally up to 10 pictures of the top surface. We can see a groove (in dark in the picture) with an increasing width, which results from the material removal processes—micro cutting and micro-chipping. Moreover, the width increases with the scratch path because as we apply a larger vertical force, we activate cracking mechanisms at a higher depths and therefore remove a larger volume of material.

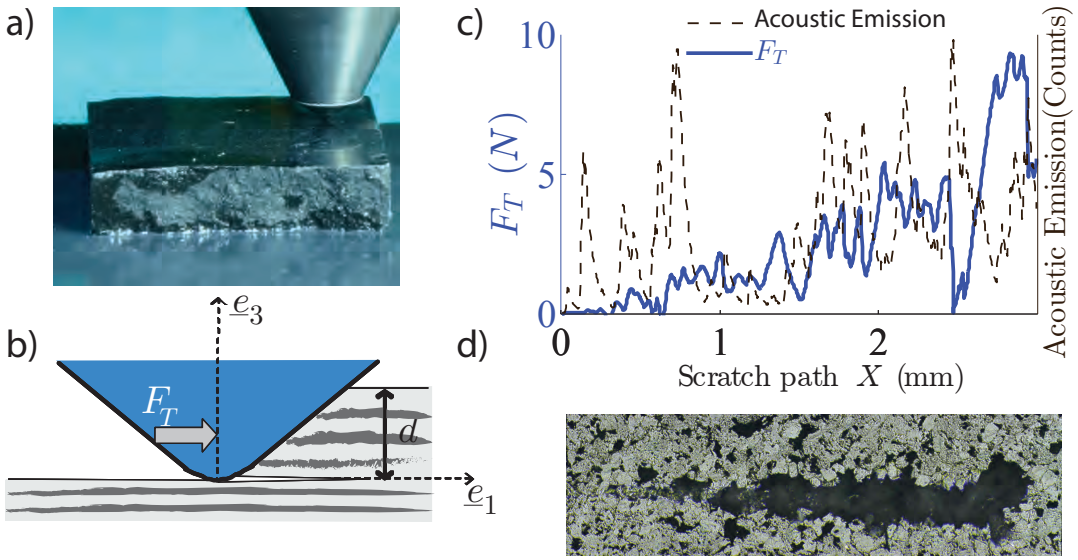

Figure 8.4: Scratch testing of gas shale: Ideal representation of a scratch test in a transversely isotropic material. Credits: Akono, Kabir, UIUC 2014. Side view a) and front view b). A vertical force is applied along with a constant speed in the scratch direction, here e_1, resulting in a horizontal force F_T and a penetration depth d. c) Acoustic emission (dotted black curve) and horizontal force (solid blue curve) recorded during a single scratch test. d) Residual groove after scratch testing.

Figure 8.5 displays the application of our fracture model to gas shale. Prior to testing, the probe tip function $2pA$ was calibrated using Lexan 934 as the reference material and by following the calibration procedure given in [116]. For each single test, both F_T are d are continuously recorded along the scratch path X, yielding a curve $(F_T(X), d(X))$ with 1000 data points. Our post-processing algorithm computes then the scratch toughness $K_s(X) = F_T/\sqrt{2pA}(X)$ as a function of the scratch path X for all 4 tests. Figure 8.5 displays the curves $(K_s, d/R)$ obtained for the campaign of tests carried on the Toarcian, Niobrara and Marcellus shale systems. $R = 200\mu$m is the probe tip radius. The fracture behavior is similar for all three materials: the scratch toughness K_s decreases as the depth d increases and converges toward an asymptotic value K_s^∞. A similar behavior had been

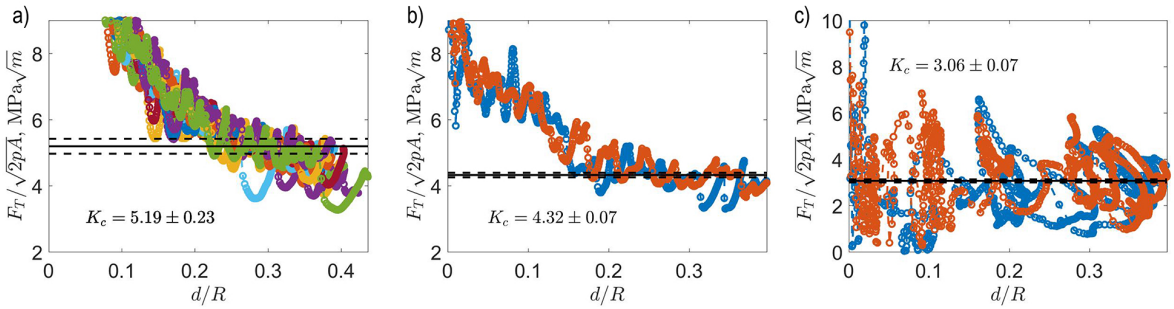

Figure 8.5: Scratch fracture scaling of gas shale. a) Marcellus shale. b) Niobrara shale. c) Toarcian. K_s is the scratch toughness given by Equation 8.2. d is the penetration depth and $R = 200$ μm is the scratch probe tip radius. Each graph correspond to 4 consecutive tests carried out over a scratch length of 3 mm for Niobrara and Toarcian. Each graph correspond to 12 tests carried out over a scratch length of 3 mm for Marcellus shale.

observed for homogeneous materials: this convergence is indicative of a ductile-to-brittle transition that is activated by the depth of penetration [112, 114, 115]. In the brittle and fracture-driven regime, the force scales as $F_T \propto d^{3/2}$ and thus the nominal strength scales as $\sigma_N \propto 1/\sqrt{d}$, which is characteristic of brittle fracture.

The next step is to apply fracture mechanics in order to estimate the fracture energy. First, we calculate the scratch toughness by taking the average value of $F_T/\sqrt{2pA}$ for all tests and for all depth values higher than the sphere-to-cone transition depth threshold, 30 μm. Table 8.2 lists the values of the scratch toughness calculated for our three materials. The values of the microscopic toughness are two to three times greater than the fracture toughness values reported at the macroscopic scale, 0.7-1.4 MPa$\sqrt{\text{m}}$. In a second step, we computed the energy release rate by applying Equation 8.5 given the elastic constants listed in Table 9.2. The results are presented in Table 8.2.

The fracture toughness reported for Marcellus specimen in the literature is 1.06 MPa$\sqrt{m}$ to 1.34 MPa$\sqrt{m}$ for different orientation of the specimen [16]. In their study, the three point bending test method is used to measure the fracture toughness of the specimens.

Table 8.2: Fracture assessment of gas shale at the microscopic scale using scratch tests. K_s is the scratch toughness calculated by application of Equation 8.2. Meanwhile, G_f is the fracture energy that is estimated using Equation 8.5.

	Toarcian	Niobrara	Marcellus
K_c (MPa$\sqrt{m}$)	3.06±0.07	4.32±0.07	5.19±0.23
G_f (N/m)	125.0	117.7	125.5

The fracture toughness of the three point bending is lower compared to scratch testing due to the larger crack tip area. In addition, the difference in the scale of the tests carried out can describe the difference due to size effect.

8.3 Toughening Mechanisms of Gas Shale

To understand the origin of the extraordinary toughness of organic-rich shale, we examined the residual groove after scratch testing. The toughening mechanisms of gas shale have not been extensively documented. Our goal is to observe and report the physical mechanisms of fracture. Figure 8.6 a)-e) show scanning electron microscope images of the residual grooves after scratch testing on gas shale. A general observation is that the crack surfaces are very rough and not smooth. Crack front roughening in heterogeneous materials can occur as a result of a mismatch in elastic and fracture toughness values between micro-constituents that lead to a non-planar crack surface. In the case of organic shale, the interaction between soft phases such as clay and hard particles such as quartz is likely to cause the crack to deflect.

Furthermore, we observe extensive 1) particle pull-out. Brochard *et al.* [197] studied the pullout phenomenon of ductile particles in a brittle matrix. Using molecular simulations, they modeled a microporous carbon-silica polymorph nanocomposite. Their work highlighted the importance of the organic-inorganic interfaces. In particular, when the interface is much weaker than the matrix, the effective fracture toughness of the composite could be enhanced by a factor of 2 for a fraction of ductile inclusions equal to 10% and by a factor of 3 for a fraction of ductile inclusions equal to 20%. We can reconsider our scratch tests and SEM results in light of their work. It appears that scratch testing triggers microscopic fracture mechanisms, perhaps as a result of the multiaxial stress field. We see significant pull out of softer phases. We also see 2) crack bridging, which in the case of ceramics [198] , cementitious materials [199] and cortical bone [200], has been reported to lead to substantial fracture toughening. Finally, we observe 3) crack branching, micro-cracking and crack trapping, although to a lesser extent.

Although the toughening mechanisms of other composite materials such as cementitious materials, cortical bone and ceramics have been actively studied, investigated and modeled; when it comes to gas shale, the current state of research is still at the early stages. However, this multi-scale fracture behavior that is characterized by various failure mechanisms must be considered while developing a rigorous and physics-based constitu-

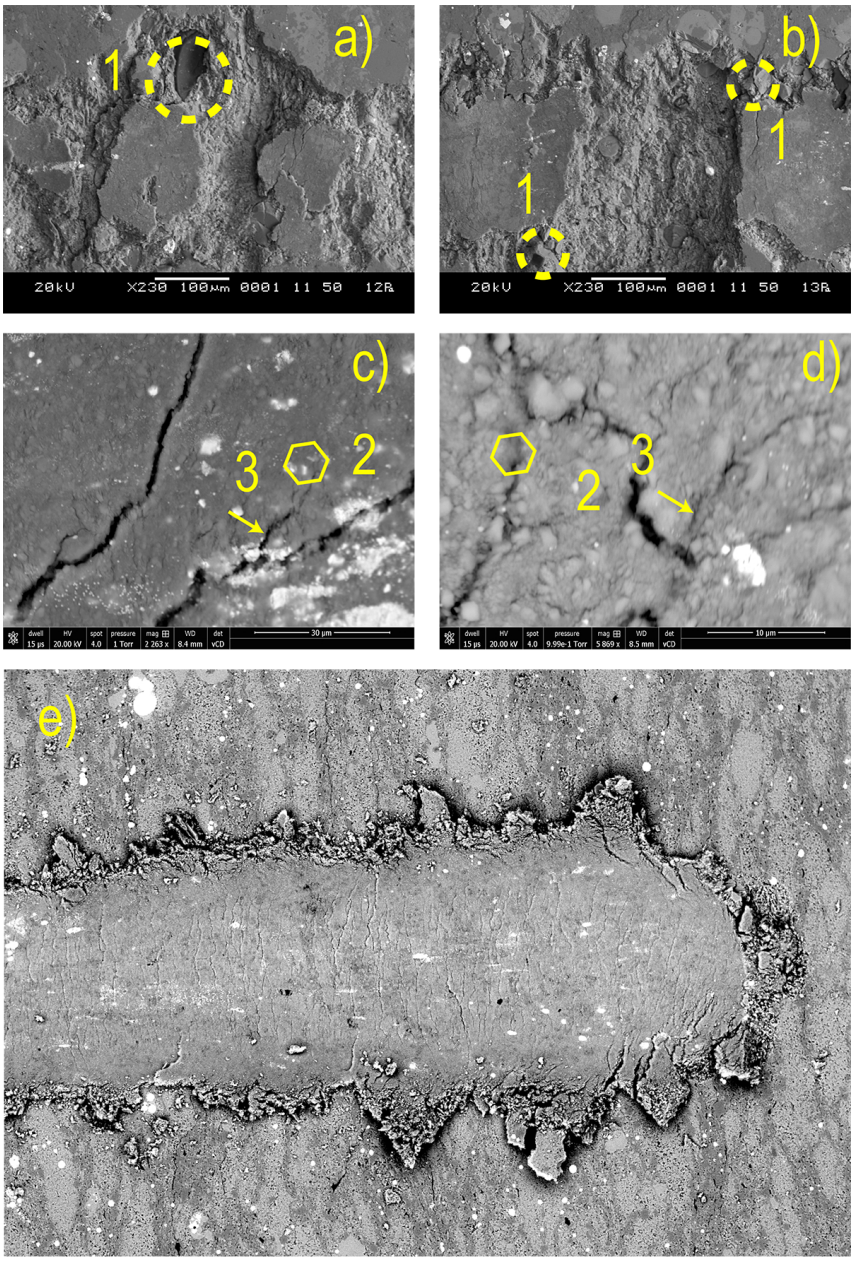

Figure 8.6: Fracture mechanisms in gas shale at the microscopic scale. Scanning electron microscopy image of residual grooves after scratch testing. Several microscopic fracture mechanisms can be observed: a) (1) particle pull-out, b) (1) particle pull-out, c) (2) crack bridging and (3) crack deflection and branching, d) (2) crack bridging and (3) crack deflection and branching, e) residual groove of scratch path with cracks observed in the groove.

tive model of the material. The main question is then how do the microstructure and composition of gas shale affect its fracture resistance. Going back to our initial problem of hydraulic fracturing, another question is what fracture mechanisms are induced and at which scale are they active. These are broad and challenging questions that go beyond the scope of this research. Nevertheless, given the scalability of scratch tests, the framework presented here will pave the way toward a more systematic fracture characterization of gas shale at multiple length scales, thereby yielding a fundamental understanding of its mechanical performance.

8.4 Conclusion

The research objective was to measure the fracture toughness of gas shale specimens. To this end, a hybrid experimental and theoretical framework was developed that integrates cutting-edge imaging techniques alongside advanced fracture mechanics and small scale mechanical testing methods. Microscopic examination revealed a porous and granular microstructure with a grain size in the range 30-100 μm for Toarcian, Marcellus and Niobrara shale specimens. The scratch fracture toughness technique was extended to shale so as to fully incorporate the heterogeneity and the anisotropy. The anisotropy was accounted for by deriving the energy release rate in orthotropic materials. The heterogeneity was accounted for via the specimen preparation method and the test parameters. In turn, a coupling between fracture and elasticity was found. As a consequence, combined scratch test results with independent elasticity measurements is used to estimate the fracture energy at the microscopic scale. It was found that gas shale exhibits exceptional fracture properties at the microscopic scale: the scratch toughness is two times higher than the macroscopic fracture toughness. Similarly, the microscopic fracture energy is twice larger than that at the macroscopic scale. Scanning electron microscopy shows evidence of toughening mechanisms such as front roughening, particle pullout and crack bridging. These findings are novel and they call for advanced constitutive models of organic-rich shale and that will be the focus of future research. In brief, the methodology and results presented here are important and can be employed to yield a fundamental insight of the mechanical behavior of gas shale. The field of application is broad including powerful geomechanical models for an optimal design of hydraulic fracturing operations as well as new generations of tough organic-inorganic engineering materials.

Chapter 9

Effect of Injection Rate and Anisotropy on Hydraulic Fracturing: Effect of Rate and Speed on Fracture Behavior of Organic-Rich Shale

9.1 Introduction

Organic-rich shale or grey shale or black shale is a unique class of organic-inorganic nanocomposite that plays a crucial role in several climate change mitigation strategies such as energy recovery from unconventional resources [4–9], carbon dioxide subsurface capture and storage [10–12], and nuclear waste geological disposal [13, 14]. Understanding the mechanical behavior of the source rock at the microscopic [15–17] and nanometer [18] length scale is key to achieve significant breakthroughs in the science and technology of horizontal well drilling and hydraulic fracturing [19–21]. CO_2 geological sequestration involves pumping industrial carbon dioxide emissions into deep permeable geologic formations at a steady rate [10]. Potential suitable formations include aquifer, depleted oil and gas fields, and coal seams. Maintaining the structural integrity of the well, preventing the occurrence of micro-seismic events and understanding potential chemo-mechanics degradation processes in the source rock due to brine exposure is a major concern [22, 23]. Although a lot of attention has been given to coal seams, depleted organic-rich shale formations [24] represent an alternative yet unexplored. The safe disposal of radioactive wastes requires

these wastes to be isolated from all ecosystems for thousands of years. Deep argillaceous formations with a low intrinsic permeability such as organic-rich shale have been investigated as potential repositories [13, 14]. Thus, it is important to understand the chemical as well as mechanistic properties and fracture properties of organic-rich shale [25].

The multi-scale nature of gas shale [138, 201, 202] complicates the mechanical characterization of the fracture response. At the macroscopic level (millimeter and above), gas shale is a layered fabric due to the geological deposition process [203, 204]. At this scale, it is common to idealize the mechanical behavior using transversely isotropic models [205]. The fracture toughness is measured via three-point bending tests on single-edge notched specimens [16, 206], double cantilever beam tests [207], burst tests [208], Brazilian disk tests [209], and chevron-notched semi-circular bending tests [179]. At the microscopic level, gas shale consists of a porous clay fabric with quartz, feldspar and pyrite inclusions [210, 211]. A wide array of advanced methods such as scanning electron microscopy, energy-dispersive spectroscopy [212], wavelength-dispersive spectroscopy [213], and X-ray diffraction [214, 215] are employed to identify the chemical composition. Mechanical characterization consists of micro-indentation testing [216], bending tests on micro-beams [217], Vickers indentation fracture [181] tests and scratch tests. At the nanometer level, the basic unit consists of kerogen molecules bonded to clay minerals (illite or smectite). Nano-indentation [7, 137, 218, 219], atomic force microscopy [220, 221] and nano-scratch tests can be used to assess the behavior. Moreover, recently, molecular dynamics and atomistic simulations [141, 222, 223] have emerged as means to predict the mechanical properties from first principles. Yet, characterizing the fracture response of gas shale at several length-scales remains a challenge.

Previously, we showed that scratch tests are a powerful means to assess the fracture behavior and the fracture micro-mechanisms [112, 224]. A nonlinear fracture mechanics analysis for articulated to measure the fracture characteristics from scratch test measurements [111, 115]. We studied both tests at the macroscopic level [111, 112, 117, 225] and at the microscopic level [111, 114–116, 119, 120, 224, 226]. The theoretical framework was implemented into an experimental protocol applicable to metal, polymers and ceramics [114, 116]. Finally, the framework was extended to heterogeneous materials such as rocks [111, 112], cement-based composites [117, 119, 225], biological tissues [226] and organic-rich shale systems [120].

Our aim is to to study the influence of mechanical loading rate and testing speed on the measured fracture toughness of organic-rich shale at the microscopic length scale. We

build on a prior analytical solution to correlate loading rate and speed to the observed scratch toughness, that was validated on polymers [227]. Our focus is on a grey and black shale material, respectively Toarcian and Niobrara, that differ in their mineralogy, total organic content, as well as their micro-structure. We connect the composition and topography to the fracture response using microscopic scratch tests and nonlinear fracture modeling. First, we introduce the materials and methods utilized in this study, then we articulate a nonlinear fracture mechanics model and apply the theory to yield fundamental insights into the fracture response of shale systems.

9.2 Experimental Investigation

In this study, we investigate two different major gas plays, Niobrara from northeastern Colorado in the United States, and Toarcian shale from the Paris basin in France. Two-inch long and one-inch round cylindrical Toarcian shale samples were provided by Total Corp. The specimens were extracted from cores at depths of 5106–5130 m. Three specimens were investigated: B1, B2, B3. As for the Niobrara formation at the southwestern Wyoming Province (SWWP), it is a sedimentary basin that formed during the Larmide orogeny (Late Cretaceous through Eocene). All specimens were kept under vacuum (10 inch of mercury) to prevent potential hydration, degassing, or drying susceptible to degrade the mechanical properties.

In order to assess the mineralogy, powder X-ray diffraction was carried out at the Frederick Seitz Materials Research Laboratory in collaboration with the Illinois State Geological Survey. Quantitative X-ray diffraction analysis of clay-bearing rocks is a very challenging and to-date there is no clear standard. We followed the protocol recommend by [147, 152]. Each specimen was cleaned and dried in a vacuum oven. Afterward, each specimen was mechanically ground down to an even particle size around 44 microns. The resulting powder was then spread on a glass slide and characterized using a Siemens/Bruker D5000 X-ray Powder Diffraction instrument. JADE^{TM}software was utilized to identify the constituents and percentages of Niobrara specimen using XRD pattern.

Table 9.1 displays the mineralogy of the Toarcian specimens as measured via X-ray diffraction analysis. The dominating micro-constituents are quartz and illite, with trace amounts of albite. Meanwhile, Niobrara's major micro-constituents are : calcite, quartz, pyrite, illite and dolomite with a weight fraction respectively of 70 %, 11.3 %, 1.2 %, 15.5

%, and 2.0 %. Letoc Eval were also carried out to evaluate the organic matter content. Based on the total organic content (TOC) of 1%, the Toarcian shale specimens can be classified as grey shales, characterized by 0.5% <TOC <2%. In contrast, a TOC above 2% enables to classify Niobrara as a black shale, with TOC≥2%.

Table 9.1: Mineral composition in weight percent of the gas shale specimens tested in this study.*Data courtesy of Total S. A., Paris, France.

Material	Toarcian B1	Toarican B2	Toarcian B3	Niobrara
TOC (%)	1*	1*	1*	2.50
Mineral, (%)				
Quartz	85.1	85.1	80.1	11.3
Illite	14	14.5	14.2	0
Illite/smectite	0	0	0	15.5
Albite	0.9	0.4	1.5	
Pyrite	0.2–1			1.2
Dolomite	-			2.0
Calcite	-			70.0

The objective of the grinding and polishing protocol is to achieve a surface roughness an order of magnitude less than the maximum penetration depth [185]. Organic-rich shale are difficult to prepare as they exhibit soft phases (clay and organic matter) that coexist with hard inclusions (pyrite and quartz particles). tend to polish the hard particles to the detriment of the softer phases that get eroded. Conventional methods such as resin-embedding under vacuum [228] must be avoided because the embedding media and gas shale exhibit a fracture toughness ($\approx$ 4 MPa$\sqrt{\mathtt{m}}$) which is comparable to that of the material ($\approx$ 1–2 MPa$\sqrt{\mathtt{m}}$). As a result, probing the fracture performance at the mesoscale ($\approx$ 1–10 μm) of a specimen embedded into epoxy resin will yield the composite behavior of the rock/epoxy composite instead of the isolated fracture response of the individual specimen.

Given these constraints, the grinding and polishing procedure is very specific to the gas shale system chosen, and is derived via an iterative process. The preparation routine involved three different steps: machining, grinding and polishing. The lubricating and cleaning media was N-decane to prevent any drying or hardening of the organic phase. Grinding occurred in three steps, using silicon carbide abrasive pads of different grit sizes. Afterward, polishing was done using soft synthetic woven cloths along with diamond particle oil suspensions of different sizes, consecutively 9 μm, 3 μm, 1 μm and 0.25 μm. Between each step of the grinding and polishing procedure, the specimens were cleansed

in an ultra sonic bath of N-Decane to prevent cross contamination. Atomic force microscopy (AFM) [30] was used to quantitatively assess the quality of the polished surface by measuring its roughness. The average root-mean squared roughness over a 50 μm $\times$ 50 μm polished surface was less than 30 nm.

Scanning electron microscopy was conducted at the Frederick Seitz Materials Science Laboratory and Beckman Institute Visualization Laboratory to identify the composition and micro-structure. Polished shale specimens were imaged using an environmental scanning electron microscope JEOL 6060LV, a high-resolution analytical SEM JEOL 7000F, and a FEI Quanta. The presence of micro- and nano-pores has been previously shown on organic-rich shale systems such as Woodford shale and Barnett [229, 230]— but not on Niobrara and Toarcian shale systems. Previous investigations have also shown the presence of clay minerals [231–233]. In this study, we aim to employ SEM as a complement to X-ray diffraction in order to identify the morphology and mineralogy and thus understand the mechanical response.

Creep indentation tests were carried out to measure the visco-elastic and plastic characteristics. Two orientations were considered: perpendicular to the bedding plane and parallel to the bedding plane. Previous studies of indentation in visco-elastic materials have connected the visco-elastic behavior to the force and depth measurements during indentation testing [95, 234]. All tests were carried out using the Anton Paar TriTech multi-scale testing platform (Anton Paar, Ashland,VA). The indenter was a Berkovich indenter whose contact area had been calibrated prior to testing using fused silica as a reference material. For each specimen and each orientation, a 10 $\times$ 10 grid (100 tests) was carried out with a maximum load of 100 mN, a loading/unloading rate of 200 mN/min and a holding phase of 480 s. Assuming a logarithmic creep behavior, characteristic of shale, the viscoelastic parameters were calculated following the methodology introduced by Vandamme *et al.* [90, 95, 234].

The scratch test consists of moving a sharp diamond stylus over the surface of a softer material under a linearly increasing load (cf. Figure 9.2) a). In this study, we used an Anton Paar (Anton Paar, Ashland VA) multi-scale testing platform with an acoustic enclosure. The stylus is a Rockwell C probe which consists of a cone with a half-apex angel of $\theta = 60^\circ$ ending in a half-sphere of radius $R = 200$ μm. The vertical force is prescribed via a piezo-actuated force feedback control loop, meanwhile the displacement is measured via high-accuracy sensors. The scratch test is performed in two steps: first, the probe scans the surface profile while applying a low constant force. Second, the vertical force

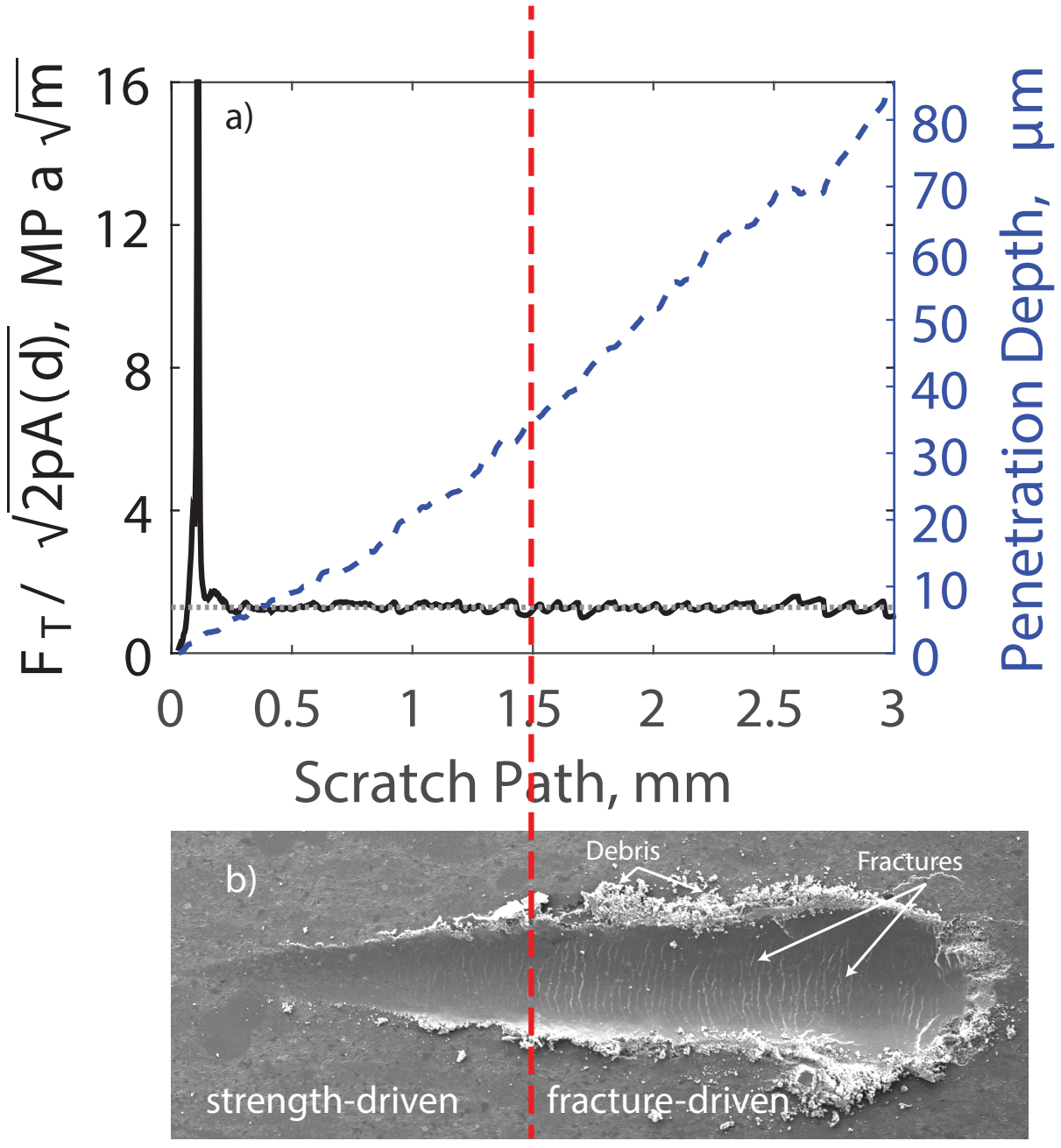

Figure 9.1: Scaling of scratch force. F_T is the horizontal scratch force, p is the perimeter, A is the horizontal projected load-bearing contact area, and d is the penetration depth. SEM images of the top surface are shown for low penetration depths—smooth groove—and high penetration depths—presence of fracture surfaces (1) and micro-debris (2). The dashed line illustrates the transition between strength-driven point and fracture-driven process.

is linearly increased as the probe moves along the scratch path. This two-step method allows for accurate testing that can account for irregular, curved or slanted specimens. An optical microscope is integrated with the scratch testing unit to facilitate pre- and post-testing microscopic examination.

We summarize our recent findings on scratch testing. We showed that scratch tests are governed by a ductile-to-brittle transition [111, 112]. For low penetration depths, failure occurs through plastic flow as the material is plastically deformed and pushed to the sides of the residual groove. Whereas for deep penetration depths, micro-fractures are generated at the center of the groove and are propagated via fracture dissipation. Based on observations at the macroscopic scale [117, 225] and at the microscopic scale [116, 120], the fracture surface is a flat semi-circular surface that originates below the scratch tip and propagates horizontally below the surface, and in the same direction as the motion of the scratch probe. As a consequence, for an axisymmetric scratch probe, the crack front is curved and perpendicular to the direction of scratch testing as shown in Figure 9.1 Furthermore, a succession of fracture surfaces is generated, instead of a single crack.

The competition between strength and fracture was modeled using the Bažant's Size Effect Law [224] as well as dimensional analysis, computational fracture mechanics [116] and nonlinear fracture mechanics theory [120]. In a fracture-driven process where plastic deformation is negligible, the scratch toughness is defined as the asymptotic value of $F_T/\sqrt{2pA}$:

$$K_s = \lim_{d \to +\infty} \frac{F_T}{\sqrt{2pA}} \tag{9.1}$$

where F_T is the measured horizontal scratch force, A is the projected horizontal area and p is the probe perimeter. $2pA$ is the scratch probe shape function which is calibrated prior to testing with a material of known fracture toughness. For homogeneous materials, a great agreement was found between the the microscopic scratch toughness and the fracture toughness measured using conventional macroscopic fracture testing methods.

The basic idea is to monitor the prevalence of fracture processes based on the force scaling. Figure 9.1 displays the evolution of the quantity $\frac{F_T}{\sqrt{2pA}}$ as a function of the scratch path for a test on organic-rich shale. For low values of the penetration depth d, the scratch groove is smooth and $\frac{F_T}{\sqrt{2pA}}$ varies greatly pointing to various sources of energy dissipation such as plastic flow, friction, visco-plasticity and fracture. In contrast, for large penetration depths, $\frac{F_T}{\sqrt{2pA}}$ reaches a steady value; meanwhile SEM reveals fracture surfaces

(1) in at the center of and microscopic debris (2) at the edges of the residual groove. As a consequence, for large penetration depths, friction and plastic flow fade and the primary means of energy dissipation are fracture dissipation and/or viscous dissipation. We focus on this regime and seek to uncouple viscous dissipation from fracture dissipation.

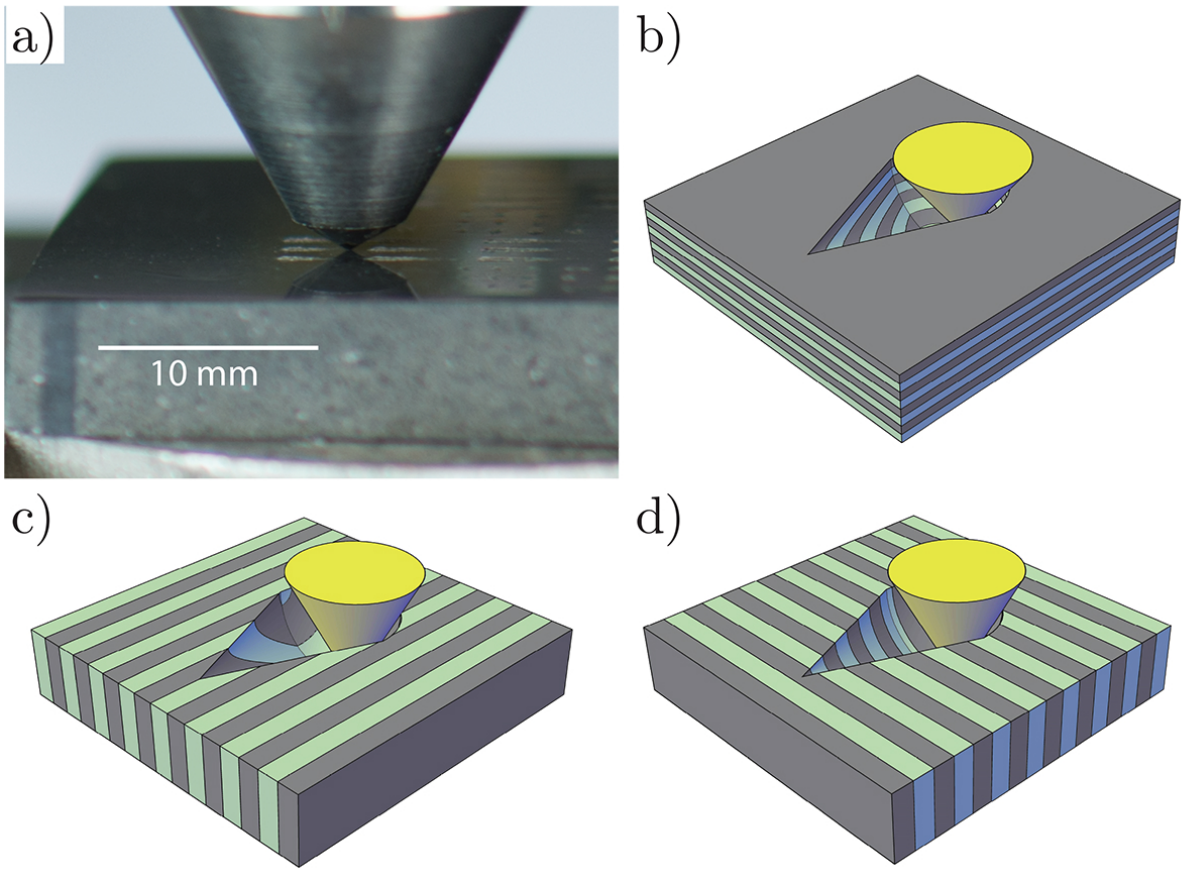

Figure 9.2: a) Digital photography of scratch on polished Niobrara specimen. Credits: Ange-Therese Akono, Pooyan Kabir, Kavya Mendu, UIUC, 2016. b)-d) Scratch orientations: (b) Short-Transverse, (c) Divider, and (d) and Arrester (d).

Recently, we extended our nonlinear fracture mechanics framework to Maxwell-type visco-elastic solids [227]. However, for organic-rich shale, the Maxwell model is ill-suited. In addition, we must account for the heterogeneity and the anisotropy. Thus, our objective is to assess the influence of the scratch speed, the loading rate and the scratch orientation on the mechanical response of gas shale specimens while accounting for the mineralogy, anisotropy and total organic content.

To this end, we carried out scratch tests for ten scratch speed values ranging from

$V = 0.8$ mm/min to $V = 12$ mm/min. The following two loading rate values were considered: $\dot{F}_V = 60$ N/min and $\dot{F}_V = 90$ N/min. In all tests, the vertical force was linearly ramped up from 0.03 N to 30 N. For each duo $(V, \dot{F}_V)$, a minimum of three consecutive scratch tests were carried out. The scratch length was selected to span several grains. The rock mineralogy and texture was consistent between different locations where the scratch test and creep tests were conducted. The short supply of Toarcian shale materials prevented us from testing all three orientations. Thus, a single orientation was considered: parallel to the bedding plane. Yet, we tested three different specimens: Toarcian B1, Toarcian B2 and Toarcian B3. We considered three orientations in the case of Niobrara shale. The aim was to measure the level of anisotropy of the fracture behavior. The three scratch orientations considered were: Short Transverse, Divider, and Arrester. These three orientations are shown in Figure 9.2 b)-d). Thus a total of 270 scratch tests were performed.

9.3 Theoretical Model

This section was developed in previous works [110, 227] and adopted herein. In previous work [111, 112, 114, 117, 224, 225], we have focused on separating fracture and plasticity in scratch testing. Herein, we select a regime where plastic dissipation is negligible, by evaluating the scratch toughness at large depths and waiting for a full convergence of the quantity $F_T/\sqrt{2pA}$ toward a horizontal line within a single scratch test, cf. Equation 9.1. Given that plastic flow is negligible, the remaining forms of energy dissipation are fracture dissipation and viscous behavior. Given those two means of energy dissipation, we consider a brittle visco-elastic behavior. In particular plastic deformation such as visco-plasticity or hypoelasticity-plasticity do not apply given plastic flow is very small.

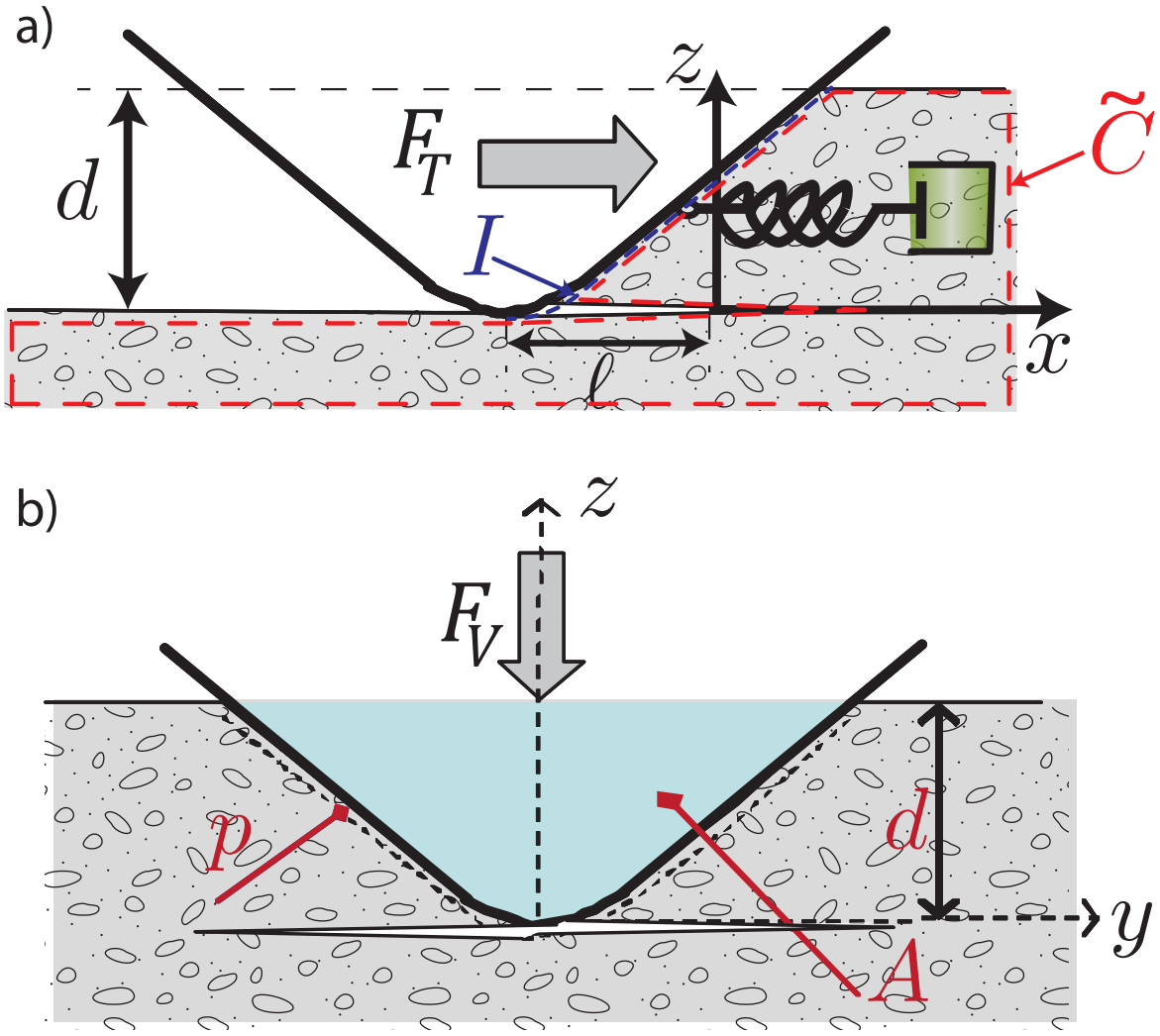

Figure 9.3: Schematic representation of a scratch testing on a visco-elastic material. a) Side view. b) Front view. F_T is the horizontal scratch force, d is the penetration depth and ℓ is the scratch length. $\tilde{C}$ is a closed contour including the crack tip. Adapted from [114, 115].

Consider a scratch test in a homogeneous viscoelastic material as schematically shown in Figure 9.3. We assume the existence of a horizontal crack of length ℓ emanating from the tip of the crack. $(\underline{e}_x, \underline{e}_y, \underline{e}_z)$ is the reference frame in Cartesian coordinates. We operate within the framework of linear viscoelasticty [235–238]. The total strain $\underline{\underline{\varepsilon}}$ can be decomposed into an elastic component, $\underline{\underline{\varepsilon}}^{el}$, and a viscous component, $\underline{\underline{\varepsilon}}^{v}$:

$$\underline{\underline{\varepsilon}} = \underline{\underline{\varepsilon}}^{el} + \underline{\underline{\varepsilon}}^{v} \tag{9.2}$$

Similarly, the volume density of the Helmholtz free energy ψ involves two contributions, the elastic strain energy $\psi^{el} = \frac{1}{2}\underline{\underline{\varepsilon}}^{el} : \mathbb{C}_0 : \underline{\underline{\varepsilon}}^{el}$ and the frozen energy $U\left(\underline{\underline{\varepsilon}}^{v}\right)$:

$$\psi = \psi^{el} + U\left(\underline{\underline{\varepsilon}}^{v}\right) \tag{9.3}$$

$\underline{\underline{\varepsilon}}^{el} = \mathbb{C}_0^{-1} : \underline{\underline{\sigma}}$ is the elastic strain which is recovered immediately upon unloading, $\underline{\underline{\sigma}}$ being the stress tensor and $\mathbb{C}_0$ being the instantaneous stiffness tensor.

The elastic energy ψ^{el} is the energy stored within a unit volume of material that is immediately recovered upon unloading. In contrast, the frozen energy is the energy stored within the material which is not immediately recovered after load removal, due to irreversible deformations of the structural skeleton taking place at the micron and nanometer levels [239]. In [227] we did not account for the frozen energy because the focus was on homogeneous materials such as polymers. However, for heterogeneous, porous and granular materials such as organic-rich shale, the frozen energy cannot be neglected. According to the Clausius-Duhem inequality, the internal viscous dissipation rate φ is given by:

$$\varphi dt = \underline{\underline{\sigma}} : d\underline{\underline{\varepsilon}} - d\psi \geq 0 \tag{9.4}$$

where $\underline{\underline{\sigma}} : d\underline{\underline{\varepsilon}}$ is the elementary work done by external forces, $d\underline{\underline{\varepsilon}}$ is an infinitesimal strain increment, and dt is the infinitesimal time increment. In other words, in the absence of fracture processes, the external work is either stored within the structure—as elastic and frozen strain energy—or dissipated via viscous processes. On the other hand, the dissipation rate can be rewritten as the sum of two terms: a volumetric dissipation term due to viscous processes in the bulk of the material and the surface dissipation associated to fracture propagation (cf. [240]):

$$\frac{d\mathcal{D}}{dt} = \int_{\Omega} \varphi d\Omega + \mathcal{G}\dot{\Gamma} \tag{9.5}$$

where $\Gamma = p\ell$ is the crack surface and Ω is the material volume. $\dot{\Gamma} = \frac{\partial \Gamma}{\partial t}$ is the partial derivative of Γ with respect to time. $\mathcal{G}$ is the energy release rate which is given by the J-integral [113, 241, 242] :

$$\mathcal{G} = \frac{1}{p} \oint_{\tilde{C}} \left[\psi n_x - \underline{T} \cdot \frac{\partial \underline{\xi}}{\partial x} \right] dS \tag{9.6}$$

$\underline{\xi}$ is the displacement vector, $\underline{T} = \underline{\underline{\sigma}} \cdot \underline{n}$ is the stress vector, and $\tilde{C}$ is a closed contour including the crack tip. $\underline{\underline{\sigma}}$ is the stress tensor, $\underline{n} = n_x \underline{e}_x + n_z \underline{e}_z$ is the outward unit vector and $(\underline{e}_x, \underline{e}_y, \underline{e}_z)$ is the reference frame in Cartesian coordinates. In the case of scratch testing, by choosing a suitable closed contour, we can rewrite Equation 9.6 as [111, 112]:

$$\mathcal{G} = \frac{1}{p} \int_I \left[\psi n_x - \underline{T} \cdot \frac{\partial \underline{\xi}}{\partial x} \right] dS \tag{9.7}$$

where I is the interface between the probe and the material. The term $1/p$ takes into account the 3-D nature of the fracture surface.

Extended Correspondence Principle

The next step consists in solving for the stress, strain, and displacement fields of a viscoelastic boundary value problem. We are looking for a stress tensor $\underline{\underline{\sigma}}(t)$, a strain tensor $\underline{\underline{\varepsilon}}(t)$ and a displacement vector $\underline{\xi}(t)$ that satisfy the equations below.

- Equilibrium:

$$\texttt{div}\ \underline{\underline{\sigma}}(t) = 0 \tag{9.8}$$

  Herein `div` designates the divergence operator [243, 244].

- Compatibility:

$$\underline{\underline{\varepsilon}}(t) = \frac{1}{2} \left(\nabla \underline{\xi}(t) + {}^T \nabla \underline{\xi}(t) \right) \tag{9.9}$$

  where ${}^T\cdot$ indicates the transpose operator and $\nabla\cdot$ represents the gradient operator.

- Boundary conditions: there is no stress applied on the top of the material and at the bottom on the crack faces. Moreover the resulting force at the interface

between the blade and the material must be equal to the applied horizontal force, the contribution of the vertical force to the fracture process being neglected:

$$\underline{\underline{\sigma}}(z = \pm\frac{d}{2}, x \geq 0, t) \cdot \underline{e}_z = 0 \tag{9.10}$$

$$\int_I \underline{\underline{\sigma}}(t) \cdot \underline{n}\, dS = F_T \underline{e}_x \tag{9.11}$$

Finally, we assume a linear viscoelastic material constitutive law. Let's decompose the strain and stress tensors into their volumetric and deviatoric parts: $\underline{\underline{\sigma}} = \underline{\underline{s}} + \sigma_m \underline{\underline{1}}$ and $\underline{\underline{\varepsilon}} = \underline{\underline{e}} + \frac{1}{3}\epsilon\underline{\underline{1}}$. Based on the Boltzmann superposition principle, the constitutive law reads [235, 236]:

$$\sigma_m(t) = \int_{-\infty}^{t} \kappa(t-u)\frac{d\epsilon}{dt}(u)du \tag{9.12}$$

$$\underline{\underline{s}}(t) = 2\int_{-\infty}^{t} \mu(t-u)\frac{d\underline{\underline{e}}}{dt}(u)du \tag{9.13}$$

where, $\kappa(t)$ is the relaxation bulk modulus and $\mu(t)$ is the relaxation shear modulus. $\underline{\underline{e}}$ is the deviatoric strain tensor. Applying the Laplace transform to Equations 9.12–9.13 yield:

$$\widehat{\sigma_m}(s) = s\widehat{\kappa}(s)\widehat{\epsilon}(s) \tag{9.14}$$

$$\widehat{\underline{\underline{s}}}(s) = 2s\widehat{\mu}(s)\widehat{\underline{\underline{e}}}(s) \tag{9.15}$$

Herein, $\widehat{g}(s)$ indicates the Laplace transform of function $g(t)$. Thus, in the Laplace domain, there is a linear relationship between the Laplace transform of the stress field and that of the strain field.

We then use the extended elastic-viscoelastic correspondence principle in order to solve the boundary value problem. The elastic-viscoelastic correspondence principle states that the solution to our boundary value problem for a linear viscoelastic material is similar to the linear elastic solution expressed in the Laplace transform space [235]. Thus by replacing viscoelastic operators instead of elastic constants, we find the Laplace transform of the solution to the time-dependent problem. In particular, the extended correspondence principle applies also to time-dependent boundary conditions as long as the loading is monotonically increasing as is the case for scratch tests [235, 245]. The key is to have a strictly increasing loading so that the boundaries of the region probed are always expand-

ing. The extended correspondence principle has been applied to model indentation cases [58, 89, 246] in which boudary of the domain increases monotonically due to increasing penetrations depths. The extended correspondence principle has also been applied to model moving cracks in viscoelastic solids [242, 247–249]. In our scratch tests, those two conditions are applied: the penetration depth increases and crack propagate; thus, the extended correspondence principle is applicable.

Plane strain conditions are considered to coincide with the LEFM solution [111, 112, 115]. Under plane strain conditions, we consider the following class of stress and strain fields:

$$\underline{\underline{\sigma}}(t) = \sigma_{xx}(t)\underline{e}_x \otimes \underline{e}_x + \sigma_{yy}(t)\underline{e}_y \otimes \underline{e}_y \tag{9.16}$$

$$\underline{\underline{\varepsilon}}(t) = \varepsilon_{xx}(t)\underline{e}_x \otimes \underline{e}_x + \varepsilon_{zz}(t)\underline{e}_z \otimes \underline{e}_z \tag{9.17}$$

where $\otimes$ designates the dyadic product [243, 244]. For this class of fields, Equations 9.8, 9.9 and 9.10 are automatically satisfied. By solving the remaining Equations 9.11–9.13, it comes:

$$\widehat{\sigma_{xx}}(s) = s\widehat{M}(s)\widehat{\varepsilon_{xx}}(s) \tag{9.18}$$

$\widehat{M}(s)$ is the Laplace transform of the plane strain modulus $M(t)$ defined by:

$$M(t) = \mathcal{L}^{-1}\left(4\widehat{\mu}(s)\frac{3s\widehat{\kappa}(s) + s\widehat{\mu}(s)}{3s\widehat{\kappa}(s) + 4s\widehat{\mu}(s)}\right) \tag{9.19}$$

Here, we use the notation $\mathcal{L}^{-1}(\cdot)$ to indicate the inverse Laplace transform operator. We also introduce M_0 as the initial plane strain modulus. If a constant strain rate $\varepsilon_{xx}(t) = \dot{\epsilon_0}t$ is applied, then, in the time domain, the stress is connected to the initial plane strain modulus M_0 via:

$$\sigma_{xx}(t) = \bar{\lambda}(t)M_0\epsilon_{xx}(t) \tag{9.20}$$

where $\bar{\lambda}$ is a *plane strain viscoelastic factor* defined by:

$$\bar{\lambda}(t) = \frac{1}{M_0 t}\mathcal{L}^{-1}\left(\frac{s\widehat{M}(s)}{s^2}\right) = \int_0^1 \frac{M(tu)}{M_0}du \tag{9.21}$$

Energy Release Rate

The elastic strain energy is given by $\psi^{el} = \frac{\sigma_{xx}^2(t)}{2M_0}$ where $M_0 = 4\mu_0(3\kappa_0 + \mu_0)/(3\kappa_0 + 4\mu_0)$, and κ_0 and μ_0 are the initial bulk and shear modulus respectively. Let's define the *energy ratio*, $\bar{\gamma}$, by the ratio of the frozen energy to the elastic strain energy $\bar{\gamma} = U\left(\underline{\underline{\varepsilon}}^v\right)/\psi^{el}$. The volume density of the Helmholtz free energy is then related to the stress components by:

$$\psi = [1 + \bar{\gamma}(t)]\,\frac{\sigma_{xx}^2(t)}{2M_0} \tag{9.22}$$

By application of Equation 9.6, the energy release is then equal to Equation 9.23.

$$\mathcal{G} = A/p\left[\frac{1}{\bar{\lambda}(t)} - \frac{1}{2}\left(1 + \bar{\gamma}(t)\right)\right]\frac{\sigma_{xx}^2(t)}{M_0} \tag{9.23}$$

On the other hand, we have: $\sigma_{xx}(t) = F_T(t)/A$. Therefore, the energy release rate reads as:

$$\mathcal{G} = \frac{1}{2M_0}\frac{F_T^2}{pA}\left[\frac{2}{\bar{\lambda}(t)} - 1 - \bar{\gamma}(t)\right] \tag{9.24}$$

where p is the perimeter of the probe and A is the projected load bearing contact area. We note the presence of a *viscoelastic correction factor*, $\mathcal{H}(t)$, that takes into account the viscoelastic dissipation. $\mathcal{H}(t)$ is related to the plane strain viscoelastic multiplicator, $\bar{\lambda}(t)$ and to the energy ratio $\bar{\gamma}(t)$ by Equation 9.25:

$$\mathcal{H}(t) = \left[\frac{2}{\bar{\lambda}(t)} - 1 - \bar{\gamma}(t)\right] \tag{9.25}$$

At this stage, we apply the fracture criterion. The crack propagates when the energy release rate reaches a threshold: $\mathcal{G} = G_f$. Thus, the condition $\mathcal{G}(t_c) = G_f$ defines the moment t_c when fracture occurs and defines the evolution of the scratch toughness as well. t_c is called the *time-to-fracture*. Therefore, by application of the fracture criterion, the evolution of the scratch toughness can be described via:

$$\frac{F_T}{\sqrt{2pA}} = \frac{K_{c0}}{\sqrt{\mathcal{H}(t_c)}} \tag{9.26}$$

with $K_{c0} = \sqrt{G_f M_0}$. Thus, we predict a coupling between fracture and the viscoelastic

behavior. In the next sections, we specify the expression of $\mathcal{H}(t)$ for standard rheological models.

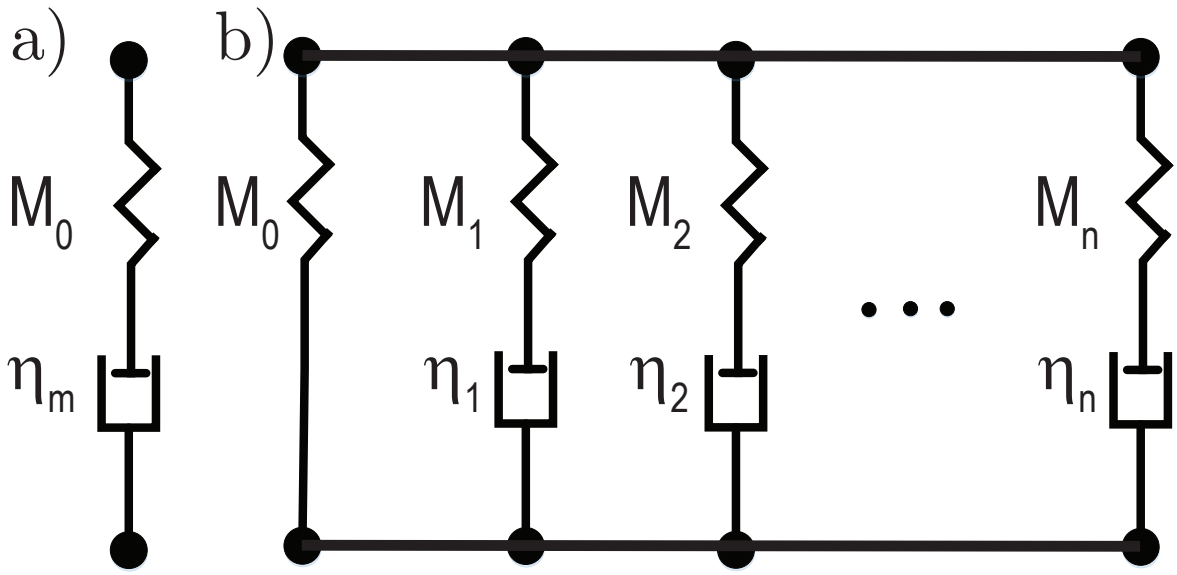

Figure 9.4: Common viscoelastic rheological models: a) Maxwell and b) Maxwell-Wiechert.

9.3.1 Application to a Maxwell Model

When studying the creep behavior of rocks, cements, and polymers, it is very common to assume a constant Poisson's ratio [95]. The Maxwell model consists of a purely viscous damper of viscosity η and a purely elastic spring of stiffness M_0 connected in series as illustrated in Figure 9.4 a). It corresponds to the case where the relaxation modulus exhibits a single characteristic time $\tau = \eta_M/M_0$. In that case, there is no frozen energy. The energy ratio and the plane strain viscoelastic factor for a Maxwell material read:

$$\bar{\gamma}(t) = 0; \quad \bar{\lambda}(t) = \frac{1 - e^{-t/\tau}}{t/\tau} \tag{9.27}$$

For $t/\tau \to 0$, $\bar{\lambda}(t) = 1$, and $F_T/\sqrt{2pA} \to K_{c0}$. In other words, the theory predicts that for short testing periods—usually achieved using high scratching speeds—, the scratch toughness converges towards a constant value, $K_{c_0} = \sqrt{G_f M_0}$. In contrast, for $t/\tau \to +\infty$, $\bar{\lambda}(t) \to 0$, and $F_T/\sqrt{2pA} \to 0$. For long testing periods—usually achieved at a slower pace—, the scratch toughness decreases to be very small and vanishing. Another

way of understanding the predicted evolution of $F_T/\sqrt{2pA}$ is by considering the scratch schematic on a Maxwell material shown in Figure 9.3. At high scratch speeds, the external work provided is stored in the piece of material in front of the blade and then released to propagate fracture surfaces; because the test is short, there is not enough time for viscous processes to develop. In contrast, for very slow tests, viscous dissipation is prevalent and the fracture dissipation becomes negligible.

9.3.2 Application to a Generalized Maxwell Model

Although very convenient, the Maxwell model neglects the fact that there can be several viscous mechanisms described by different characteristic time constants. Another limitation of the Maxwell model, is that it cannot account for the presence of frozen energy that occurs due to permanent structural changes in porous and granular materials [239]. In the case of complex viscous mechanisms, it is best to use the generalized Maxwell model also known as the Maxwell-Wiechert or Prony series. The generalized Maxwell model can be thought of as several Maxwell units in series as illustrated in Figure 9.4 b). Each Maxwell unit i is characterized by a stiffness $M_i = p_i M_0$ and a viscosity η_i resulting in a characteristic time $\tau_i = \eta_i/M_i$. M_0 is the initial plane strain modulus and $\{p_i\}$ are the Prony series parameters. The plane strain modulus is defined by:

$$M(t) = M_0 \left(p_0 + \sum_{i=1}^{n} p_i \exp(-t/\tau_i) \right) \tag{9.28}$$

The generalized Maxwell model is versatile and can be employed to fit a wide array of relaxation curves. The Maxwell-Wiechert model is usually represented via a series of individual Maxwell units in parallel. In this case, the plane strain visco-elastic coefficient is given by a weighted average of functions $\bar{\lambda}_i$ defined by:

$$\bar{\lambda}(t) = \sum_{i=0}^{n} p_i \bar{\lambda}_i(t) \tag{9.29}$$

$$\bar{\lambda}_0 = 1; \quad \bar{\lambda}_i = \frac{1 - e^{-t/\tau_i}}{t/\tau_i}, i = 1...n \tag{9.30}$$

For a Prony series, the Helmholtz free energy is the sum of the contribution from each Maxwell unit. In turn, the frozen energy is non-zero and the energy ratio reads:

$$\bar{\gamma}(t) = \sum_{i=0}^{n} p_i \left[\frac{\bar{\lambda_i}(t)}{\sum_{i=1}^{n} p_i \bar{\lambda_i}} \right]^2 - 1 \tag{9.31}$$

For slow speeds, $V \propto 1/t \to 0$, $t/\tau \to +\infty$, $\bar{\lambda}(t) \to p_0$, and $F_T/\sqrt{2pA} \to \sqrt{p_0} K_{c0}$. For high speeds, $F_T/\sqrt{2pA} \to K_{c0}$, with $K_{c0} = \sqrt{G_f M_0}$. In other words, due to the frozen energy, at slow speeds, the scratch toughness is small but non-zero. In the next steps, we will apply our theoretical model to shed light on the influence of the loading rate and scratching speed on the scratch testing of organic-rich shale materials.

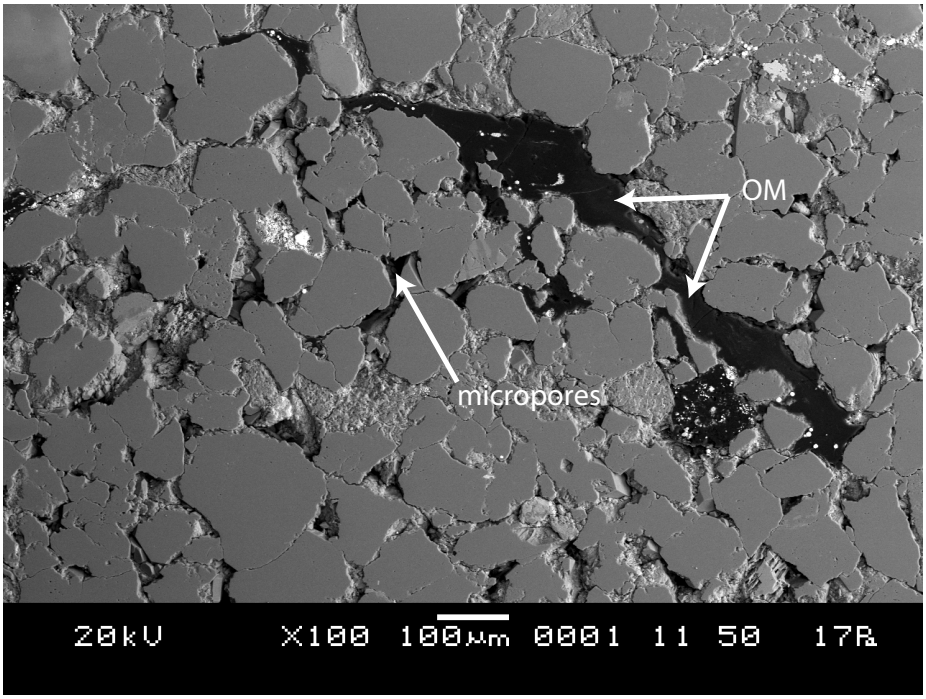

Figure 9.5: Scanning electron microscopy of Toarcian gas shale. (1) Organic-rich pocket. (2) Micro-pore.

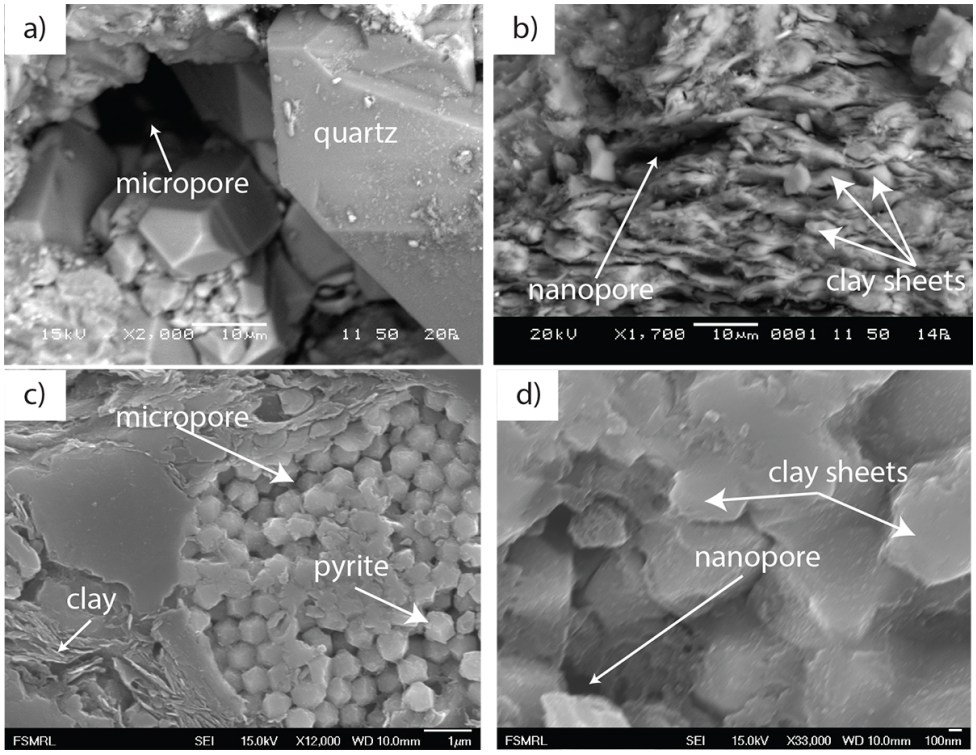

Figure 9.6: Nano-scale constituents of Toarcian (a)-b)) and Niobrara (c)-d)) shale. a) Quartz crystal. b) Illite platelets. c) pyrite framboids and d) illite flakes.

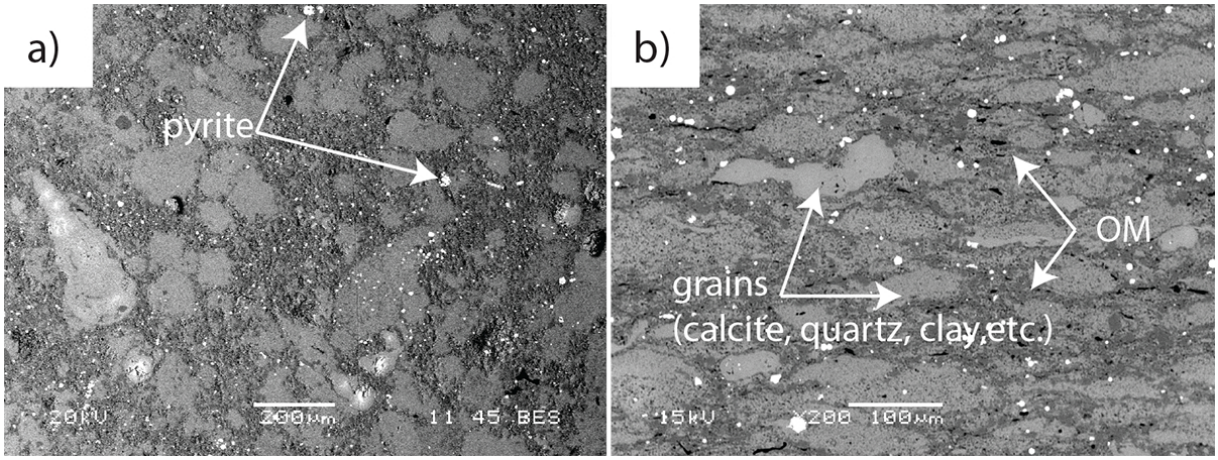

Figure 9.7: a) SEM image of Niobrara shale in the bedding plane. b) SEM image of Niobrara shale perpendicular to the bedding plane. OM stands for organic matter. Courtesy of Prof. Akono

9.4 Does Organic-Rich Shale Creep?

9.4.1 Microstructure and Chemistry

The micro-structure and chemistry are important elements that govern the mechanical response of shale systems [250–253]. As such, micro-structural and chemical characterization is key to obtain true insights into the fracture response. To this end, we employ scanning electron microscopy and environmental scanning electron microscopy. Figure 9.5, Figure 9.6 and Figure 9.7 display scanning electron microscopy images of both grey shale—Toarcian— and black shale—Niobrara—specimens. The goal of the SEM is to highlight some features on the microstructure and composition and they complement the XRD analysis. As shown in Figure 9.5, a granular and heterogeneous micro-structure was observed for Toarcian specimens with a grain size of 50–100 μm. Given the grain size, we considered only tests for which the width of the scratch path in the fracture-driven domain is 300 μm and above; in addition, the minimum scratch length considered was 0.3 mm. Thus for all scratch lengths considered,—0.3 mm to 6 mm—the volume probed was large enough to be representative of the material at the meso-scale.

No significant anisotropy was observed for Toarcian shale. In Figure 9.5, among grains, we can observe black pockets 1) corresponding to organic-rich phases as well as micro-pores 2) inside and at the interface of grains. As for Niobrara shale shown in Figure 9.7 a)–b), there is a striking anisotropy. A laminar micro-structure is observed for a transverse cut, with the particles being elongated in the horizontal direction. In contrast, within the bedding plane, the particle arrangement is disordered. The composition is also non-uniform: dark grey pockets correspond to organic-rich phases; meanwhile the light grey inclusions represent clay or calcite and the white particles represent pyrite particles. By organic-rich pocket or phases, we mean clay composites where the micro- and nanopores are filled with gaseous kerogen or kerogen particles are adsorbed to clay minerals.

A closer look is necessary to properly identify micro- and nano-constituents. For instance, Figure 9.6 displays high-resolution scanning electron micro-graphs of both Toarcian and Niobrara shale with magnification levels ranging from $\times$1,700–$\times$33,000. Figure 9.6 a) shows the presence of 10-μm long hexagonal quartz crystals along with a 15-μm round micro-pore on Toarcian shale. Figure 9.6 displays 100-nm thick clay platelets vertically stacked as well as the existence of nano-pores with a 200-nm average size. The findings of our E/SEM imaging are in agreement with the results from X-ray diffraction

analysis.

The micro-structural observations points to a wide range of viscous processes that originate at different length-scales. At the microscopic levels, viscous processes are generated due to the friction between grains and the change in free volume in the granular skeleton [138]. At the nanometer length-scale, the sliding of clay nanoplatelets gives rise to viscous dissipation [254–258]. . Furthermore, creep is also linked to the presence of organic matter: recent studies showed that kerogen is a cross-linked polymer [259]. As such, chain rotations, chain entanglements and chain sliding are potential bulk energy dissipation mechanisms [260].

9.4.2 Viscoelastic Behavior

According to Equation 9.26, it is important to evaluate the viscoelastic behavior so as to decouple stress relaxation and fracture. To this end, 600 creep indentation tests were carried out as explained in previous sections, cf. Figure 9.8 a). Given a single creep indentation test, the contact creep compliance $L(t)$ is measured from the depth increment during the holding phase $\Delta h(t)$ according to [90, 95, 234]:

$$L(t) - \frac{1}{M_0} = \frac{2a_U \Delta h(t)}{P_{max}} \tag{9.32}$$

where $a_U = S/(2M_0)$ is the contact radius, $S = dP/dh$ is the indentation stiffness and M_0 is the initial indentation modulus. Figures 9.8 b)–c) display the vertical load history as well as a representative load-depth curve. The initial indentation modulus M_0 is calculated from the initial unloading slope, cf. Figure 9.8 b), according to the Oliver & Pharr method [79]. Figure 9.8 displays the increment of indentation depth under constant vertical load, during the holding phase. A logarithmic creep response was observed, which is common in sedimentary and igneous rocks [261, 262]. For a logarithmic creep, the contact creep compliance is of the form $L(t) = \frac{1}{M_0}\left(1 + \frac{M_0}{4C}\ln\left(1 + \frac{t}{\tau_{cr}}\right)\right)$ where C is the contact creep modulus and τ_{cr} is the characteristic time of the material.

Table 9.2 lists the visco-elasto-plastic constants—M_0, C, τ_{cr}, and H—measured for both Toarcian and Niobrara shale specimens. Our experiments support the general observation that in earth materials, stiffness and strength are positively correlated. Grey shale (Toarcian) are much stiffer and stronger than black shale (Niobrara) that is more compliant and softer. Grey shale specimens exhibit high hardness values due to their

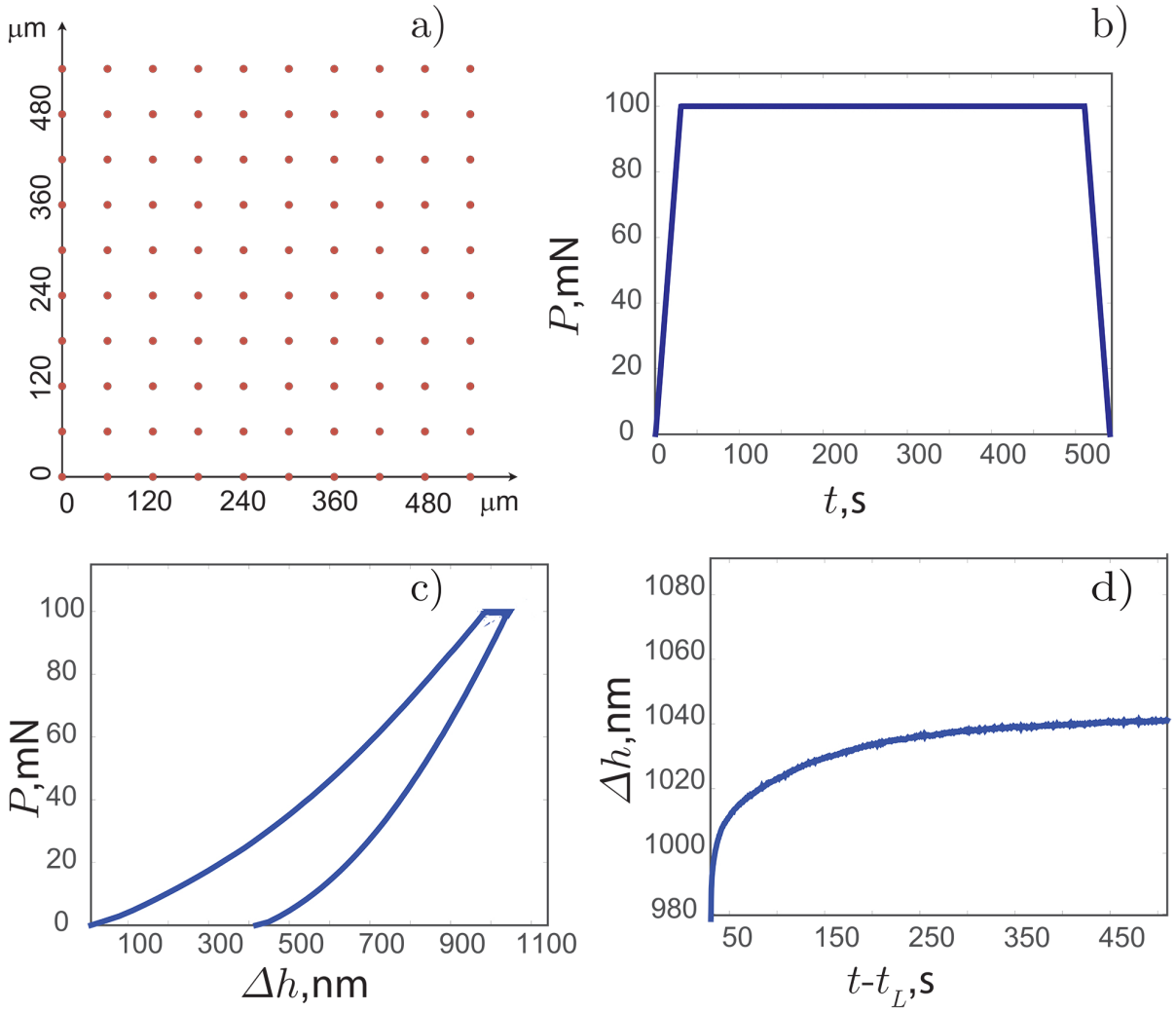

Figure 9.8: a) Micro-indentation grid. b) Prescribed load history. c) Representative load-depth curve. d) Increment of indentation depth during holding phase. P is the prescribed vertical load, $t_L = 30$ s is the duration of the loading step, Δh is the depth increment during the holding phase and t is the time.

high quartz content. In contrast, black shale are softer and more compliant due to the higher amount of clay and organic matter. Moreover, the high volume fraction of clay and organic matter is favorable to viscous process such as sliding movement between clay nanosheets or chain rotations in kerogen. As a results, black shale exhibit a lower contact creep modulus C compared to grey shale. Furthermore, Niobrara shale exhibit a slight anisotropy due to the laminar microstructure, cf. Figure 9.7 and the presence of clay minerals, cf. Figure 9.6 d).

Table 9.2: Logarithmic Creep Constants for grey (Toarcian B1, B2, and B3) and black (Niobrara) shale systems and for different orientations. M_0 is the initial indentation modulus, C is the contact creep modulus, τ_{cr} is the logarithmic creep characteristic time, and H is the indentation hardness.

Material	M_0 (GPa)	C (GPa)	τ_{cr} (s)	H(GPa)
B1	52.73	414.6	0.134	5.42
B2	58.76	587.6	0.067	6.14
B3	57.58	431.2	0.113	6.00
Niobrara-$\perp$ to bedding plane	47.84	97.0	0.116	1.07
Niobrara-$\parallel$ to bedding plane	48.04	104.3	0.130	1.11

Table 9.3: Coefficients of plane strain modulus described: $M(t)/M_0 = p_0 + \sum_i p_i \exp(-t/\tau_i)$, cf. Equation 9.28. The values of M_0 are given in Table 9.2.

Material	p_0	p_1	p_2	p_3	τ_1 (s)	τ_2 (s)	τ_3 (s)
B1	0.79	0.109	0.030	0.069	1.30	21.27	142.85
B2	0.83	0.050	0.061	0.062	1.05	2.55	103.20
B3	0.79	0.087	0.054	0.068	0.97	6.65	104.60
Niobrara-$\perp$ to Bedding	0.49	0.313	0.090	0.100	1.41	18.21	158.75
Niobrara-$\parallel$ to Bedding	0.50	0.289	0.105	0.102	1.21	12.33	141.44

Based on the creep behavior, the relaxation behavior was evaluated. The creep compliance $L(t)$—measured via creep indentation tests— and the plane strain relaxation modulus $L(t)$ are conjugate quantities. In particular, the following equations hold [235,

236]:

$$\int_0^t M(t-u)L(u)du = \int_0^t L(t-u)M(u)du = t \tag{9.33}$$

$$\widehat{M}(s)\widehat{L}(s) = \frac{1}{s^2} \tag{9.34}$$

where s is a complex number frequency parameter in the Laplace domain.

Thus given, the creep compliance, $L(t)$, we can calculate the plane strain relaxation modulus $M(t)$ through Laplace inversion. A numerical Laplace inversion algorithm was carried out [263] to calculate the plane strain relaxation modulus $M(t)$. The logarithmic creep leads to a continuum spectrum of relaxation times. In turn, this continuum spectrum points to the multiple source of viscous dissipation in organic-rich shale: granular microstructure, clay fabric and organic matter. We discretize the continuum spectrum into a Pony series representation, cf. Equation 9.28. Table 9.3 gives the plane strain relaxation modulus function for each material in each orientation. The calculated Prony series representation is given for each material and each orientation. As expected, black shale–which creeps more because of the high clay fraction and total organic content—exhibits a lower p_0 coefficient.

9.4.3 Fracture Processes During Scratch Testing

Environmental scanning electron microscopy was utilized to examine the presence of fracture surfaces in Niobrara shale during scratch testing. We focus on the fracture-driven regime (cf. Figure 9.1 b) and seek to understand the nature and shape of the generated fracture surfaces. In Figure 9.9 a), c), and d), we see the presence of debris inside an at the edges of the groove. The debris are a result of material removal processes. Figure 9.9 b) shows a micro-crack with a crack front which is curved and perpendicular to the direction of scratch testing. Due to the width of the crack, 50 nm, it is not possible to tell whether the generated crack surface is vertical or horizontal. Nevertheless, Figure 9.9 supports the hypothesis of a semi-circular horizontal crack that originates below the tip of the indenter and propagates outward and forward below the surface. Furthermore, Figure 9.9 a) shows a succession of micro-cracks pointing to several consecutive micro-fracture events. In this regime where fracture is predominant, the scratch force scales as $F_T \propto \sqrt{2pA}$ as shown in Figure 9.1. Due to the scaling of the force and the physical evidence of fracture phenomena, it is reasonable to consider ductile behavior negligible

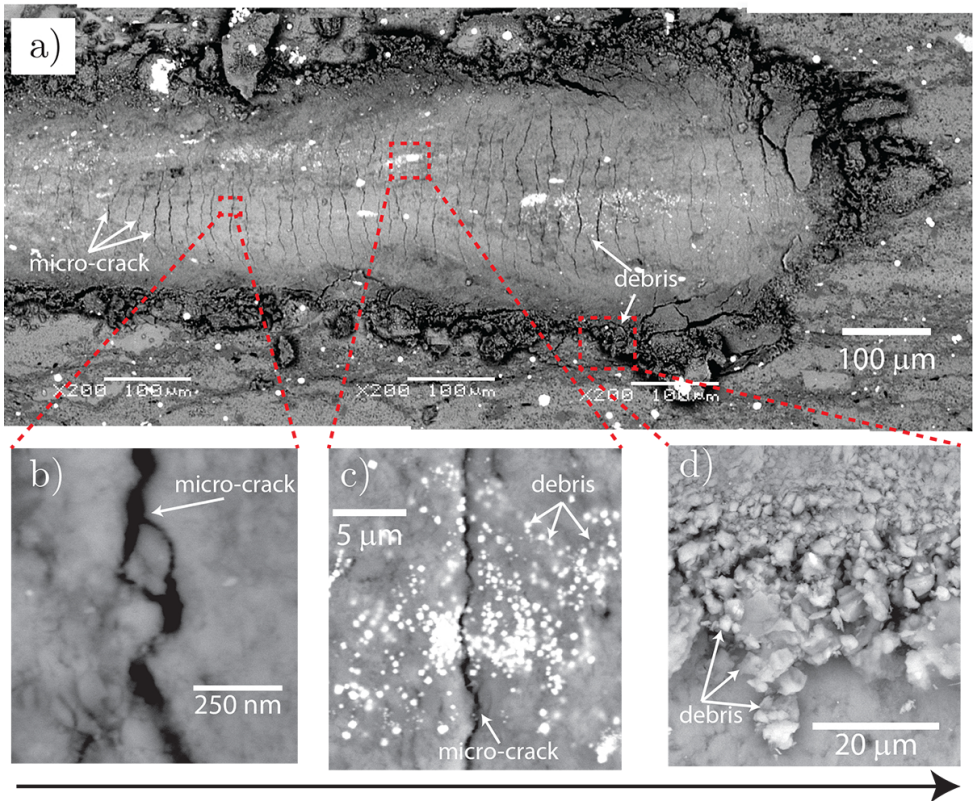

Figure 9.9: Fracture processes in organic-rich shale during scratch testing: ESEM images of top surface after testing. a) Presence of a residual groove with debris and fracture surfaces. b) Micro-crack. c) Micro-crack and debris. d) Debris at the edge of the groove.

and adopt a nonlinear visco-elastic fracture modeling as done in previous section.

9.5 Influence of Rate on Fracture Behavior

Figure 9.10 displays the scratch toughness $F_T/\sqrt{2pA}$ for 360 scratch tests carried out on grey shale—Toarcian— and black shale—Niobrara—specimens at different scratch speeds and loading rates. Each data point corresponds to three consecutive scratch tests carried out under a constant speed and loading rate. By considering the force and depth measurements at large penetration depths, and taking into account the scratch probe shape function, one can calculate the apparent toughness K_s from Equation 9.1 as shown in Figure 9.1. For all six specimens and all three scratch orientations—defined in Figure 9.2—, the scratch toughness K_s increases when the scratch speed V increases. Given a loading rate $\dot{F}_V$, at low speeds, the scratch toughness is small; however, as the scratch speed increases by nearly two orders of magnitude, the scratch toughness is multiplied by two.

At first, the increase in scratch toughness with the scratch speed could be attributed to the frictional properties of shale materials. In fact, for clay-rich materials, the friction increases linearly with the logarithm of sliding velocity [264, 265]. The origin of the time-dependent increase of friction is the indentation creep effect [266, 267]. When two surfaces are brought in contact, each contact point locally behaves as a small indent. As time increases the depth of penetration increases and so does the local contact area. As the top surface slides forth, the old contact points are discontinued as a new population of contact points is forged. However, this transition from old contact points to new ones is continuous as no microscopic crack was observed. Thus the friction increase has a different origin from the rate-dependent scratch tests: indentation creep for the former versus stress relaxation and fracture for the latter. In addition, no microscopic fracture surface was observed in speed-dependent friction tests. In contrast, Figure 9.9 shows the presence of microscopic fracture surfaces during scratch testing. Thus, the frictional behavior of clay-bearing material is not a suitable observation for the evolution of the scratch toughness with the scratch speed.

On the contrary, the significant increase of the scratch toughness with the scratch speed is evidence of a competition between viscous dissipation and fracture processes. For Toarcian B1 and B2 specimens, we note a convergence of the scratch toughness K_s at high speeds towards a constant value which appears to be invariant with respect to the

loading rate. A more detailed analysis is needed to identify a potential rate-independent toughness value. As expected, for Niobrara shale, the scratch toughness varies with the scratch orientation. The scratch toughness is higher for the divider orientation than for the short transverse or the arrester.

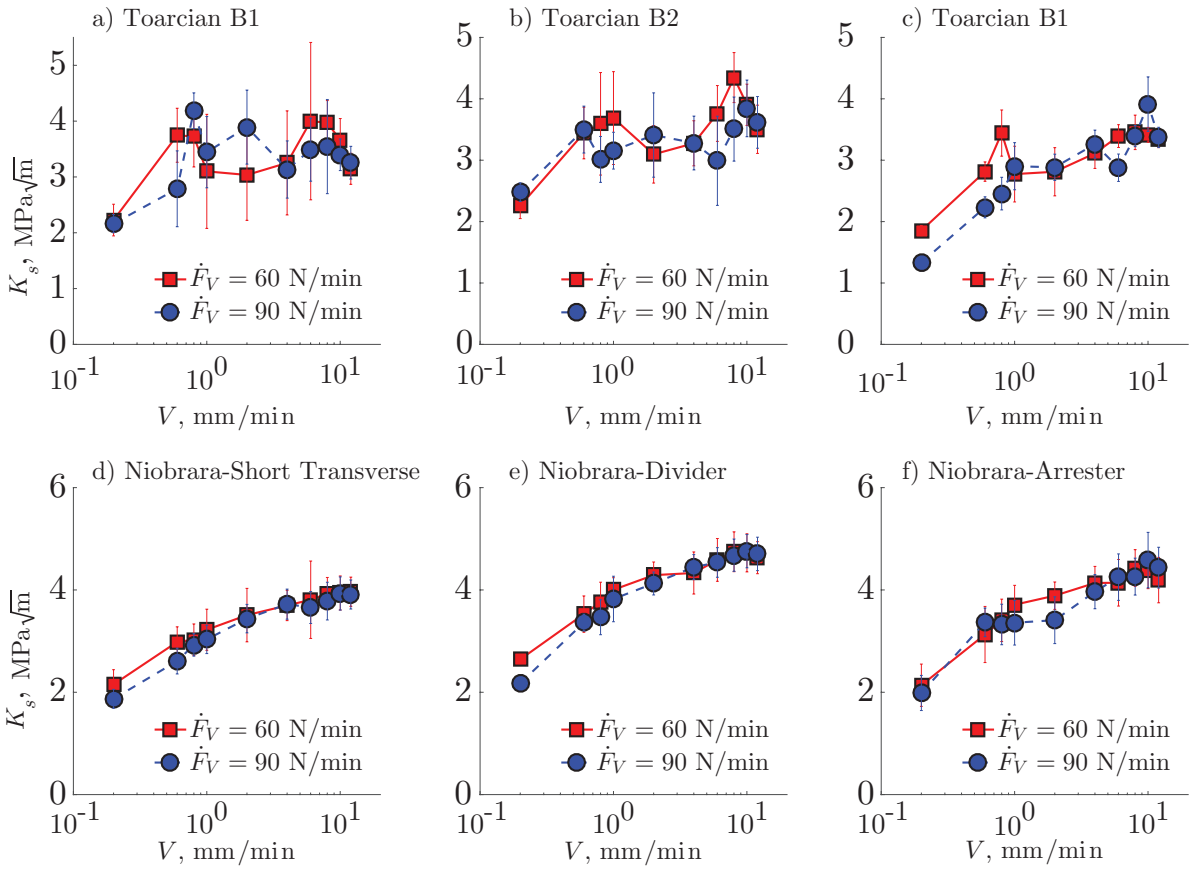

Figure 9.10: Scratch test data on grey (Toarcian) and black (Niobrara) shale specimens. a) Toarcian B1 specimen. b) Toarcian B2 specimen. c) Toarcian B3 specimen. d) Niobrara-Short Transverse orientation e) Niobrara-Divider orientation f) Niobrara-Arrester orientation. Two loading rates: 60 N/min and 90 N/min were considered.

9.5.1 Intrinsic Fracture Toughness

We implement our theoretical model, cf. Equation 9.26 in order to describe the observed scratch response. To this end, we integrated the scratch tests and indentation data. First, we must correlate the scratch time-to-fracture t_c to prescribed rates. From Dimensional Analysis, the scratch toughness is related to the loading rate $\dot{F}_V$, scratch speed V and

mechanical constants—M_0, K_c, and τ_{cr}—according to [110, 227]:

$$K_s = \mathcal{F}_2 \left(\frac{K_c^2/M_0^2}{\tau_{cr} V}, \frac{\dot{F}_V}{V} \frac{M_0}{K_c^2} \right) \tag{9.35}$$

Therefore, we identify two invariants: $\frac{K_c^2/M_0^2}{\tau_{cr} V}$ and $\frac{\dot{F}_V}{V} \frac{M_0}{K_c^2}$ Thus, we introduce two dimensionless material constants, c and V_0 that link the time-to-fracture to the scratching speed and the loading-rate-to-scratching-speed ratio [110, 227]:

$$\frac{t_c}{\tau_{cr}} = c \frac{\dot{F}_V}{V} + \frac{V_0}{V} \tag{9.36}$$

The parameter t_c/τ_{cr} characterizes the relative importance of viscous dissipation. For $t_c/\tau_{cr} \gg 1$, bulk viscous dissipation is predominant, whereas, for $t_c/\tau_{cr} \ll 1$, viscous processes are negligible. $\frac{1}{c}$ has units of a surface energy. V_0 is a critical speed value induced by the fracture process that captures the influence of the scratching speed for tests performed with a constant vertical force. τ_{cr} is the logarithmic creep characteristic time of the material.

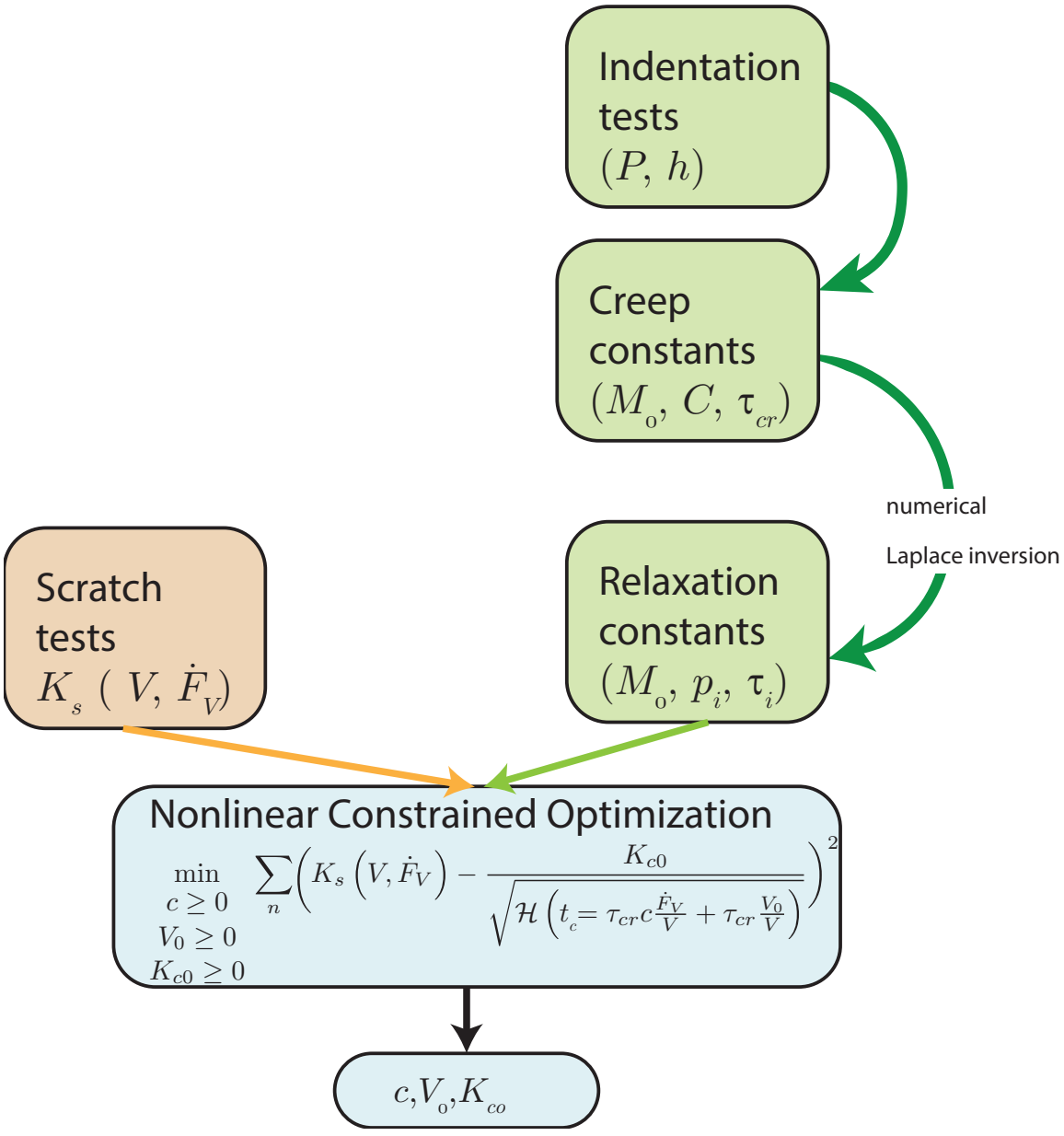

Figure 9.11: Intrinsic fracture toughness assessment: workflow.

Figure 9.11 illustrates our workflow process. Step 1: scratch test data are collected for various scratch speeds V and loading rates $\dot{F}_V$ as shown in Figure 9.10. Step 2: Indentation tests are carried out as illustrated in Figure 9.8. Step 3: the viscoelastic creep constants are extracted from the indentation test data by application of the indentation viscoelastic model by Vandamme and coworkers [90, 95, 234]. The viscoelastic characteristics are reported in Table 9.2. Step 4: the plane strain relaxation modulus $M(t)$ is calculated. Step 5: a nonlinear constrained optimization algorithm is performed to calculate the model parameters c, V_0, and K_{c0} by minimizing the equation below:

$$\min_{c,V_0,K_c} \sum_n \left(K_s\left(V, \dot{F}_V\right) - \frac{K_{c0}}{\sqrt{\mathcal{H}\left(t_c\right)}} \right)^2 \tag{9.37}$$

where $n \in [1, N]$ refers to the number of scratch tests performed ($N = 60$ per material and per orientation). $\mathcal{H}$ is the viscoelastic correction factor for a Generalized Maxwell model defined by Equations 9.25, 9.29,9.30, and 9.31.

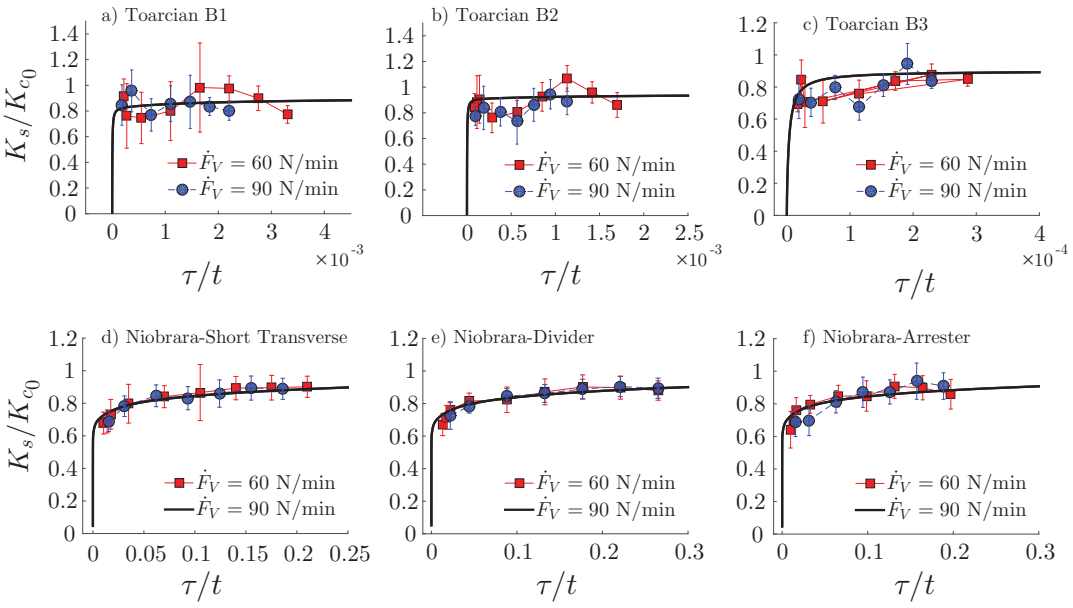

Figure 9.12: Intrinsic fracture toughness assessment: analytical model vs. experimental data on grey (Toarcian), and black (Niobrara) shale. a) B1 specimen. b) B2 specimen. c) B3 specimen. d) Niobrara-Short Transverse orientation. e) Niobrara-Divider orientation. f) Niobrara-Arrester orientation. τ_{cr} is the logarithmic creep characteristic time calculated in Table 9.2 whereas t_c is the time-to-fracture given by Equations 9.36 and 9.37.

Figure 9.12 confronts the theoretical model with experimental scratch test data. Figure 9.12 displays the scratch toughness as a function of τ_{cr}/t_c where the time-to-fracture t_c is given by Equation 9.36 and τ_{cr} is the logarithmic creep characteristic time. For all three Toarcian shale specimens and the three orientations for Niobrara shale, the analytical model is able to accurately reproduce the experimental data. Thus, although in organic-rich shale there is a strong coupling between creep and fracture, by carefully selecting the scratch speed and loading rate, it becomes possible to reduce the effect of viscous behavior.

Table 9.4: Intrinsic fracture toughness: generalized Maxwell model. K_{c0} is the rate-independent fracture toughness, and c and V_0 are material parameters that describe the coupling between creep and fracture. The root mean squared error (RMSE) is provided.

Material	K_{c0} (MPa$\sqrt{m}$)	c ($\frac{mm}{N}$)	V_0 ($\frac{mm}{min}$)	RMSE
B1	4.09	57.20	0.81	0.3198
B2	4.07	117.78	1.25	0.3747
B3	4.02	582.43	0.54	0.36
Niobrara-Short Transverse	4.40	0.2462	42.36	0.1288
Niobrara-Divider	5.26	0.001	45.23	0.1337
Niobrara-Arrester	4.88	0.09	55.42	0.2254

Table 9.4 summarizes the computed values of K_{c0}, c and V_0 for all six specimens and three orientations. Herein, the rate-independent fracture toughness is $K_{c0} = \sqrt{G_f M_0}$. Where as the grey shale specimens exhibit similar values of c and V_0, for black shale, c is an order of magnitude smaller and v is an order of magnitude larger. Ultimately, the scratch toughness K_s is a function of the intrinsic fracture toughness K_c, the time-to-fracture t_c and the viscoelastic correction factor $\mathcal{H}$, which depends on the viscoelastic properties. Thus, the material constants c and v_0 cannot be compared separately. Nevertheless, the low root mean squared error, point toward the validity and accuracy of our modeling approach to represent the observed mechanical behavior.

For grey shale (Toarcian), the rate-independent fracture toughness is in the range 4.02–4.09 MPa$\sqrt{\text{m}}$. As for black shale (Niobrara), the intrinsic fracture toughness is in the range 4.40–5.26 MPa$\sqrt{\text{m}}$. There is a stark anisotropy that can be traced back to the presence of clay minerals as well as the layered microstructre. The rate-independent fracture toughness is highest for the divider orientation and is lowest for the short trans-

verse orientation. These findings are in agreement with previous reports of anisotropy in fracture behavior as witnessed in Mancos shale [209] and oil shale [206]. Furthermore, at the nanometer length-scale, atomistic simulations reveal an intrinsic anisotropic fracture behavior of clay [223]. In illite, in mode II, mechanical energy is dissipated by the sliding of clay layers thereby inhibiting crack propagation [223]. As a consequence, the fracture toughness is higher for crack perpendicular to the layers than along the toughness of illite or smectite as measured via molecular dynamics is 0.12 MPa$\sqrt{m}$ for fracture along the clay layers and 0.61 MPa$\sqrt{m}$ for fracture perpendicular to the clay layers.

9.5.2 Composition-Strength-Toughness Relationships in Organic-Rich Shale

Our fracture tests reveal that black shale (Niobrara) exhibits a higher fracture toughness Niobrara compared to grey shale (Toarcian). A first, this finding may seem counter-intuitive given that grey shale are stronger and stiffer than black shale. However, one must take into account the mineralogy, the presence of kerogen, and the nature of the kerogen-clay interfaces. The high toughness of Niobrara is due to its micro-consituents: clay and kerogen. In turn Toarcian shale specimen exhibit lower fracture toughness values due to the high quartz content. The fracture toughness of quartz is 0.8 for silica and 1.1 Mpa$\sqrt{m}$ for α-cistobalite (metastable silica crystal) as measured via experiments and via atomistic simulations [197]. In contrast, the toughness of kerogen—which is a microporous amorphous polymer–as measured via atomistic modelling is 1.6 MPa$\sqrt{m}$. This value is in agreement with microscopic observation of a tough polymeric kerogen phase [259]. Thus, the higher fracture toughness of kerogen compared to quartz explains the higher fracture resistance of black shale.

Another explanation for the exceptional fracture resistance of black shale is the presence on intrinsic toughening mechanism at the nanometer length-scale. A potential mechanism is the unfolding of macromolecules and the rupture of sacrificial bonds via a repeatable and reversible process. Abousleiman et al. [259] carried out bending test on micro-machined Woodford shale beams at the mciroscopic scale. For beams with a high organic content, they observed that post-failure the presence of a residual ligament still connecting the severed micro-beam to its base. Abousleiman et al, explained the presence of the rod-like polymer by the high tensile strength of kerogen. However, in our experiments, a higher organic content led to a decrease in strength characteristics.

Thus, an alternative explanation is the presence of sacrificial bonds and hidden length as in the case in mineralized collagen fibrils [268]: when a force is applied to bone, the organic matrix is stretched leading to the rupture of sacrificial bonds. These bonds are weak and reformable bonds that break in order to dissipate energy and protect the integrity of more critical bonds. As a consequence of these sacrificial bonds and the hidden length available, more energy is required to break bone. In the case of kerogen, a plausible mechanism is the unfolding of macromolecules (hidden length) and the breaking of sacrificial bonds leading to a partial crack closure. This theory is able to explain Abousleiman's observations as well as our observations of a small crack gap (50 nm). Nevertheless, in order to fully test this hypothesis, additional tests are required at the nanometer level, which will be the focus of future investigations.

Another intrinsic toughening mechanism is due to the presence of weak clay-kerogen interfaces. Molecular dynamics revealed low toughness value at the silica-kerogen interface is only 0.6 MPa$\sqrt{m}$. The weak nanoscale interfaces promotes crack deflection and crack bridging, which dissipates energy. This principle—toughness through weak interfaces– is very common in mineralized biological tissues. For instance, nacre consists in a staggered array of brittle aragonite (crystalline form of calcium carbonate) platelets cemented by a 5% volume fraction of bio-glue made of proteins and polysaccharides. Whereas the mineral brings strength, the weak interfaces provide energy dissipation mechanism such as crack deflection, crack bridging, inter-granular friction and crack trapping. As a consequence, the effective toughness of nacre is order of magnitude greater than that of aragonite. Our resuls suggests that similar mechanisms are at work in organic-rich shale systems. Last but not least, at the microscopic scale, extrinsic toughening mechanisms such as crack bridging, crack deflection, and particle pull-out explain the gap between the macroscopic and the microscopic values of the fracture toughness [120].

9.6 Influence of Viscous Behavior on Fracture Behavior

The objective is to understand the influence of consideration of viscous dissipation of the hydraulic fracture at the reservoir length-scale. I employ an existing fracture model for reservoir in the literature. The model is a two dimensional elastic solution under plane strain conditions. The fracturing fluid leak off is neglected due to low permeability of the

source rock. An incompressible viscous fluid of viscosity, μ which is injected at a constant rate, Q_0, and with a finite non-zero fluid lag. The half crack length is l while the portion of the crack filled with fracturing fluid is l_f and $\xi_f = l_f/l$ is the fluid lag. I consider two case, one the Niobrara shale system without viscous dissipation and Niobrara with viscous dissipation. The focus is on the evolution of the fluid lag, ξ_f at early times.

The governing equation of the hydraulic fracturing solutions are developed based on lubrication theory, linear elastic fracture mechanics model crack propagation criterion. In addition, the fracture opening is provided by the Snedon and Lowengrubb non-local elasticity relation.

The MKO parametric space [25, 269–271] where the K-space represent the toughness driven solution. The M-space represents the viscosity driven solution. Three invariants (Equations 9.38–9.41) are of great importance to capture the physics of the problem [272, 273].

$$\mathcal{K}_m = \frac{K'}{M^{3/4} Q_0^{1/4} (\mu')^{1/4}} \tag{9.38}$$

$$\mathcal{M}_k = \frac{M^3 Q_0 \mu'}{(K')^4} \tag{9.39}$$

$$\tag{9.40}$$

$$\mathcal{T}_m = \frac{-p_t}{E'} \left(\frac{Mt}{\mu'} \right)^{1/3} \tag{9.41}$$

$\mathcal{T}_m$ is the underpressure time, whereas both the viscosity $\mathcal{M}_k$ and the toughness $\mathcal{K}_m$ scalings determine the propagation regime [25, 272, 273]. Herein, the parameters for the model assumed to be $\mu = 0.3$ cP, $\sigma_0 = 25$ MPa, and $Q_0 = 0.2$ m^3/s.

Figure 9.13 displays the predicted fluid lag ξ_f as a function of the underpressure time $\mathcal{T}_m$ for the two different cases of Niobrara shale materials. Given the low non-zero values of the toughness scaling and for early propagation times, the small underpressure, small toughness solution prevails. Thus the fluid lag is solution of an implicit equation [272]. The fluid lag is higher for the case of Niobrara without consideration of viscous dissipation

whereas the fluid lag is lower if the viscous dissipation is considered. Thus, consideration of viscous dissipation when calculating the fracture toughness of the reservoir rock is necessary.

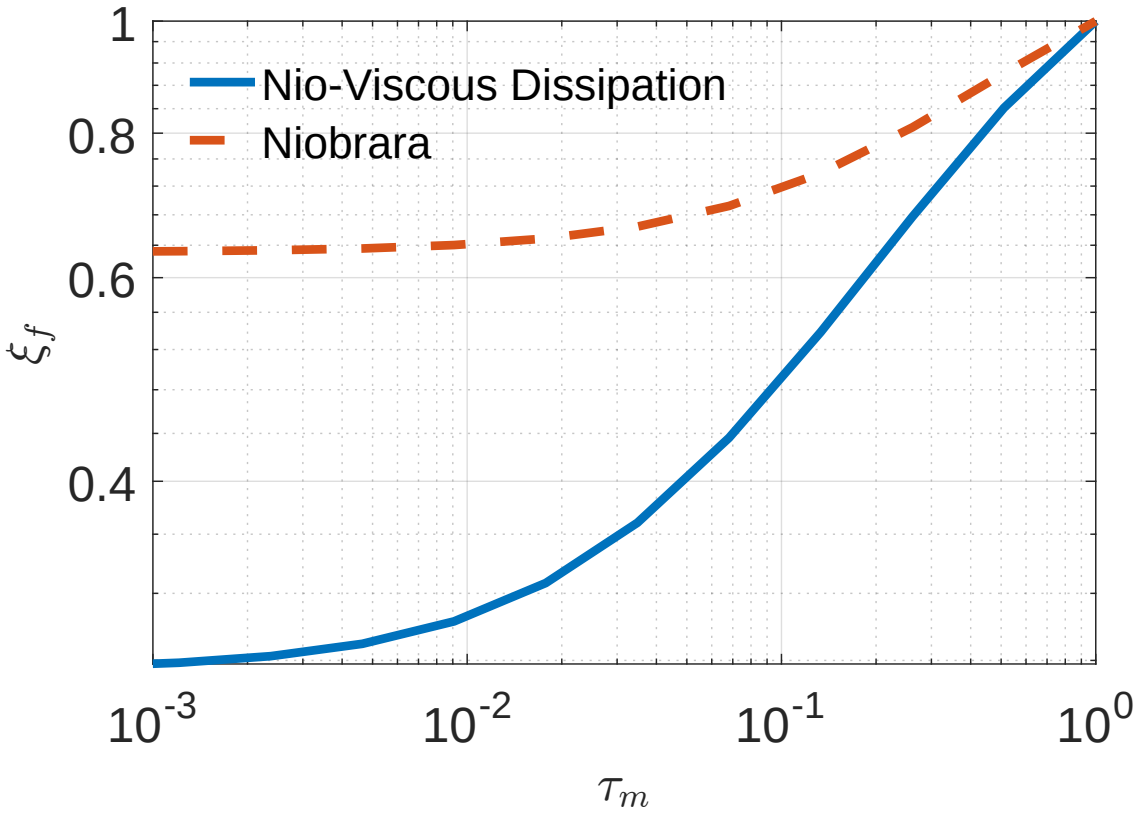

Figure 9.13: Influence of Viscous Dissipation Consideration on Hydraulic Fracturing Solution. Fluid lag ξ_f is a dimensionless parameter. τ_m is the underpressure time that is dimensionless. Code courtesy of Prof. Akono.

9.7 Conclusion

Our focus was to assess the influence of orientation, rates, composition and morphology on the fracture behavior of organic-rich shale at the microscopic level. Thus, we carried out microscopic scratch tests on both black (Niobrara) and grey (Toarcian shale) specimens. Our microscopic tests combined with advanced micro-structural characterization

and nonlinear fracture mechanics modeling tests show that creep and fracture are coupled phenomena in shale systems. By combining scratch tests and micro-indentations tests, it was possible to decouple stress relaxation and fracture so as to evaluate the rate-independent fracture toughness at the microscopic scale. Our experiments bring new insights into the fracture of organic-rich shale materials. Even at low concentrations, the organic matter greatly influences the strength, creep and fracture characteristics of black shale. In particular, the exceptional toughness of black shale is due to toughening mechanisms operating at the nanometer scale in the kerogen and at the clay-kerogen interface. Furthermore, the fracture behavior is anisotropic as a combined result of a layered micro-structure as well as an intrinsic fracture behavior of clay. These findings are important and will inform advanced physics-based constitutive materials law for geo-mechanics simulation in energy-related applications such as hydraulic fracturing in unconventional reservoirs or CO_2/nuclear waste storage into depleted organic-rich shale wells.

Part IV

Fluid-Rock Reactions Impact on Mechanical Integrity: Geological CO_2 Storage

Chapter 10

Mt. Simon Sandstone

10.1 Introduction

Fossil fuels such as coal, oil and natural gas currently provide and are expected to continue provide the vast majority of energy needed to sustain societies. These fuels contain high percentages of one source of carbon element. Thus, burning these fossil fuels carbon reacts with oxygen to produce CO_2. Due to the reliance on fossil fuels for both energy production and industrial processes, the amount of CO_2 in the atmosphere has increased since the Industrial Revolution. This increase in the CO_2 production leads to increase in global temperatures due to heat radiating back from Earth's surface and getting trapped in the Earth's atmosphere. The use of natural gas and coal will continue to play a critical role in generating electricity for the next several decades. Thus, carbon dioxide mitigation is needed to control the atmospheric emissions. There are several methodology to reduce CO_2 emissions, e.g. end-use fuel switching, power generation efficiency and fuel switching and carbon capture and storage (CCS). The United Nations Intergovernmental Panel on Climate Change concluded that CCS was a technology with potential for important contributions to the mitigation of green house gas emissions by 2030 [26]. CCS is an inevitable component of the broad portfolio of approaches and technologies that will be needed if climate change is to be successfully addressed.

Carbon capture and storage (CCS) is the separation and capture of carbon dioxide from the emission of industrial processes before release into the atmosphere and storage of the CO_2 in some state for long periods of time. A key aspect of CCS is the amount of carbon storage resources available to effectively help reduce the greenhouse gas emissions. Three main storage resources for this purpose are oil and natural gas reservoirs,

unmineable coal and saline formations. The highest amount of storage resource estimate is saline formations [274]. Thus, CCS enables different industries to continue to operate while emitting fewer greenhouse gases, making a powerful tool for mitigating CO_2 in the atmosphere. Carbon dioxide should be stored underground as a supercritical fluid. Supercritical condition is where the temperature is exceeding 31.1 °C and pressure is exceeding 72.9 atm (1,057 psi). This temperature and pressure only occurs at depths below the Earth's surface of about 800 m (2,600 feet). At these temperatures and pressures, carbon dioxide has some properties like a gas and some properties like a liquid. The main advantage of storing CO_2 in this state is the reduction in volume compare to standard temperature and pressure conditions. The reduction in volume is of an order of magnitude where assuming a 100 volume of CO_2 will reduce to 0.27 volume at supercritical state.

One of the primary challenges to geological carbon sequestration is operational expenses. The greatest cost of in this procedure is the cost of capture. The highest amount of storage source of geologic storage is brine saturated formations. There is not direct revenue source from storing CO_2 in geological formations, thus storage must be completed through a government mandate. CO_2 storage in oil reservoirs may lead to oil production while storage in saline formations represents an additional operating cost. This cost may be offset by a credit system or a government support. There has been several studies to assess the applicability of CO_2 storage in several countries. The GEODISC program in Australia [275] investigated the possibility of sequestrating CO_2 in sedimentary basins. Another study in Algeria, the In Salah storage project has been providing many insights into the challenges of CO_2 subsurface sequestration [276–278]. Norway registered the first CO_2 storage commercial project [279, 280]. In another project, a pilot project was carried out for more than six years to store CO_2 in a mature reservoir [281].

The main technical challenges remaining relate to risk associated with CO_2 injection and long-term storage. One of the most important challenge remaining is the induced seismicity. It raises concerns that geological carbon storage will result in damage to infrastructure and and near the ground surface. This might induce fractures within the reservoir or overlying caprock. These two risks can lead to reduced storage capacity or reservoir leakage. The storage site selection and design is an important step which aims to identify and avoid sites with mechanically weak subsurface features or that are likely to induce seismicity [282–284]. In simplest terms, the primary objective of a single injection well is the adequate storage and containment of CO_2. Another objective is the ability to monitor over the life of the project the pressure in the storage formation and the CO_2

plume distribution [285, 286]. It is typical to inject CO_2 using the lowest pressure and smallest areas possible to reduce costs (less CO_2 compression) and the physical "footprint": the smaller the pore volume leased, the lower the costs of leasing/purchasing and monitoring efforts. The greater awareness of the possibility of induced seismicity results in an emphasis on injection without any recorded seismic events [287, 288]. In turn, any record of seismic event may potentially lead to a reduction in injection rates (i.e. injection pressure) or a complete cease of the injection operations. Consequently, seismic monitoring (including micro-seismic) has become one of the most important aspect for site screening, selection, design and operational considerations for CO_2 storage.

Here a review of some of the active large scale CO_2 is presented. The Sleipner CGS project is located offshore Norway and utilizes the world's first offshore-based CO_2 capture facility [279]. The CO_2 is stored in the Utsira formation at a depth of 800–1000 m below the sea surface. Water depth is at 82m. The Utsira formation contains a 200–300 m thick sandstone unit, with sime thin (¡1m) shale strings. The formation water is saline, with high porosity (38%) and permeability (1-8 Darcy). The Utsira formation is overlayed by a thick shale caprock, with some silty intervals in the upper part. To take CO_2 far away from the producing wells and from the production platform to avoid any external corrosion of casing [289].

In Salah CGS project is onshore, in the middle of the Sahara desert, and the saline storage formation is Carboniferous Sandstone, 2,000 m deep, 20 km thick with low permeability (around 10 millidarcy). Three horizontal wells around 1,800 m long were required to achieve sufficient injectivity. Another project is the Snøhvit (Snow White) project, in the Barnets Sea offshore Norway, which started injection of CO_2 from an liquified natural gas (LNG) plant in 2008. CO_2 is captured onshore and transported in a 150 km subsea pipeline ending in a subsea template and a well. The CO_2 is continuously flowing along and injected at a depth of 2,600 m below sea level into Tubaen formation. Here sandstone units have permeabilities of several hundred milli darcy. These are some of the project CGS project that are active large scale CO_2 storage projects.

10.2 Mt. Simon Sandstone Basin

The Illinois Basin is a cratonic basin located in the Midwest (central portion of the United States) which provides an important resource for pilot testing, cf. Figure 10.1 b). The Cambrian-age Mt. Simon Sandstone follows the Precambrian granite basement

of the Illinois Basin. The Mt. Simon is a pervasive siliciclastic unit that can range over 792 m. The upper Mt. Simon transition to Eau Claire to Mt. Simon, which serves as the cap rock for CO_2 storage. The Illinois Basin covers an area over 155,399 km^2 and contains a regionally significant saline reservoir. The Mt. Simon Sandstone has an assessed storage capacity of 11–150 billion tons, as reported by the U. S. Department of Energy (www.netl.doe.gov). Figure 10.1 illustrates the Illinois Basin, which extends throughout most of Illinois, Southwestern Indiana, and Western Kentucky.

The Mt. Simon Sandstone is the host formation for the current pilot study on CO_2 storage at the Illinois Basin-Decatur Project (IBDP). This site is located in Decatur, Illinois where 1 million metric tons of CO_2 were injected between November 2011 and November 2014. The specimens in this investigation came from verification well 1 (VW1), which was designed for deep reservoir monitoring. In particular, the specimens were cored from VW1, between a depth of 2110.7 m (6925 ft.) to 2111.4 m (6927 ft.) below ground. A detailed study of seismicity was undertaken as part of a United States Department Of Energy funded demonstration project, i.e., Illinois Basin Decatur Project (IBDP) [290, 291]. A significant number of micro-seismic events were recorded during and after the CO_2 injection operations [292]. The IBDP was part of their Regional Carbon Sequestration Partnership program that included measurement of micro-seismicity [293]. Injection started at IBDP in November 2011 into the lower most part of the Cambrian Mt. Simon Sandstone at depth of 2141-2149m (7025-7050 ft.), which overlies the crystalline basement composed of rhyolite [294]. Figure 10.1 illustrates the storage capacity of the Mt Simon sandstone formation. Generally, crystalline basement rocks are known to have fractures, and IBDP well logs indicate the presence of fractures. CO_2 injection at a rate of 1000 tons per day occurred from November 2011 until November 2014 [295]. The injection pressure rate was kept well below the fracture propagation pressure as determined by a step-rate test [294]. For about 18 months, the pre-injection seismicity was measured: less than 10 events with a magnitude below 1.5 were recorded; these events were attributable to the geologic formation—i.e. after industrial and distant natural earthquakes were removed from the data set [296]. In contrast, during the 3 years of injection over 4700 events were recorded. These events are shown on a map in Figure 10.2. These seismic events were determined to originate in the lower Mt. Simon Sandstone as well as the underlying crystalline basement rock. Many of these events were grouped into several, parallel, 3-dimensional elongated clusters centered from 1200 to 2700 ft. from the injection well. The magnitude of all 4700 events were under 1.2 and only 6 % of the events were over

magnitude zero [292].

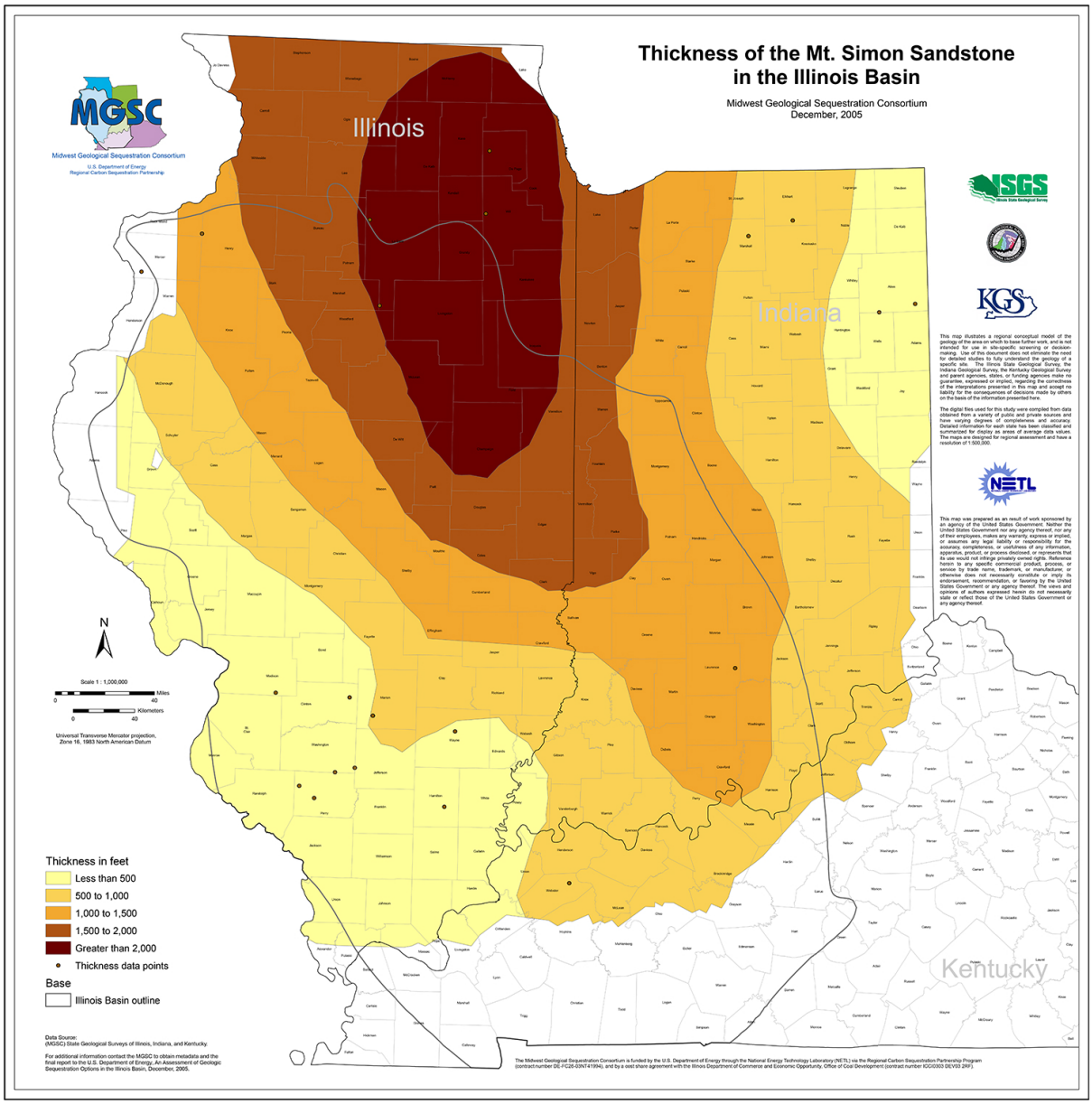

Figure 10.1: Illinois Basin Decatur Project storage site. Thickness of the Mt. Simon sandstone in the Illinois Basin is shown. The darker color shows a higher thickness. Adopted from [297].

10.3 Illinois Basin Decatur Project

Another notable observation was the presence of post-injection seismic events. After CO_2 subsurface injection, the pore pressure decreased and approached the initial pressure. However, during this time, specific microseismic events continued to occur within the previously defined clusters. Nevertheless, the post-injection seismic events were more randomly distributed compared to those occurring during injection. Moreover, relative to all events located during injection, most of the post-injection events were closer to the injection well and the projected CO_2 plume. These observations of significant microseismic activity during and after CO_2 injection call for a deeper understanding of the geo-chemo-mechanical interaction between the reservoir rock, supercritical liquid CO_2 and brine, which is the purpose of the following Chapters.

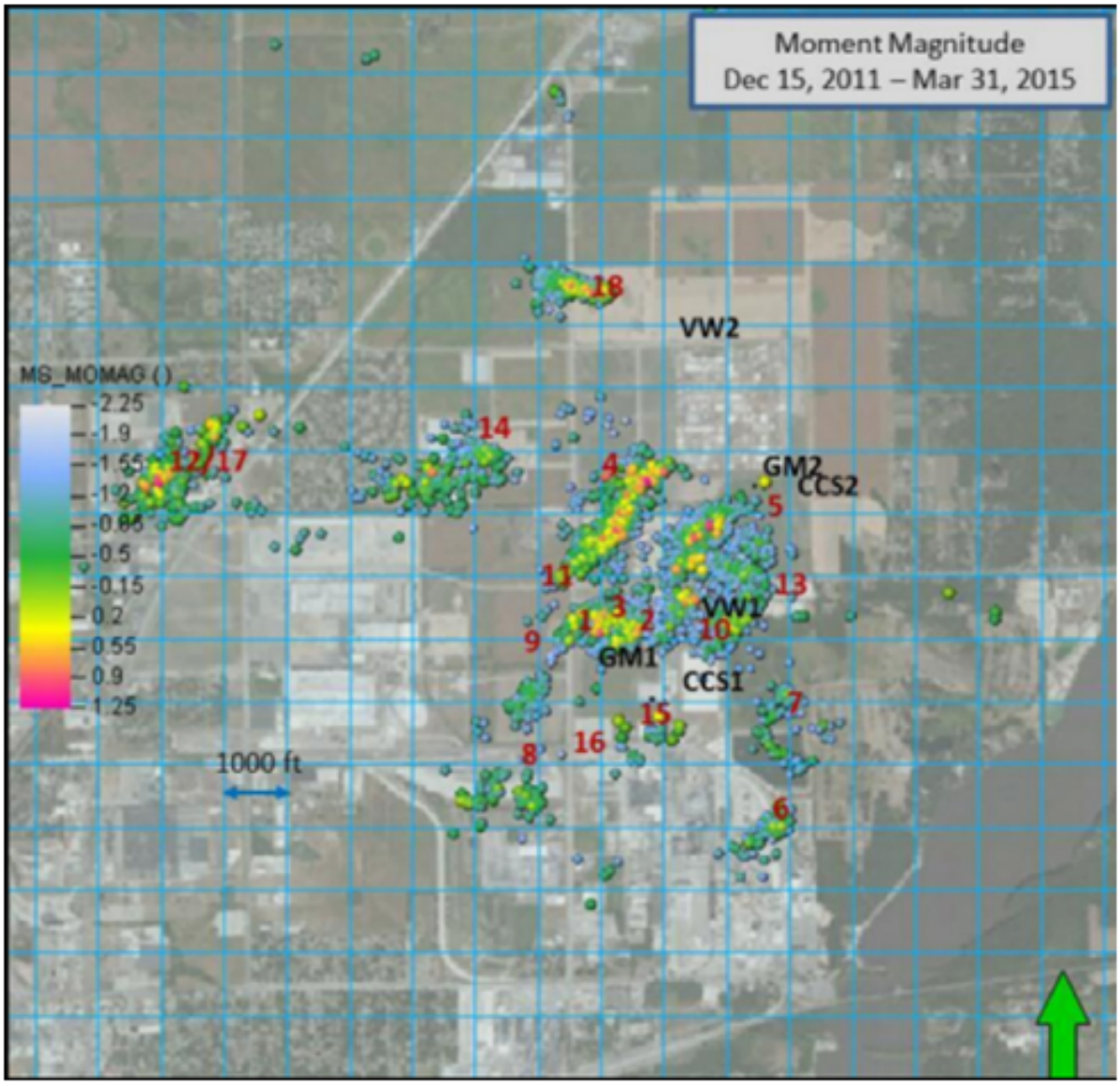

Figure 10.2: Illinois Basin Decatur Project seismicity map from December 2011 to Mar 2015. Adopted from [293].

Although geological carbon sequestration is a strategy to continue to meet the world's energy needs using fossil fuels, there are several risks. On the one hand, the underground storage option offers enough capacity worldwide and the potential ability to store CO_2 for long geological periods. Sedimentary rocks with a low permeability – one the order of 1.3 10^{-14} m^2—and a high porosity—on the order of 15% to 20%– represents an excellent alternative for CO_2 subsurface capture and storage. On the other hand, CO_2 geological sequestration presents many risks such as fault activation, fracture opening, leakage of CO_2 to the surface, and ground surface elevation. For instance, in the In-Salah project in Algeria, a surface uplift of 5 mm per year was observed using interferometric synthetic aperture radar satellite surveillance [277, 298]. Further analysis revealed that the uplift of the ground surface may be due to pressure changes, geomechanical changes, and geochemical reactions in the subsurface. To prevent leakage to the surface, a layered formation with a tight capstone rock is usually preferred. Geomechanics analysis is essential to provide a risk assessment of geological carbon sequestration operations, assess the likelihood of different failure mechanisms along with their dependence on prescribed parameters. Geomechanics enable to identify safe injection pressure limits and determine a safe location for injection wells, away from faults at risk to be activated [299]. Herein, the goal is to maintain zonal insulation, capstone integrity, and reservoir hydromechanical integrity. Geomechanics is also an indispensable tool to monitor injection operations and yield quantitative predictions of field observations. An example of a fully-disciplinary approach is the study by Bissel et al. [298] that utilizes a wide range of computational tools and models to monitor CO_2 injection operations in the In-Salah system. The prediction of multi-scale reservoir simulation models was compared to observation of CO_2 plume using seismic monitoring as well as micro-seismic events recorded via geophones. In turn, predictive, physics-based mathematical geomechanical models will contribute to increase society acceptance and help to monitor the outcome of the injected CO_2.

Presently, a primary technical challenge and hurdle to widespread CO_2 subsurface storage is the possibility of seismic activity triggered by geological carbon dioxide injection. Many hypotheses have been proposed to rationalize the observed seismic events. Nevertheless, more scientific research is crucial to enhance the current understanding, improve the current state-of-the-art in science and technology of GCS, and inform the drafting of local and global standards and regulations. In the oil and gas industry, induced seismicity due to increase in pore pressure is a serious concern that had led to significant regulatory changes. A recent example is successful large hydraulic fracture

treatments in shale formations. To stimulate a high number of wells, a large amount of fracturing fluid is required, which must be disposed of upon completion. A common practice is to set central disposal wells capable of injecting daily large volumes of fluid into thick, high-porosity, and high-permeability geologic formations. Often these geologic formations are made of basal sandstones immediately adjacent to pre-Cambrian crystalline basement rock (e.g. granite and rhyolite). Many of the large magnitude seismic events recorded were attributed to the disposal of fluids in high porosity formations and not to the hydraulic fracture treatment itself.

10.4 Microstructural Characterization of Unaltered Mt. Simon Sandstone

Here, a detail experimental investigation of fabric, mineralogy and characterization of Mt. Simon sandstone is presented.

X-ray powder diffraction was carried out at the Fredrick Seitz Materials Research Laboratory in collaboration with the Illinois State Geological Survey to determine to mineralogical composition of Mt. Simon sandstone. A reliable quantitative analysis of clays still remains a challenge [145, 146, 151]. There are four general approaches for XRD-based quantification for clay minerals: known addition [148], absorption-diffraction [149], full-pattern-fitting [150, 151], and the use of mineral intensity factors [152, 153]. In this study, we employ the mineral intensity factors method and assume that the sum of all phase quantities in a sample is 100 %. Quantitative X-ray diffraction analysis of clay-bearing sandstones is a very challenging task, and a proper procedure should be followed [154]. Thus, a detailed preparation procedure developed by the Illinois State Geological Survey was used in this study [300, 301].

We used scanning electron microscopy (SEM), environmental scanning electron microscopy (ESEM), and energy-dispersive spectroscopy (EDS) to expand our understanding of the fabric and composition of the Mt. Simon micro-structure. Scanning electron microscopy and back-scattered electron microscopy was conducted at the Frederick Seitz Materials Science Laboratory and Microscopy Suite of the Beckman Institute Imaging Group at the University of Illinois at Urbana-Champaign, using a JEOL 6060 LV and a FEI Quanta FEG 450 respectively. Scanning electron microscopy was performed at low vacuum (1 Torr) without coating the specimens. The accelerating voltage ranged

from 15 kV to 20 kV, with the working distance ranging from 6 mm to 10 mm, and the magnification levels ranging from 100X to 10,000X.

Figure 10.3 demonstrates the progression in grinding and polishing procedure through optical microscopy images. The removal of scratches from the previous steps are evident. The surface of the polished specimen is reflective of the overhead lights.

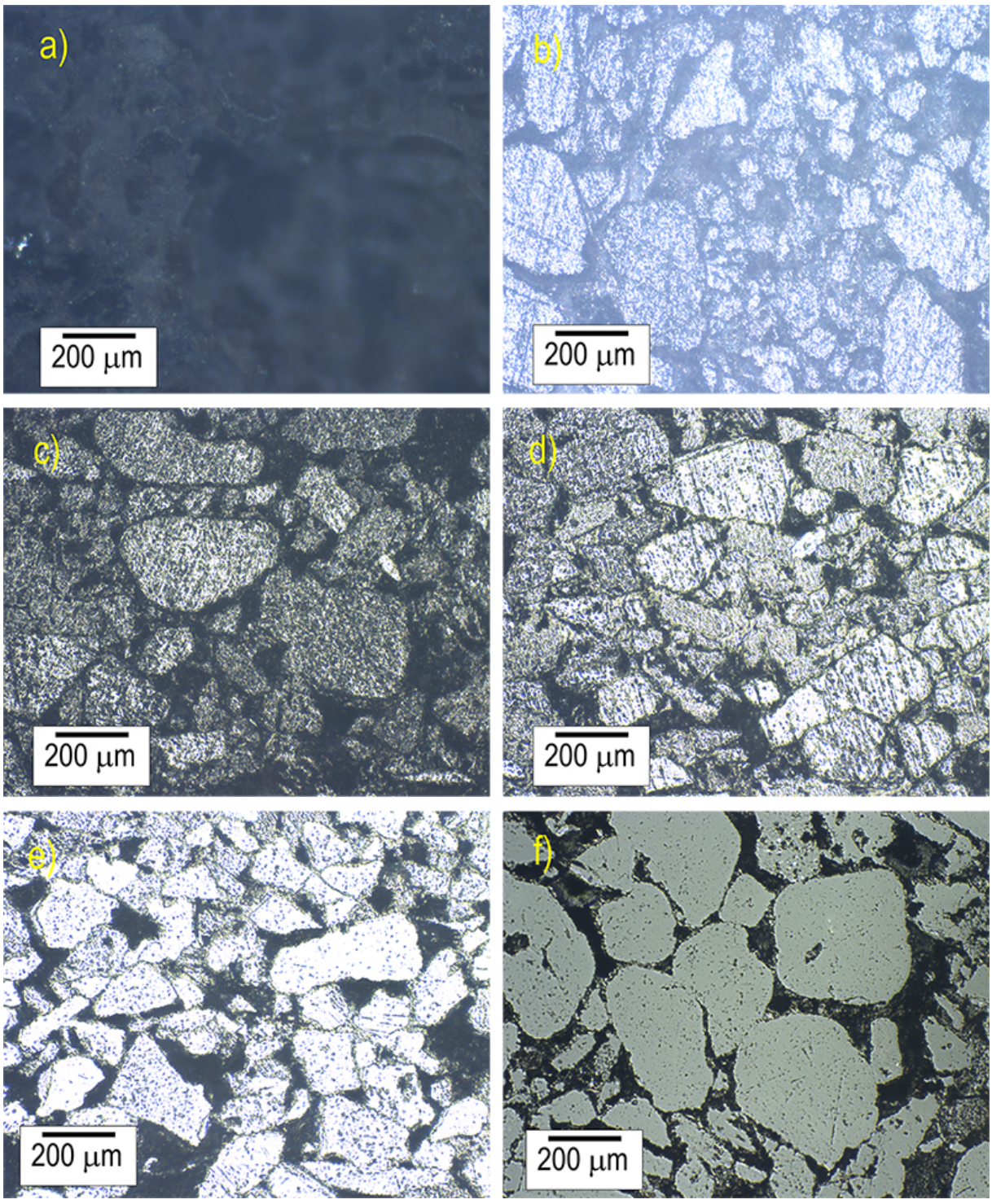

Figure 10.3: Optical microscope image of a) unpolished Mt. Simon, b) after 400 grit size, c) 600 grit size, d) 800 grit size, e) 3 micrometer, f) 0.3 micrometer.

Figure 10.4 displays back-scattered scanning electron microscopy (BSE) images of unaltered Mt. Simon cores in the bedding plane at magnification levels ranging from 100X to 10,000X. Figure 10.4 a) shows a granular and heterogeneous microstructure. Chemical components are identified based on their gray levels. K-feldspar grains are shown in light gray whereas quartz grains are shown in dark gray. The grain size ranges from 50 to 500 μm. Figure 10.4 b) shows the presence of 10-100 μm micropores in the inter-granular space. Figure 10.4 c) shows clay nanosheets surrounding clay fabric around the grain with nanopore sizes of 500-2,000 nm in diameter. The observations of a two-scale porosity is presented in this figure. Thus, a porous, granular and multiphase microstructure is observed. Moreover, the grains are not spherical. The BSE findings are also in agreement with the X-ray powder diffraction analysis that revealed three major mineral phases—quartz (57 % wt.), feldspar (35 % wt.), and siderite (5 % wt.)–with the clay being the cement between grains.

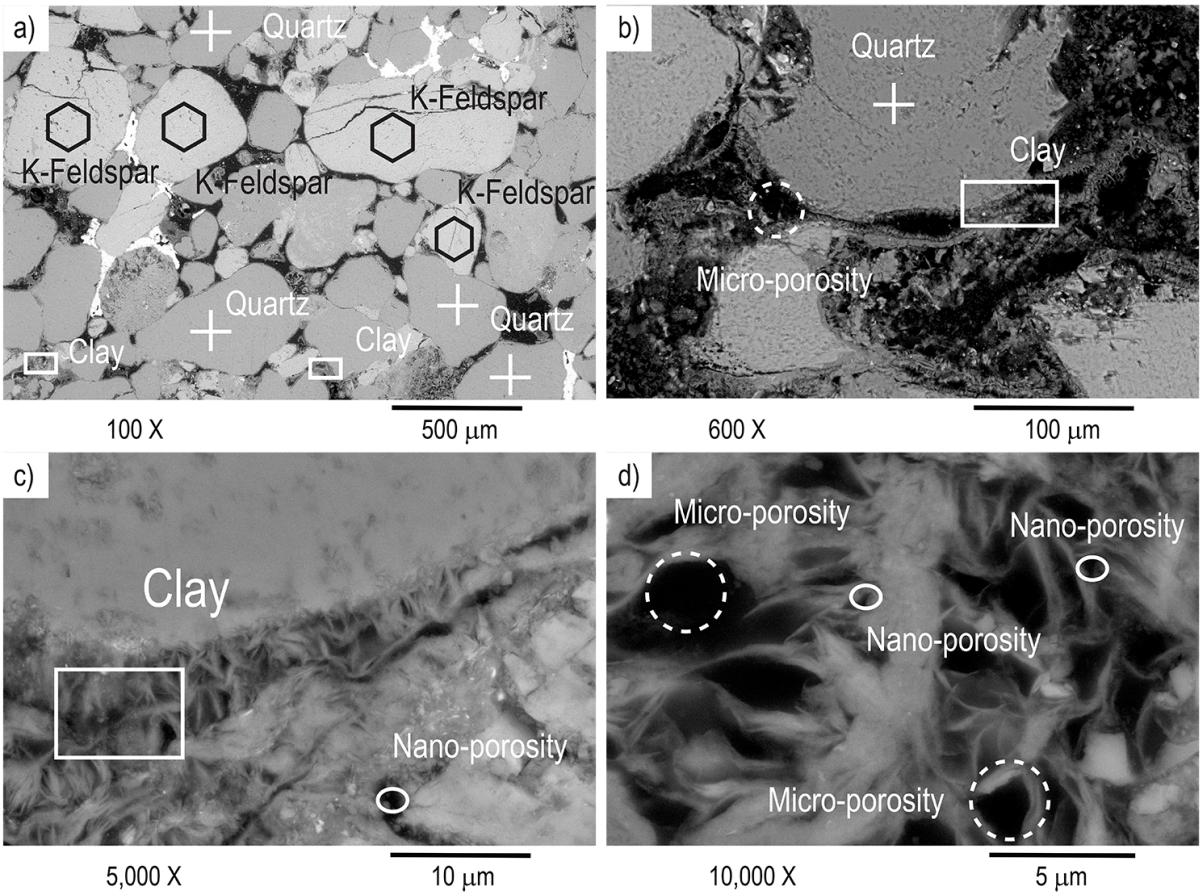

Figure 10.4: Back scattered scanning electron images of Mt. Simon sandstone in the bedding plane at a) 100X magnification, b) 600X magnification, c) 5,000X magnification, d) 10,000X magnification.

In addition, Figure 10.5 demonstrates additional scanning electron microscopy images of Mt. Simon.

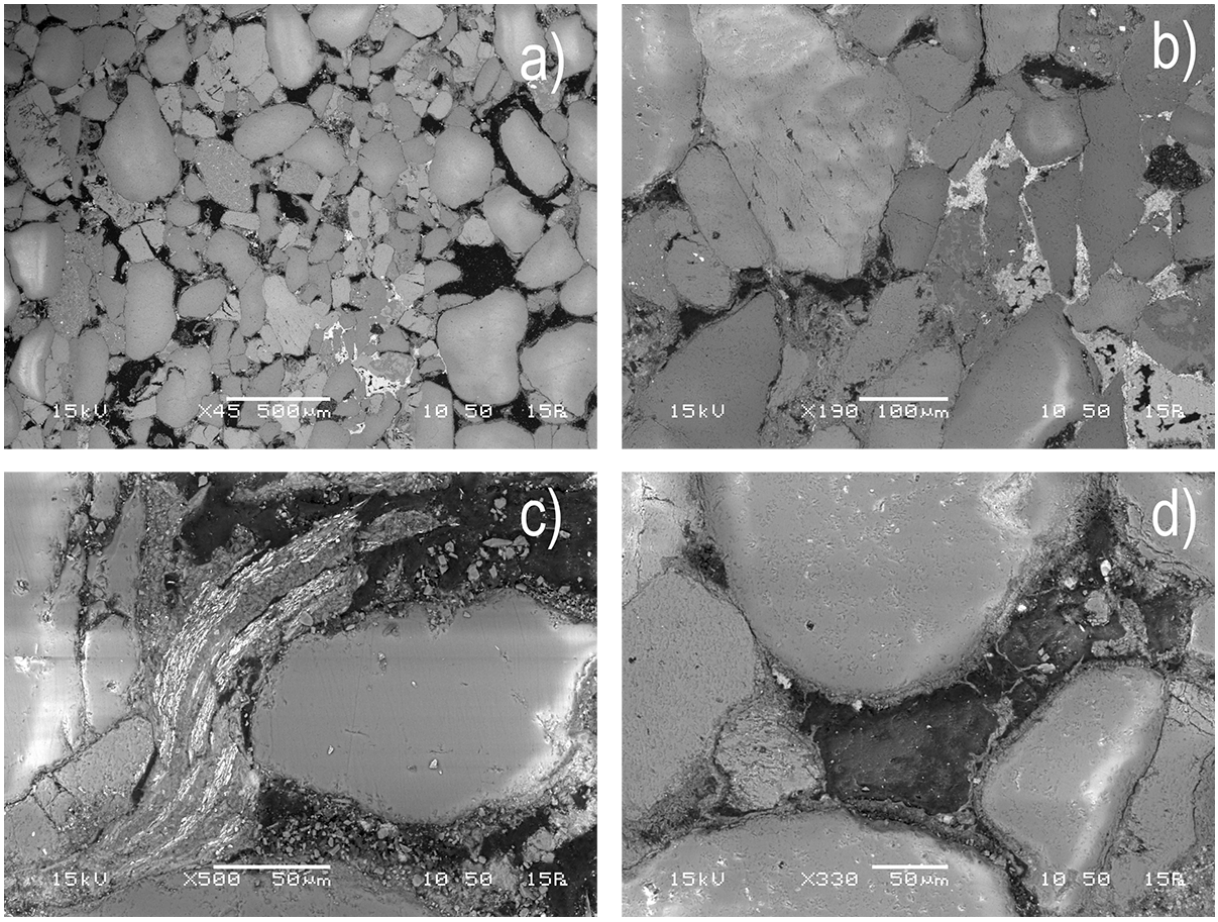

Figure 10.5: Scanning electron microscopy images of Mt. Simon sandstone: a) 45X magnification, b) 190X magnification, c) 500X magnification, d) 330X magnification. All the images are taken using a JEOL 6060LV in low vacuum without coating the specimen.

Figure 10.6 illustrates the diffractogram for the Mt. Simon specimen. The specimen is prepared from the verification well 1 from the depth 6925 feet. The specimen is prepared according to the previous chapters.

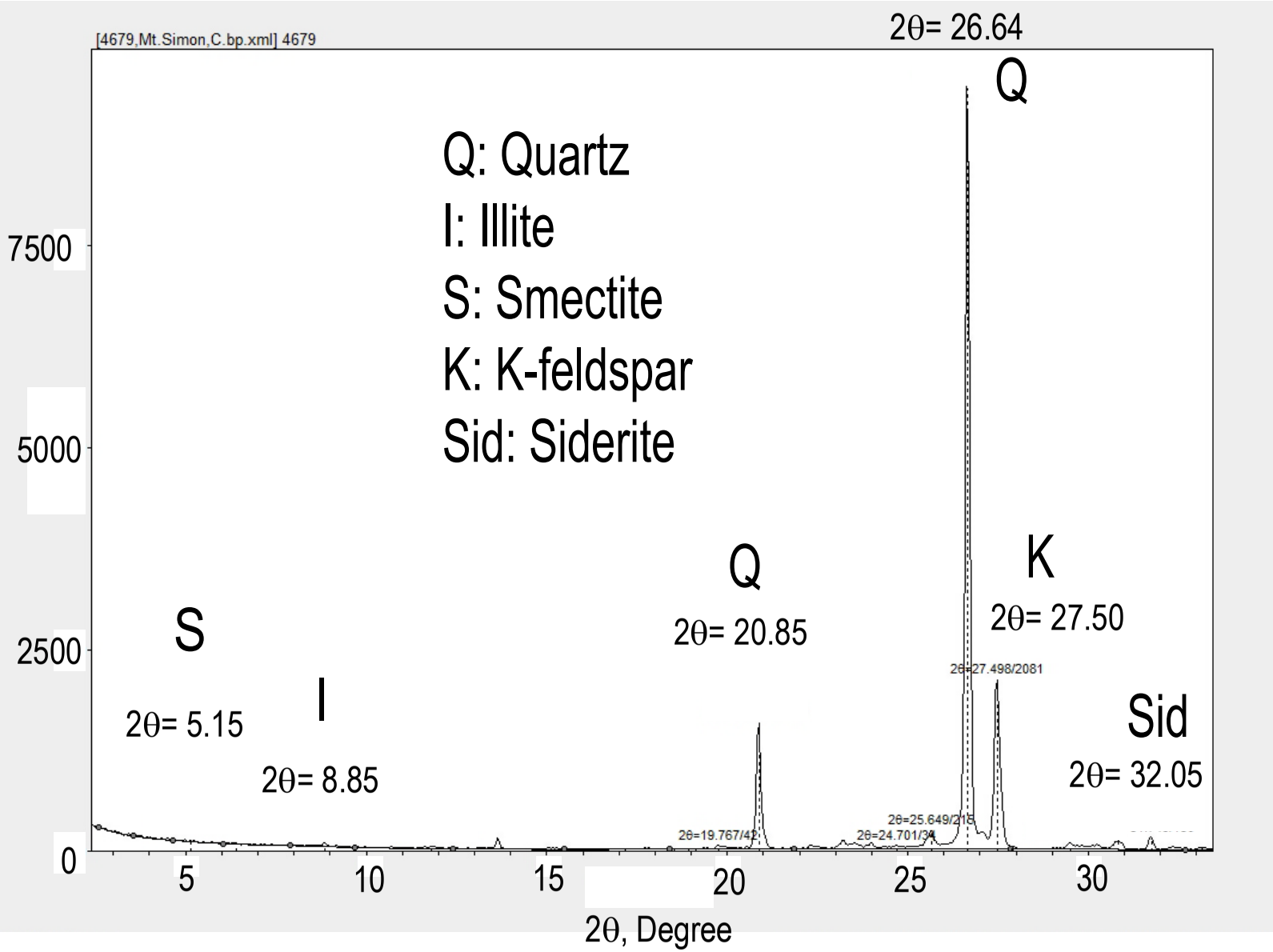

Figure 10.6: X-ray diffraction diagram, 2θ scan from a powder sample prepared from Mt. Simon specimen.

10.5 Incubation Experiments on Mt. Simon Sandstone

Six alteration regimens were applied to investigate fluid-rock interactions in Mt. Simon sandstone. For the first two alteration regimens, the fluid was a CO_2-saturated brine, at high temperature high pressure conditions: (52 °C, 17.2 MPa) and (50 °C, 22.7 MPa). The third alteration regimen involved deionized water. For the remaining three alteration regimens, the fluid was brine and incubation took place at room temperature, 22 ° C, and atmospheric pressure, 0.1 MPa. Three different brine solutions were synthesized for incubation at room temperature. The solutions differ in their concentration of NaCl, KCl, and MgCl. The brine solutions were found to be slightly acidic with a pH of 5, as measured by a pH probe. The exact composition of each solution is given in Table 10.1.

The incubation of specimen at high temperature and high pressure is carried out in Prof. Werth 's lab (AS4 specimen). The second specimen at high temperature and high pressure is carried out in Prof. Tsotsis 's lab (AS1 specimen). The schematic of the experimental setup for incubation for CO_2-saturated brine is shown in Figure 10.7.

Table 10.1: Chemical salt concentrations in brine solution recipes. Recipe 1= high sodium chloride content-medium ionic strength, Recipe 2= high potassium chloride-highest ionic strength, Recipe 3= moderate concentration-lowest ionic strength.

Salts	Recipe 1	Recipe 2	Recipe 3
NaCl (g/l)	111.6	74.95	37.47
$CaCl_2.2H_2O$ (g/l)	78.35	48.74	24.37
$MgCl_2.6H_2O$ (g/l)	16.52	16.73	8.36
KCl (g/l)	4.31	150.00	75.00
$SrCL_2.6H_2O$ (g/l)	2.37	0.12	0.06
LiCl (g/l)	9.36	2.43	1.21
pH	5	5	5

Figure 10.7 displays the experimental set-up utilized for the CO_2-saturated incubation. A custom-built high pressure and temperature cell was used, as shown in Figure 10.7. The cell consists of a hollow stainless steel cylinder with an outer diameter of 96.5 mm and an inner diameter of 25.4 mm, and an interior volume of 20 mL. The cell can withstand pressures of up to 68.9 MPa. The cell is sealed with two Teflon O-rings with four equally spaced ports around the cylinder, for brine introduction, CO_2 injection, pressure release, and pressure monitoring. The supercritical liquid CO_2 is connected to a Teledyne Isco fluid pump and injected into a stainless steel reactor for equilibration with the synthetic

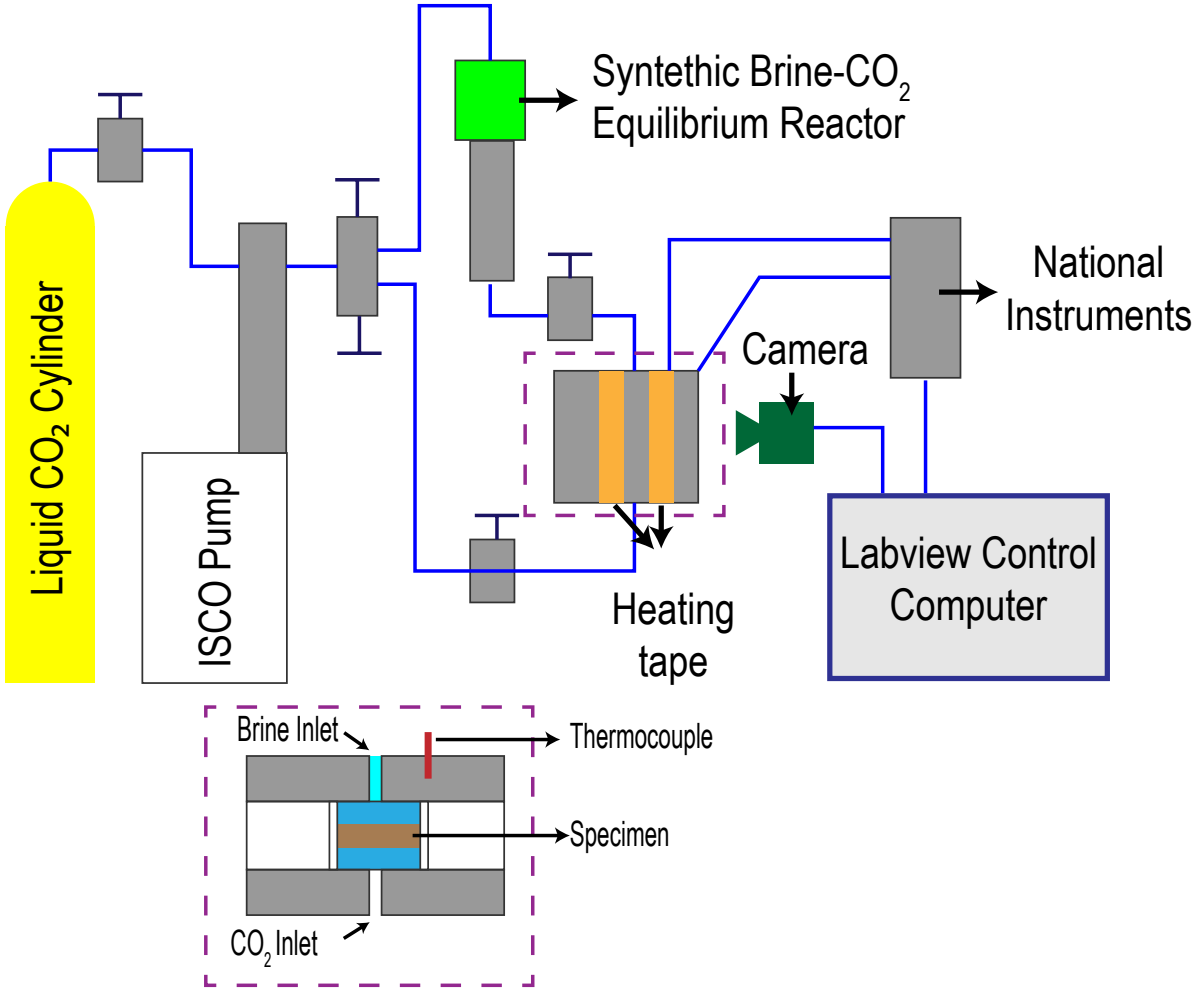

Figure 10.7: Schematic of the Experimental Setup for incubation in CO_2-saturated brine. Adopted from Prof. Werth Group.

brine. The temperature of the cell was regulated using thermocouples.

Table 10.2 summarizes our alteration protocol. Specimen 6925-AS4 was embedded in epoxy resin and then aged in CO_2-saturated brine at 50 °C and 3290 psi for 28 days. Specimen 6925-AS1 was incubated in a CO_2-saturated brine at 52 °C and 2500 psi for seven days. Specimen 6925-DI, 6925-B1, 6925-B2, and 6925-B3 were incubated in deionized water, brine recipe 1, brine recipe 2, and brine recipe 3, respectively, for 14 days at room temperature and room pressure.

Table 10.2: Alteration protocols utilized in this study. AS4 alteration was performed by Prof. Werth Group. AS1 alteration was performed by Prof. Tsotsis Group.

Specimen name	Fluid	Incubation Time	Temperature	Pressure
6925-AS4	CO_2-saturated brine	28 days	50 °C	3290 psi
6925-AS1	CO_2-saturated brine	7 days	52 °C	2500 psi
6925-DI	Deionized water	14 days	22 °C	15 psi
6925-B1	Brine recipe 1	14 days	22 °C	15 psi
6925-B2	Brine recipe 2	14 days	22 °C	15 psi
6925-B3	Brine recipe 3	14 days	22 °C	15 psi
6925-U	N. A.	N. A.	N. A.	N. A.
6927-U	N. A.	N. A.	N. A.	N. A.

10.6 Conclusion

In this Chapter, a comprehensive review of the sequestration projects is presented. In particular, the Illinois Basin Decatur Project is reviewed where the CO_2 was injected for three years. This review demonstrates the large scale sequestration project and the main problems during and after injection such as extensive micro-seismic events, leak off, and pressure drop-off. The most important issue is the micro-seismicity during and after injection at the site of the project. The large scale field projects are reviewed. The Illinois Basin Decatur Project is reviewed with the detail of injection of CO_2 in the host rock reservoir. In addition, a comprehensive review of reservoir rock characterization is presented. A review of the experimental plan for incubation of specimens is presented here.

Chapter 11

Impact of Fluid-Rock Reactions on Elastic Properties of Mt. Simon Sandstone

11.1 Introduction

Geological carbon sequestration consists of capturing man-made CO_2 emissions and injecting them into the viable formations. The international Energy Agency has identified carbon capture and storage (CSS) as a significant option necessary to stabilize greenhouse gas concentrations in the atmosphere. The CCS identified as the third largest percentage (22%) of the necessary reductions from industrial and power sources (United States Carbon Utilization and Storage Atlas, 2012). The approach is currently being explored in many regions around the world [275, 277, 302, 303]. Pilot carbon dioxide injection and storage has been performed at sites such as the Illinois Basin Decatur Project (IBDP), where microseismicity was recorded at or far from the injection site. Therefore, a fundamental understanding of fluid-rock interactions and their effect on the mechanical behavior of the host rock is essential to promote sustainable geological carbon sequestration systems. Despite the current understanding of fluid-rock interactions in geological materials, novel characterization methods are needed to resolve the changes in micrometer length scales. Mostly, experiments have been carried out at the macroscopic scale to investigate the fluid-rock interactions. Waza et al. [304], experimentally investigated the effect of water on the velocity of crack propagation in an andesite and a basalt specimen using a

double torsion method. They found that water increases the rate of crack propagation and results in a decrease of strength in silicate rocks. In another study, Holder et al. [305], experimentally investigated the subcritical crack growth parameters for several sedimentary rocks, where the increase in moisture content increased the susceptibility of samples to subcritical crack growth.

Several studies [306, 307] investigated the effect of dissolution mechanisms on sandstone permeability and porosity. In these studies, they concluded that the porosity and permeability will increase with chemical or mechanical alterations. Furthermore, Grgic and Giraud [308] characterized the influence of different type of fluids on the poromechanical coupling as well as chemical effects on the porous rock structure. They found out that the micro-crack damage plays a major role in the creep response of hard porous rocks and on the evolution of the static elastic properties. In addition, the concluded the chemical effect of fluid is related to the development of stress corrosion reactions at the crack tips which enhance subcritical crack growth. In another study, Rathnaweera et al. [309], studies the influence of different fluids on the mechanical behavior of sandstone, where they concluded that fluid chemistry plays an important role in the strength, Young's modulus and failure mode of Hawkesbury sandstone. However, these methods characterized the mechanical properties at the macroscopic scale and relied on far-field measurements. In a recent study, Sun et al. [310], studies Crystal Geyser rocks and reported a degradation of mechanical properties after exposure to reactive CO_2 water using scratch tests. Although, they only performed a constant vertical load scratch test for their study. Thus, our research objective is to apply advanced nanomechanical testing experiments, in conjunction with physics-based models to predict the changes in mechanical response due to fluid-rock alterations in sandstone samples from the Illinois Basin. In addition, the Mt. Simon microstructure was characterized before and after fluid-rock reactions using advanced imaging techniques such as environmental scanning electron microscopy and energy dispersive spectroscopy. Grid nanoindentation was carried out before and after fluid-rock reactions to capture porosity changes.

11.2 Materials and Methods

The Illinois Basin is a Paleozoic depositional located in the Midwest, underlying most of Illinois, and extending into southwestern Indiana and western Kentucky (cf. Figure 11.1). The formation consists of a granite basement followed by the Argenta formation

and then the Mt. Simon formation. The Mt. Simon is a pervasive siliciclastic unit that can range over 792 m. The Eau Claire formation conformably overlies the upper Mt. Simon formation and serves as the cap rock for CO_2 storage. The Mt. Simon Sandstone has an assessed storage capacity of 11-150 billion tons of CO_2 as reported by the U.S. Department of Energy (United States Carbon Utilization and Storage Atlas, 2012). The Mt. Simon Sandstone is the host formation for the demonstration project for CO_2 storage at the Illinois Basin-Decatur Project (IBDP). The project is located in Macon County, Illinois where 1 million metric tons of CO_2 were injected between November 2011 and November 2014 [290]. The specimens for this study were extracted from verification well 1 (VW1), which was utilized for deep reservoir monitoring. In particular specimens were cored from VW1, between the depths of 2110.74 m (6925 ft.) to 2110.88 m (6925.44 ft.).

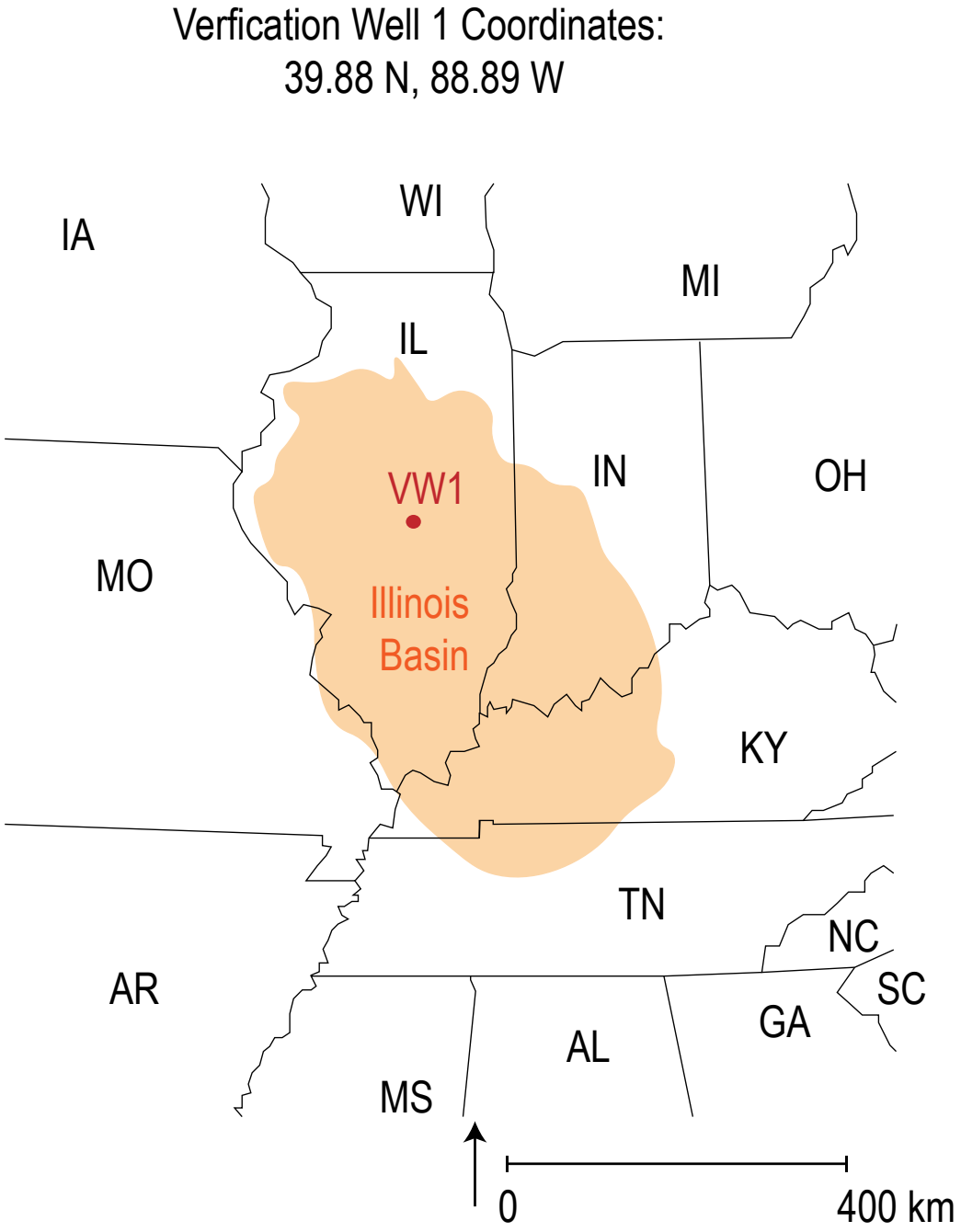

Figure 11.1: Location of Verification Well 1 in IBDP project in Illinois Basin. Adopted from [292].

We used a wide collection of advanced microstructural characterization techniques, environmental scanning microscopy, statistical nanoindentation. These characterization and analytical tools expand our understanding of the composition, porosity and mechanical response of the Mt. Simon microstructure. A polishing procedure was developed to yield a surface finish with a roughness of several nanometers. A major challenge was the heterogeneous nature of the Mt. Simon sandstone. The first step was to embed the specimen in epoxy to preserve its microstructure. Next, a linear precision diamond saw was used to cut the specimen. Afterward, a series of silicon carbide grinding pads were used at various speeds and pressures. This progressive process was utilized to remove subsurface damage induced by previous steps. Polishing was carried out using aluminum oxide pads with different gradations: 9 μm, 3 μm, 1 μm and 0.3 μm. In between each step, the surface was cleansed using an ultrasonic bath. In addition, optical microscopy was used to observe the progress in grinding and polishing. Furthermore, the quality of our polishing procedures was assessed using atomic force microscopy, where the average root-mean squared roughness over a 25 μm $\times$ 25 μm area for polished Mt. Simon was less than 30 nm. Specimens were incubated in a high relative humidity chamber (85 % relative humidity) after polishing. The specimens were extracted from the chamber at intervals to find the effect of incubation time on the mechanical properties of specimens. All specimens used in this study were cored from the same depth to minimize the effect of sample heterogeneity.

We employed scanning electron microscopy (SEM), environmental scanning electron microscopy (ESEM), and energy-dispersive spectroscopy (EDS) to broaden our understanding of the fabric and composition of the Mt. Simon micro-structure. Scanning electron microscopy and back-scattered electron microscopy were conducted at the Fredrick Seitz Materials Science Laboratory and at the Microscopy Suite of the Beckman Institute Group at the University of Illinois at Urbana-Champaign, using a JEOL 6060 LV and a FEI Quanta FEG 450 respectively. In addition, we used a FEI Quanta FEG 650 at the EPIC facility at Northwestern University at NUANCE Center. Scanning electron microscopy imaging was performed at low vacuum (1 Torr) and without coating the specimens to preserve its microstructure. The accelerating voltage ranged from 15 kV to 25 kV, working distance ranged from 6 mm to 10 mm, and the magnification levels ranged from 500X to 20,000X. The specimens were quickly rinsed with ethanol before scanning electron microscopy to remove any surface contamination.

Statistical nano-indentation or grid indentation testing is commonly used to develop

maps of several constituents in heterogeneous materials [92, 216, 311–313]. Herein, all indentation tests were carried out using an Anton Paar nano-indentation module (Anton Paar, Ashland, VA). Figure 11.2 demonstrates a schematic of an indentation test where the load and penetration depth is measured every 70 ms. Moreover, each indentation test consists of a loading, holding and unloading section. The vertical force P is linearly increased up to 5 mN, held constant for 5 s and then linearly decreased. High accuracy force and depth sensors were employed with a resolution of 0.01 μN and 0.01 nm, respectively. A diamond Berkovich tip was used and its contact area was calibrated prior to testing using fused silica as reference material.

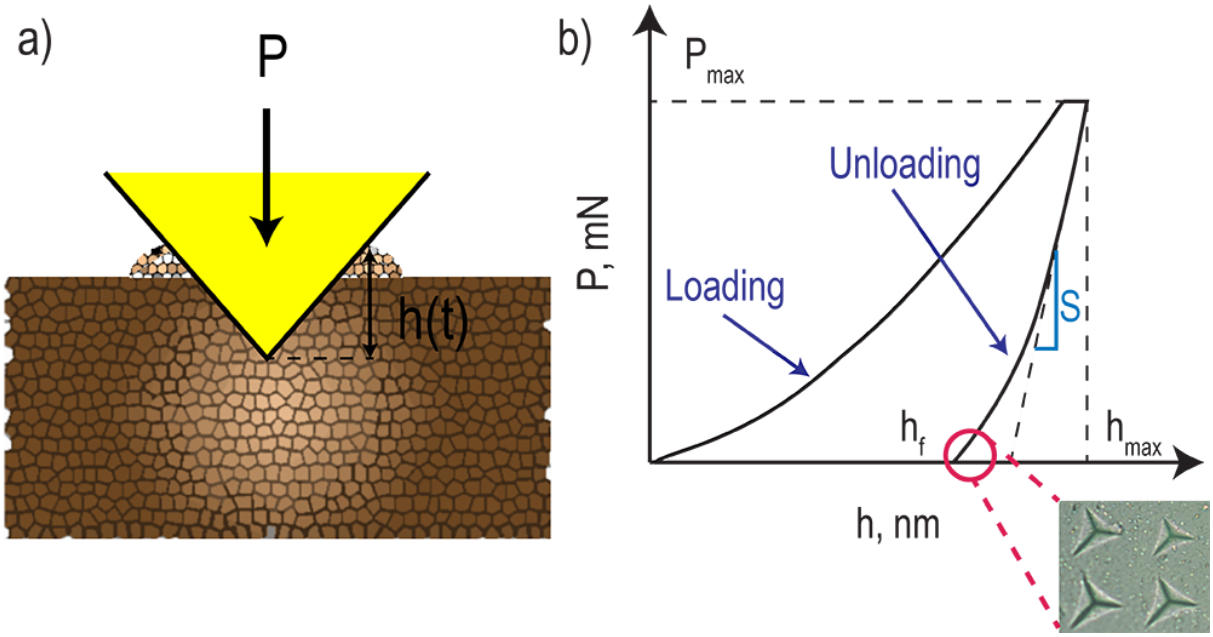

Figure 11.2: a) Schematic of indentation test on Mt. Simon sandstone, b) Schematic of a typical vertical force-penetration depth curve for indentation testing.

Figure 11.2 displays a typical vertical force-penetration depth curve during an indentation, where the plane strain indentation modulus and indentation hardness are calculated according to the Oliver and Pharr method [79, 314]. The spacing between the indents were 20 μm to preclude interaction between individual indents. The grid indentation consists of conducting a large grid of indentations over the surface of the heterogeneous medium of interest. Each indentation experiment could be regarded as statistically independent. This principle enables us to identify the microscopic phases by representing

the experimental probability density functions of the local elastic characteristic using a Gaussian mixture model. The grid size for specimens are 20 × 20, 15 × 15, 10 × 10 and 15 × 15 for Day 0, Day 1, Day 2 and Day 5 respectively.

11.3 Micro-structural Observations

Figure 11.3 shows the granular and heterogeneous microstructure of Mt. Simon sandstone. The gray levels in the back-scattered images identify the difference between chemical compositions of grains. K-feldspar grains are shown in light gray whereas quartz grains are shown in dark gray. The grain size ranges from 50 to 500 μm. Figure 11.3 shows the presence of 10-50 μm micropores in the intergranular space. In addition, we observe the presence of clay surrounding the grains with a nanometer pore size. The structure of the clay shown in Figure 11.3 is captured after grinding and polishing procedure which confirms the presence of clay particles after polishing. Figure 11.3a) demonstrates the effect of incubation on the microstructure of the Mt. Simon sandstone after 1 day of incubation. The residue on the intergranular space shows the precipitation on this area of the specimen. Figure 11.3b) shows a focused image of the inter-granular area with cubic salt formed on around the clay particles. Furthermore, Figure 11.3b) demonstrates the precipitation of salts in the intergranular area.

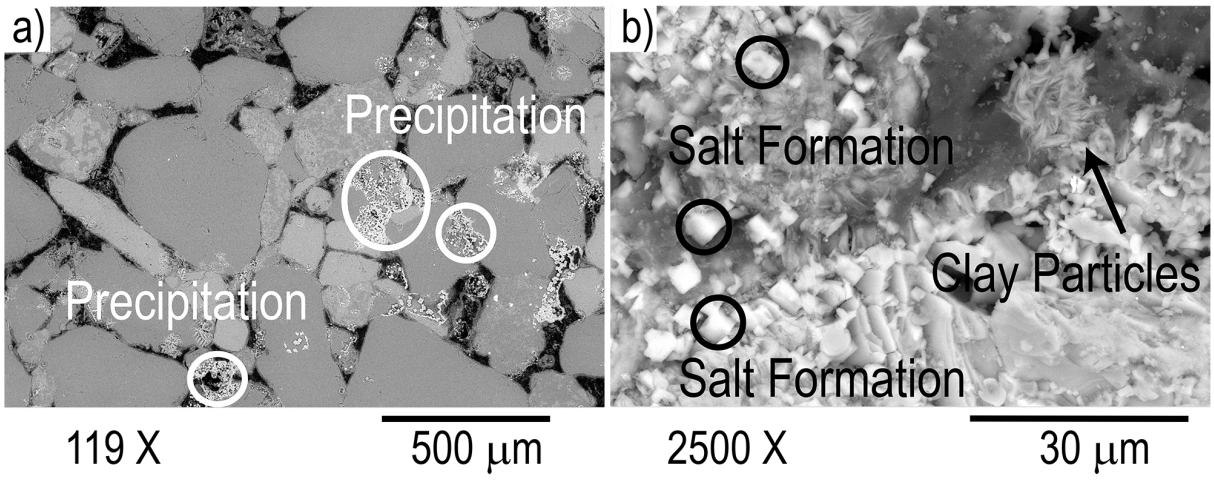

Figure 11.3: Back-scattered scanning electron microscopy images of Mt. Simon sandstone at a) Day 1 and b) Day 2.

11.4 Mechanical Alterations

Figure 11.4 represents the experimental probability density function (PDF) as well as the deconvoluted phases on the same graph for each grid of indentation data. The horizontal axis of this figure shows the indentation modulus while vertical axis represents the density of that indentation modulus. We decompose the experimental PDF into four different phases, where the first phase indicates the porosity due to its lowest indentation modulus. The epoxy used has a low indentation modulus, one order of magnitude lower than micro-constituents of Mt. Simon. This low mechanical property of epoxy result in identification of porosity from microconstituent of Mt. Simon. Each phase modeled as a Gaussian distribution with a mean value, μ and standard deviation value, σ. The mean and standard deviation of four phases for each test is summarized in Table 11.2. Moreover, microscopic results obtained from grid indentation data is utilized to connect the mechanical properties from microscopic scale to macroscopic level. An average medium theory is used to predict the average indentation modulus for bulk modulus using Hashin-Shtrikman theory where the indentation value of each point is considered and the average mechanical property is calculated.

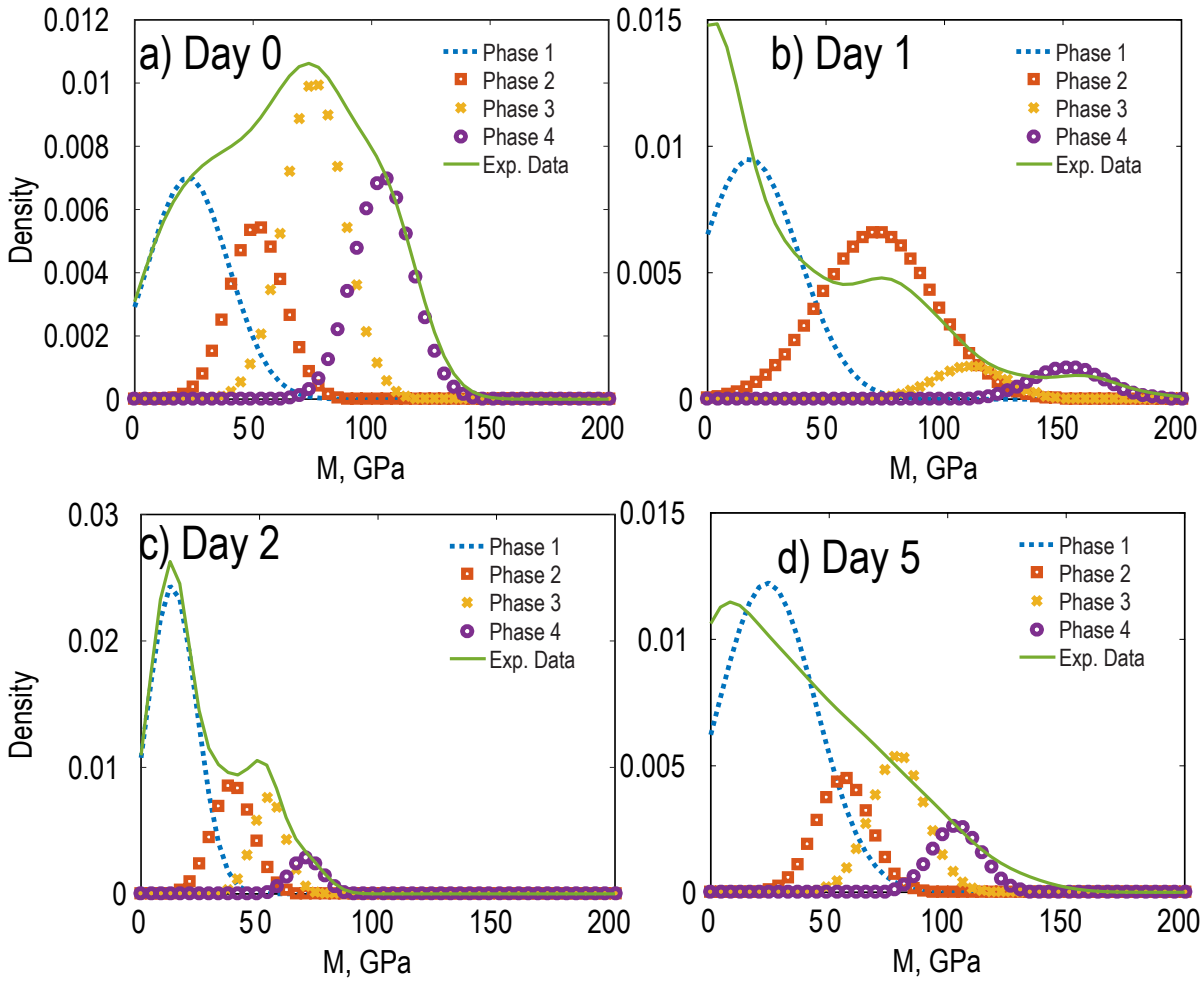

Figure 11.4: Frequency plots of indentation modulus with fitted Gaussian curve for a) Day 0, b) Day 1, c) Day 2 and d) Day 5.

Table 11.1: Summary of nanoindetation test results on Mt. Simon sandstone.

Specimen	Day 0	Day 1	Day 2	Day 5
Predicted M_{Macro} (GPa)	36.22	24.49	21.93	22.74
Surface Roughness (nm)	36	58	289	478
Porosity (%)	30	49	63	63

Table 11.1 summarizes the result of nanoindentation and atomic force microscopy measurements on different specimens. In this study, we found that the fracture toughness of the Mt. Simon sandstone decreases with exposure to humidity over time. The porosity of the samples increased as the interaction time increased. In addition, as summarized in Table 11.1, an increase in roughness is measured with AFM. Also, a decrease in predicted macroscopic modulus is observed (cf. Table 11.1).

A decrease in fracture toughness was observed after incubation of Mt. Simon specimen in high relative humidity. This decrease in fracture toughness suggests several feasible mechanisms, for instance dissolution of grains, precipitation of secondary phase and swelling of clays. The dissolution of quartz and feldspar grains at this short fluid-rock interaction timespan is not feasible. While, the precipitation of salt as well as reactions of water vapor with other constituents of Mt. Simon sandstone are feasible mechanisms of reactions. The quartz and K-feldspar grains are less reactive with water at room temperature, whereas the clay particles are more susceptible to water reactions. Aksu et al. [315], showed that the clay swelling occurred almost instantaneously after water-clay contact using micro-CT images. The environmental scanning electron microscopy images of Mt. Simon reveals montmorillonite clay structure present in Mt. Simon sandstone studied here. As observed in Figure 311.3a) the precipitation occurs more in intergranular areas. We observe that the precipitation density and covered area increases as the incubation time increase for Mt. Simon sandstone. In addition, we observe these precipitants are mostly concentrated around intergranular and clay rich regions. Figure 11.5 demonstrates the morphology of smectite particles where it's surrounded by precipitation from the fluid-rock interaction experiments in a unique scanning electron microscopy image.

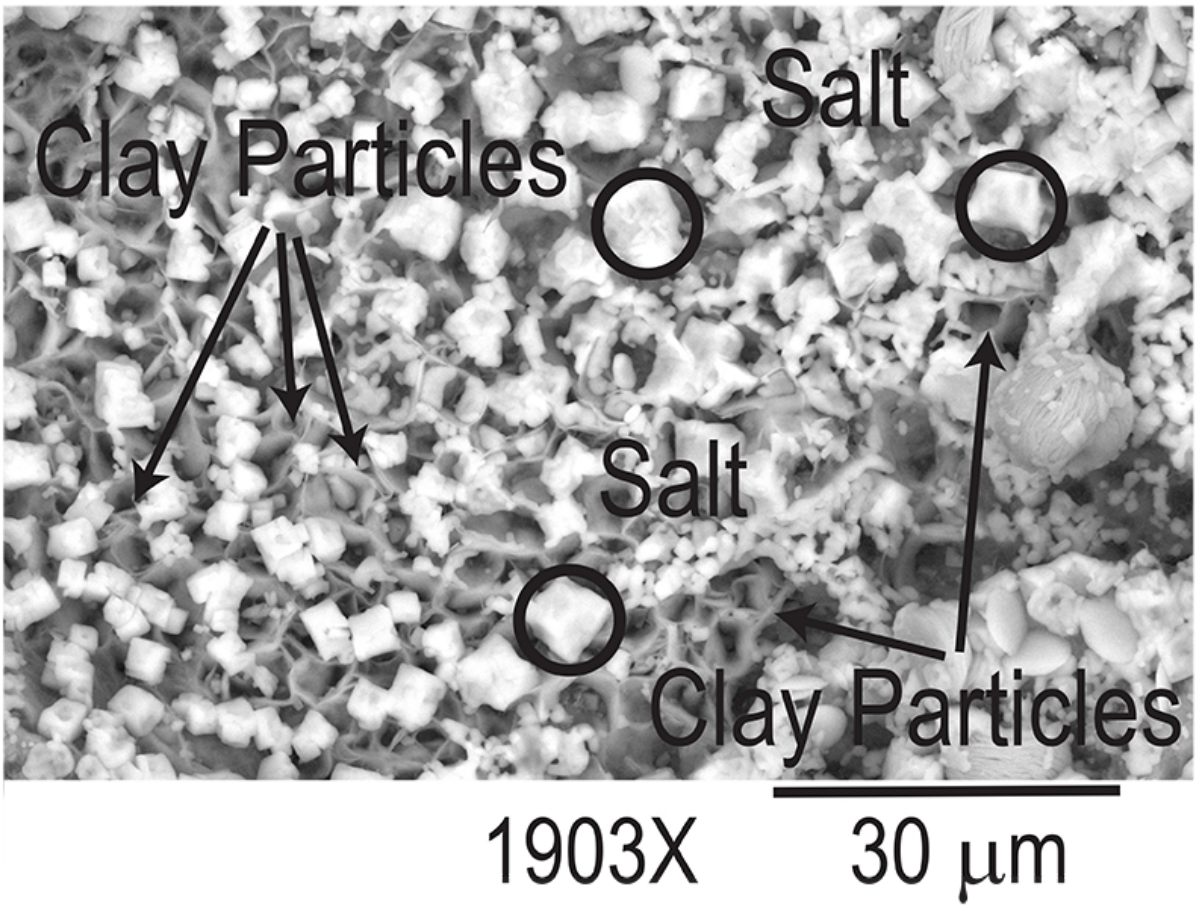

Figure 11.5: Back-scattered scanning electron microscopy image of clay particles and salt precipitation on clay particles Mt. Simon sandstone at Day 5.

Table 11.2: Summary of Grid nanoindentation deconvolution tests carried out on Mt. Simon sandstone for Day 0, Day 1, Day 2 and Day 5. μ: average for Gaussian distribution model. σ: standard deviation for Gaussian distribution model. Vol.: Volume Fraction.

	Phase	μM (GPa)	σM (GPa)	μH (GPa)	σH (GPa)	Vol. (%)
Day 0	1	22.6	17.1	0.5	0.9	30
	2	51.3	11.66	2.5	2.5	16
	3	75.7	12.7	5.1	5.1	32
	4	104.7	12.5	8.9	8.8	22
Day 1	1	17.9	20.6	0.4	1.1	49
	2	71.6	24.1	3.5	2.1	40
	3	110.8	15.2	7.3	0.9	5
	4	152.1	15.8	9.2	1.0	5
Day 2	1	13.2	10.3	0.1	0.2	63
	2	38.5	8.7	0.5	0.2	19
	3	54.1	6.8	1.1	0.4	13
	4	69.5	6.9	3.1	0.7	5
Day 5	1	23.9	20.5	0.4	0.9	63
	2	55.9	11.4	2.2	1.0	13
	3	79.1	11.8	4.4	1.3	16
	4	103.7	10.6	7.1	1.1	7

We construe that clay particles take the water vapor present in their surroundings and swell. The uptake of water by montmorillonite appears to be controlled by the competitive hydrogen bonding between water molecules and between water and silica tetrahedral [316]. Furthermore, Katti and Katti [317], demonstrated that relative swelling of montmorillonite is attributed to the disorientation of the clay platelets and the hydration of platelets and moving them apart. Segad et al. [318], found out that more of the swelling takes places between the tactoids and not between the single platelets. A 40–100 percent increase in volume percentage of clays are observed after swelling. This swelling of clay particles can occur promptly after interaction with water. We construe this to mean that, as clay layers move apart because of water interaction, clay particles exert force on the grain boundaries where the weaker grains undergo a prescribed strain which result in creation of microcracks in grains. This microcracking of grains, produce a weaker matrix of grains and decrease the fracture toughness of the Mt. Simon sandstone after fluid-rock interaction. Figure 11.6a) demonstrates the salt formation in addition to micro-cracking on the grains after 5 Days of incubation. Figure 11.6b) demonstrates another case of microcracking on feldspar grains where the presence of clay, epoxy and the grain is evident. The clay particles are surrounding the grain particles and coating them extensively.

This microcracking will decrease the strength of grains and thus decrease the fracture toughness.

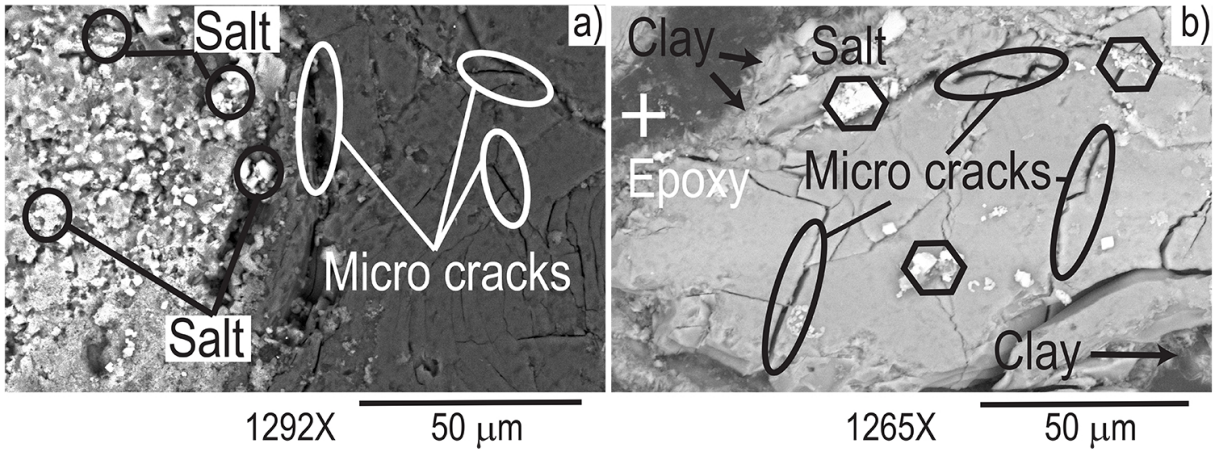

Figure 11.6: Back-scattered scanning electron microscopy images of Mt. Simon sandstone: a-b) Day 5 incubation.

An increase in porosity was observed as summarized in Table 1 from analyzing the grid statistical nanoindentation on Mt. Simon sandstone. The grid nanoindentation tests are deconvoluted using mixture modeling technique. The summary of nanoindentation deconvolution tests are shown in Table 11.2. The increase in porosity can be attributed to the swelling of the clays as well as microcarking of grains. In addition, the predicted elastic properties of the Mt. Simon decrease as the incubation time increases due to increase in porosity and weakening of the grains. The plain strain indentation modulus decreases as the incubation time increases (cf. Table 11.1), where most of this decrease of elastic property is assigned to increase in porosity and micro-cracking of grains. In similar studies [319, 320], researchers reported a decrease in the elastic modulus of limestone/sandstone after exposure to acid and carbonated water. This increase in porosity can be attributed to two different phenomena, one is the swelling of clay particles and disorientation of the clay platelets. Second, fluid-rock interactions and its effect on microcracking of grains. For instance, Rimmelé et al. [321], reported an increase in porosity of sandstone after incubation in CO_2-saturated water for a short duration. Similarly, Luquot and Gouze, 2009 noted an increase in porosity during tests on limestone samples exposed to CO_2-enriched fluid, where these changes are attributed to dissolution and/ or precipitation.

11.5 Multi-scale Thought Model of Sandstone

A detailed multi-scale thought model of sandstone is developed based on the microstructural observation of the Mt. Simon specimen. A conceptual multi-scale model was formulated for the Mt. Simon sandstone in order to connect the local behavior at the nano- and microscopic length scales to intrinsic properties at the macroscopic scale. Figure 11.7 a) illustrates the model. At the macroscopic scale, the core level, the material is modeled as a homogeneous isotropic solid. At the microscale or pore level, the material is modeled as a granular multi-phase solid. Hard grains made of quartz or siderite and microscopic air voids are embedded in a matrix made of nanoporous feldspar. In particular, at the microscopic level, the air void, feldspar and quartz phases exhibit distinct morphologies. At the nanometer length-scale or nanopore level, the representative elementary volume consists of solid feldspar with uniformly dispersed nanopores.

Figures 11.7 b) and c) compare our model to prior conceptual models published in the scientific literature for rock within the context of CO_2-induced rock-fluid interaction. Sun et al. [310] formulated a bonded-particle model for sandstone at the microscopic length scale using the discrete element method (Figure 11.7 c.). They investigated the influence of the inter-particle cement on the effective response. However, they did not account for the porosity, at both the nano- and micro-scale. In addition, their model considered the solid skeleton to be homogeneous despite the high heterogeneity of sandstone. In contrast, Nguyen et al. [322] built a model which accounts for the dual-scale porosity, (Figure 11.7 b). The nano-porosity is concentrated in the clay phase surrounding the micro-scale grains, thus limiting the model to high clay volume fractions. Furthermore, although different solid phases are considered at the micro-scale, a similar morphology was assumed for all solid phases. Their model is inadequate for Mt. Simon sandstone as the clay fraction, 1 % wt, is too small to be sensed using grid indentation. Furthermore, they omitted to take into account the influence of the particle morphology on the effective mechanical response. On the other hand, our three-level model captures the heterogeneous and porous nature of the Mt. Simon sandstone. Next, we present statistical method and the nonlinear upscaling model to describe the mechanical response.

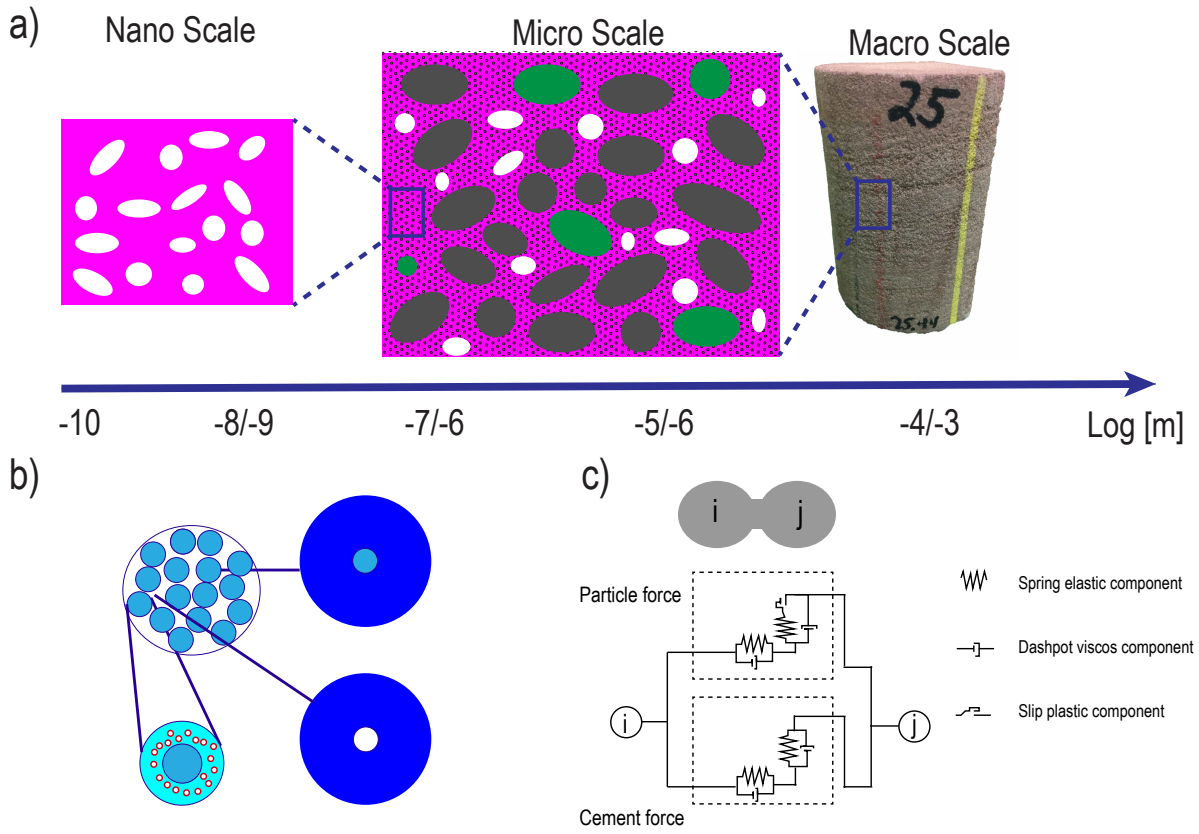

Figure 11.7: a) Multi-scale model of Mt. Simon sandstone. Level 1: Solid feldspar with nanoporosity. Level 2: Heterogeneous grains of quartz, sidertite, and micropores in a nanoporous feldspar domain. Level 3: Homogeneous material response at macroscopic length scale. Adopted from [323], b) Thought model from Nguyen et al. [322], c) Thought model from Sun et al. [310].

Two grid of indentation for AS4 and AS1 is presented here to see the effect of CO_2 incubation on the porosity and the values of different phases. Figure 11.8 illustrates the constructed continuous phase map for an AS1 specimen. Figure 11.8 b) illustrates the optical microscopy image of the indented area. The conionous phase map roughly represent the probed area.

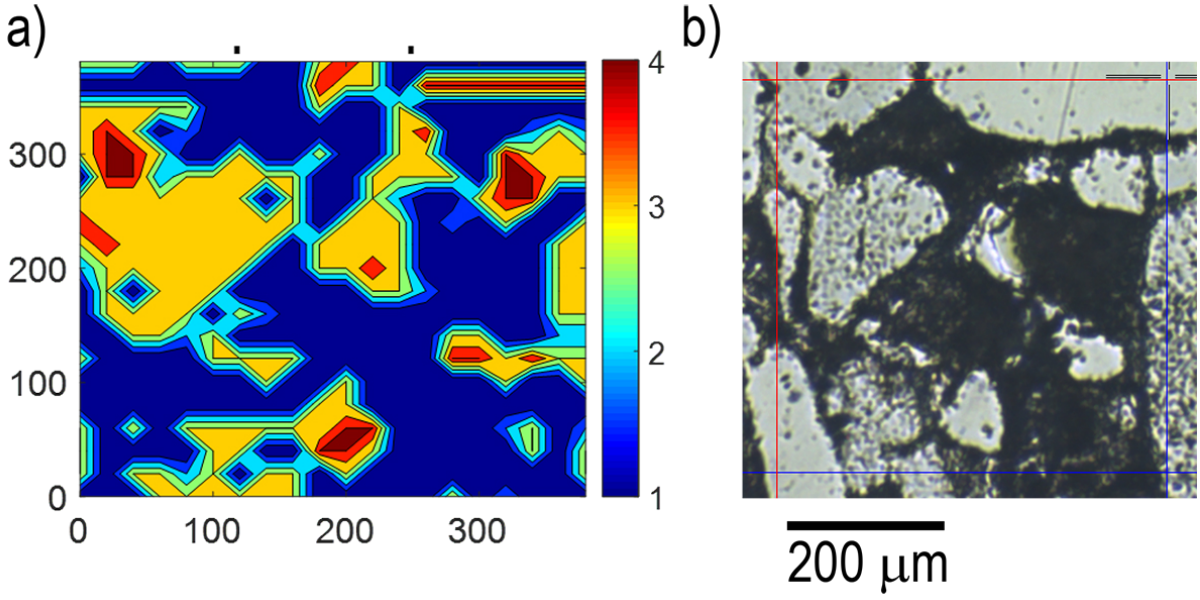

Figure 11.8: a) Continuous phase map of deconvolution of statistical nanoindentation on AS1 specimen. The tests are carried out on a 20 by 20 grid of indents. b) Optical microscopy of indented area for AS1 specimen. AS1 specimen was aged at Prof. Tsotsis research group.

Table 11.3 summarizes the results of deconvolution of nanoindentation grid tests for AS1 and AS4 specimens. The porosity (phase 1) increase in the case of AS1 compare to Day 0 alteration specimen.

Similarly, Figure 11.9 demonstrates the phase map constructed for the AS4 specimen. Qualitatively, the amount of dark blue increase for AS1 compared to original specimen. This illustrate an increase in the porosity of specimen.

In addition, the indentation modulus is used to predict the mechanical response in the macroscopic length scale using a micromechanics approach. This calculation results in a predicted bulk modulus for AS1 and AS4 as 33.44 GPa and 28.54, respectively.

Table 11.3: Summary of Grid nanoindentation deconvolution tests carried out on Mt. Simon sandstone for AS1 and AS4. μ: average for Gaussian distribution model. σ: standard deviation for Gaussian distribution model. Vol.: Volume Fraction.

	Phase	μM (GPa)	σM (GPa)	μH (GPa)	σH (GPa)	Vol. (%)
AS1	1	11.03	19.77	0.15	0.18	45
	2	49.41	17.20	1.14	0.20	16
	3	89.13	21.50	7.64	3.63	33
	4	125.03	14.18	12.79	0.58	5
AS4	1	4.68	2.39	0.28	0.13	19
	2	21.63	13.03	1.49	1.06	20
	3	56.89	20.55	4.88	2.27	22
	4	102.51	23.26	11.62	2.89	38

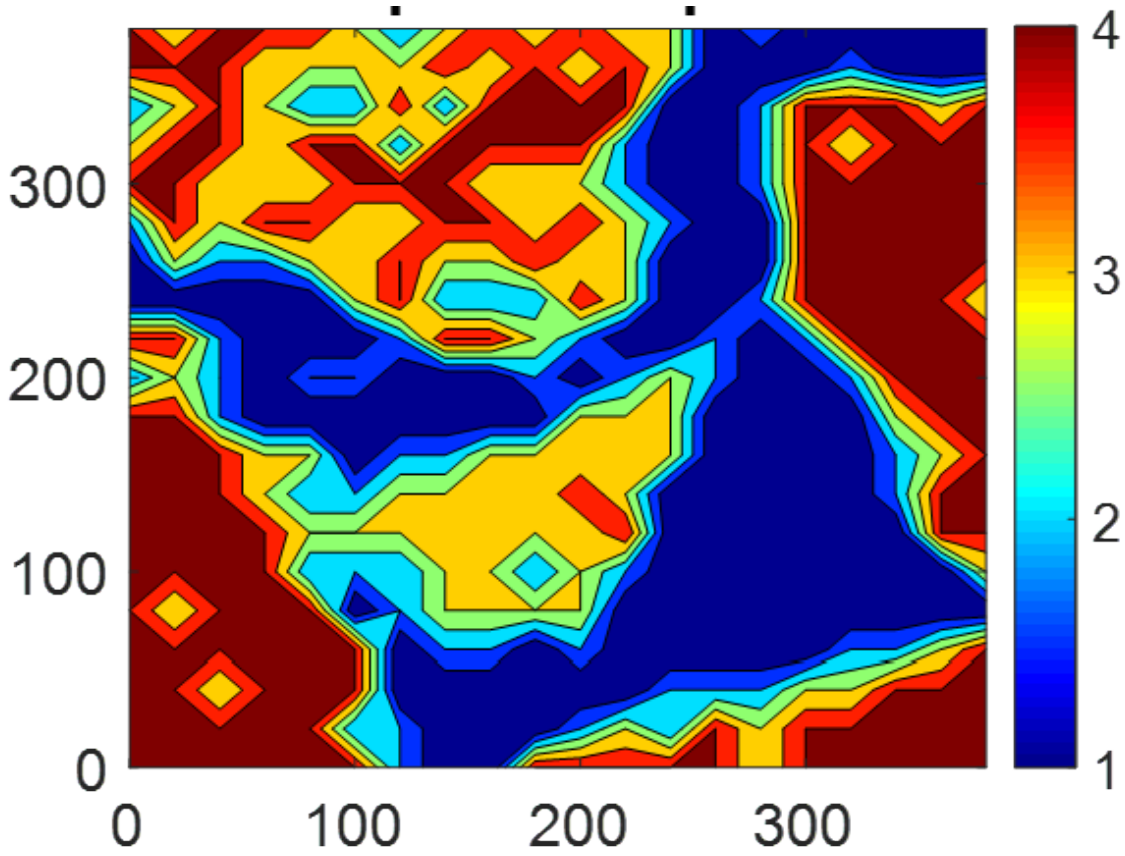

Figure 11.9: a) Continuous phase map of deconvolution of statistical nanoindentation on AS4 specimen. The tests are carried out on a 20 by 20 grid of indents. AS4 specimen was aged at Prof. Werth research group.

11.6 Conclusion

We used experimental micro-mechanical testing such as nanoindentation to characterize the fluid-rock reactions for short exposure time to high humidity using 4 different specimens. Furthermore, we utilized finite mixture modeling for grid nanoindentations to capture the changes in elastic properties and fracture toughness of altered specimens. An increase in porosity is observed using grid nanoindentation tests. While a decrease in fracture toughness was observed with an increase in time of fluid-rock interaction. The precipitation of salt was observed using environmental scanning electron microscopy imaging.

Chapter 12

CO_2-Induced Degradation of Fracture Behavior of Mt. Simon Sandstone

12.1 Introduction

In this Chapter, the goal is to find the effect of geochemical reactions on fracture toughness of sandstone. The incubation experiments performed are summarized here for fracture toughness characterization. The microscratch experiments performed here will be summarized and the details of the specimen preparation. Furthermore, the geochemical reactions and the geomechanical alterations and their effect at macroscopic scale and on the reservoir is presented.

12.2 Scratch Testing on Mt. Simon Sandstone

The first protocol is to test the fracture toughness without epoxy impregnation. The second approach is to epoxy mount the specimens without vacuum. The third is a series of vacuum impregnation with several different epoxies. The first epoxy is this study is an acrylic resin where it cures at room temperature. The second epoxy is a heat curing epoxy with a viscosity of 32 cps, this epoxy has a peak exotherm around 170 °C and the epoxy cures at 55 °C. The third epoxy is a higher viscosity epoxy with a peak exotherm at 30 °C and the epoxy cures at room temperature. In the next session a series of experimental

result is shown to summarize the reasoning behind choosing one preparation for further testing.

12.3 Influence of Surface Preparation Method on Fracture Results

As described in previous sections the microscratch experiments can be used to characterize the fracture toughness of heterogeneous materials. The fracture toughness is measured by utilizing the horizontal force measurements as well as the depth measurements. The scratch tests are performed on to capture the fracture toughness of different specimens. For example, Figure 12.1 demonstrates the results of a series of scratch tests on a not embedded specimen. This specimen is prepared using the grinding and polishing procedure described in previous chapters. The scratch tests are characterized at a maximum force of 7N over a length of 3 mm with a speed of 6mm/min, total of 9 different tests are carried out on this specimen. Figure 12.1 a) demonstrates the fracture toughness of the specimen and the R_a value. This value characterizes a indirect measurements of roughness of the specimen, a mean average of surface roughness measured with a small force on specimen. The fracture toughness is K_c =0.32±0.17 MPa$\sqrt{m}$. The high value of standard variation on the fracture toughness as well as the high value of the roughness demonstrates that the surface of the specimen is polished enough to meet the criteria for scratch testing. In addition, Figure 12.1 b) illustrates the panorama optical microscopy image of the scratch path and there is no visible groove. The red arrow in this figure shows the scratch path. The visual inspection of the specimen shows the movement of grains instead of breaking of grains. This behavior alter the fracture properties of the material.

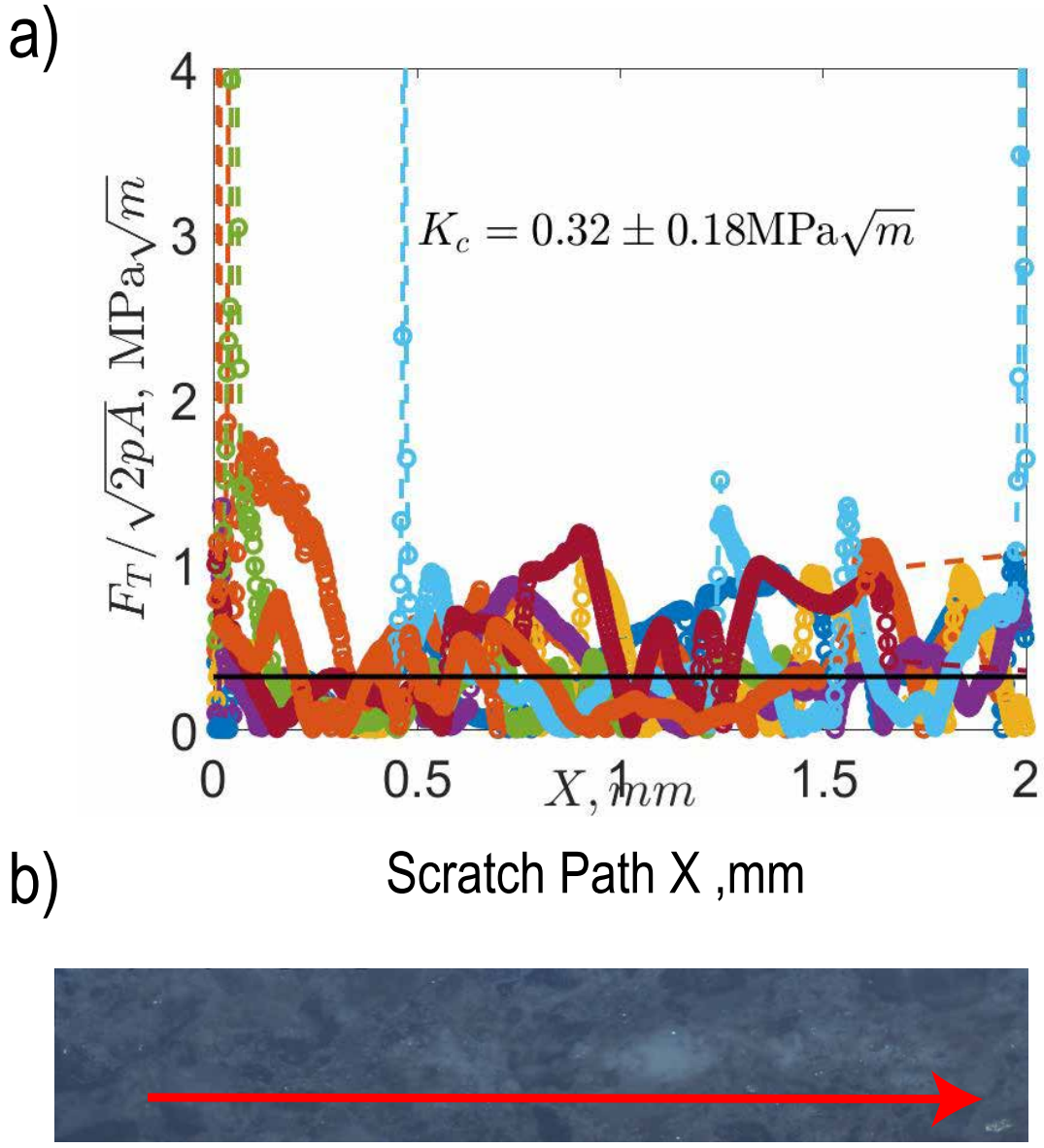

Figure 12.1: Scratch scaling for Mt. Simon sandstone: 6925-U. $F_T/\sqrt{2pA}$ values for scratch length X. The specimen is not embedded. The solid line shows the value of fracture toughness,K_c in MPa$\sqrt{m}$. The red line shows the scratch path direction.

The second protocol is mounting the specimen in epoxy without using vacuum system. The method is developed to eliminate the movement of the quartz particles in the scratch testing. Figure 12.2 demonstrates the result of scratch testing for embedded specimens in epoxy. The embedding process is done at room temperature and over 9 hours. This figure consists of 3 sub-figures (Figure 12.2a-c), where the Figure 12.2a illustrates the results of scratch tests with a maximum force of 7N, 3mm length and 9 different paths. The fracture toughness is characterized as K_c =0.39±0.19 MPa$\sqrt{m}$. This demonstrates the same trend on the fracture toughness, a high standard deviation with a high value of Ra =10.70μm. Figure 12.2 b–c illustrates two different specimens tested with a maximum force of 4N, 3mm length and total of 16 tests carried out on these specimens. The fracture toughness variation decrease for these specimens given the lower maximum force compared to the first set of tests. This protocol shows an improvement in the optical microscopy panorama images of scratch tests.

The next step to improve the preparation process is to vacuum embedding the specimens. The vacuum impregnation setup is developed for filling the pores as much as possible. The specimens are vacuum embedded with the use of three epoxies, acrylic resin, heat cured resin and room temperature cured resin.

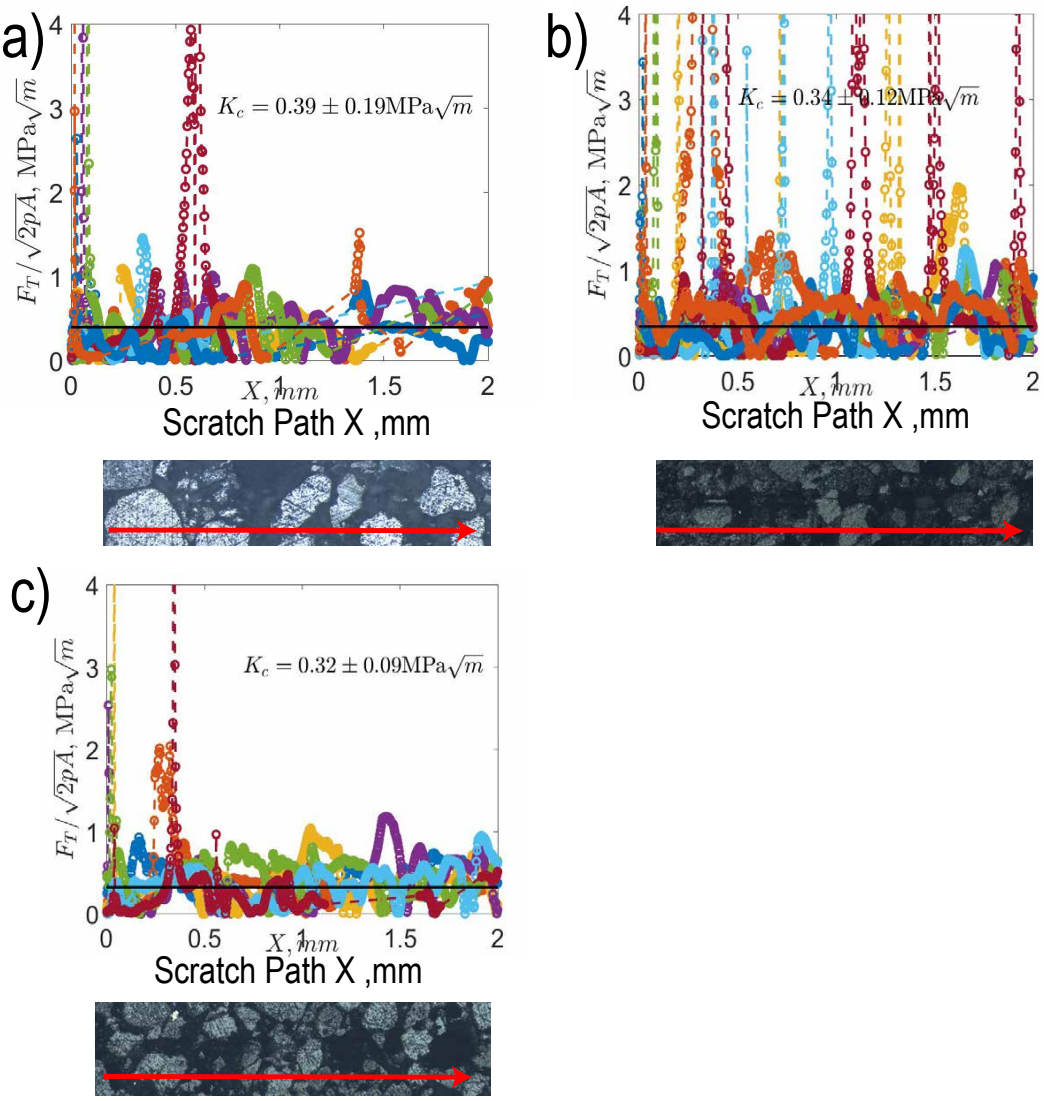

Figure 12.2: Scratch scaling for Mt. Simon sandstone: 6925-U. $F_T/\sqrt{2pA}$ values for scratch length X. The resin embedded specimen. The solid line shows the value of fracture toughness,K_c in MPa$\sqrt{m}$. The red line shows the scratch path direction.

Figure 12.3 demonstrates the results of scratch testing on vacuum embedded specimen in acrylic resin. Figure 12.3a-c illustrates the three different specimens with a maximum of 4N load, 3mm length and total of 15 tests. The fracture toughness for this procedure resulted in K_c =0.55±0.10 MPa$\sqrt{m}$ on average. This shows that the variation of scratch toughness has decreased dramatically from the two previous procedures. The root average roughness, R_a is between 1.55 μm and 0.99 μm. Thus, this hows a significant decrease in the roughness of the surface. In addition, a set of atomic force microscopy characterization is performed, where the root mean squared roughness is 164 nm for a 40 μm × 40 μm area.

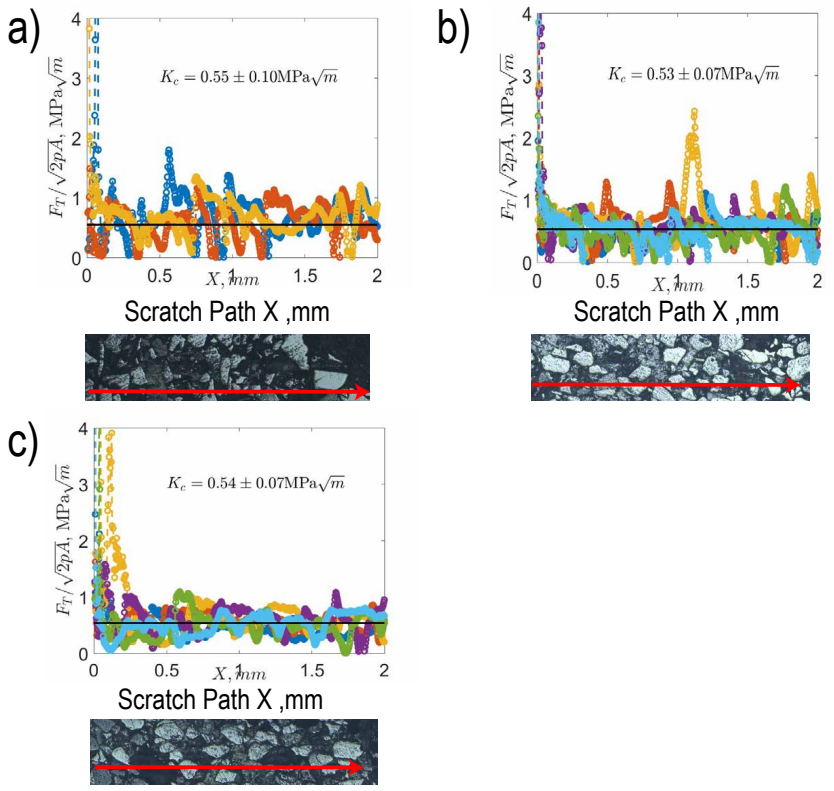

Figure 12.3: Scratch scaling for Mt. Simon sandstone: 6925-U. $F_T/\sqrt{2pA}$ values for scratch length X. The acrylic resin vacuum embedded. The solid line shows the value of fracture toughness,K_c in MPa$\sqrt{m}$. The red line shows the scratch path direction.

In addition to the acrylic epoxy, a heat cured epoxy is evaluated to find the best embedding medium. Figure 12.4 illustrate the vacuum embedded with heat cured epoxy. Figure 12.4a-b illustrates the scratch tests from two set of specimens with the maximum scratch force of 4N, scratch length of 3mm and 12 tests in total. The fracture toughness

value is K_c =0.74±0.07 MPa$\sqrt{m}$ and K_c =0.62±0.11 MPa$\sqrt{m}$. The root mean squared roughness of these tests are 0.63 μm and 0.99 μm. Although the values of fracture toughness and roughness are in acceptable ranges but the high peak exotherm of this epoxy prevents of utilizing this epoxy. There might be thermal damage due to this high peak temperature of epoxy curing.

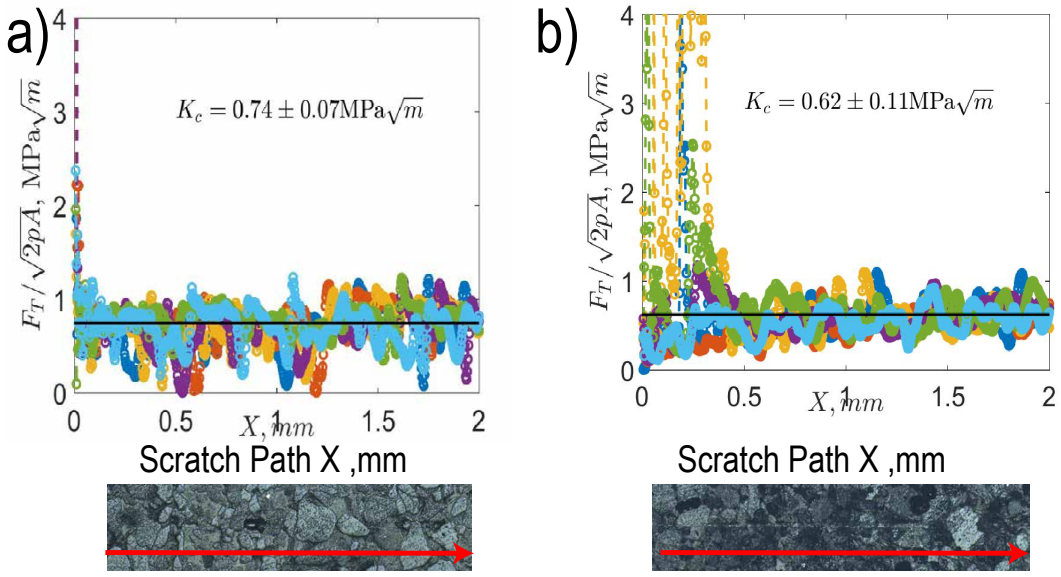

Figure 12.4: Scratch scaling for Mt. Simon sandstone: 6925-U. $F_T/\sqrt{2pA}$ values for scratch length X. The heat cured vacuum embedded. The solid line shows the value of fracture toughness,K_c in MPa$\sqrt{m}$. The red line shows the scratch path direction.

The last procedure is devoted to an epoxy with a higher curing time in room temperature, 9 hours. The maximum exotherm for this epoxy is 30 °C. The benefit of this low temperature is preservation of the specimen structure as well as low thermal damage. The vacuum embedded specimens for this case is done with EpoThin$^{\text{TM}}$. Figure 12.5 illustrates the two tests carried out with a maximum force of 4N, scratch length of 3mm and total of 6 tests. The fracture toughness is K_c =0.53±0.13 MPa$\sqrt{m}$ and K_c =0.41±0.07 MPa$\sqrt{m}$. The mean average surface roughness of this procedure is R_a = 0.95 μm and 1.66 μm for two specimens respectively. The atomic force microscopy analysis resulted in a root mean squared roughness of 36 nm for 40 μm × 40 μm area. The specimen here is prepared with a high speed diamond saw.

The implementation of vacuum impregnation significantly improved the quality of optical microscopy images of scratch tests and reduced the mean average roughness of

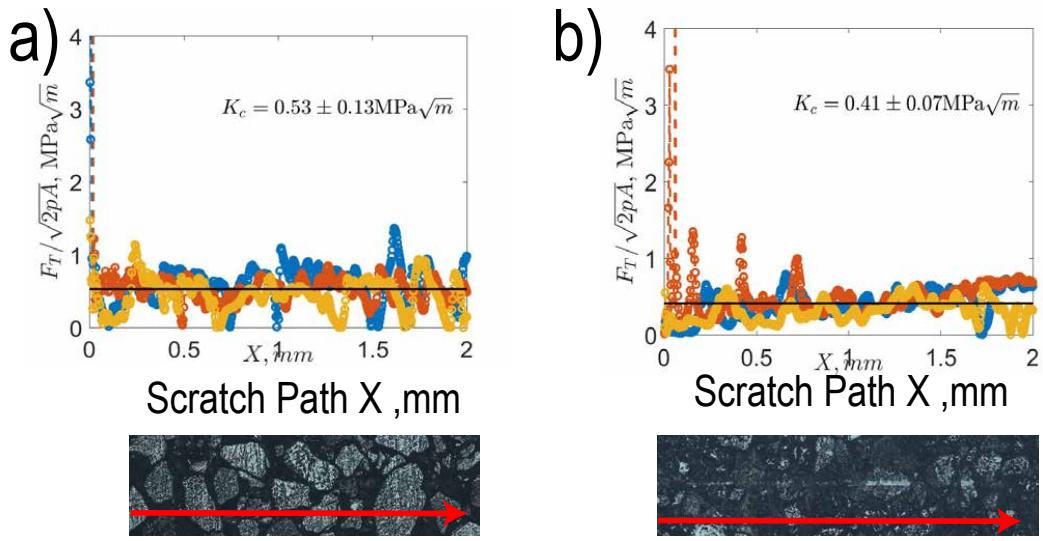

Figure 12.5: Scratch scaling for Mt. Simon sandstone: 6925-U. $F_T/\sqrt{2pA}$ values for scratch length X. The Epothin vacuum embedded and cut with high speed saw. The solid line shows the value of fracture toughness,K_c in MPa$\sqrt{m}$. The red line shows the scratch path direction.

surfaces. The next step is to use a slow speed diamond saw to cut the specimens. Figure 12.6 illustrates the result of scratch testing for vacuum embedded with room temperature curing epoxy while cutting the specimen with low speed diamond saw. Figure 12.6a demonstrates the result of 7 scratch tests with a maximum force of 4N and resulted in K_c =0.71±0.21 MPa$\sqrt{m}$. Figure 12.6b represents 6 scratch tests with a maximum of 30N, 3mm scratch length. This procedure results in K_c =0.88±0.25 MPa$\sqrt{m}$. The mean average surface roughness, R_a is 0.63 μm and 1.2 μm, respectively.

Thus, a detailed experimental study is carried out to find the most suitable epoxy where the structure of the specimen is reserved and the fracture toughness characterization results in reasonable standard deviation of fracture toughness values. In addition, an optical microscopy comparison of these steps will be helpful.

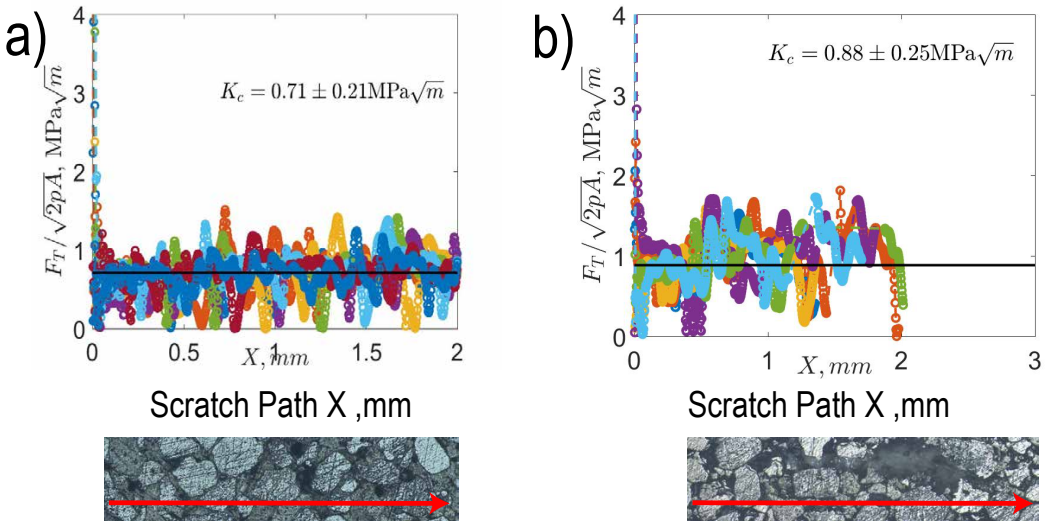

Figure 12.6: Scratch scaling for Mt. Simon sandstone: 6925-U. $F_T/\sqrt{2pA}$ values for scratch length X. The Epothin vacuum embedded and cut with slow speed saw. The solid line shows the value of fracture toughness,K_c in MPa$\sqrt{m}$. The red line shows the scratch path direction.

12.4 Effect of Chemical Alterations on Fracture Toughness

As mentioned in chapter 10, different chemical alterations are carried out to assess the effect of different chemical alterations on mechanical performance of the host rock. Figure 12.7 demonstrates the schematic of the experimental setup for incubation in CO_2-saturated brine.

Figure 12.8 demonstrates the fracture toughness as well as the panorama image of the scratch test for an unaged specimen. The fracture toughness K_c =0.88 $\pm$ 0.25 MPa$\sqrt{m}$ for the unaged specimen and the average mean roughness is R_a=1.2 μm. The maximum force of 30 N with a scratch length of 3mm, a speed of 6 mm/min and six tests are carried out.

Next, a presentation of several geochemical reactions are presented. The first series of geochemical reactions are performed in the room temperature and pressure. The specimens were cut into suitable pieces. The specimens were kept in a tight container for 14 days. After the incubation the specimens are extracted and dried out under a vacuum before testing. The chemical composition of brine recipies used in this incubation

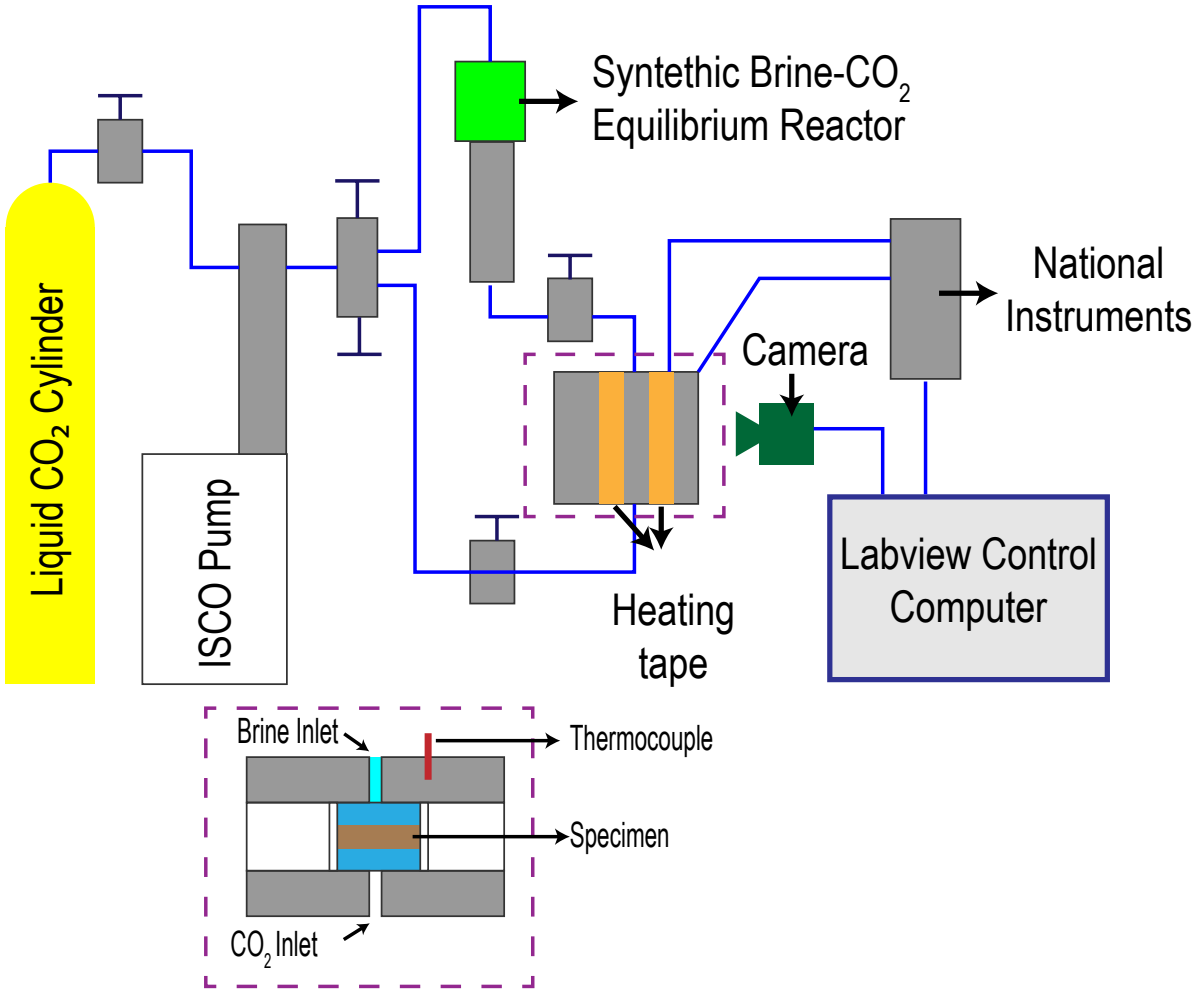

Figure 12.7: Schematic of the Experimental Setup for incubation in CO_2-saturated brine. Adopted from [324].

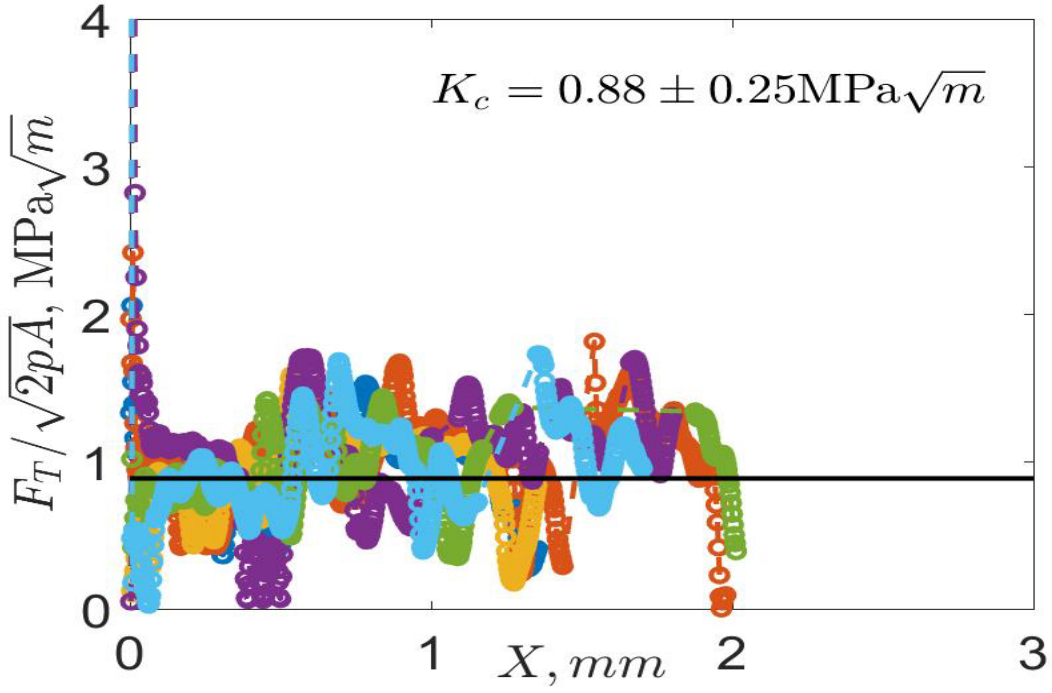

Scratch Path X, mm

Figure 12.8: Scratch scaling for Mt. Simon sandstone: 6925-U. $F_T/\sqrt{2pA}$ values for scratch length X. The solid line shows the value of fracture toughness,K_c in MPa$\sqrt{m}$.

experiments is presented in Chapter 10.

Figure 12.9 illustrates the scratch tests results for maximum load of 30 N, scratch length of 3mm, speed of 6 mm/min and total of 9 tests. The pH of the deionized water (DI) was measured at 6. The results illustrates fracture toughness of K_c =0.91 $\pm$ 0.14 MPa$\sqrt{m}$. The average roughness is measured at R_a = 0.8 μm. The fracture toughness shows an increase with respect to the unaged specimen on the mean value but still falls within the standard deviation of the unaged specimen.

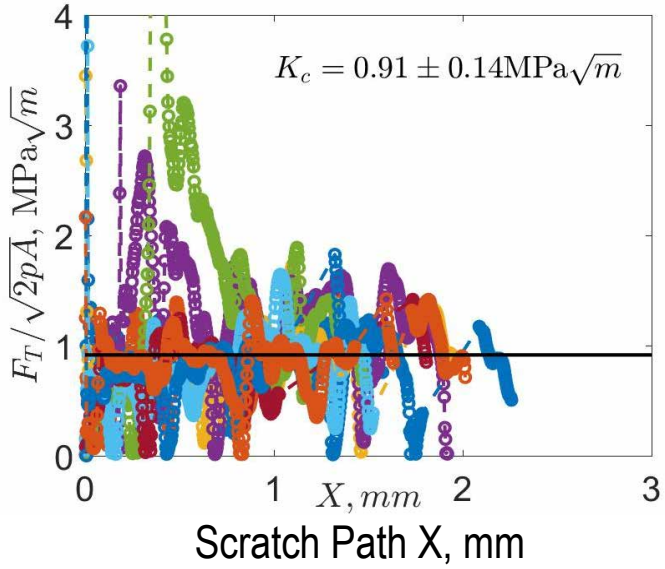

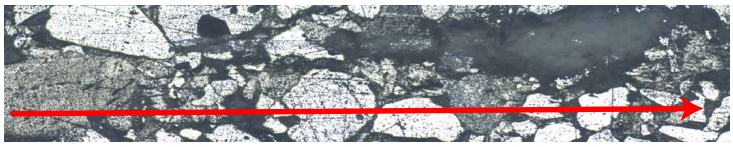

Figure 12.9: Scratch scaling for Mt. Simon sandstone: 6925-DI. $F_T/\sqrt{2pA}$ values for scratch length X. The solid line shows the value of fracture toughness,K_c in MPa$\sqrt{m}$.

Figure 12.10 summarizes the results of scratch testing on Brine Recipe 1 samples. The tests are carried out at maximum load of 30N, scratch length of 3mm, speed of 6mm/min and total of 7 scratch tests. The solution has a high concentration of salts and the pH is measured at 5 for this solution. The fracture toughness K_c =0.84 $\pm$ 0.08 MPa$\sqrt{m}$. This shows that the fracture toughness did not decrease significantly after incubation in this solution.

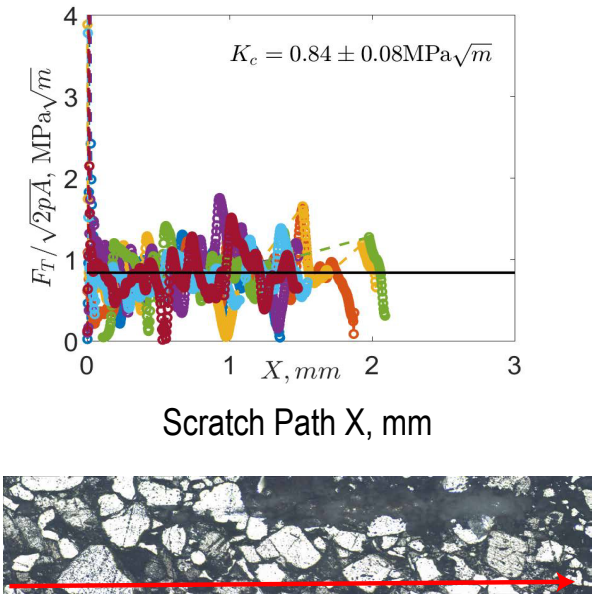

Figure 12.10: Scratch scaling for Mt. Simon sandstone: 6925-B1. $F_T/\sqrt{2pA}$ values for scratch length X. The solid line shows the value of fracture toughness,K_c in MPa$\sqrt{m}$.

Next, Figure 12.11 illustrates the results of scratch testing on Brine Recipe 2. This brine is higher in the KCL content compared to the recipe 1. The tests are carried out at 30 N, 3mm length and total of 9 tests. The fracture toughness from this specimen is evaluated as K_c =0.51 $\pm$ 0.15 MPa$\sqrt{m}$. Incubation in this high concentration of KCL resulted in a significant decrease in the value of fracture toughness.

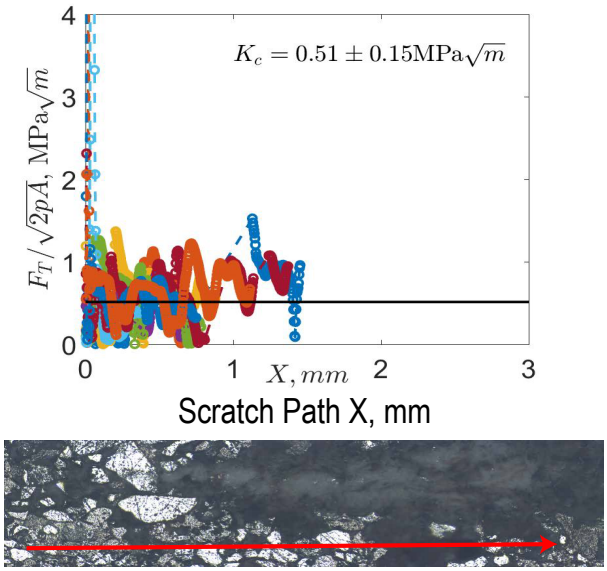

Figure 12.11: Scratch scaling for Mt. Simon sandstone: 6925-B2. $F_T/\sqrt{2pA}$ values for scratch length X. The solid line shows the value of fracture toughness,K_c in MPa$\sqrt{m}$.

The last geochemical reaction in room temperature and pressure is done on Brine Recipe 3. Figure 12.12 summarizes the results of scratch testing for this recipe. The tests are carried out at maximum load of 30 N, 3mm length, 6mm/min and total of 7 tests. The fracture toughness is K_c =0.97 $\pm$ 0.13 MPa$\sqrt{m}$. The mean average roughness is R_a = 1.6 μm. The pH of the solution is measured at 5. The concentration of KCL is lower in this solution. The fracture toughness has not decreased at this incubation experiment.

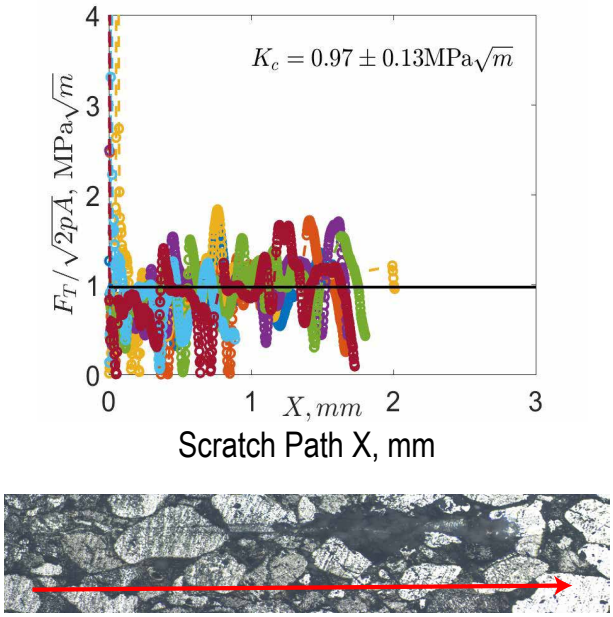

Figure 12.12: Scratch scaling for Mt. Simon sandstone: 6925-B3. $F_T/\sqrt{2pA}$ values for scratch length X. The solid line shows the value of fracture toughness,K_c in MPa$\sqrt{m}$.

In the next part of this chapter, the aging experiments with brine-saturated CO_2 is presented. These experiments are divided into two different protocol. First one, is aging the specimen at 52 °C and 3290 psi in the incubation chamber presented in Chapter 10 for 28 days. Figure 12.13 demonstrates the results of scratch testing for aging the Mt. Simon sandstone for 28 days. Scratch tests are performed with a maximum load of 30N, scratch length of 3mm and total of seven scratch tests are carried out. The fracture toughness is K_c =0.33 ± 0.12 MPa$\sqrt{m}$. The average mean roughness, R_a, is 1.2 μm. There is a significant decrease in fracture toughness in this case in comparison to the unaged specimen.

Furthermore, two more specimens are tested for aging in brine-saturated CO_2 conditions. These specimens are aged for 7 days at 50 °C and 2500 psi. Figure 12.14 demonstrates the results of scratch testing on the 7 days aged specimen. The scratch tests are performed with a maximum vertical force of 30N, scratch length of 3mm and total of 7 tests. The fracture toughness is K_c =0.76 ± 0.20 MPa$\sqrt{m}$ while the average mean roughness, R_a is 0.7 μm.

The second specimen aged in brine-saturated CO_2 conditions for 7 days at 50 °C and 2500 psi. Figure 12.15 illustrates the results of scratch testing on the second specimen.

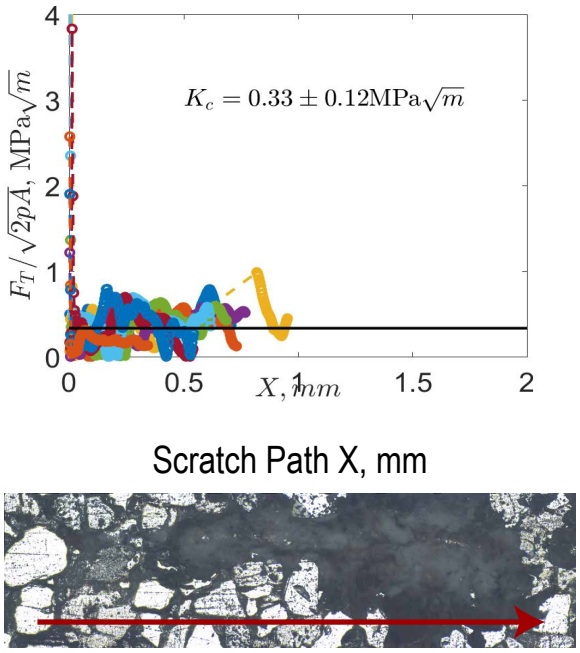

Figure 12.13: Scratch scaling for Mt. Simon sandstone: 6925-AS4. $F_T/\sqrt{2pA}$ values for scratch length X. The solid line shows the value of fracture toughness,K_c in MPa$\sqrt{m}$.

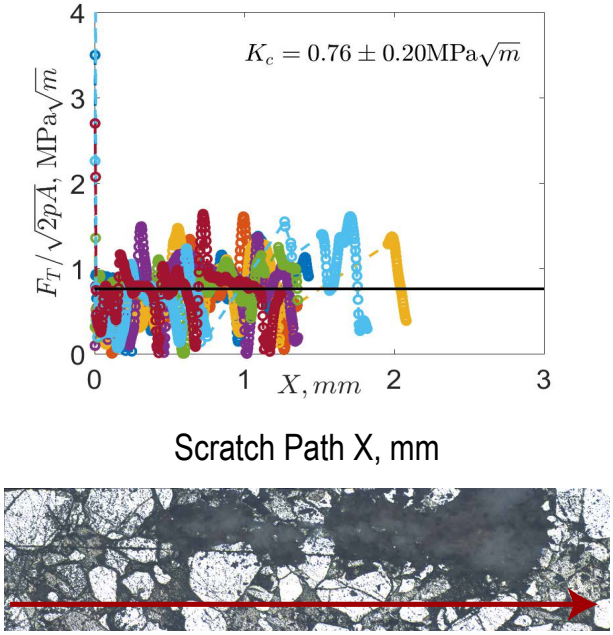

Figure 12.14: Scratch scaling for Mt. Simon sandstone: 6925-AS1-SP1. $F_T/\sqrt{2pA}$ values for scratch length X. The solid line shows the value of fracture toughness,K_c in MPa$\sqrt{m}$.

The maximum vertical load is 30N, 3mm of scratch length and total of 7 scratch tests. The fracture toughness is K_c =0.66 $\pm$ 0.23 MPa$\sqrt{m}$ while the average surface roughness, R_a, is 0.5 μm.

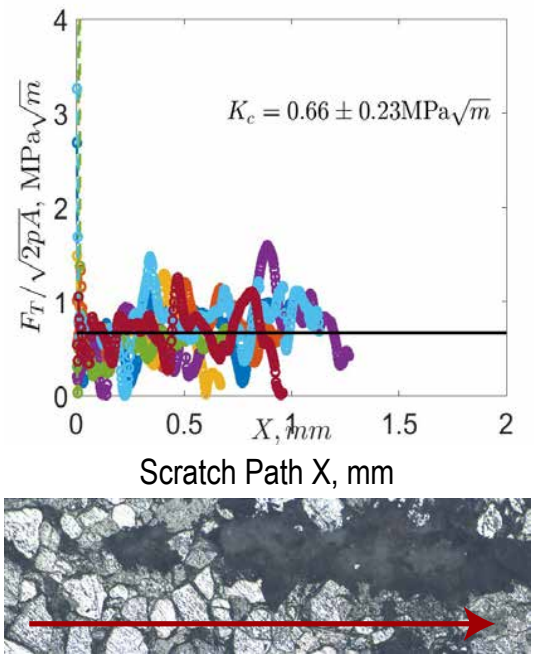

Figure 12.15: Scratch scaling for Mt. Simon sandstone: 6925-AS1-SP2. $F_T/\sqrt{2pA}$ values for scratch length X. The solid line shows the value of fracture toughness,K_c in MPa$\sqrt{m}$.

12.5 Microscopic Scale Investigation of Unaltered Mt. Simon specimen

The next step in understanding the geochemical alterations and its effect on geomechanical properties is illustrated with scanning electron microscopy. The extent of geochemical alterations are investigated with environmental scanning electron microscopy. Figure 12.16 illustrates the microstructural fabric of Mt. Simon sandstone. The sandstone has granular microstructure with coated clay particles. In this figure, presence of clay particles on the grain surface and grain boundary is obvious.

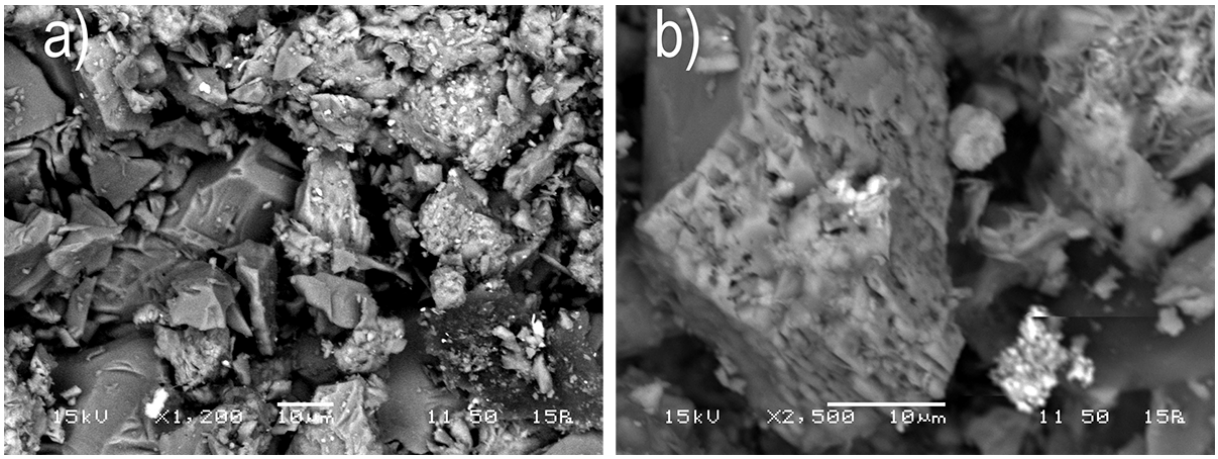

Figure 12.16: Scanning electron microscopy imaging of Mt. Simon sandstone before polishing.

One of the main concerns regarding the polishing and grinding of porous media is removal of phases from the fabric of the material. Figure 12.17 illustrates the granular fabric of the specimen after grinding and polishing. The presence of clay particles in inter-granular space is shown in this figure. Figure 12.17 illustrates two scale porosity for the Mt. Simon sandstone fabric.

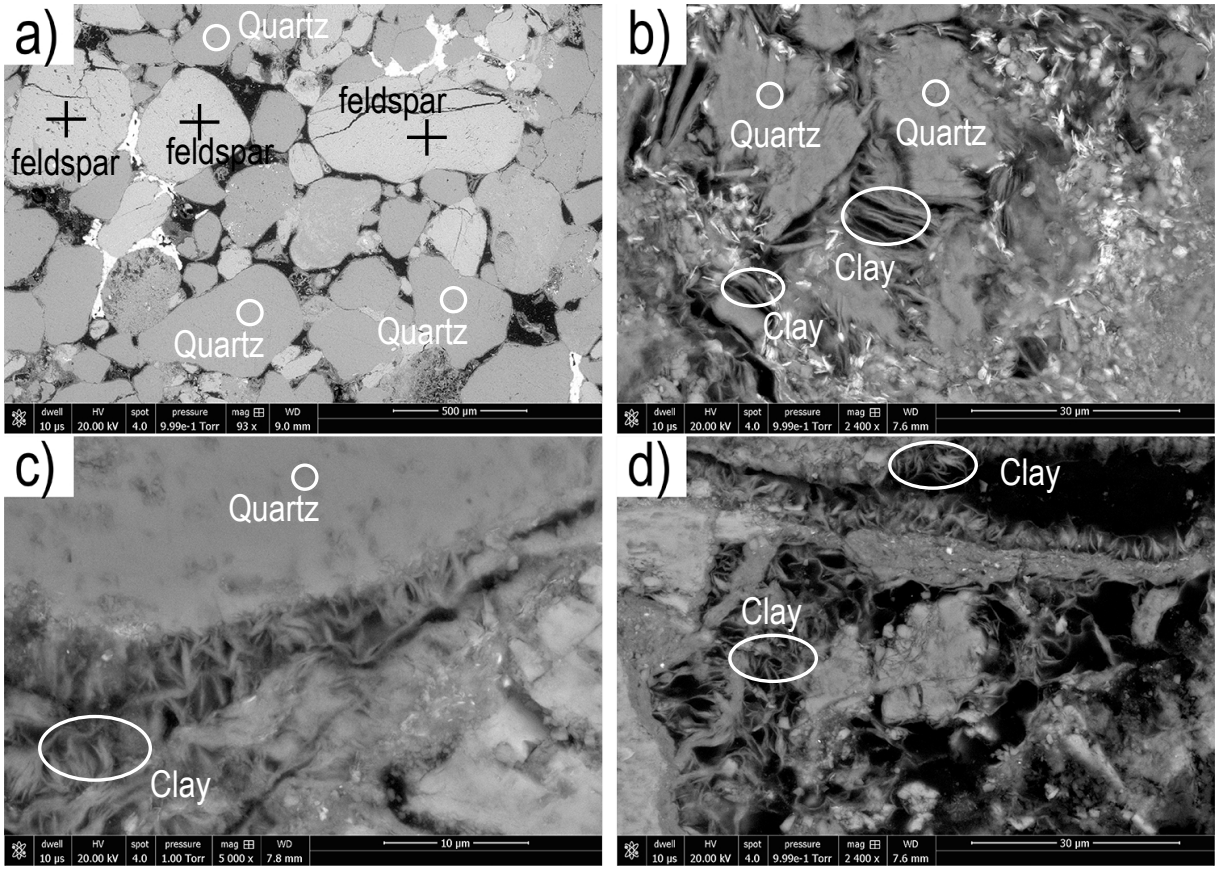

Figure 12.17: Scanning electron microscopy imaging: a–d) Mt. Simon sandstone after grinding and polishing.

12.6 Microstructure of CO_2-altered Mt. Simon Sandstone

A clearer understanding is achieved by examining the microstructure of Mt. Simon sandstone, before and after aging. Here, we examine the stitched image of scanning electron microscope for altered specimen. In addition, a scratch groove is imaged to observe different mechanism present in fracture of Mt. Simon sandstone. Figure 12.18 demonstrates a high quality scanning electron image of 100 scanning electron microscopy images. These 100 images are stitched together to demonstrate the detail of grains and their boundaries. Figure 12.18 illustrates a debonding of the surrounding clay from the grain particles. In addition, a breaking of K-feldspar grains are observed in this image. The quartz grains are intact with complete integrity. The cracking of K-feldspar grains are more concentrated around the grain contacts with higher concentrations of clay at these locations.

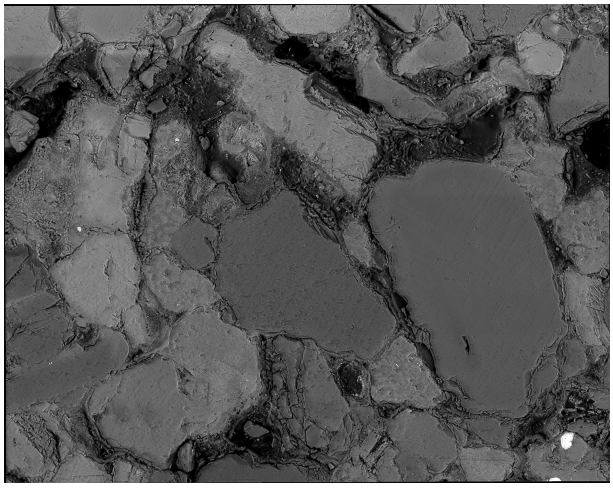

Figure 12.18: Scanning electron microscopy imaging of AS4 specimen. AS4= 28 days of aging at 50 °C and 3290 psi.

Lastly, Figure 12.19 demonstrates the scratch groove on a Mt. Simon sandstone aged for 28 days at 50 °C and 3290 psi. The scratch path shows the cracking of the grains, dislocating of the grains, crushing of the grains and crack propagation in the groove.

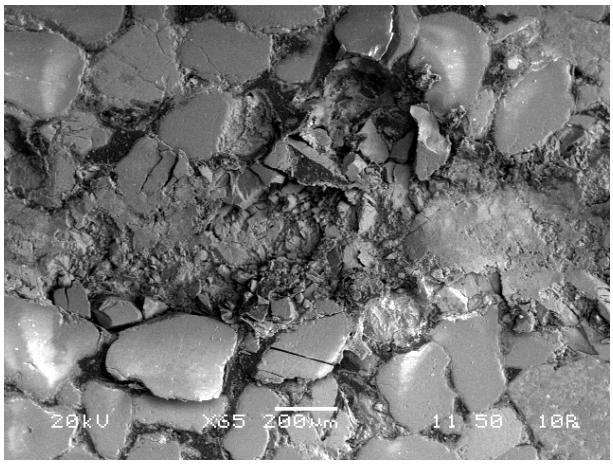

Figure 12.19: Scanning electron microscopy imaging of AS4 specimen. Zoomed in image of scratch groove. AS4= 28 days of aging at 50 °C and 3290 psi.

Furthermore, Figure 12.20 illustrates the scratch groove for Mt. Simon sandstone, unaged specimen. In these figures, micro-cracking, chipping, pull out and branching of the fracture path is visible. The scratch path shows the fracture processes involved in the process of the path. In the first portion of the scratch path when the depth is small the fracture is not dominated and as the depth increases the fracture processes increase and result in chipping, micro-cracking and particle pull out. This illustrates the presence of fracturing events during the test where the stylus is moved on the surface of the specimen.

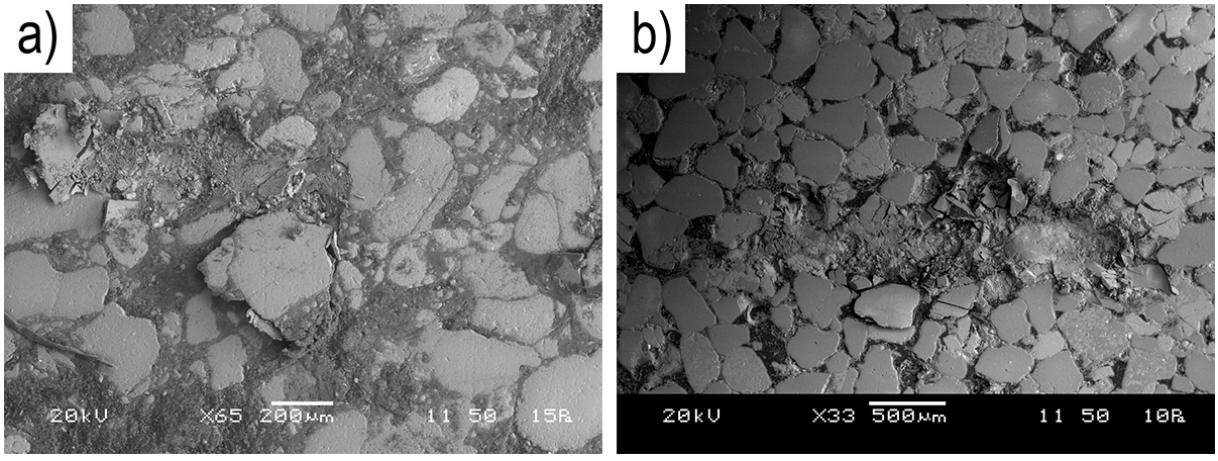

Figure 12.20: Scanning electron microscopy imaging of Mt. Simon sandstone after scratch testing. The residual groove shows the fracture processes after scratch testing.

12.7 Influence of Incubation on Fracture Behavior

The summary of the scratch testing for all of the seven specimens are presented here. Figure 12.21 illustrates the fracture toughness values of 7 specimens in this investigation. The fracture toughness remains almost constant, within the standard deviation range for unaged, incubation in deionized water for 14 days, incubation in brine recipe 3 for 14 days, incubation in brine recipe 1. The fracture toughness of incubation in brine recipe 2 for 14 days resulted in a significant drop in fracture toughness. The fracture toughness for unaged specimen is, K_c =0.88±0.25 MPa$\sqrt{m}$ while fracture for brine recipe 2 has dropped to K_c =0.51±0.15 MPa$\sqrt{m}$. This decrease can be attributed to the high amount of KCL in brine recipe 2. The high concentration of KCl can result in dissolution of feldspar phases. The most significant decrease is for AS4 specimen, incubation in brine-sc-CO_2 for 28 days at 52 °C and 22.7 MPa, where fracture toughness is K_c =0.33±0.12 MPa$\sqrt{m}$. This decrease can be attributed to microcracking of feldspar grains or de-bonding of clay particles from the grains. In addition, the precipitation of secondary phases can induce some weakness in the fabric and decrease the fracture toughness. The exact source of this phenomenon needs more experimental data, as well as a modeling framework to understand the effects of geochemical reactions on fracture toughness of this granular host rock.

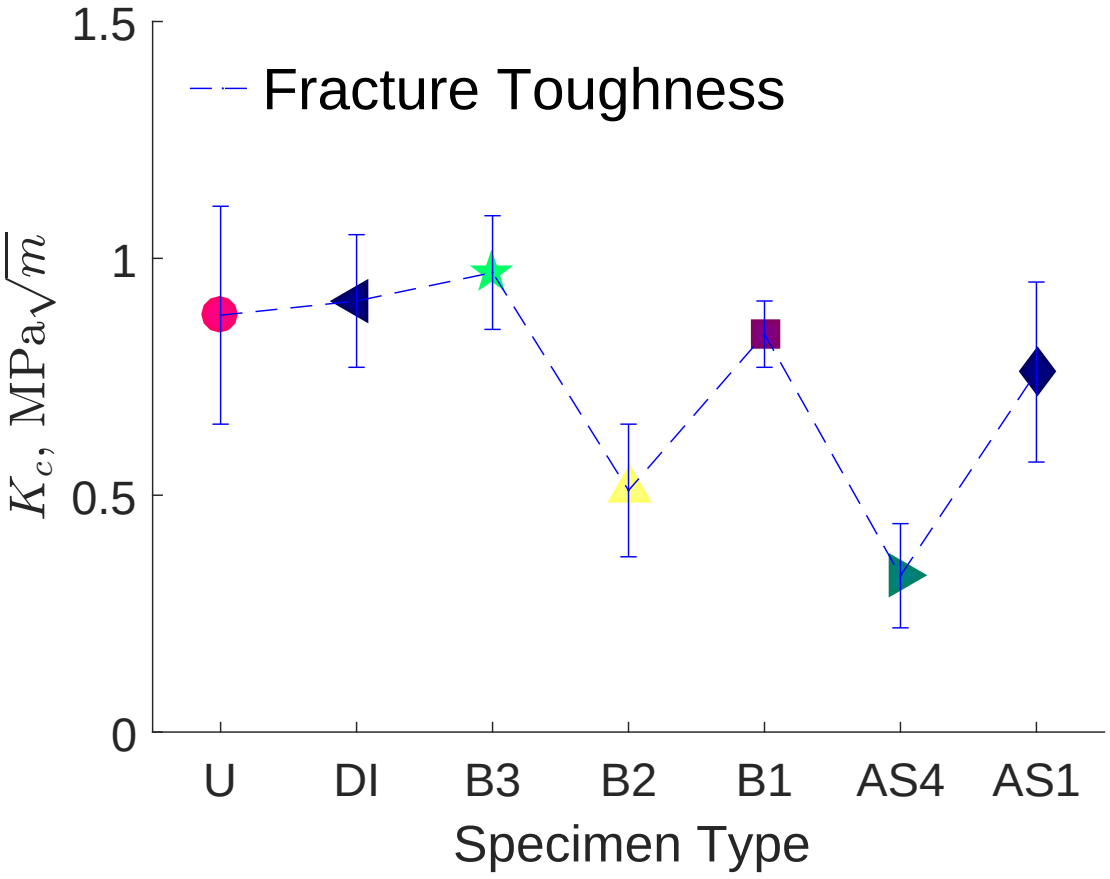

Figure 12.21: Fracture toughness of Mt. Simon sandstone for several specimens. U= unaltered, DI= incubation in deionized water for 14 days, B3= incubation in brine recipe 3 for 14 days, B2= incubation in brine recipe 2 for 14 days, B1= incubation in brine recipe 1 for 14 days, AS4= incubation in brine/sc-CO_2 for 28 days at 52°C and 22.7 MPa, AS1= incubation in brine/sc-CO_2 for 7 days at 50°C and 17.2 MPa.

12.8 Conclusion

In this Chapter, a comprehensive review of different incubation experiments are presented. The research objective was to measure the fracture toughness of sandstone specimens. To this end, a hybrid experimental and theoretical framework is developed that integrates cutting-edge imaging techniques alongside advanced fracture mechanics and small scale mechanical testing methods. Microscopic examination revealed a porous and granular microstructure with a grain size in the range 5-100 μm. The heterogeneity was accounted for via the specimen preparation method and the test parameters. In addition, a through experimental procedure is descried to find the most compatible embedding media. In turn, a relation between fracture toughness and the embedding media and method is observed. As a consequence, the scratch test results are carried out on the same preparation procedure for the rest of the study. The results of scratch testing on several alteration experiments demonstrate a decrease in fracture toughness after exposure to CO_2-saturated brine solution for 28 days, whereas this decrease was smaller in the case of 7-day alteration procedure.

Part V

Conclusions

Chapter 13

Summary of Results and Perspectives

13.1 Summary of Main Findings

At the outset of this thesis, the ultimate goal of this study was defined to be the implementation of the Materials Science paradigm for sedimentary rocks, that is the assessment of the link between mineral composition, microstructure and mechanical performances. This Chapter presents a summary of this implementation for organic-rich shale and sandstone. Based on the findings and contributions some future research is proposed.

13.2 Summary of Main Findings

The study revealed the following scientific findings about the microstructure of organic-rich shale and sandstone and its link with mineral composition and mechanical performance. Below is the summary of the main findings in different parts of this study.

- To this end, a hybrid experimental and theoretical framework that integrates cutting-edge imaging techniques alongside advanced fracture mechanics and small scale mechanical testing methods is developed. Microscopic examination revealed a porous and granular microstructure for organic-rich shale materials. The scratch fracture toughness technique is extended to organic-rich shale to fully incorporate the heterogeneity and the anisotropy of this naturally occurring composite. The anisotropy is accounted for by deriving the energy release rate in orthotropic materials. The

heterogeneity is accounted for via the specimen preparation method and the test parameters. In turn, a coupling between fracture and elasticity is found. As a consequence, combined scratch test results with independent elasticity measurements are utilized to estimate the fracture energy at the microscopic scale. It was found that gas shale exhibits exceptional fracture properties at the microscopic scale: the scratch toughness is two times higher than the macroscopic fracture toughness. Similarly, the microscopic fracture energy is twice larger than that at the macroscopic scale. Scanning electron microscopy shows evidence of toughening mechanisms such as front roughening, particle pullout and crack bridging. These findings are novel and they call for advanced constitutive models of organic-rich shale. In brief, the methodology and results presented here are important and can be employed to yield a fundamental insight of the mechanical behavior of gas shale.

- The focus of Chapter nine was to assess the influence of orientation, rates, composition and morphology on the fracture behavior of organic-rich shale at the microscopic level. Thus, microscopic scratch tests were carried out on both black, Niobrara, and gray, Toarcian shale specimens. The microscopic tests combined with advanced microstructural characterization and nonlinear fracture mechanics modeling tests show that creep and fracture are coupled phenomena in shale systems. By combining scratch tests and micro-indentations tests, it was possible to decouple stress relaxation and fracture to evaluate the rate-independent fracture toughness at the microscopic scale. The experiments bring new insights to the fracture of organic-rich shale materials. Even at low concentrations, the organic matter greatly influences the strength, creep and fracture characteristics of black shale. In particular, the exceptional toughness of black shale is due to toughening mechanisms operating at the nanometer scale in the kerogen and at the clay-kerogen interface. Furthermore, the fracture behavior is anisotropic as a combined result of a layered microstructure as well as an intrinsic fracture behavior of clay. These findings are important and will inform advanced physics-based constitutive materials law for geomechanics simulation in energy-related applications such as hydraulic fracturing in unconventional reservoirs and geological CO_2 storage in deep saline formations.

- A multiscale nanomechanics framework is formulated to investigate fluid-rock reactions in Mt. Simon sandstone using statistical nanoindentation integrated with nonlinear micromechanics. Several specimens were tested, corresponding to six different

alteration cycles and leading to thousands of individual indentation tests. There is an excellent agreement between the porosity measured by statistical nanoindentation and values measured using X-ray diffraction, mercury intrusion porosimetry, helium pycnometry, and flow perporometry. Nanoindentation results indicate that alkali feldspar dissolution occurs during incubation regimes in slightly acidic brine and in CO_2-saturated brine. An increase in microporosity, and a decrease in nanoporosity is also observed. At the macroscopic length-scale, a weakening of the rock is predicted, and this is confirmed by independent macroscopic measurements. The framework presented is unique, as it directly ties local changes in composition to macroscopic alterations in the effective mechanical response while accounting for the morphology, heterogeneity and multi-scale nature of Mt. Simon sandstone.

13.3 Research Contributions

The implementation of the materials science paradigm for organic-rich shale and sandstone required the development of new indentation analysis technique and new scratch analysis technique, which are listed below:

- A suite of micro-mechanical experimental and analytical tools were generated to properly characterize the multi-scale mechanics of sedimentary rocks. Novel developments in characterization are related to the modeling of anisotropy based on geometric descriptions of the underlying microstructure of shale, particle shapes and orientation distributions of particles, and intrinsic elastic properties of material constituents.

- The multi-scale framework approach developed in this thesis represents a comprehensive modeling framework that could be extended to other geochemical reactions as well as other sedimentary rocks, soils and cement-based composites. In particular, the implementation of micro-mechanical characterization with statistical nanoindetation of nanoscale constituents advances the true objective of muli-scale modeling of linking grain-scale and engineering properties.

- The yield design approach for the homogenization of strength properties based on the LCC theory is developed in this work. This homogenization method offers an improved framework for modeling of strength properties of frictional materials compared to existing formulations. The predictive capabilities of the model in terms of

supported strength regimes are helpful in different sedimentary rocks. The extensive analysis of the LCC-based strength homogenization model ensures a well-defined domain for its application.

13.4 Industrial Benefit

Associated with the scientific contributions are industrial benefits:

- The micromechanics approach for the prediction of fracture and strength becomes a novel, physics-based alternative for industrial applications. Departing from purely empirical methods, the modeling framework pursued in this thesis demonstrates the significance of incorporating grain-scale behaviors probed by nanotechnologies into engineering predictive models;

- For seismic events in geological sequestration, new understanding of the nano-scale origin of geomechanical alterations due to geochemical alterations may drive more accurate interpretations of seismic logging data. In particular, a careful combination of material constitutive modeling and strength modeling could provide a direct link between seismic data and strength behavior of sandstone host rocks.

13.5 Limitations and Suggestions for Future Research

The presence of microcracks and crack-like porosity, which are often difficult to characterize or quantify, introduces structural sources of anisotropy that could significantly alter the macroscopic response of these sedimentary rocks. While experimental techniques, such as X-ray tomography, are advancing the microstructural assessment of shale, future developments related to micromechanics modeling may include fracture formulations in order to fully simulate and predict the behaviors of shale rock masses at scales relevant to engineering applications.

The homogenization scheme designed to estimate the macroscopic mechanical behavior needs to be updated for a four-phase material with prestress. In addition, the model can be extended for a case of altered sandstone. The observed discrepancy on the strength of sandstone can be attributed to micro-cracking during the geochemical alterations. A deeper scrutiny of the reasons for this discrepancy is necessary. If it is confirmed that

cracking is a governing mechanism of failure at the macroscopic scale, an extension of the strength description that incorporates the fracture parameters needs to be developed.

Modeling of the sandstone and its phases has been performed within the framework of continuum mechanics. The analogy of the mechanical behavior of sandstone with the granular materials suggest however that the use of granular mechanics could be well-suited to model sandstone. Such an analysis might help to explain the micro-cracking of feldspar phases with geochemical alterations, which for now remains unexplained.

13.6 Perspectives

Civil infrastructures are usually built to last for at least for decades, sometimes for much longer. For instance, nuclear waste storage sites are intended to retain structural integrity for hundreds of years. Another example of these infrastructures are saline formations for storage of supercritical CO_2 where the storage sites are intended to retain structural integrity for hundreds of years. For these critical structures, the knowledge of the material behavior on time scales comparable to that of the structure is required. Obviously, this is not experimentally practical without exposing the material for a long duration time or an intensive environment for a shorter period of time.

This study suggests that to identify the fracture toughness and strength behavior probing the nanoscale enables an assessment of long term macroscopic behavior that is orders of magnitude different in time scales. Given the potential impact of such an approach, I hope this study will incite consideration of small scale testing and the equivalence of length-time equivalence for other natural composites.

Bibliography

1. EIA, U. Annual energy outlook 2013. *US Energy Information Administration, Washington, DC,* 60–62 (2013).
2. Insight, I. G. The economic and employment contributions of shale gas in the United States. *Prepared for America's Natural Gas Alliance by IHS Global Insight (USA), Washington, DC: America's Natural Gas Alliance* (2011).
3. Boyer, C., Clark, B., Jochen, V., Lewis, R. & Miller, C. K. Shale gas: A global resource. *Oilfield Review* **23,** 28–39 (2011).
4. Bažant, Z. & Chau, V. *Vast system of dense intersecting fractures: a key feature of hydraulic fracturing of gas shale* in *50th US rock mechanics/geomechanics symposium* (2016).
5. Bažant, Z. P. & Chau, V. T. in *New Frontiers in Oil and Gas Exploration* 435–460 (Springer, 2016).
6. Bažant, Z. P., Salviato, M., Chau, V. T., Viswanathan, H. & Zubelewicz, A. Why fracking works. *Journal of Applied Mechanics* **81,** 101010 (2014).
7. Han, Y., Al-Muntasheri, G., Katherine, L. H. & Abousleiman, Y. N. *Tensile mechanical behavior of kerogen and its potential implication to fracture opening in kerogen-rich shales (KRS)* in *50th US Rock Mechanics/Geomechanics Symposium* (2016).
8. King, G. E. Hydraulic fracturing 101: what every representative, environmentalist, regulator, reporter, investor, university researcher, neighbor, and engineer should know about hydraulic fracturing risk. *Journal of Petroleum Technology* **64,** 34–42 (2012).
9. King, G. E. *Thirty years of gas shale fracturing: What have we learned?* in *SPE Annual Technical Conference and Exhibition* (2010).

10. Frailey, S. M., Damico, J. & Leetaru, H. E. Reservoir characterization of the Mt. Simon Sandstone, Illinois Basin, USA. *Energy Procedia* **4,** 5487–5494 (2011).

11. Holloway, S. An overview of the underground disposal of carbon dioxide. *Energy Conversion and Management* **38,** S193–S198 (1997).

12. Xie, H., Li, X., Fang, Z., Wang, Y., Li, Q., Shi, L., Bai, B., Wei, N. & Hou, Z. Carbon geological utilization and storage in China: current status and perspectives. *Acta Geotechnica* **9,** 7–27 (2014).

13. Chiantore, V. t. & Gera, F. Fracture permeability of clays: a review. *Radioactive Waste Management and the Nucear Fuel Cycle* **7,** 253–277 (1986).

14. De Windt, L., Cabrera, J. & Boisson, J. Radioactive waste containment in indurated shales: comparison between the chemical containment properties of matrix and fractures. *Geological Society, London, Special Publications* **157,** 167–181 (1999).

15. Alfi, M., Yan, B., Cao, Y., An, C., Killough, J. E. & Barrufet, M. A. Microscale porosity models as powerful tools to analyze hydrocarbon production mechanisms in liquid shale. *Journal of Natural Gas Science and Engineering* **26,** 1495–1505 (2015).

16. Li, W., Jin, C. & Cusatis, G. in *New Frontiers in Oil and Gas Exploration* 389–434 (Springer, 2016).

17. Yan, B., Alfi, M., Wang, Y. & Killough, J. E. *A new approach for the simulation of fluid flow in unconventional reservoirs through multiple permeability modeling* in *SPE Annual Technical Conference and Exhibition* (2013).

18. Kumar, V., Sondergeld, C. H. & Rai, C. S. *Nano to macro mechanical characterization of shale* in *SPE Annual Technical Conference and Exhibition* (2012).

19. Abbas, S., Lecampion, B. & Prioul, R. *Competition between transverse and axial hydraulic fractures in horizontal wells* in *SPE Hydraulic Fracturing Technology Conference* (2013).

20. Jeffrey, R. G., Bunger, A., Lecampion, B., Zhang, X., Chen, Z., van As, A., Allison, D. P., De Beer, W., Dudley, J. W. & Siebrits, E. *Measuring hydraulic fracture growth in naturally fractured rock* in *SPE annual technical conference and exhibition* (2009).

21. Lecampion, B. & Desroches, J. *Simultaneous initiation of multiple transverse hydraulic fractures from a horizontal well* in *48th US rock mechanics/geomechanics symposium* (2014).

22. Altman, S. J., Aminzadeh, B., Balhoff, M. T., Bennett, P. C., Bryant, S. L., Cardenas, M. B., Chaudhary, K., Cygan, R. T., Deng, W. & Dewers, T. Chemical and hydrodynamic mechanisms for long-term geological carbon storage. *The Journal of Physical Chemistry C* **118,** 15103–15113 (2014).

23. Xu, T., Apps, J. A. & Pruess, K. Mineral sequestration of carbon dioxide in a sandstone–shale system. *Chemical geology* **217,** 295–318 (2005).

24. Kang, S. M., Fathi, E., Ambrose, R. J., Akkutlu, I. Y. & Sigal, R. F. Carbon dioxide storage capacity of organic-rich shales. *SPE Journal* **16,** 842–855 (2011).

25. Detournay, E. Mechanics of hydraulic fractures. *Annual Review of Fluid Mechanics* **48,** 311–339 (2016).

26. Field, C. B., Barros, V. R., Dokken, D., Mach, K., Mastrandrea, M., Bilir, T., Chatterjee, M., Ebi, K., Estrada, Y. & Genova, R. *IPCC, 2014: Climate Change 2014: Impacts, Adaptation, and Vulnerability. Part A: Global and Sectoral Aspects. Contribution of Working Group II to the Fifth Assessment Report of the Intergovernmental Panel on Climate Change* 2014.

27. Administration, U. E. I. *U.S. Energy Information Administration* `www.eia.gov`.

28. Of the Intergovernmental Panel on Climate Change, W. G. I. *et al. Carbon dioxide capture and storage* 2005.

29. Winter, N. B. & Winter, N. B. *Scanning electron microscopy of cement and concrete* (WHD Microanalysis, 2012).

30. Butt, H.-J., Cappella, B. & Kappl, M. Force measurements with the atomic force microscope: Technique, interpretation and applications. *Surface Science Reports* **59,** 1–152 (2005).

31. Binnig, G., Rohrer, H., Gerber, C. & Weibel, E. Surface studies by scanning tunneling microscopy. *Physical Review Letters* **49,** 57 (1982).

32. Binnig, G., Rohrer, H., Gerber, C. & Weibel, E. 7× 7 reconstruction on Si (111) resolved in real space. *Physical Review Letters* **50,** 120 (1983).

33. Pohl, D. W., Denk, W. & Lanz, M. Optical stethoscopy: Image recording with resolution $\lambda/20$. *Applied Physics Letters* **44,** 651–653 (1984).

34. Lewis, A., Isaacson, M., Harootunian, A. & Muray, A. Development of a 500 Å spatial resolution light microscope: I. light is efficiently transmitted through $\lambda/16$ diameter apertures. *Ultramicroscopy* **13,** 227–231 (1984).

35. Binnig, G., Quate, C. F. & Gerber, C. Atomic force microscope. *Physical Review Letters* **56,** 930 (1986).

36. Dubovik, V. & Tugushev, V. Toroid moments in electrodynamics and solid-state physics. *Physics Reports* **187,** 145–202 (1990).

37. Hulteen, J. C. & Van Duyne, R. P. Nanosphere lithography: A materials general fabrication process for periodic particle array surfaces. *Journal of Vacuum Science & Technology A: Vacuum, Surfaces, and Films* **13,** 1553–1558 (1995).

38. Fowler, S. B., Best, R. B., Herrera, J. L. T., Rutherford, T. J., Steward, A., Paci, E., Karplus, M. & Clarke, J. Mechanical unfolding of a titin Ig domain: structure of unfolding intermediate revealed by combining AFM, molecular dynamics simulations, NMR and protein engineering. *Journal of Molecular Biology* **322,** 841–849 (2002).

39. Hugel, T. & Seitz, M. The study of molecular interactions by AFM force spectroscopy. *Macromolecular Rapid Communications* **22,** 989–1016 (2001).

40. Koljonen, K., Österberg, M., Johansson, L.-S. & Stenius, P. Surface chemistry and morphology of different mechanical pulps determined by ESCA and AFM. *Colloids and Surfaces A: Physicochemical and Engineering Aspects* **228,** 143–158 (2003).

41. Engel, A. & Müller, D. J. Observing single biomolecules at work with the atomic force microscope. *Nature Structural and Molecular Biology* **7,** 715 (2000).

42. Hoh, J. H. & Hansma, P. K. Atomic force microscopy for high-resolution imaging in cell biology. *Trends in Cell Biology* **2,** 208–213 (1992).

43. Parot, P., Dufrêne, Y. F., Hinterdorfer, P., Le Grimellec, C., Navajas, D., Pellequer, J.-L. & Scheuring, S. Past, present and future of atomic force microscopy in life sciences and medicine. *Journal of Molecular Recognition* **20,** 418–431 (2007).

44. Research, A. *Atomic Force Microscope Instruments* `www.asylumresearch.com`.

45. *Electron Microprobe Instrumentation* https://nau.edu/cefns/labs/electron-microprobe/glg-510-class-notes/instrumentation/.

46. JEOL. *A Guide to Scanning Microscope Observation* http://www.geology.wisc.edu/~johnf/g777/JEOLguide.pdf.

47. JEOL. *Scanning Electron Microscope Instruments* www.jeolusa.com.

48. FEI. *Scanning Electron Microscope Instruments* www.fei.com.

49. FEI. *Scanning Electron Microscope Instruments* www.nuance.northwestern.edu.

50. Bragg, W. H., WL Bragg, B., *et al.* The reflection of X-rays by crystals. *Proceedings of the Royal Society of London A* **88,** 428–438 (1913).

51. Fultz, B. & Howe, J. in *Transmission Electron Microscopy and Diffractometry of Materials* 1–57 (Springer, 2013).

52. Borodich, F. M. & Galanov, B. A. Self-similar problems of elastic contact for non-convex punches. *Journal of the Mechanics and Physics of Solids* **50,** 2441–2461 (2002).

53. Borodich, F. M., Keer, L. M. & Korach, C. S. Analytical study of fundamental nanoindentation test relations for indenters of non-ideal shapes. *Nanotechnology* **14,** 803 (2003).

54. Boussinesq, J. *Application des potentiels à l'étude de l'équilibre et du mouvement des solides élastiques: principalement au calcul des déformations et des pressions que produisent, dans ces solides, des efforts quelconques exercés sur une petite partie de leur surface ou de leur intérieur: mémoire suivi de notes étendues sur divers points de physique, mathematique et d'analyse* (Gauthier-Villars, 1885).

55. Hertz, H. Hertzs Miscellaneous Papers–Chapters 5 and 6. *ed: Macmillan, London, UK* (1896).

56. Love, A. E. H. The stress produced in a semi-infinite solid by pressure on part of the boundary. *Philosophical Transactions of the Royal Society of London. Series A, Containing Papers of a Mathematical or Physical Character* **228,** 377–420 (1929).

57. Love, A. Boussinesq's problem for a rigid cone. *The Quarterly Journal of Mathematics* **10,** 161–175 (1939).

58. Johnson, K. L. & Johnson, K. L. *Contact mechanics* (Cambridge university press, 1987).

59. Sneddon, I. N. The relation between load and penetration in the axisymmetric Boussinesq problem for a punch of arbitrary profile. *International Journal of Engineering Science* **3,** 47–57 (1965).

60. Harding, J. & Sneddon, I. *The elastic stresses produced by the indentation of the plane surface of a semi-infinite elastic solid by a rigid punch* in *Mathematical Proceedings of the Cambridge Philosophical Society* **41** (1945), 16–26.

61. Torres-Torres, D., Munoz-Saldana, J., Gutierrez-Ladron-de Guevara, L., Hurtado-Macias, A. & Swain, M. Geometry and bluntness tip effects on elastic–plastic behaviour during nanoindentation of fused silica: experimental and FE simulation. *Modelling and Simulation in Materials Science and Engineering* **18,** 075006 (2010).

62. Banerjee, A., Bernoulli, D., Zhang, H., Yuen, M.-F., Liu, J., Dong, J., Ding, F., Lu, J., Dao, M. & Zhang, W. Ultralarge elastic deformation of nanoscale diamond. *Science* **360,** 300–302 (2018).

63. Bredl, J., Dany, M., Schneider, H.-C. & Kraft, O. Instrumented indentation at elevated temperatures for determination of material properties of fusion relevant materials. *Nuclear Materials and Energy* **9,** 502–507 (2016).

64. Pethicai, J., Hutchings, R. & Oliver, W. C. Hardness measurement at penetration depths as small as 20 nm. *Philosophical Magazine A* **48,** 593–606 (1983).

65. Doerner, M. F. & Nix, W. D. A method for interpreting the data from depth-sensing indentation instruments. *Journal of Materials research* **1,** 601–609 (1986).

66. Pethica, J., Hutchings, R. & Oliver, W. Composition and hardness profiles in ion implanted metals. *Nuclear Instruments and Methods in Physics Research* **209,** 995–1000 (1983).

67. Loubet, J. L., Georges, J. M. & Meille, G. in *Microindentation Techniques in Materials Science and Engineering* (ASTM International, 1985).

68. Stone, D., LaFontaine, W., Alexopoulos, P., Wu, T.-W. & Li, C.-Y. An investigation of hardness and adhesion of sputter-deposited aluminum on silicon by utilizing a continuous indentation test. *Journal of Materials Research* **3,** 141–147 (1988).

69. Gilman, J. Hardness–a strength microprobe. *The Science of Hardness Testing and Its Research Applications, ASM, Metals Park* (1973).

70. Oliver, W. Progress in the development of a mechanical properties microprobe. *MRS Bulletin* **11,** 15–21 (1986).

71. Oliver, W., McHargue, C. & Zinkle, S. Thin film characterization using a mechanical properties microprobe. *Thin Solid Films* **153,** 185–196 (1987).

72. Paar, A. *Nanoindetation Tester (NHT2)* `www.anton-paar.com`.

73. Hertz, H. On the contact of elastic solids. *Z. Reine Angew. Mathematik* **92,** 156–171 (1881).

74. McElhaney, K., Vlassak, J. & Nix, W. Determination of indenter tip geometry and indentation contact area for depth-sensing indentation experiments. *Journal of Materials Research* **13,** 1300–1306 (1998).

75. Hendrix, B. The use of shape correction factors for elastic indentation measurements. *Journal of Materials Research* **10,** 255–257 (1995).

76. Larsson, P.-L., Giannakopoulos, A., Söderlund, E., Rowcliffe, D. & Vestergaard, R. Analysis of Berkovich indentation. *International Journal of Solids and Structures* **33,** 221–248 (1996).

77. Cheng, Y.-T. & Cheng, C.-M. Scaling approach to conical indentation in elastic-plastic solids with work hardening. *Journal of Applied Physics* **84,** 1284–1291 (1998).

78. Cheng, Y.-T. & Cheng, C.-M. Scaling relationships in conical indentation of elastic-perfectly plastic solids. *International Journal of Solids and Structures* **36,** 1231–1243 (1999).

79. Oliver, W. C. & Pharr, G. M. An improved technique for determining hardness and elastic modulus using load and displacement sensing indentation experiments. *Journal of Materials Research* **7,** 1564–1583 (1992).

80. Ashby, M. Indentation creep. *Materials Science and Technology* **8,** 594–601 (1992).

81. Hill, R. Similarity analysis of creep indentation tests. *Proceedings of the Royal Society of London A* **436,** 617–630 (1992).

82. Storåkers, B. & Larsson, P.-L. On Brinell and Boussinesq indentation of creeping solids. *Journal of the Mechanics and Physics of Solids* **42,** 307–332 (1994).

83. Mesarovic, S. D. & Fleck, N. A. *Spherical indentation of elastic–plastic solids* in *Proceedings of the Royal Society of London A: Mathematical, Physical and Engineering Sciences* **455** (1999), 2707–2728.

84. Cheng, Y.-T. & Cheng, C.-M. Scaling relationships in indentation of power-law creep solids using self-similar indenters. *Philosophical Magazine Letters* **81,** 9–16 (2001).

85. Kutty, T., Ganguly, C. & Sastry, D. Development of creep curves from hot indentation hardness data. *Scripta Materialia* **34,** 1833–1838 (1996).

86. Sakai, M. & Shimizu, S. Indentation rheometry for glass-forming materials. *Journal of non-Crystalline Solids* **282,** 236–247 (2001).

87. Fischer-Cripps, A. A simple phenomenological approach to nanoindentation creep. *Materials Science and Engineering: A* **385,** 74–82 (2004).

88. Radok, J. R. M. Visco-elastic stress analysis. *Quarterly of Applied Mathematics* **15,** 198–202 (1957).

89. Lee, E. H. & Radok, J. R. M. The contact problem for viscoelastic bodies. *Journal of Applied Mechanics* **27,** 438–444 (1960).

90. Vandamme, M., Tweedie, C. A., Constantinides, G., Ulm, F.-J. & Van Vliet, K. J. Quantifying plasticity-independent creep compliance and relaxation of viscoelastoplastic materials under contact loading. *Journal of Materials Research* **27,** 302–312 (2012).

91. Vandamme, M. & Ulm, F.-J. Viscoelastic solutions for conical indentation. *International Journal of Solids and Structures* **43,** 3142–3165 (2006).

92. DeJong, M. J. & Ulm, F.-J. The nanogranular behavior of CSH at elevated temperatures (up to 700 C). *Cement and Concrete Research* **37,** 1–12 (2007).

93. Constantinides, G., Chandran, K. R., Ulm, F.-J. & Van Vliet, K. Grid indentation analysis of composite microstructure and mechanics: Principles and validation. *Materials Science and Engineering: A* **430,** 189–202 (2006).

94. Constantinides, G. & Ulm, F.-J. The nanogranular nature of C–S–H. *Journal of the Mechanics and Physics of Solids* **55,** 64–90 (2007).

95. Vandamme, M. *The nanogranular origin of concrete creep: a nanoindentation investigation of microstructure and fundamental properties of calcium-silicate-hydrates* PhD thesis (Massachusetts Institute of Technology, 2008).

96. Gathier, B. *Multiscale strength homogenization: application to shale nanoindentation* PhD thesis (Massachusetts Institute of Technology, 2008).

97. Dempster, A. P., Laird, N. M. & Rubin, D. B. Maximum likelihood from incomplete data via the EM algorithm. *Journal of the Royal Statistical Society. Series B (methodological),* 1–38 (1977).

98. McLachlan, G. J. & Basford, K. E. *Mixture models: Inference and applications to clustering* (Marcel Dekker, 1988).

99. McLachlan, G. & Peel, D. *Finite mixture models* (John Wiley & Sons, 2004).

100. McLachlan, G. & Krishnan, T. *The EM algorithm and extensions* (John Wiley & Sons, 2007).

101. Ortega, J. A. *Microporomechanical modeling of shale* PhD thesis (Massachusetts Institute of Technology, 2009).

102. Fraley, C. & Raftery, A. E. MCLUST: Software for model-based cluster analysis. *Journal of Classification* **16,** 297–306 (1999).

103. Fraley, C. & Raftery, A. E. Model-based clustering, discriminant analysis, and density estimation. *Journal of the American Statistical Association* **97,** 611–631 (2002).

104. Fraley, C. & Raftery, A. E. Model-based methods of classification: using the mclust software in chemometrics. *Journal of Statistical Software* **18,** 1–13 (2007).

105. Deirieh, A. A. M. *Statistical nano-chemo-mechanical assessment of shale by wave dispersive spectroscopy and nanoindentation* PhD thesis (Massachusetts Institute of Technology, 2011).

106. Axen, N., Kahlman, L. & Hutchings, I. Correlations between tangential force and damage mechanisms in the scratch testing of ceramics. *Tribology International* **30,** 467–474 (1997).

107. Bhansali, K. J. & Kattamis, T. Z. Quality evaluation of coatings by automatic scratch testing. *Wear* **141,** 59–71 (1990).

108. Bull, S., Rickerby, D., Matthews, A., Leyland, A., Pace, A. & Valli, J. The use of scratch adhesion testing for the determination of interfacial adhesion: the importance of frictional drag. *Surface and Coatings Technology* **36,** 503–517 (1988).

109. Gonczy, S. T. & Randall, N. An ASTM standard for quantitative scratch adhesion testing of thin, hard ceramic coatings. *International Journal of Applied Ceramic Technology* **2,** 422–428 (2005).

110. Akono, A.-T. *Assessment of fracture properties and rate effects on fracture of materials by micro scratching: application to gas shale* PhD thesis (Massachusetts Institute of Technology, 2013).

111. Akono, A.-T. & Ulm, F.-J. Scratch test model for the determination of fracture toughness. *Engineering Fracture Mechanics* **78,** 334–342 (2011).

112. Akono, A., Reis, P. M. & Ulm, F. Scratching as a fracture process: From butter to steel. *Physical Review Letters* **106,** 204302 (2011).

113. Rice, J. R. A path independent integral and the approximate analysis of strain concentration by notches and cracks. *Journal of Applied Mechanics* **35,** 379–386 (1968).

114. Akono, A.-T., Randall, N. X. & Ulm, F.-J. Experimental determination of the fracture toughness via microscratch tests: application to polymers, ceramics, and metals. *Journal of Materials Research* **27,** 485–493 (2012).

115. Akono, A.-T. & Ulm, F.-J. Fracture scaling relations for scratch tests of axisymmetric shape. *Journal of the Mechanics and Physics of Solids* **60,** 379–390 (2012).

116. Akono, A.-T. & Ulm, F.-J. An improved technique for characterizing the fracture toughness via scratch test experiments. *Wear* **313,** 117–124 (2014).

117. Akono, A.-T., Ulm, F.-J. & Bažant, Z. P. Discussion: Strength-to-fracture scaling in scratching. *Engineering Fracture Mechanics* **119,** 21–28 (2014).

118. Anderson, K. & Akono, A.-T. Microstructure–toughness relationships in calcium aluminate cement–polymer composites using instrumented scratch testing. *Journal of Materials Science* **52,** 13120–13132 (2017).

119. Johnson, C. V., Chen, J., Hasparyk, N. P., Monteiro, P. J. & Akono, A. T. Fracture properties of the alkali silicate gel using microscopic scratch testing. *Cement and Concrete Composites* **79,** 71–75 (2017).

120. Akono, A.-T. & Kabir, P. Microscopic fracture characterization of gas shale via scratch testing. *Mechanics Research Communications* **78,** 86–92 (2016).

121. Tourtelot, H. A. Origin and use of the word "shale". *American Journal of Science* **258,** 335–343 (1960).

122. Boggs, S. *Petrology of sedimentary rocks* (Cambridge University Press, 2009).

123. Van Olphen, H. & Hsu, P. H. An Introduction to Clay Colloid Chemistry. *Soil Science* **126,** 59 (1978).

124. Aylmore, L. & Quirk, J. Domain or turbostratic structure of clays. *Nature* **187,** 1046 (1960).

125. Mitchell, J. K. & Soga, K. *Fundamentals of soil behavior* (John Wiley & Sons New York, 2005).

126. Terzaghi, K., Peck, R. B. & Mesri, G. *Soil mechanics in engineering practice* (John Wiley & Sons, 1996).

127. Stephansson, O., Hudson, J. & Jing, L. *Coupled thermo-hydro-mechanical-chemical processes in Geo-Systems* (Elsevier, 2004).

128. Lambe, T. W. & Whitman, R. V. *Soil mechanics SI version* (John Wiley & Sons, 2008).

129. Longstaffe, F. J., Hardie, L. A., Coniglio, M., Church, M. J. & Middleton, G. V. *Encyclopedia of sediments and sedimentary rocks* (Springer Netherlands, 2003).

130. Dembicki Jr, H. Three common source rock evaluation errors made by geologists during prospect or play appraisals. *AAPG Bulletin* **93,** 341–356 (2009).

131. Sayers, C. The elastic anisotrophy of shales. *Journal of Geophysical Research: Solid Earth* **99,** 767–774 (1994).

132. Dewhurst, D. N. & Siggins, A. F. Impact of fabric, microcracks and stress field on shale anisotropy. *Geophysical Journal International* **165,** 135–148 (2006).

133. Hall, P., Mildner, D. & Borst, R. Pore size distribution of shaley rock by small angle neutron scattering. *Applied Physics Letters* **43,** 252–254 (1983).

134. Horsrud, P., Sønstebø, E. & Bøe, R. Mechanical and petrophysical properties of North Sea shales. *International Journal of Rock Mechanics and Mining Sciences* **35,** 1009–1020 (1998).

135. Pearson, F. What is the porosity of a mudrock? *Geological Society, London, Special Publications* **158,** 9–21 (1999).

136. Katsube, T., Mudford, B. S. & Best, M. Petrophysical characteristics of shales from the Scotian shelf. *Geophysics* **56,** 1681–1689 (1991).

137. Bennett, K. C., Berla, L. A., Nix, W. D. & Borja, R. I. Instrumented nanoindentation and 3D mechanistic modeling of a shale at multiple scales. *Acta Geotechnica* **10,** 1–14 (2015).

138. Ulm, F.-J. & Abousleiman, Y. The nanogranular nature of shale. *Acta Geotechnica* **1,** 77–88 (2006).

139. Ortega, J. A., Ulm, F.-J. & Abousleiman, Y. The effect of the nanogranular nature of shale on their poroelastic behavior. *Acta Geotechnica* **2,** 155–182 (2007).

140. Ortega, J. A., Ulm, F.-J. & Abousleiman, Y. The nanogranular acoustic signature of shale. *Geophysics* **74,** D65–D84 (2009).

141. Monfared, S. & Ulm, F.-J. A molecular informed poroelastic model for organic-rich, naturally occurring porous geocomposites. *Journal of the Mechanics and Physics of Solids* **88,** 186–203 (2016).

142. Li, W., Rezakhani, R., Jin, C., Zhou, X. & Cusatis, G. A multiscale framework for the simulation of the anisotropic mechanical behavior of shale. *International Journal for Numerical and Analytical Methods in Geomechanics* **41,** 1494–1522 (2017).

143. Chau, V. T., Bažant, Z. P. & Su, Y. Growth model for large branched three-dimensional hydraulic crack system in gas or oil shale. *Philosophical Tranactions of the Royal Society A* **374,** 20150418 (2016).

144. Li, C., Caner, F. C., Chau, V. T. & Bažant, Z. P. Spherocylindrical microplane constitutive model for shale and other anisotropic rocks. *Journal of the Mechanics and Physics of Solids* **103,** 155–178 (2017).

145. Ottner, F., Gier, S., Kuderna, M. & Schwaighofer, B. Results of an inter-laboratory comparison of methods for quantitative clay analysis. *Applied Clay Science* **17,** 223–243 (2000).

146. Srodon, J., Drits, V. A., McCarty, D. K., Hsieh, J. C. & Eberl, D. D. Quantitative X-ray diffraction analysis of clay-bearing rocks from random preparations. *Clays and Clay Minerals* **49,** 514–528 (2001).

147. Al-Jaroudi, S. S., Ul-Hamid, A., Mohammed, A.-R. I. & Saner, S. Use of X-ray powder diffraction for quantitative analysis of carbonate rock reservoir samples. *Powder Technology* **175,** 115–121 (2007).

148. Hughes, R. E., Moore, D. & Glass, H. Qualitative and quantitative analysis of clay minerals in soils. *Quantitative Methods in Soil Mineralogy,* 330–359 (1994).

149. Norrish, K. & Taylor, R. Quantitative analysis by X-ray diffraction. *Clay Minerals Bulletin* **5,** 98–109 (1962).

150. Weidler, P., Luster, J., Schneider, J., Sticher, H. & Gehring, A. The Rietveld method applied to the quantitative mineralogical and chemical analysis of a ferralitic soil. *European Journal of Soil Science* **49,** 95–105 (1998).

151. Hillier, S. Accurate quantitative analysis of clay and other minerals in sandstones by XRD: comparison of a Rietveld and a reference intensity ratio (RIR) method and the importance of sample preparation. *Clay Minerals* **35,** 291–302 (2000).

152. Moore, D. M. & Reynolds, R. C. *X-ray Diffraction and the Identification and Analysis of Clay Minerals* (Oxford university press New York, 1989).

153. Kahle, M., Kleber, M. & Jahn, R. Review of XRD-based quantitative analyses of clay minerals in soils: the suitability of mineral intensity factors. *Geoderma* **109,** 191–205 (2002).

154. Brindley, G. & Brown, G. Quantitative X-ray mineral analysis of clays. *Crystal Structures of Clay Minerals and their X-ray Identification* **5,** 411–438 (1980).

155. Jenkyns, H. The early Toarcian (Jurassic) anoxic event-stratigraphic, sedimentary, and geochemical evidence. *American Journal of Science* **288,** 101–151 (1988).

156. Tissot, B., Califet-Debyser, Y., Deroo, G. & Oudin, J. Origin and evolution of hydrocarbons in early Toarcian shales, Paris Basin, France. *AAPG Bulletin* **55,** 2177–2193 (1971).

157. Katz, B. in *Petroleum Source Rocks* 51–65 (Springer, 1995).

158. Bessereau, G., Huc, A. & Carpentier, B. Distribution of organic matter in the Liassic series of the Paris basin: an example of organic heterogeneity in a source rock interval. *Generation, Accumulation and Production of Europe's Hydrocarbons II. Special Publication of the European Association of Petroleum Geoscientists* **2,** 117–125 (1992).

159. Kuuskraa, V., Stevens, S. H. & Moodhe, K. D. *Technically recoverable shale oil and shale gas resources: an assessment of 137 shale formations in 41 countries outside the United States* (US Energy Information Administration, US Department of Energy, 2013).

160. Finn, T. M. & Johnson, R. C. Niobrara total petroleum system in the southwestern Wyoming province. *USGS Petroleum* (2005).

161. Pollastro, R. M. & Scholle, P. A. Exploration and development of hydrocarbons from low-permeability chalks–an example from the Upper Cretaceous Niobrara Formation, Rocky Mountain region (1986).

162. Coleman Jr, J. L., Milici, R. C., Cook, T. A., Charpentier, R. R., Kirshbaum, M., Klett, T. R., Pollastro, R. M. & Schenk, C. J. *Assessment of undiscovered oil and gas resources of the Devonian Marcellus Shale of the Appalachian Basin province* tech. rep. (US Geological Survey, 2011).

163. Vasconcelos, G., Lourenco, P., Alves, C. & Pamplona, J. Ultrasonic evaluation of the physical and mechanical properties of granites. *Ultrasonics* **48,** 453–466 (2008).

164. Sack, D. A. & Olson, L. D. Advanced NDT methods for evaluating concrete bridges and other structures. *NDT & E International* **28,** 349–357 (1995).

165. Hassan, M., Burdet, O. & Favre, R. Ultrasonic measurements and static load tests in bridge evaluation. *NDT & E International* **28,** 331–337 (1995).

166. Far, M. E., Hardage, B. & Wagner, D. *Inversion of elastic properties of fractured rocks from AVOAZ data Marcellus Shale example* in *2013 SEG Annual Meeting* (2013).

167. Budiansky, B. On the elastic moduli of some heterogeneous materials. *Journal of the Mechanics and Physics of Solids* **13,** 223–227 (1965).

168. Hill, R. The essential structure of constitutive laws for metal composites and polycrystals. *Journal of the Mechanics and Physics of Solids* **15,** 79–95 (1967).

169. Eshelby, J. D. The determination of the elastic field of an ellipsoidal inclusion, and related problems. *Proceedings of the Royal Society of London* **241,** 376–396 (1957).

170. Barthélémy, J.-F., Souque, C. & Daniel, J.-M. Nonlinear homogenization approach to the friction coefficient of a quartz-clay fault gouge. *International Journal for Numerical and Analytical Methods in Geomechanics* **37,** 1948–1968 (2013).

171. Marion, D., Nur, A., Yin, H. & Han, D.-H. Compressional velocity and porosity in sand-clay mixtures. *Geophysics* **57,** 554–563 (1992).

172. Wang, Z., Wang, H. & Cates, M. E. Effective elastic properties of solid clays. *Geophysics* **66,** 428–440 (2001).

173. Mavko, G., Mukerji, T. & Dvorkin, J. *The rock physics handbook: Tools for seismic analysis of porous media* (Cambridge university press, 2009).

174. Simmons, G. & Wang, H. Single crystal elastic constants and calculated aggregate properties (1971).

175. Carmichael, R. S. *Physical properties of rocks and minerals* (CRC press Boca Raton, 1989).

176. Kumar, V., Curtis, M. E., Gupta, N., Sondergeld, C. H. & Rai, C. S. *Estimation of elastic properties of organic matter in Woodford Shale through nanoindentation measurements* in *SPE Canadian Unconventional Resources Conference* (2012).

177. Hansen, E., Mulvaney, D. & Betcher, M. Water resource reporting and water footprint from Marcellus Shale development in West Virginia and Pennsylvania. *Downstream Strategies* **30** (2013).

178. Lhomme, T., Detournay, E. & Jeffrey, R. *Effect of fluid compressibility and borehole radius on the propagation of a fluid-driven fracture* in *Proceedings of 11th International Conference on Fracture* (2005), 5899–5904.

179. Sierra, R., Tran, M., Abousleiman, Y. & Slatt, R. *Woodford shale mechanical properties and the impacts of lithofacies* in *44th US Rock Mechanics Symposium and 5th US-Canada Rock Mechanics Symposium* (2010).

180. Chandler, M., Meredith, P. & Crawford, B. *Experimental Determination of the Fracture Toughness and Brittleness of the Mancos Shale, Utah* in *Geophysical Research Abstracts, 75th EAGE Conference & Exhibition incorporating SPE EUROPEC* (2012).

181. Liu, Y. Fracture toughness assessment of shales by nanoindentation. *Master's thesis, University of Massachusetts Amherst, Amherst, MA. http://scholarworks. umass. edu/cee_geotechnical/4* (2015).

182. Swain, M. & Lawn, B. *Indentation fracture in brittle rocks and glasses* in *International Journal of Rock Mechanics and Mining Sciences & Geomechanics Abstracts* **13** (1976), 311–319.

183. Quinn, G. D. & Bradt, R. C. On the Vickers indentation fracture toughness test. *Journal of the American Ceramic Society* **90,** 673–680 (2007).

184. Woodbury, J. & Vogel, T. A rapid, economical method for polishing thin sections for microprobe and petrographic analyses. *American Mineralogist* **51** (1970).

185. Miller, M., Bobko, C., Vandamme, M. & Ulm, F.-J. Surface roughness criteria for cement paste nanoindentation. *Cement and Concrete Research* **38,** 467–476 (2008).

186. Frasca, B., Savoye, S., Wittebroodt, C., Leupin, O. & Michelot, J.-L. Comparative study of Se oxyanions retention on three argillaceous rocks: Upper Toarcian (Tournemire, France), Black Shales (Tournemire, France) and Opalinus Clay (Mont Terri, Switzerland). *Journal of Environmental Radioactivity* **127,** 133–140 (2014).

187. Abousleiman, Y. N., Tran, M. H., Hoang, S., Bobko, C. P., Ortega, A. & Ulm, F.-J. *Geomechanics field and laboratory characterization of the Woodford Shale: The next gas play* in *SPE Annual Technical Conference and Exhibition* (2007).

188. Klein, C. *The 22nd edition fo the manual of mineral science (after James D. Dana)* 2002.

189. Slatt, R. M. & O'Brien, N. R. Pore types in the Barnett and Woodford gas shales: Contribution to understanding gas storage and migration pathways in fine-grained rocks. *AAPG Bulletin* **95,** 2017–2030 (2011).

190. Maldonado, A., Batzle, M. & Sonnenberg, S. *Mechanical properties of the Niobrara Formation* in *AAPG-RMS 2011 Annual Meeting* **25** (2011), 29.

191. Bull, S. Failure mode maps in the thin film scratch adhesion test. *Tribology International* **30,** 491–498 (1997).

192. Randall, N., Favaro, G. & Frankel, C. The effect of intrinsic parameters on the critical load as measured with the scratch test method. *Surface and Coatings Technology* **137,** 146–151 (2001).

193. Irwin, G. R. Analysis of stresses and strains near the end of a crack traversing a plate. *Journal of Applied Mechanics* (1957).

194. Griffith, A. A. & Eng, M. VI. The phenomena of rupture and flow in solids. *Philosophical Transactions of the Royal Society of London A* **221,** 163–198 (1921).

195. Laubie, H. H. *Linear elastic fracture mechanics in anisotropic solids: Application to fluid-driven crack propagation* PhD thesis (Massachusetts Institute of Technology, 2013).

196. Laubie, H. & Ulm, F.-J. Plane-strain crack problem in transversely isotropic solids for hydraulic fracturing applications. *Journal of Engineering Mechanics* **140,** 04014092 (2014).

197. Brochard, L., Hantal, G., Laubie, H., Ulm, F. J. & Pellenq, R. J.-M. *Fracture mechanisms in organic-rich shales: Role of Kerogen* in *Poromechanics V: Proceedings of the Fifth Biot Conference on Poromechanics* (2013), 2471–2480.

198. Bower, A. F. & Ortiz, M. A three-dimensional analysis of crack trapping and bridging by tough particles. *Journal of the Mechanics and Physics of Solids* **39,** 815–858 (1991).

199. Cotterell, B. & Mai, Y.-W. *Fracture mechanics of cementitious materials* (CRC Press, 2014).

200. Zimmermann, E. A., Launey, M. E. & Ritchie, R. O. The significance of crack-resistance curves to the mixed-mode fracture toughness of human cortical bone. *Biomaterials* **31,** 5297–5305 (2010).

201. Ulm, F., Constantinides, G., Delafargue, A., Abousleiman, Y., Ewy, R., Duranti, L., McCarty, D. & Cheng, A. Material invariant poromechanics properties of shales. *Poromechanics III. Biot Centennial (1905–2005), AA Balkema Publishers, London,* 637–644 (2005).

202. Ulm, F.-J., Delafargue, A. & Constantinides, G. in *Applied micromechanics of porous materials* 207–288 (Springer, 2005).

203. Vernik, L. & Nur, A. Ultrasonic velocity and anisotropy of hydrocarbon source rocks. *Geophysics* **57,** 727–735 (1992).

204. Wenk, H.-R., Lonardelli, I., Franz, H., Nihei, K. & Nakagawa, S. Preferred orientation and elastic anisotropy of illite-rich shale. *Geophysics* **72,** E69–E75 (2007).

205. Sayers, C. M. The effect of kerogen on the elastic anisotropy of organic-rich shales. *Geophysics* **78,** D65–D74 (2013).

206. Schmidt, R. A. Fracture-toughness testing of limestone. *Experimental Mechanics* **16,** 161–167 (1976).

207. Hulstrom, L. C. *The determination of fracture toughness in Westerly granite using the double cantilever beam technique* PhD thesis (Michigan Technological University, 1979).

208. Clifton, R., Simonson, E., Jones, A. & Green, S. Determination of the critical-stress-intensity factor K Ic from internally pressurized thick-walled vessels. *Experimental Mechanics* **16,** 233–238 (1976).

209. Chandler, M. R., Meredith, P. G., Brantut, N. & Crawford, B. R. Fracture toughness anisotropy in shale. *Journal of Geophysical Research: Solid Earth* **121,** 1706–1729 (2016).

210. Eseme, E., Urai, J., Krooss, B. & Littke, R. Review of mechanical properties of oil shales: Implications for exploitation and basin modelling. *Oil Shale* **24,** 159–175 (2007).

211. Sergeyev, Y., Grabowska-Olszewska, B., Osipov, V., Sokolov, V. & Kolomenski, Y. The classification of microstructures of clay soils. *Journal of Microscopy* **120,** 237–260 (1980).

212. Abedi, S., Slim, M., Hofmann, R., Bryndzia, T. & Ulm, F.-J. Nanochemo-mechanical signature of organic-rich shales: a coupled indentation–EDX analysis. *Acta Geotechnica* **11,** 559–572 (2016).

213. Deirieh, A., Ortega, J., Ulm, F.-J. & Abousleiman, Y. Nanochemomechanical assessment of shale: a coupled WDS-indentation analysis. *Acta Geotechnica* **7,** 271–295 (2012).

214. Bunger, A. P., Sarout, J., Kear, J., Delle Piane, C., Detournay, E., Josh, M. & Dewhurst, D. N. Experimental chemoporoelastic characterization of shale using millimeter scale specimens. *Journal of Petroleum Science and Engineering* **118,** 40–51 (2014).

215. Killough, J. E., Wei, C., Liu, H., Yan, B., Qin, G., Wang, H. & Guo, W. *Characterization and analysis on petrophysical parameters of a marine shale gas reservoir* in *SPE Western Regional & AAPG Pacific Section Meeting 2013 Joint Technical Conference* (2013).

216. Akono, A.-T. & Kabir, P. in *New Frontiers in Oil and Gas Exploration* 209–233 (Springer, 2016).

217. Hull, K. L. & Abousleiman, Y. N. in *New Frontiers in Oil and Gas Exploration* 335–366 (Springer, 2016).

218. Abedi, S., Slim, M. & Ulm, F.-J. Nanomechanics of organic-rich shales: the role of thermal maturity and organic matter content on texture. *Acta Geotechnica* **11,** 775–787 (2016).

219. Zeszotarski, J. C., Chromik, R. R., Vinci, R. P., Messmer, M. C., Michels, R. & Larsen, J. W. Imaging and mechanical property measurements of kerogen via nanoindentation1. *Geochimica et cosmochimica acta* **68,** 4113–4119 (2004).

220. Ahmadov, R., Vanorio, T. & Mavko, G. Confocal laser scanning and atomic-force microscopy in estimation of elastic properties of the organic-rich Bazhenov Formation. *The Leading Edge* **28,** 18–23 (2009).

221. Eliyahu, M., Emmanuel, S., Day-Stirrat, R. J. & Macaulay, C. I. Mechanical properties of organic matter in shales mapped at the nanometer scale. *Marine and Petroleum Geology* **59,** 294–304 (2015).

222. Bousige, C., Ghimbeu, C. M., Vix-Guterl, C., Pomerantz, A. E., Suleimenova, A., Vaughan, G., Garbarino, G., Feygenson, M., Wildgruber, C. & Ulm, F.-J. Realistic molecular model of kerogen's nanostructure. *Nature Materials* **15,** 576 (2016).

223. Hantal, G., Brochard, L., Laubie, H., Ebrahimi, D., Pellenq, R. J.-M., Ulm, F.-J. & Coasne, B. Atomic-scale modelling of elastic and failure properties of clays. *Molecular Physics* **112,** 1294–1305 (2014).

224. Akono, A.-T. Energetic size effect law at the microscopic scale: application to progressive-load scratch testing. *Journal of Nanomechanics and Micromechanics* **6,** 04016001 (2016).

225. Akono, A.-T. & Bouché, G. A. Rebuttal: Shallow and deep scratch tests as powerful alternatives to assess the fracture properties of quasi-brittle materials. *Engineering Fracture Mechanics* **158,** 23–38 (2016).

226. Kataruka, A., Mendu, K., Okeoghene, O., Puthuvelil, J. & Akono, A.-T. Microscopic assessment of bone toughness using scratch tests. *Bone Reports* **6,** 17–25 (2017).

227. Akono, A.-T. & Ulm, F.-J. Microscopic toughness of viscous solids via scratching: from amorphous polymers to gas shale. *Journal of Nanomechanics and Micromechanics* **7,** 04017009 (2017).

228. Abousleiman, Y., Tran, M., Hoang, S., Ortega, J. A. & Ulm, F.-J. Geomechanics field characterization of Woodford Shale and Barnett Shale with advanced logging tools and nano-indentation on drill cuttings. *The Leading Edge* **29,** 730–736 (2010).

229. Loucks, R. G., Reed, R. M., Ruppel, S. C. & Jarvie, D. M. Morphology, genesis, and distribution of nanometer-scale pores in siliceous mudstones of the Mississippian Barnett Shale. *Journal of Sedimentary Research* **79,** 848–861 (2009).

230. Sondergeld, C. H., Ambrose, R. J., Rai, C. S. & Moncrieff, J. *Micro-structural studies of gas shales* in *SPE Unconventional Gas Conference* (2010).

231. Bai, B., Elgmati, M., Zhang, H. & Wei, M. Rock characterization of Fayetteville shale gas plays. *Fuel* **105,** 645–652 (2013).

232. Curtis, M. E., Cardott, B. J., Sondergeld, C. H. & Rai, C. S. Development of organic porosity in the Woodford Shale with increasing thermal maturity. *International Journal of Coal Geology* **103,** 26–31 (2012).

233. Josh, M., Esteban, L., Delle Piane, C., Sarout, J., Dewhurst, D. & Clennell, M. Laboratory characterisation of shale properties. *Journal of Petroleum Science and Engineering* **88,** 107–124 (2012).

234. Vandamme, M. & Ulm, F.-J. Nanogranular origin of concrete creep. *Proceedings of the National Academy of Sciences* **106,** 10552–10557 (2009).

235. Christensen, R. *Theory of viscoelasticity: an introduction* (Elsevier, 2012).

236. Pipkin, A. C. *Lectures on viscoelasticity theory* (Springer Science & Business Media, 2012).

237. Ward, I. M. & Hadley, D. W. *An introduction to the mechanical properties of solid polymers* (John Wiley & Sons Ltd.; John Wiley & Sons, Inc., 1993).

238. Lakes, R. S. *Viscoelastic materials* (Cambridge University Press, 2009).

239. Coussy, O. & Ulm, F.-J. Creep and plasticity due to chemo-mechanical couplings. *Archive of Applied Mechanics* **66,** 523–535 (1996).

240. Ulm, F.-J. & Coussy, O. *Mechanics and durability of solids* (Prentice Hall, 2003).

241. Cherepanov, G. P. Crack propagation in continuous media: PMM vol. 31, no. 3, 1967, pp. 476–488. *Journal of Applied Mathematics and Mechanics* **31,** 503–512 (1967).

242. Schapery, R. Correspondence principles and a generalizedJ integral for large deformation and fracture analysis of viscoelastic media. *International Journal of Fracture* **25,** 195–223 (1984).

243. Chaves, E. W. *Notes on continuum mechanics* (Springer Science & Business Media, 2013).

244. Salençon, J. *Handbook of continuum mechanics: General concepts thermoelasticity* (Springer Science & Business Media, 2012).

245. Graham, G. The correspondence principle of linear viscoelasticity theory for mixed boundary value problems involving time-dependent boundary regions. *Quarterly of Applied Mathematics* **26,** 167–174 (1968).

246. Oyen, M. Analytical techniques for indentation of viscoelastic materials. *Philosophical Magazine* **86,** 5625–5641 (2006).

247. Schapery, R. A. A theory of crack initiation and growth in viscoelastic media. *International Journal of Fracture* **11,** 141–159 (1975).

248. Paulino, G. H. & Jin, Z.-H. A crack in a viscoelastic functionally graded material layer embedded between two dissimilar homogeneous viscoelastic layers–antiplane shear analysis. *International Journal of Fracture* **111,** 283–303 (2001).

249. Jin, Z.-H. & Paulino, G. H. A viscoelastic functionally graded strip containing a crack subjected to in-plane loading. *Engineering Fracture Mechanics* **69,** 1769–1790 (2002).

250. Torsaeter, M., Vullum, P. E. & Nes, O.-M. *Nanostructure vs. Macroscopic properties of mancos shale* in *SPE Canadian Unconventional Resources Conference* (2012).

251. Yang, Y., Sone, H., Hows, A. & Zoback, M. *Comparison of brittleness indices in organic-rich shale formations* in *47th US Rock Mechanics/Geomechanics Symposium* (2013).

252. Yoon, H., Dewers, T. A. & Heath, J. E. *Nanopore control on shale gas transport in shale mudstones.* tech. rep. (Sandia National Laboratories (SNL-NM), Albuquerque, NM (United States), 2013).

253. Zargari, S., Prasad, M., Mba, K. C. & Mattson, E. D. Organic maturity, elastic properties, and textural characteristics of self resourcing reservoirs. *Geophysics* **78,** D223–D235 (2013).

254. Lemaıtre, A. Rearrangements and dilatancy for sheared dense materials. *Physical Review Letters* **89,** 195503 (2002).

255. Rassouli, F. & Zoback, M. *A comparison of short-term and long-term creep experiments in unconventional reservoir formations* in *50th US Rock Mechanics/Geomechanics Symposium* (2016).

256. Sone, H. & Zoback, M. D. Mechanical properties of shale-gas reservoir rocks—Part 1: Static and dynamic elastic properties and anisotropy. *Geophysics* **78,** D381–D392 (2013).

257. Sone, H. & Zoback, M. Time-dependent deformation of shale gas reservoir rocks and its long-term effect on the in situ state of stress. *International Journal of Rock Mechanics and Mining Sciences* **69,** 120–132 (2014).

258. Sone, H. & Zoback, M. D. Mechanical properties of shale-gas reservoir rocks—Part 2: Ductile creep, brittle strength, and their relation to the elastic modulusMechanical properties of gas shale—Part 2. *Geophysics* **78,** D393–D402 (2013).

259. Abousleiman, Y., Hull, K., Han, Y., Al-Muntasheri, G., Hosemann, P., Parker, S. & Howard, C. The granular and polymer composite nature of kerogen-rich shale. *Acta Geotechnica* **11,** 573–594 (2016).

260. Lin, Y.-H. *Polymer viscoelasticity: basics, molecular theories, experiments, and simulations* (World Scientific, 2011).

261. Lomnitz, C. Application of the logarithmic creep law to stress. *Journal of Geophysical Research* **67,** 365–368 (1962).

262. Lomnitz, C. Creep measurements in igneous rocks. *The Journal of Geology* **64,** 473–479 (1956).

263. Valsa, J. & Brančik, L. Approximate formulae for numerical inversion of Laplace transforms. *International Journal of Numerical Modelling: Electronic Networks, Devices and Fields* **11,** 153–166 (1998).

264. Ruina, A. Slip instability and state variable friction laws. *Journal of Geophysical Research: Solid Earth* **88,** 10359–10370 (1983).

265. Dieterich, J. H. & Kilgore, B. D. Direct observation of frictional contacts: New insights for state-dependent properties. *Pure and Applied Geophysics* **143,** 283–302 (1994).

266. Bowden, F. P. & Tabor, D. *The friction and lubrication of solids* (Oxford university press, 2001).

267. Dieterich, J. H. & Conrad, G. Effect of humidity on time-and velocity-dependent friction in rocks. *Journal of Geophysical Research: Solid Earth* **89,** 4196–4202 (1984).

268. Fantner, G. E., Hassenkam, T., Kindt, J. H., Weaver, J. C., Birkedal, H., Pechenik, L., Cutroni, J. A., Cidade, G. A., Stucky, G. D. & Morse, D. E. Sacrificial bonds and hidden length dissipate energy as mineralized fibrils separate during bone fracture. *Nature Materials* **4,** 612 (2005).

269. Wang, Z.-Q. & Detournay, E. The tip region of a near-surface hydraulic fracture. *Journal of Applied Mechanics* (2018).

270. Garagash, D. & Detournay, E. The tip region of a fluid-driven fracture in an elastic medium. *Journal of Applied Mechanics* **67,** 183–192 (2000).

271. Savitski, A. & Detournay, E. Propagation of a penny-shaped fluid-driven fracture in an impermeable rock: asymptotic solutions. *International Journal of Solids and Structures* **39,** 6311–6337 (2002).

272. Garagash, D. I. Propagation of a plane-strain hydraulic fracture with a fluid lag: Early-time solution. *International Journal of Solids and Structures* **43,** 5811–5835 (2006).

273. Detournay, E. Propagation regimes of fluid-driven fractures in impermeable rocks. *International Journal of Geomechanics* **4,** 35–45 (2004).

274. Of Energy, U. D. *CARBON STORAGE ATLAS - FIFTH EDITION* `https://www.netl.doe.gov/research/coal/carbon-storage/atlasv`.

275. Bradshaw, J. & Rigg, A. The GEODISC program: research into geological sequestration of CO2 in Australia. *Environmental Geosciences* **8,** 166–176 (2001).

276. Mathieson, A., Midgely, J., Wright, I., Saoula, N. & Ringrose, P. In Salah CO2 Storage JIP: CO2 sequestration monitoring and verification technologies applied at Krechba, Algeria. *Energy Procedia* **4,** 3596–3603 (2011).

277. Rutqvist, J., Vasco, D. W. & Myer, L. Coupled reservoir-geomechanical analysis of CO2 injection at In Salah, Algeria. *Energy Procedia* **1,** 1847–1854 (2009).

278. Michael, K., Golab, A., Shulakova, V., Ennis-King, J., Allinson, G., Sharma, S. & Aiken, T. Geological storage of CO 2 in saline aquifers—a review of the experience from existing storage operations. *International Journal of Greenhouse Gas Control* **4,** 659–667 (2010).

279. Torp, T. A. & Gale, J. Demonstrating storage of CO2 in geological reservoirs: The Sleipner and SACS projects. *Energy* **29,** 1361–1369 (2004).

280. Maldal, T. & Tappel, I. *-CO 2 Underground Storage for Snøhvit Gas Field Development* in *Greenhouse Gas Control Technologies-6th International Conference* (2003), 601–606.

281. Chalaturnyk, R. *Geomechanical characterization of the Weyburn Field for geological storage of CO2* in *1st Canada-US Rock Mechanics Symposium* (2007).

282. Rodosta, T. D., Litynski, J. T., Plasynski, S. I., Hickman, S., Frailey, S. & Myer, L. US Department of energy's site screening, site selection, and initial characterization for storage of CO2 in deep geological formations. *Energy Procedia* **4,** 4664–4671 (2011).

283. Oldenburg, C. M. Screening and ranking framework for geologic CO 2 storage site selection on the basis of health, safety, and environmental risk. *Environmental Geology* **54,** 1687–1694 (2008).

284. Bachu, S. Screening and ranking of sedimentary basins for sequestration of CO 2 in geological media in response to climate change. *Environmental Geology* **44,** 277–289 (2003).

285. Chabora, E. R. & Benson, S. M. Brine displacement and leakage detection using pressure measurements in aquifers overlying CO2 storage reservoirs. *Energy Procedia* **1,** 2405–2412 (2009).

286. Nogues, J. P., Nordbotten, J. M. & Celia, M. A. Detecting leakage of brine or CO2 through abandoned wells in a geological sequestration operation using pressure monitoring wells. *Energy Procedia* **4,** 3620–3627 (2011).

287. Walsh, F. R. & Zoback, M. D. Oklahoma's recent earthquakes and saltwater disposal. *Science Advances* **1,** e1500195 (2015).

288. Ellsworth, W. L. Injection-induced earthquakes. *Science* **341,** 1225942 (2013).

289. Baklid, A., Korbol, R. & Owren, G. *Sleipner Vest CO2 disposal, CO2 injection into a shallow underground aquifer* in *SPE Annual Technical Conference and Exhibition* (1996).

290. Finley, R. J., Frailey, S. M., Leetaru, H. E., Senel, O., Couëslan, M. L. & Scott, M. Early operational experience at a one-million tonne CCS demonstration project, Decatur, Illinois, USA. *Energy Procedia* **37,** 6149–6155 (2013).

291. Frailey, S., Finley, R. & Rupp, J. A. Illinos basin, Midwest carbon dixoide EOR challenges may be surmontable. *Oil and Gas Journal* **111,** 64–73 (2013).

292. Bauer, R. A., Carney, M. & Finley, R. J. Overview of microseismic response to CO 2 injection into the Mt. Simon saline reservoir at the Illinois Basin-Decatur Project. *International Journal of Greenhouse Gas Control* **54,** 378–388 (2016).

293. Will, R., El-Kaseeh, G., Jaques, P., Carney, M., Greenberg, S. & Finley, R. Microseismic data acquisition, processing, and event characterization at the Illinois Basin–Decatur Project. *International Journal of Greenhouse Gas Control* **54,** 404–420 (2016).

294. Frailey, S. M. & Finley, R. J. *Overview of the Midwest Geologic Sequestration Consortium Pilot Projects* in *SPE International Conference on CO2 Capture, Storage, and Utilization* (2010).

295. Will, R., Smith, V., Lee, D. & Senel, O. Data integration, reservoir response, and application. *International Journal of Greenhouse Gas Control* **54,** 389–403 (2016).

296. Smith, V. & Jaques, P. Illinois Basin–Decatur Project pre-injection microseismic analysis. *International Journal of Greenhouse Gas Control* **54,** 362–377 (2016).

297. Training, S. & Program, E. *Maps* `www.sequestration.org`.

298. Bissell, R., Vasco, D., Atbi, M., Hamdani, M., Okwelegbe, M. & Goldwater, M. A full field simulation of the in Salah gas production and CO2 storage project using a coupled geo-mechanical and thermal fluid flow simulator. *Energy Procedia* **4,** 3290–3297 (2011).

299. Hawkes, C., McLellan, P., Zimmer, U. & Bachu, S. *Geomechanical Factors Affecting Geological Storage of CO in Depleted Oil and Gas Reservoirs* in *Canadian International Petroleum Conference* (2004).

300. Freiburg, J. T., Morse, D. G., Leetaru, H. E., Hoss, R. P. & Yan, Q. *A Depositional and Diagenetic Characterization of the Mt. Simon Sandstone at the Illinois Basin-Decatur Project Carbon Capture and Storage Site, Decatur, Illinois, USA* tech. rep. (Illinois State Geological Survey, Prairie Research Institute, University of Illinois, 2014).

301. Yoksoulian, L., Freiburg, J., Butler, S., Berger, P. & Roy, W. Mineralogical alterations during laboratory-scale carbon sequestration experiments for the Illinois Basin. *Energy Procedia* **37,** 5601–5611 (2013).

302. Benson, S. M. & Cole, D. R. CO2 sequestration in deep sedimentary formations. *Elements* **4,** 325–331 (2008).

303. Zoback, M. D. & Gorelick, S. M. Earthquake triggering and large-scale geologic storage of carbon dioxide. *Proceedings of the National Academy of Sciences* **109,** 10164–10168 (2012).

304. Waza, T., Kurita, K. & Mizutani, H. The effect of water on the subcritical crack growth in silicate rocks. *Tectonophysics* **67,** 25–34 (1980).

305. Holder, J., Olson, J. E. & Philip, Z. Experimental determination of subcritical crack growth parameters in sedimentary rock. *Geophysical Research Letters* **28,** 599–602 (2001).

306. Colón, C. F. J., Oelkers, E. H. & Schott, J. Experimental investigation of the effect of dissolution on sandstone permeability, porosity, and reactive surface area1. *Geochimica et Cosmochimica Acta* **68,** 805–817 (2004).

307. Hu, D., Zhou, H., Zhang, F. & Shao, J.-F. Evolution of poroelastic properties and permeability in damaged sandstone. *International Journal of Rock Mechanics and Mining Sciences* **47,** 962–973 (2010).

308. Grgic, D. & Giraud, A. The influence of different fluids on the static fatigue of a porous rock: Poro-mechanical coupling versus chemical effects. *Mechanics of Materials* **71,** 34–51 (2014).

309. Rathnaweera, T., Ranjith, P., Perera, M., Haque, A., Lashin, A., Al Arifi, N., Chandrasekharam, D., Yang, S., Xu, T., Wang, S. & E, Y. CO2-induced mechanical behaviour of Hawkesbury sandstone in the Gosford basin: An experimental study. *Materials Science and Engineering: A* **641,** 123–137 (2015).

310. Sun, Y., Aman, M. & Espinoza, D. N. Assessment of mechanical rock alteration caused by CO2 water mixtures using indentation and scratch experiments. *International Journal of Greenhouse Gas Control* **45,** 9–17 (2016).

311. Ulm, F.-J., Vandamme, M., Bobko, C., Alberto Ortega, J., Tai, K. & Ortiz, C. Statistical indentation techniques for hydrated nanocomposites: concrete, bone, and shale. *Journal of the American Ceramic Society* **90,** 2677–2692 (2007).

312. Randall, N. X., Vandamme, M. & Ulm, F.-J. Nanoindentation analysis as a two-dimensional tool for mapping the mechanical properties of complex surfaces. *Journal of Materials Research* **24,** 679–690 (2009).

313. Zhu, W., Fonteyn, M., Hughes, J. & Pearce, C. in *Nanotechnology in Construction 3* 403–408 (Springer, 2009).

314. Oliver, W. C. & Pharr, G. M. Measurement of hardness and elastic modulus by instrumented indentation: Advances in understanding and refinements to methodology. *Journal of Materials Research* **19,** 3–20 (2004).

315. Aksu, I., Bazilevskaya, E. & Karpyn, Z. Swelling of clay minerals in unconsolidated porous media and its impact on permeability. *GeoResJ* **7,** 1–13 (2015).

316. Karaborni, S., Smit, B., Heidug, W., Urai, J. & Van Oort, E. The swelling of clays: molecular simulations of the hydration of montmorillonite. *Science* **271,** 1102–1104 (1996).

317. Katti, K. & Katti, D. Effect of clay-water interactions on swelling in montmorillonite clay. *Department of Civil Engineering and Construction North Dakota State University, Fargo* (2001).

318. Segad, M., Jonsson, B., Åkesson, T. & Cabane, B. Ca/Na montmorillonite: structure, forces and swelling properties. *Langmuir* **26,** 5782–5790 (2010).

319. Marbler, H., Erickson, K. P., Schmidt, M., Lempp, C. & Pollmann, H. Geomechanical and geochemical effects on sandstones caused by the reaction with supercritical CO 2: an experimental approach to in situ conditions in deep geological reservoirs. *Environmental Earth Sciences* **69,** 1981–1998 (2013).

320. Vialle, S. & Vanorio, T. Laboratory measurements of elastic properties of carbonate rocks during injection of reactive CO2-saturated water. *Geophysical Research Letters* **38** (2011).

321. Rimmelé, G., Barlet-Gouédard, V. & Renard, F. Evolution of the petrophysical and mineralogical properties of two reservoir rocks under thermodynamic conditions relevant for CO2 geological storage at 3 km depth. *Oil & Gas Science and Technology–Revue de l'Institut Français du Pétrole* **65,** 565–580 (2010).

322. Nguyen, M., Bemer, E. & Dormieux, L. *Micromechanical modeling of carbonate geomechanical properties evolution during acid gas injection* in *45th US Rock Mechanics/Geomechanics Symposium* (2011).

323. Akono, A.-T., Kabir, P., Shi, Z., Fuchs, S., Tsotsis, T., Jessen, K., Werth, C. & Goodman, A. Modeling CO2-Induced Alterations in Mt. Simon Snadstone via Nanomechanics-Under Review. *Rock Mechanics and Rocj Engineering* (2018).

324. Fuchs, S. J. *Geochemical and geomechanical alteration of Mt. Simon sandstone due to prolonged contact with CO2-saturated brine during carbon sequestration* PhD thesis (2017).